PB88-166814

Fundamental Combustion Research Applied to Pollution Formation. Volume 2A
Physics and Chemistry of Two-Phase Systems Flame Combustion Processes

Energy and Environmental Research Corp.
Irvine, CA

Prepared for

Environmental Protection Agency
Research Triangle Park, NC

Jan 88

U.S. Department of Commerce
National Technical Information Service
NTIS

PB88-166814

EPA/600/7-88/001a
January 1988

FUNDAMENTAL COMBUSTION RESEARCH APPLIED TO POLLUTION FORMATION

Volume IIa. Physics and Chemistry of Two-Phase Systems: Flame Combustion Processes

by

W. R. Seeker and M. P. Heap
Energy and Environmental Research Corporation
18 Mason
Irvine, California 92714

EPA Contract No. 68-02-2631
EPA Project Officer: W. Steven Lanier
Air and Energy Engineering Research Laboratory
Research Triangle Park, North Carolina 27711

AIR AND ENERGY ENGINEERING RESEARCH LABORATORY
OFFICE OF RESEARCH AND DEVELOPMENT
U.S. ENVIRONMENTAL PROTECTION AGENCY
RESEARCH TRIANGLE PARK, NC 27711

REPRODUCED BY
U.S. DEPARTMENT OF COMMERCE
NATIONAL TECHNICAL
INFORMATION SERVICE
SPRINGFIELD, VA. 22161

TECHNICAL REPORT DATA

(Please read Instructions on the reverse before completing)

1. REPORT NO. EPA/600/7-88/001a	2.	3. RECIPIENT'S ACCESSION NO. PB88 166814/AS
4. TITLE AND SUBTITLE Fundamental Combustion Research Applied to Pollution Formation; Volume IIa. Physics and Chemistry of Two-Phase Systems: Flame Combustion Processes		5. REPORT DATE January 1988
		6. PERFORMING ORGANIZATION CODE
7. AUTHOR(S) W. R. Seeker and M. P. Heap		8. PERFORMING ORGANIZATION REPORT NO.
9. PERFORMING ORGANIZATION NAME AND ADDRESS Energy and Environmental Research Corporation 18 Mason Irvine, California 92714		10. PROGRAM ELEMENT NO.
		11. CONTRACT/GRANT NO. 68-02-2631
12. SPONSORING AGENCY NAME AND ADDRESS EPA, Office of Research and Development Air and Energy Engineering Research Laboratory Research Triangle Park, NC 27711		13. TYPE OF REPORT AND PERIOD COVERED Final; 1/77 - 9/80
		14. SPONSORING AGENCY CODE EPA/600/13

15. SUPPLEMENTARY NOTES Project officer W. S. Lanier is no longer with the Agency. For details, contact William P. Linak, Mail Drop 65, 919/541-5792.

16. ABSTRACT

The reports included in this three-part volume describe eight studies by various investigators, to better understand the physics and chemistry of two-phase combustion with respect to pollution formation. Volume IIa describes mechanisms of fuel nitrogen processing in large-scale utility flames burning pulverized coal and heavy fuel oils, in three parts: (1) high temperature decomposition and combustion of pulverized coal (EERC), (2) detailed measurement of long pulverized coal flames for the characterization of pollutant formation (International Flame Research Foundation), and (3) heavy oil combustion in shear layers (United Technologies Research Center).

17. KEY WORDS AND DOCUMENT ANALYSIS

a. DESCRIPTORS		b. IDENTIFIERS/OPEN ENDED TERMS	c. COSATI Field/Group	
Pollution	Nitrogen	Pollution Control	13B	07B
Combustion	Nitrogen Oxide (NO)	Stationary Sources	21B	
Research	Pulverized Fuels	Fundamental Research	14F	21D
Physics	Fuel Oil		20A	
Chemistry			07A	
Flames				

18. DISTRIBUTION STATEMENT Release to Public	19. SECURITY CLASS *(This Report)* Unclassified	21. NO. OF PAGES 282
	20. SECURITY CLASS *(This page)* Unclassified	22. PRICE

EPA Form 2220-1 (9-73)

NOTICE

This document has been reviewed in accordance with U.S. Environmental Protection Agency policy and approved for publication. Mention of trade names or commercial products does not constitute endorsement or recommendation for use.

ABSTRACT

This document is one of the series of reports describing work performed under the Fundamental Combustion Research (FCR) Applied to Pollution Formation Program (EPA Contract 68-02-2631). The FCR program was structured under a master contract concept with Energy and Environmental Research (EER) as the prime contractor and with individual studies performed either under subcontract or directly by EER. Volume IIA of the final report series provides project reports from three studies on the physics and chemistry of two-phase flames. The first study reported was conducted by EER and was designed to develop plausible physical models of coal particle combustion and pollution processes. This was accomplished by making non-intrusive observations of burning coal particles along with pyrometry and chemical analysis of sampled solid and gas phase products. The second reported study in this volume was performed by the International Flame Research Foundation and provides detailed in-flame measurements from long, pulverized coal-flames. Data from this study augments the limited data base characterizing pollution formation processes in practical-scale flames. The final reported study in this volume was conducted by United Technologies Research Laboratories. It was designed as an initial investigation into the combustion of heavy oil spray combustion in shear layers.

TABLE OF CONTENTS

Page

INTRODUCTION 1

Part I. THE HIGH TEMPERATURE DECOMPOSITION AND COMBUSTION OF PULVERIZED COAL (EER) I

1.0 INTRODUCTION I-1
2.0 EXPERIMENTAL I-4
3.0 RESULTS I-34
4.0 SUMMARY I-75
5.0 RECOMMENDATIONS FOR FUTURE WORK I-91
6.0 REFERENCES I-93
7.0 ACKNOWLEDGEMENTS I-95

Part II. DETAILED MEASUREMENTS IN LONG PULVERIZED COAL FLAMES FOR THE CHARACTERIZATION OF POLLUTION FORMATION (IFRF) II

1.0 INTRODUCTION II-2
2.0 EXPERIMENTAL CONDITIONS II-5
3.0 EXPERIMENTAL RESULTS II-16
4.0 FURTHER EVALUATION OF RESULTS II-92
5.0 CONCLUSIONS II-105
6.0 REFERENCES II-107
7.0 TABLES OF FLAME POINT DATA II-108
8.0 PHOTOGRAPHS OF FLAMES II-123

Part III. HEAVY OIL SPRAY COMBUSTION IN SHEAR LAYERS (UTRC) III

1.0 INTRODUCTION III-3
2.0 APPARATUS - DESIGN AND DESCRIPTION III-4
3.0 TEST RESULTS III-23
4.0 CONCLUSIONS III-36
5.0 REFERENCES III-37

INTRODUCTION

The final reports for the three individual projects which make up the Flame Combustion Processes program element are separately presented in subsequent sections. The first report covers a project involved with the study of high temperature decomposition and oxidation of pulverized coal particles under flame type conditions. The purpose of this report was to describe the fundamental processes that accompany the combustion of pulverized coal and the associated formation of nitric oxide. Despite the fact that coal has been burned for decades and has been the subject of study for nearly as long, little is actually known about the physical processes occurring to the individual coal particles and their close environment. This knowledge was not required to simply burn coal. However, this information would be extremely useful if the goal is to design a combustion system which not only burns the coal but also controls the combustion environment in such a way as to limit pollution formation during the process. For example, the reaction temperature is of paramount importance to the conversion of reduced nitrogen species to NO_x and to the amount of nitrogen species evolved from the coal during devolatilization. Thus, one means of controlling NO_x formation is to control the temperature history. However, because of the two phase nature of the flame, there are several reaction temperatures (including the flame, particle, gas and film around the particle) which may respond differently to changes in combustion environment. Until recently the flame temperature typically was only calculated and measurements of the gas temperature and (even less often) the particle temperature were seldom performed. Thus, the definition of the various temperatures, the determination of how combustion parameters and coal type influence the temperatures and the determination of how these in turn influence the processing of fuel nitrogen, are specific goals of the EER study.

Another approach that could be used to develop combustion modification control techniques is to utilize mathematical models which adequately describe the important physical and chemical processes. These models would allow limit case and parameter screening studies to be performed which are difficult if not impossible to perform on actual combustion systems. Such models are also invaluable for the interpretation and extrapolation of pilot scale results.

However, without the insight gained from actually observing coal particles burning, it would not be easy to develop the models. The EER study was designed to supply information on the microscale phenomenon that occurs around individual particles in an environment which simulates those encountered in large scale turbulent diffusion flames, that would be of direct use for model development.

The final objective of the EER study was to define the various processes and time frames for reactions involving pulverized coal particles and the interactions of these processes with the pollutant formation processes. This information is useful for interpretation of other data in Volume II as well as other volumes. This section thus provides the framework for the detailed discussions of these processes in other sections.

The second study in this major program element was undertaken at the International Flame Research Foundation (IFRF). This study was in many ways complementary to the EER pulverized coal study by extending detailed measurements to large pulverized coal flames. However, there was no attempt to uncouple chemistry from the fluid dynamics. The purpose of this program was to utilize state-of-the-art measuring techniques to characterize a number of long pulverized coal flames under well-defined input and boundary conditions.

The IFRF work is restricted to measurements of pulverized coal flames with all axial flow and the use of a very simple double concentric, parallel flow burner system. Such burner systems produce "long" flames which are far-field dominated and where the heat release is protracted. While such flames exhibit the real characteristics of certain classes of furnace flames, the results are more amenable to analysis, and a knowledge of mean residence time could provide the necessary link between the flow field and the reaction kinetics.

Measurements in these flames included the determination of local gas and solids compositions and concentrations, temperatures, and radiative and aerodynamic characteristics in sufficient detail that the data can be used for the validation of prediction procedures both for the global combustion process and for specific phenomena relating to coal particle combustion. This characterization can aid model development as well as providing information which will be of direct value to other EPA programs.

The third study which made up the Flame Combustion Processes program element was directed at heavy fuel oil combustion and was performed by the United Technologies Research Center (UTRC). The oxidation of the nitrogen chemically bound in the fuel is the dominant source of nitrogen oxide (NO_x) emissions from heavy oil fired combustion systems as it is for coal fired systems. A number of research programs have shown that chemical characteristics of the fuel, chemical and thermal gas phase environment, and details of fuel/oxidizer contacting have a first order impact on NO_x emission levels. Studies have been underway for at least a decade (and continue still) to define the gas phase chemical kinetic pathways and reaction rates describing oxidation of fuel bound nitrogen to NO_x (see Volume I of the FCR Final Report). Other current studies are examining, in a global sense, the interaction of fuel oil atomization and combustor aerodynamics (see Volume IV). Valuable information on droplet burning rates was generated in studies dating back to the 1940's and further refinement of those results with emphasis on pollutant emissions are currently underway.

A continuing difficulty in development of combustion modification technology for NO_x control is how to apply limit case fundamental research results to practical combustion hardware. Most of the pertinent chemical kinetic data on NO_x formation has been obtained in shock tubes, flat flame burners or stirred reactors which purposefully minimize the influence of fuel/air contacting. Similarly, most fundamental droplet combustion studies have been performed with uniform gas phase backgrounds or in laminar plug flow environments.

In a practical boiler flame the injected oil droplets typically experience an initial hot, fuel rich region prior to encounter with an aerodynamic shear zone. Droplet residence time in the hot, fuel rich zone, strength and location of the shear region and the angle with which the droplets intersect the shear region are all parameters controlled by the detailed design features of the burner. Further complicating application of fundamental data to practical burner design is the fact that droplets generally burn as a cloud rather than as single isolated spheres.

The UTRC study was intended to bridge the gap between limit case droplet (and gas phase chemistry) experimental studies and the significantly more complex practical oil spray flame. To accomplish that goal requires a specially designed experimental facility incorporating most of the dominant features of a practical flame, yet with sufficient control and characterization to permit application of fundamental understanding to data analysis. Specifically, the experiment must begin with injection of an array of droplets with known but variable initial diameter into a hot fuel-rich region of combustion products. Both the temperature and stoichiometry of this region must be controllable. As in a practical flame, a bounding shear layer (of variable strength) must separate the hot, rich zone from a stream of cooler oxidizer. Further, the residence time of the droplets in the rich region and the ballistic characteristics of shear layer entry by the drop, must be controllable.

The UTRC report describes the design, construction, and initial testing of an experimental facility satisfying the above requirements. It must be emphasized that experimental results of a truly fundamental or basic nature are not to be expected. Rather, it is hoped that experimental conditions are sufficiently controllable and characterized to:

1. allow data analysis based on fundamental understanding, and

2. provide detailed insight into the interactions and phenomena controlling NO_x formation in practical heavy oil flames.

I. THE HIGH-TEMPERATURE DECOMPOSITION AND COMBUSTION OF PULVERIZED COAL

Prepared by:

W. R. Seeker
G. S. Samuelsen
J. C. Kramlich
M. P. Heap

Energy and Environmental Research Corporation
18 Mason
Irvine, CA 92714

TABLE OF CONTENTS

Section Page

1.0 INTRODUCTION I-1

2.0 EXPERIMENTAL I-4

2.1 Reactor Systems I-4
2.2 Diagnostics I-11

2.2.1 Burner Characterization I-14
2.2.2 Physical Analysis I-17
2.2.3 Thermal Analysis I-22
2.2.4 Chemical Analysis I-27

2.3 Fuel Selection I-30

3.0 RESULTS I-34

3.1 The High Temperature Thermal Decomposition and Oxidation of Other Coal Types I-34

3.1.1 Physical Phenomenon I-34
3.1.2 Chemical Phenomenon I-45

3.2 The High Temperature Thermal Decomposition and Oxidation of Other Coal Types I-50

3.2.1 Physical Phenomenon I-53
3.2.2 Thermal Phenomenon I-59
3.2.3 Chemical Phenomenon I-66

4.0 SUMMARY AND DISCUSSION 1-75

4.1 Soot Formation I-75
4.2 Coal Nitrogen Behavior I-76
4.3 Modeling Volatile Oxidation I-82

5.0 RECOMMENDATIONS FOR FUTURE WORK I-91

6.0 REFERENCES I-93

7.0 ACKNOWLEDGEMENTS I-94

LIST OF FIGURES

Figure Page

1.1 Phenomena Affecting Pollutant Formation in a Pulverized-Coal Flame I-2

2.1 Flat Flame Burner and Particle Injection System I-5

2.2 Estimated Transient Temperature Behavior of Center Line of Carrier Tube Flow and Linear Temperature Responses I-7

2.3 Reactant Supply System I-9

2.4 Fluidized Bed Feeder for Coal Flow Rates of 1.0 to 10 gm/min I-10

2.5 Fluidized Bed Calibration for Pulverized Coal Feed I-12

2.6 Reactor System I-13

2.7 Sodium D-Line Reversal Optics and Strip Lamp Calibration . . I-15

2.8 Sodium Line Reversal Measurements of Gas Temperature in Thermal Decomposition Reactor I-16

2.9 Holography and Reconstruction Systems I-19

2.10 High Speed and Single Flame Shadowgrapn Systems I-21

2.11 Two-Color Pyrometry System I-25

2.12 Comparison of Gas Temperature Measured by Sodium Line Reversal and Inert Particle temperatures Measured by Two-Color Pyrometry I-26

2.13 Extractive Probe I-28

2.14 Fuel NO as a Function of Fuel Nitrogen Content I-31

3.1 Physical Behavior of 80 um Four Corners NM Coal Particles in Lean Methane Air Flame I-36

3.2 Size Distribution Profile for 80 Four Corners NM Bituminous Coal in a Lean Methane/Air Flame I-38

LIST OF FIGURES (Continued)

Figure		Page
3.3	Holograms, Micrographs and Particle Pyrometry of 80 um Four Corners NM Coal Particles	I-39
3.4	Influence of Injection Velocity on Volatile Trail for Utah Bituminous Coal Particles	I-41
3.5	High-Speed Shadowgraphs of Reactions 80 um Bituminous Coal Particles (Speed Between Images - 1 msec)	I-42
3.6	Schematic of Pulverized Coal Combustion Model	I-44
3.7	Influence of Particle Size on the Thermal and Physical Phenomenon LFour Corners NM Coal)	I-46
3.8	Component Burnout Profiles for 80 um Four Corners NM Bituminous Coal in a Lean CH_4/Air Flame	I-47
3.9	Gas Phase Composition Profiles for 80 um Four Corners NM Bituminous Coal in a Lean Methane/Air Flame	I-49
3.10	Solid Phase Composition Profile--40 um Four Corners	I-51
3.11	Gas-Phase Composition Profiles for 40 um Four Corners NM Coal in a Lean Methane/Air Flame	I-52
3.12	Scanning Electron Micrographs of Untreated Pulverized Coals	I-54
3.13	Physical Phenomenon Associated With Beulah Lignite Particle Decomposition (CH_4/Air Flame, 35% Excess Air)	I-55
3.14	Surface Area Changes for Beulah Montana Lignite in Lean Methane/Air Flame	I-57
3.15	The Effect of Coal Type on Physical and Thermal Phenomenon Associated With Pulverized Coal Decomposition	I-58
3.16	Two-Color Temperature Profiles of 80 um Four Corners NM Bituminous Coal and a Single Pass Char	I-60
3.17	Two-Color Temperature Profiles for Pulverized Coal Samples in Lean Methane/Air Flame	I-61
3.18	Volatile Calorific Yield and Maximum Particle Temperature Excess	I-63
3.19	Comparison of Two-Color Response With and Without Oxygen Present (Four Corners NM 80 um)	I-65

LIST OF FIGURES (Continued)

Figure Page

3.20 Solids Composition Profile--Utah Bituminous I-67

3.21 Gas-Phase Composition Profile for Utah Bituminous Coal in a Lean Methane/Air Flame I-68

3.22 Solid Composition Profile--Beulah Lignite I-69

3.23 Component Burnout and Elemental Analysis Profiles for Savage Montana Lignite in a Lean Methane/Air Flame I-70

3.24 Gas-Phase Composition Profile for Beulah ND Lignite in a Lean Methane/Air Flame I-71

3.25 Component Burnout and Elemental Analysis Profiles for Single Pass Four Corner NM 80 um Char in Lean Methane/Air Flame I-72

4.1 Nitrogen Burnout and Yields for 80 um Four Corner NM Coal in a Lean CH_4/Air Flame I-78

4.2 Nitrogen Yield Profiles as NO Based on Solid Phase Composition Measurements I-79

4.3 Predicted Nitrogen Burnout Profile From Particle Temperature History and Nitrogen Pyrolysis Correlation (Pohl and Sarofim, 1976) and 40 um Four Corners NM Coal . I-80

4.4 Influence of Coal Feed Rate on Conversion Efficiency of Coal-Nitrogen to NO for 40 um Four Corners NM Coal . . I-81

4.5 Σ(XN) Speciation for 80 um Bituminous τ = 10 ms I-84

4.6 Predicted Cloud Temperature, O_2 Profile, and CH_4 Profile for Spherical Diffusion Flame as a Function of Devolatilization Time, τ for 80 um Particles I-85

4.7 Predicted Behavior for Bituminous Coal Particle Cloud as a Function of Particle Size I-86

4.8 Predicted Cloud Behavior for 80 um Bituminous Particles as a Function of Free-Stream Oxygen Concentration (τ = 10 msec) I-88

LIST OF FIGURES (Concluded)

Figure Page

4.9 Predicted Thermal and Chemical Profiles for 80 um Bituminous Pariticles as a Function of Gas Temperature (τ = 10 msec) I-89

4-10 Predicted Profiles for Bituminous and Lignite Clouds With Devolatilization Time of 100 msec I-90

LIST OF TABLES

Table Page

2.I Physical Diagnostic Techniques I-18

2.II Chemical Analysis Techniques I-29

2.III Coal Analyses I-33

3.I Volatile Calorific Yields, Temperature Overshoots, and Ignition Distance I-64

3.II Peak Levels and Positions of Volatile Species I-74

1.0 INTRODUCTION

The uncertainty in the supply of clean-burning natural gas and distillate oils has resulted in a closer inspection of the relatively abundant energy source, coal. As a combustion source in larger scale utility boilers, the traditional approach has been to first pulverize the coal into a fine powder in the size range of 1-200 um. A pulverized coal burner is then used to inject the coal into the combustion chamber and to control the mixing of the coal and air streams. The resulting two phase flame is uniquely different from flames associated with either natural gas or oils. Primarily, the flame characteristics are intimately tied up with the sequence of events which occur to individual coal particles as they move into the high temperature zone and are heated by convection and radiation. The delineation of these events for coal particles under flame-like conditions is one of the objectives of this program. The description of the events will include information on three distinct areas: physical behavior, thermal behavior and chemical behavior.

The direct combustion of pulverized coal also has several problems of primary concern, including emissions of NO_x, SO_x, and particulate. Due to the countless variables involved with coal, a better understanding of the fundamental aspects of both the combustion process and the pollution formation process would enhance the ability to develop pollution control techniques. It is arguable that a complete understanding is not a prerequisite for the efficient and clean use of pulverized coal, but it is unarguable that such a knowledge would ameliorate that capability.

A schematic representation of a pulverized coal flame is shown in Figure 1.1 along with a delineation of some of the critical questions still unanswered concerning the combustion of pulverized coal and the generation of pollution. These questions involve many of the basic processes underway as a particle decomposes and burns. An understanding of the physical processes occurring in the flame zone is mandatory if the relevant phenomenon are to be modeled correctly.

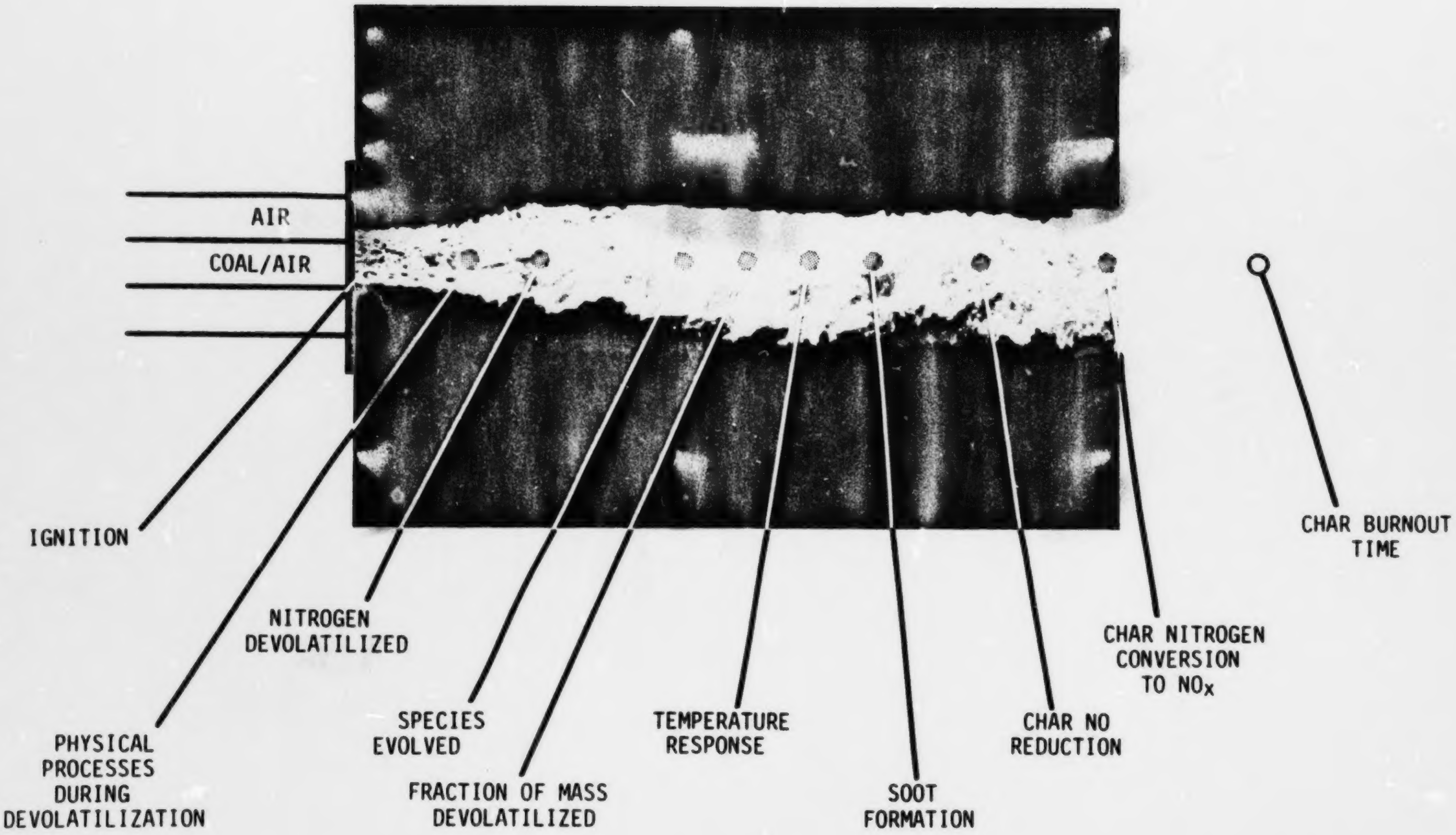
AIR
COAL/AIR
IGNITION
NITROGEN DEVOLATILIZED
PHYSICAL PROCESSES DURING DEVOLATILIZATION
SPECIES EVOLVED
FRACTION OF MASS DEVOLATILIZED
TEMPERATURE RESPONSE
SOOT FORMATION
CHAR NO REDUCTION
CHAR NITROGEN CONVERSION TO NO$_x$
CHAR BURNOUT TIME

- FUEL EFFECTS
- INFLUENCE OF TIME/TEMPERATURE/STOICHIOMETRY HISTORY

Figure 1.1. Phenomena Affecting Pollutant Formation in a Pulverized-Coal Flame.

One example of a process that is intertwined with the other chemical, thermal and physical phenomenon is coal particle ignition. The flame ignition distance is of considerable importance to practical burner design since it is the controlling parameter for flame stability and premixing. For example, lifted, long turbulent diffusion flames are known to produce substantially higher NO_x levels than attached flames. Advanced burner designs for low NO_x combustion of pulverized coal attempt to control air/fuel mixing and rely on rapid ignition with no or controllable premixing. A simplified treatment of particle ignition assumes that volatiles are released uniformly around the particle and burn in a spherical element in the gaseous boundary layer. This will significantly increase the temperature of the particle/boundary layer microsystem. Alternatively, if convective forces pull the volatiles away from the particle surface, then the volatiles may mix and react in the free stream without an immediate impact upon particle temperatures. The presence of a volatile cloud surrounding a particle can also impact particle ignition and subsequent heterogeneous reaction by shielding the surface from oxygen.

The goal of this program was to aid in obtaining and confirming plausible physical models of coal particle combustion and pollution formation. This was accomplished by combining the use of non-obtrusive observations of burning particles along with pyrometry and chemical analysis of sampled solid and gas phase products. The approach taken was to simulate the backmixed near field of a pulverized coal flame by injecting sized coal particles into a hydrocarbon supported flat flame. A specially designed laminar flat flame burner assembly was constructed for this purpose which allowed optical access for laser holography, shadowgraphy, high speed photography and optical pyrometry, and mechanical probing access for chemical analysis. By combining measurements of the physical, chemical and thermal behavior of reacting coal particles, it was hoped to link the physics of the thermal decomposition process with the evolution of pollutant precursor species and their subsequent oxidation.

2.0 EXPERIMENTAL

2.1 Reactor Systems

Any reactor system has to meet several criteria if it is to yield useful data concerning the decomposition of pulverized coal which can be interpreted as being representative of phenomenon occurring to particles in pulverized coal flames. The requirements were first delineated by Badzioch (Field et al, 1967) as follows:

1) The heating rate must be fast, in the range of 10^4 to 10^5 K/sec;
2) The decomposition time should be controllable and the products rapidly quenched;
3) The temperature (both particle and gas) of decomposition should be well defined and be in the appropriate range of pulverized coal flames;
4) The particles should be in suspension to match the contacting between the volatiles and char in a flame;
5) The time/temperature history should be precisely known.

In addition to these general criteria, there are a few specific design criteria that arise from the process under investigation and the diagnostic techniques to be utilized. A partial list of these includes:

1) Since the experimental objective is to simulate a pulverized coal flame environment, the gas-phase environment should be vitiated air composed of volatile products, partially oxidized products, and coal particles along with oxygen.
2) The system should have optical and mechanical probing access suitable for the selected diagnostic techniques.
3) The coal concentration should be controllable from single particle to concentrations up to those found in flames (200 mg/liter).

The technique which can be employed to meet all of the above criteria is to inject pulverized coal particles into a one-dimensional laminar flow reactor designed for optical and mechanical probing. The reactor utilized in this study consisted of a sintered metal, flat flame burner manufactured to specifications by McKenna Products, Co. The burner (Figure 2-1) had a 27.6 cm (3 in.) square

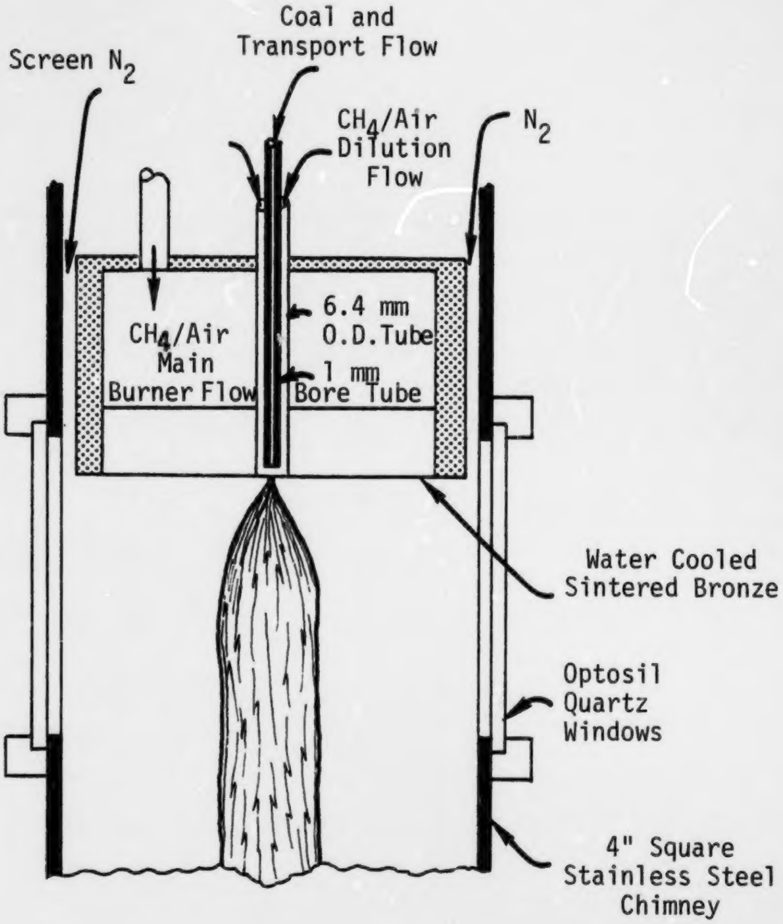
Coal and Transport Flow
Screen N_2
CH_4/Air Dilution Flow
N_2
6.4 mm O.D.Tube
CH_4/Air Main Burner Flow
1 mm Bore Tube
Water Cooled Sintered Bronze
Optosil Quartz Windows
4" Square Stainless Steel Chimney

Figure 2.1. Flat Flame Burner and Particle Injection System.

active area of 1.6 cm thick sintered bronze (-100, +150 mesh) and was mounted in a stainless steel housing. The burner size was chosen in an attempt to shield the center-line temperature from the cool outside surroundings. The burner was water-cooled by a tubular coil embedded in the sintered disk. Along the centerline a 6.35 mm (.250 in.) copper tube was calcined into the burner perpendicular to the face, through which the coal particles were injected.

The size of the central carrier tube was selected based on two guidelines: 1) small enough that there is not significant thermal shielding of the center flow by the bulk flow from the tube and 2) large enough so that the velocity of the carrier flow can be matched to the velocity of the burner to prevent disturbances by the carrier flow. In order to meet the first requirement it is necessary to estimate the heat-up rate along the center line of an imaginary tube of the same diameter as the carrier tube, i.e., with no mixing of the carrier flow and the burner flow. For the purpose of estimation, it is assumed that the heat transfer within the imaginary carrier boundary is by conduction alone but at the boundary between the tube and the bulk flow, the convective transfer rate is dominant. Under these constraints the problem is the classical problem of transient heat conduction in a cylinder which has previously been solved numerically (Eckert and Drake, 1972). From supplied graphs of the Fourier modulus versus the non-dimensional temperature, the transient response of the centerline temperature can be estimated given a diameter for the carrier tube and a flame temperature (usually taken at 2000 K). Two different diameters were investigated, 3.2 mm and 6.4 mm. The estimated response for the two tube diameters, along with linear temperature responses, are shown in Figure 2-2. Since the above analysis ignores mixing and internal convection, it underestimates the response time, but it is useful for design purposes. These data indicate that the centerline of the 6.4 mm tube has an initial heating rate of at least 10^5 K/sec. This value is close to the heating rate normally estimated for particles in pulverized coal flame. Therefore, it appears that the 6.4 mm will satisfy the first requirement.

The ability to match the carrier flow and burner flow velocities depends on the flow rate of the carrier gas and the flame speed of the burner. The flame speed can vary from 15 cm/sec for the lean limit of CH_4/Air to 300 cm/ sec for a stoichiometric H_2/Air flame. It is desirable to maintain the particle density at a typical level associated with pulverized coal burners taken to be 200 mg/liter. This requires a coal-feed rate of 1 to 10 gm/min for a 6.4 mm carrier tube. With

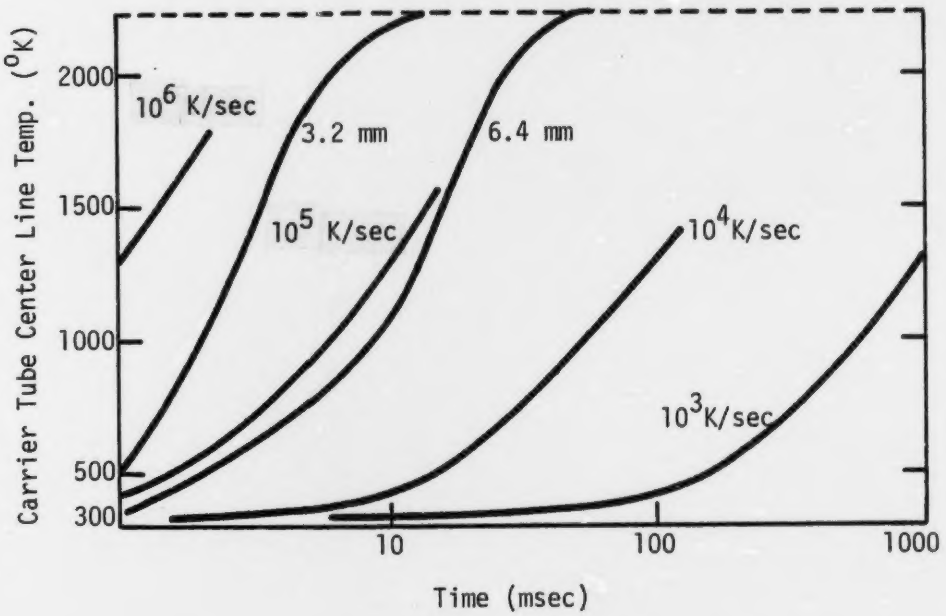

Figure 2.2. Estimated Transient Temperature Behavior of Center Line of Carrier Tube Flow and Linear Temperature Responses.

the normal dilution rates for the Smith-type fluidized bed feeder (Hamor and Smith, 1971), the velocities of the carrier flow and the flame speeds can be matched at all the expected test conditions with the 6.4 mm tube except near the lean-limit of a CH_4/Air flame where it may be necessary to lower the particle number density to maintain matched conditions.

The nominal operating conditions of the reactor were taken to be a stoichiometric CH_4/Air flame with a 6.4 mm diameter coal carrier tube operating with 200 mg/liter of coal. Under these conditions the coal stream is expected to have little thermal influence on the support flame. This conclusion arises from the observation that less than 0.5 percent of the heat available in the flame is necessary to heat the carrier flow to the flame temperature. This was confirmed experimentally by placing a thermocouple in the coal stream and then terminating the feed. The thermocouple reading was found to change by less than 50°K for all axial distances tested.

As previously mentioned, the burner system was designed for use with three fuels: CH_4, CO and H_2. A schematic of the gas manifold system is shown in Figure 2-3 and cons[illegible] of five primary legs. It had the capability of using air or mixing an ar[illegible]cial nitrogen-free oxidizer. The regulating valves were chosen so as to allow control of the flow coefficient in the range appropriate for the control of the flow rates considering the size of the burner and the different fuels and operating conditions. Each primary leg was divided into two branches, one for the burner flow and one for the fluidized bed feeder flow. Using this branching, the manifold had the capability of fluidizing and transporting the coal with gas of the same composition as was in the burner flow. Such a technique eliminated uncertainties in the mixing time between the carrier gas and bulk gas flows.

The fluidized bed feeder was of a Smith-type design constructed from plexiglass and PVC fittings, schematically represented in Figure 2-4. The distribution plate was a sintered stainless steel disk held in a PVC union. The fluidizing gas (1 l/min) entered from below the disk and passed uniformly up through the disk and the bed of pulverized coal. The bed was constructed of two plexiglass sections, a 5.1 cm diameter bottom tube of 15 cm length connected through a PVC transition to a 10 cm diameter tube, 38 cm in height. The pressure of the bed was monitored using two magnehelics of different ranges (0-50 in w.g. and 0-150 in w.g.). The bed exhausted at the top flange through a fritted glass cylinder

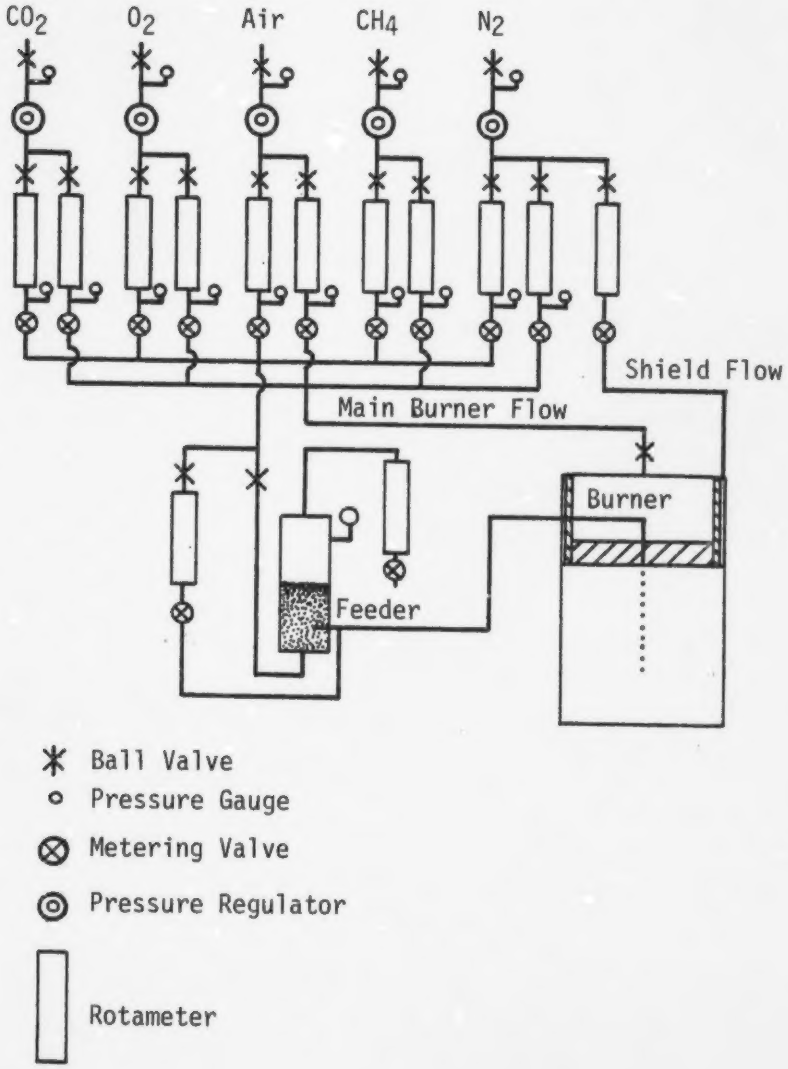
CO2
O2
Air
CH4
N2
Shield Flow
Main Burner Flow
Burner
Feeder
Ball Valve
Pressure Gauge
Metering Valve
Pressure Regulator
Rotameter

Figure 2.3. Reactant Supply System.

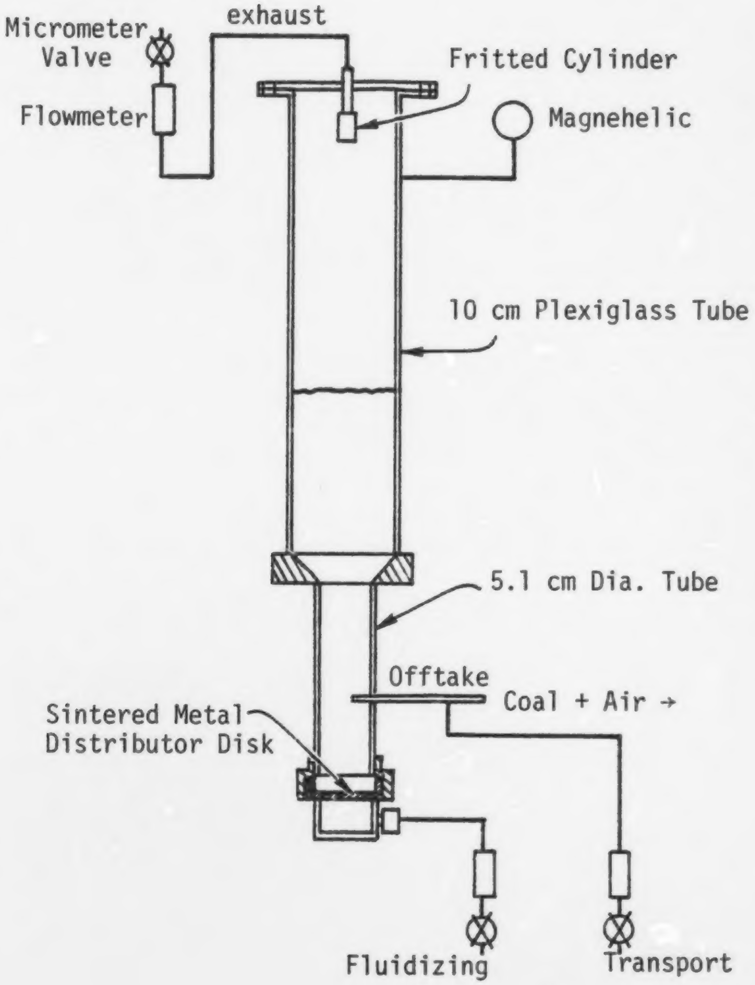
exhaust
Micrometer Valve
Flowmeter
Fritted Cylinder
Magnehelic
10 cm Plexiglass Tube
5.1 cm Dia. Tube
Offtake
Coal + Air →
Sintered Metal Distributor Disk
Fluidizing
Transport

Figure 2.4. Fluidized Bed Feeder for Coal Flow Rates of 1.0 to 10 gm/min.

tube which was connected to a rotameter and micrometer head regulating valve. A coal off-take tube with a 1 mm bore was inserted near the center of the lower section. By varying the bed pressure through the use of the micrometer valve, the coal mass flow rate was controlled. The design flow rate range for this particular fluidized bed feeder was from 1.0 to 10 gm/min. The coal flow, along with transport air which is added to prevent line blockage, was then directed to the central tube of the burner where the coal was injected into the flame.

The analysis of fluidized beds of this kind (Altenkirch, et al, 1978) indicates that the feed rate is controlled by the pressure drop through the off-take tube. Because of this, the solid flow rate should vary linearly with the bed pressure and increase with decreasing transport flow. This behavior was found to hold true for this bed as well, as shown in Figure 2-5.

The flat flame was downfired within a 10 cm square stainless steel chimney in order to reduce heat loss and prevent cross-flow interactions (Figure 2-6). A small amount of inert gas flow was introduced around the burner housing next to the chimney walls in an attempt to cool the material and prevent carbon deposition. High quality fused silica windows (7.6 cm diameter x 3.2 mm thick, Optosil 1) were mounted on two opposing sides of the 91 cm long chimney for holography measurements. A 7.6 cm x 30.5 cm flat plate of Vycor was mounted on a third side for measuring particle/droplet temperatures using the two-color pyrometry system and for high speed photography. The vertical positioning of the burner and chimney relative to a stationary optical probing height was accomplished through the use of an Unislide assembly. The assembly consisted of a dovetail mechanism connected to a lead-screw driven by a stepping motor which was controlled by a digital pre-set indexer. The chimney rested on a flat plate which slides on vertical support rods. Total vertical movement of the chimney using this positioning system was 90 cm corresponding to approximately 500 msec of residence time.

2.2 Diagnostics

The diagnostic techniques utilized in this study were chosen to allow a complete characterization of the burner conditions as well as allowing a complete characterization of the physical, chemical, and thermal properties of the two phase flame.

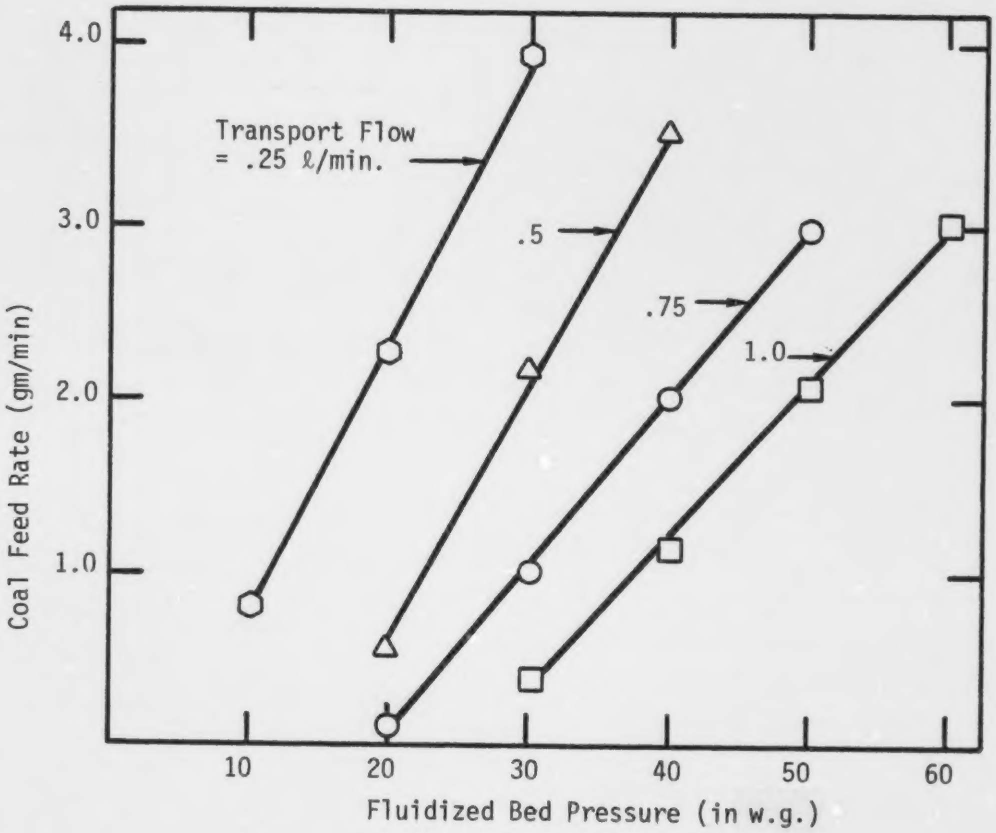

Figure 2.5 Fluidized Bed Calibration for Pulverized Coal Feed.

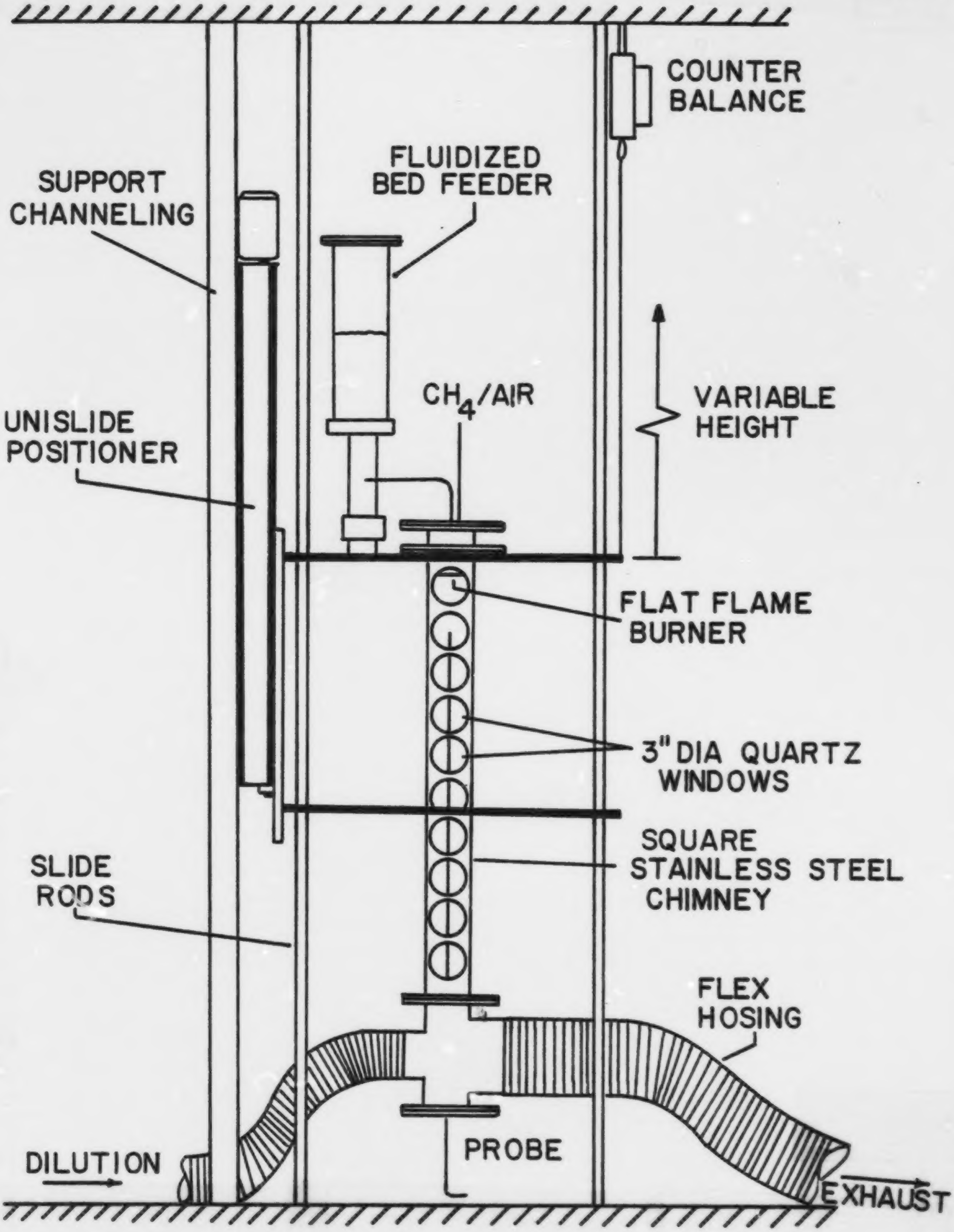
COUNTER BALANCE
FLUIDIZED BED FEEDER
SUPPORT CHANNELING
CH_4/AIR
VARIABLE HEIGHT
UNISLIDE POSITIONER
FLAT FLAME BURNER
3" DIA QUARTZ WINDOWS
SQUARE STAINLESS STEEL CHIMNEY
SLIDE RODS
FLEX HOSING
DILUTION
PROBE
EXHAUST

Figure 2.6. Reactor System.

2.2.1 Burner Characterization

Besides the input flows which are defined by the gas mixing panel described above, the most important burner characteristic is the gas temperature. It is critical to the interpretation of the data to know the thermal history to which a particle has been subjected. The gas temperature profile of the flame reactor was experimentally defined by two different techniques: sodium line reversal and uncoated thermocouple measurements.

The optical system designed for the sodium line reversal measurements is shown in Figure 2.7. A GE strip lamp was used as the reference source which was calibrated with a disappearing filament pyrometer. The measured brightness temperature was then corrected for the emissivity of tungsten by the procedure outlined by Gaydon and Hurle (1963) to obtain the true strip temperature. Two lenses were used to focus the lamp image at the center line of the reactor and at the spectrometer entrance. Ray tracing indicated that the limiting aperture was completely filled with light from the strip lamp, thus assuring that the photomultiplier did not receive light from the reactor against which there was no background.

Sodium was introduced into the reactor in the form of either salt vapor or small salt crystals. The salt was carried by the dilution flow into the central tube (6.3 mm), and thus was restricted to the center line of the burner flow. In this manner, the measurements were made only of the center temperature to which the coal particles are subjected without interference from the cooler edges of the flow. The sodium D-line at 589.3 nm was isolated with an Engis-Hilger 600 cm spectrometer whichwas adJusted to maximize the signal height when salt was sprayed into the reactor. The reversal temperature was determined by observing the photomultiplier signal on a digital oscilloscope and adjusting the lamp current until the reversal point was indicated.

Measurements of the gas temperature by this technique are shown in Figure 2.8. The temperature was found to peak at stoichiometric conditions indicating consistency between the gas temperature measurements and the gas flow measurements of equivalence ratio. The shift below the adiabatic flame temperature was on the order expected due to heat transfer to the cooled burner and cold walls. The measured temperature decline, 27°C/cm or approximately 5°C/msec, is much less

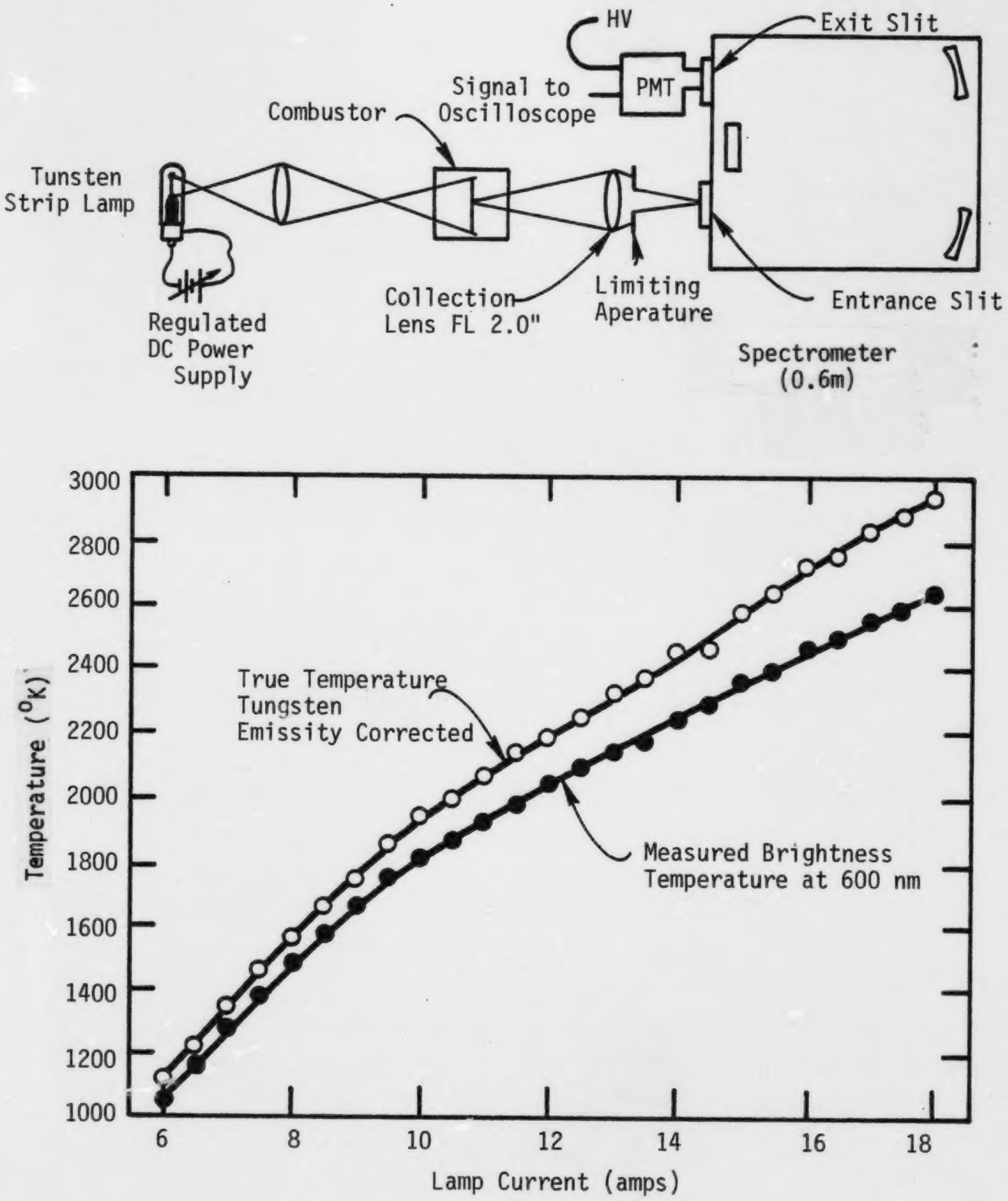

Figure 2.7. Sodium D-Line Reversal Optics and Strip Lamp Calibration.

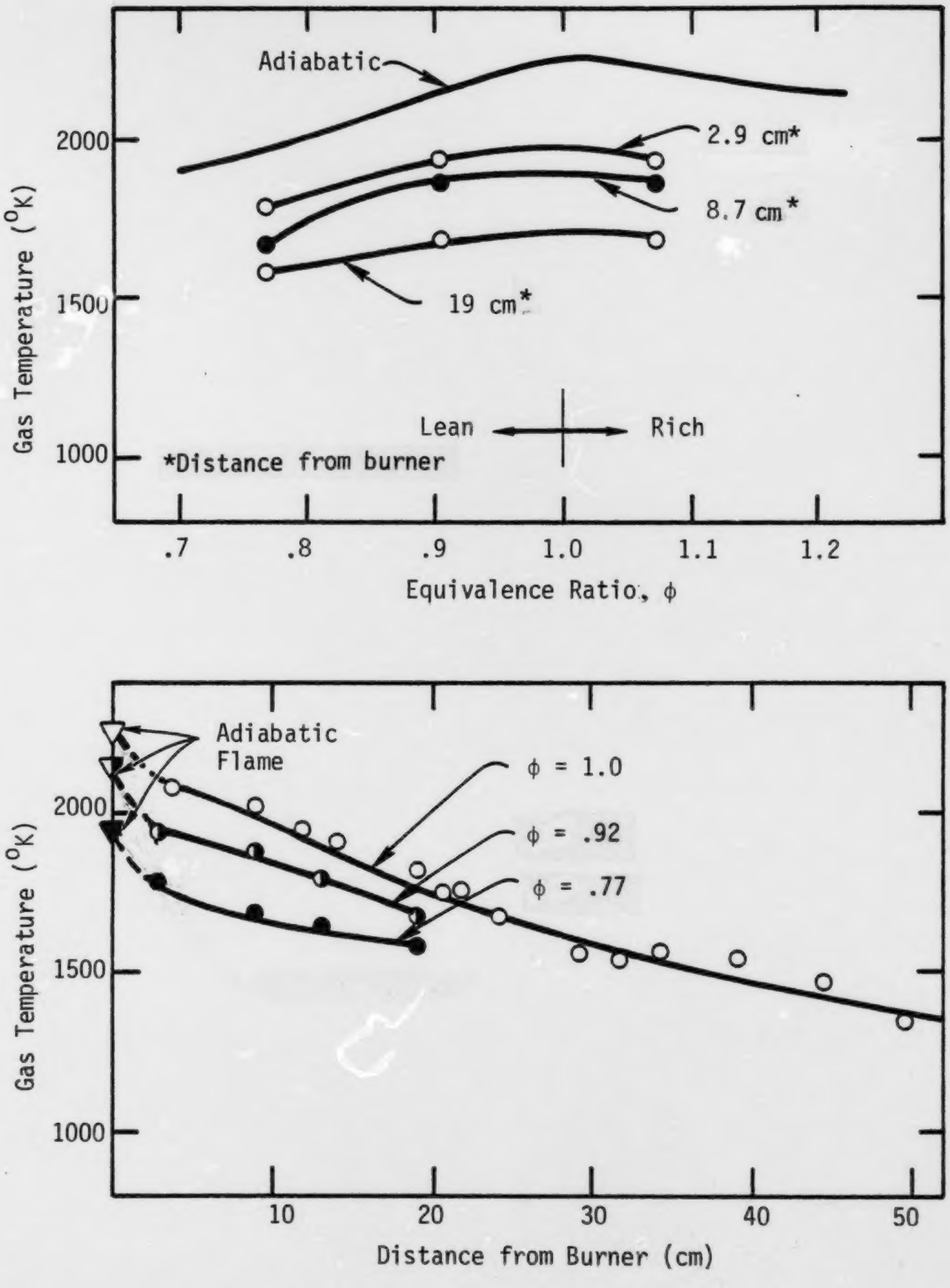

Figure 2.8. Sodium Line Reversal Measurements of Gas Temperature in Thermal Decomposition Reactor.

than would be expected from a plug flow analysis of the burner flow. This discrepancy is indicative of the laminar nature of the flow and the fact that the measured temperature is at the center line of the reactor which is well insulated from the surroundings.

Thermocouple measurements were performed with a variety of small bead uncoated thermocouples under the same conditions as the reversal measurements. This allowed a calibration of the radiative correction factor for each of the thermocouples so that they could be subsequently utilized for more rapid characterization of the burner temperatures.

2.2.2 Physical Analysis

One of the major emphases of this program was the elucidation of the physical phenomenon occurring during the thermal decomposition of pulverized coal particles. That which was desired was both static and dynamic in situ visualization, as well as quantitative measurements of the particle structural changes (i.e., surface morphology, particle size and surface area). The array of physical measurements employed are delineated in Table 2-I.

The primary visualization technique utilized during the initial phases of this program was holography. Holography has the distinct advantage over other visual techniques in that particles need not be in a given plane of focus due to the ability to reconstruct the three dimensional field. Hence, focusing optics can be applied to the reconstructed field In order to get a particular particle in focus. Figure 2.9 is a schematic representation of how the camera was applied to the thermal decomposition reactor along with the reconstruction system assembled at EER. The holocamera used, which was supplied by Spectron Development Laboratories, is described in more detail elsewhere (Trolinger and Heap, 1979 and Appendix A). The important features of this application include the fact that the image was premagnified before recording to a power of three. This feature when combined with high quality optics and near image plane focusing afforded a resolution of near 3 um. However, with imperfect windows and a two phase flame (i.e., during actual operation), the resolution limit was reduced to near 10 um. The use of a pulsed ruby laser with a pulse width of 20 nsec was more than adequate to reduce image smear to a negligible amount even for particles moving at the maximum achievable speeds of 500 cm/sec.

TABLE 2.I

PHYSICAL DIAGNOSTIC TECHNIQUES

	Type	Description	Utilization
VISUALIZATION	Holography	SDL Holocamera EER Reconstruction System	Three Dimensional Recording of Magnified Particle Field
	Shadowgraphy	Microflash Shadowgraphy System Constructed During Program	Single Frame Recording of Particle Field in High Resolution and Magnification
	High Speed Photography	HYCAM Shadowgraph System Constructed During Program	Up to 10,000 Frames/Sec. Recording of Magnified Particle Field
STRUCTURAL	Micrographs	Scanning Electron Micrographs of Impacted Samples	Surface Morphology and Particle Sizing
	Surface Area Analysis	Quantachrome BET Surface Area Analyzer	Extracted Sample Surface Area
	Particle Size Analysis	Malvern Laser Diffraction Particle Size Analyzer	Extracted Sample Size Distribution

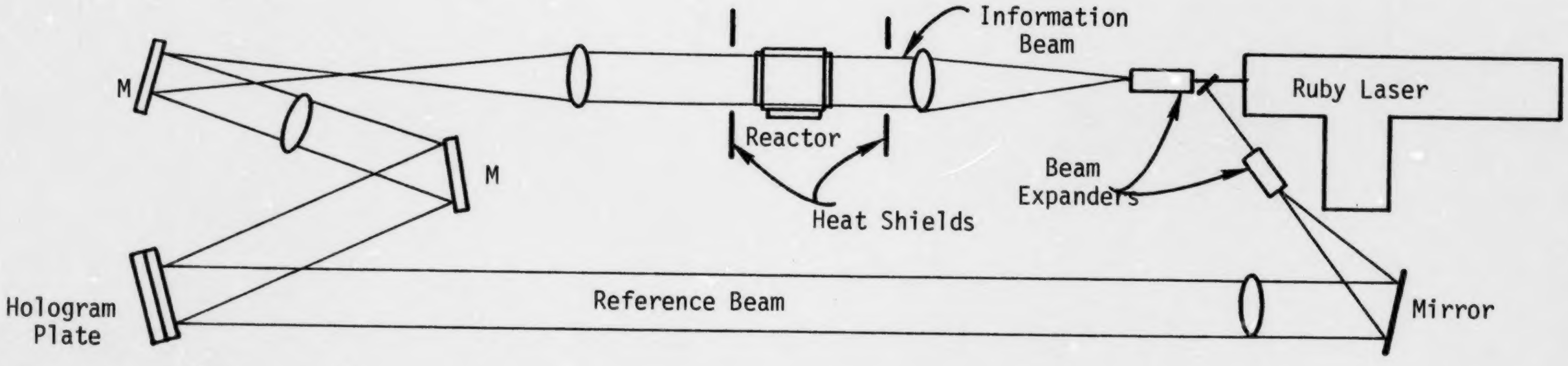
Information Beam
Ruby Laser
M
Reactor
M
Beam Expanders
Heat Shields
Hologram Plate
Reference Beam
Mirror

(A) HOLOCAMERA

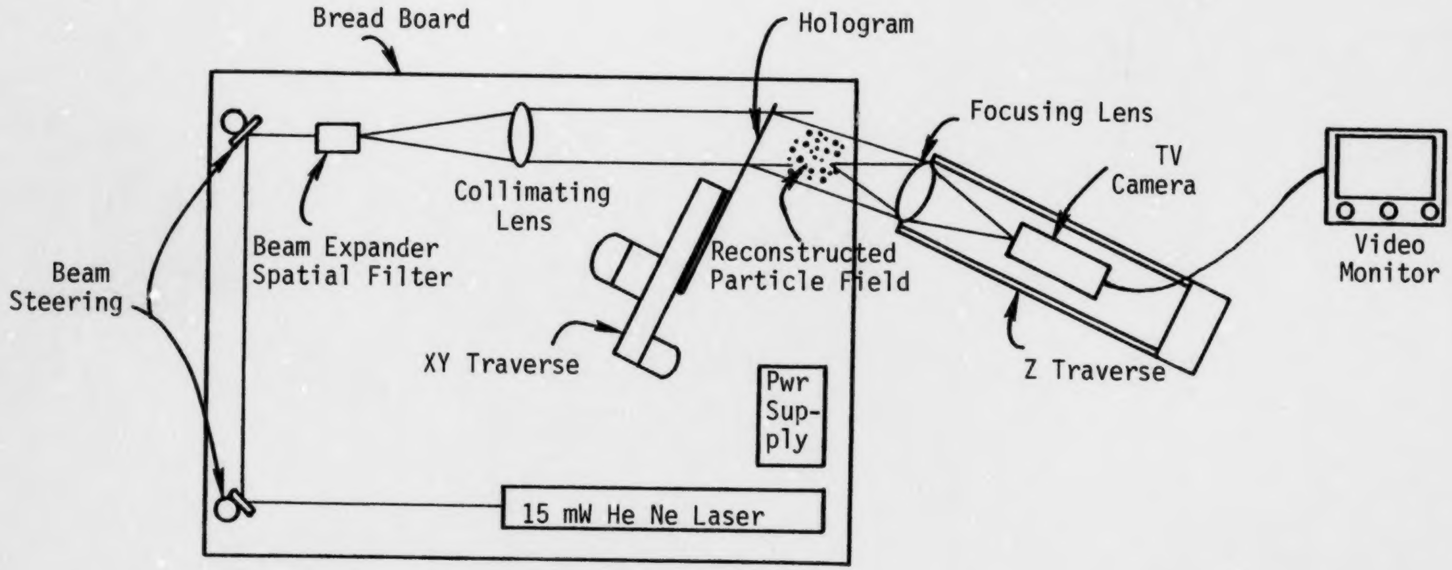
Bread Board
Hologram
Focusing Lens
TV Camera
Collimating Lens
Beam Expander Spatial Filter
Beam Steering
Reconstructed Particle Field
Video Monitor
XY Traverse
Z Traverse
Pwr Sup-ply
15 mW He Ne Laser

(B) RECONSTRUCTION SYSTEM

Figure 2.9. Holography and Reconstruction Systems.

Because of the relatively narrow zone over which the particles were spread, it was possible to employ high resolution shadowgraph techniques. These techniques have the advantages of simplicity (no reconstruction is required), high resolution, sensitivity to density gradients, and multiple nigh speed framing 1 capability. Two separate techniques were employed for single framing and high speed photography, as shown in Figure 2.10. The light source for the shadowgraph system was an EG and G Microflash which produced a point spark of light with a pulse width of 500 nsec. The light was focused through an aperture and collimated through the combustor. An optimized achromatic lens acted as a pre-magnification lens for an OM-2 macrophotography bellows camera. In order to minimize interference from the flame continuum radiation, a shutter was placed at the focal point of the premagnification lens and synchronized at 1/125 sec with the microflash pulse. The high speed shadowgraphy system used similar optics, but employed a continuous mercury arc lamp (Oriel, 1000 W) and a Hycam high speed camera with a 4 inch focal length lens mounted on an extension tube (2 inches and 4 inches). The 16 mm rotating prism camera was utilized full frame up to 10,000 frames per second.

In addition to the in situ visualization of particles, samples were withdrawn from the reacting stream and viewed with a scanning electron microscope. The particle extraction probe consisted of a water cooled tube positioned in the side of the burner and a small removable stainless steel plate held on an extension rod. The cold plate was pushed into the coal stream and rapidly retracted before the plate temperature could change significantly. The plate was then removed from the probe and coated with copper before SEM analysis. This technique allowed the capture of very fragile soot and char structures which would not survive aprobe extraction train without fracturing.

The other structural analysis performed included the analysis of the particle size and surface area for extracted samples. Samples were withdrawn with an isokinetic water cooled stainless steel probe and collected in sintered metal and glass fiber filters. The particulate catch was analyzed for surface area using a BET single point analysis (Quantachrome) with either nitrogen or carbon dioxide as the absorbate. The outgasing procedure selected was cyclic absorbation/desorption since thermal outgasing was found to change the surface area of lignites. Size analysis of the catch included microscopic counting as well as Malvern laser diffraction measurements.

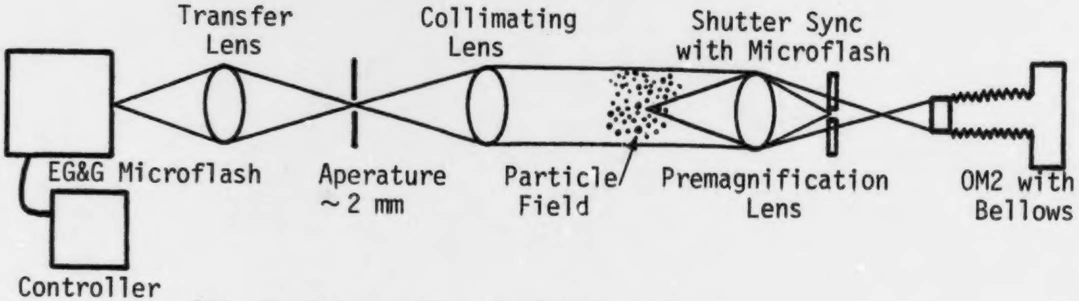
Transfer Lens
Collimating Lens
Shutter Sync with Microflash
EG&G Microflash
Aperature ~ 2 mm
Particle Field
Premagnification Lens
OM2 with Bellows
Controller

(A) Shadowgraph System (Single Frame)

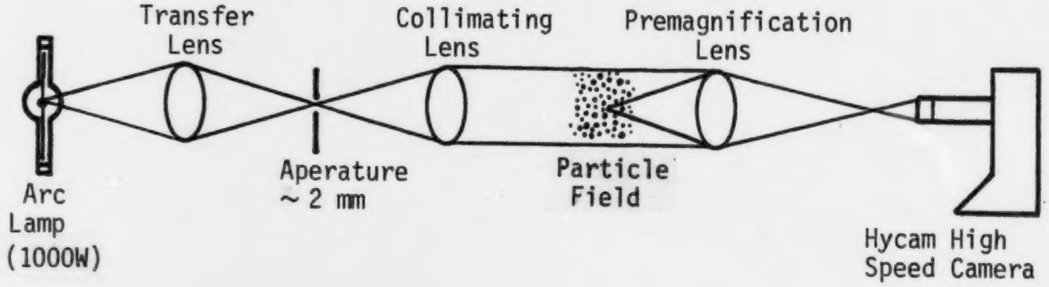
Transfer Lens
Collimating Lens
Premagnification Lens
Arc Lamp (1000W)
Aperature ~ 2 mm
Particle Field
Hycam High Speed Camera

(B) High Speed Shadowgraph System (Up to 10,000 fps)

Figure 2.10. High Speed and Single Flame Shadowgraph Systems.

2.2.3 Thermal Analysis

Optical pyrometry techniques are commonly used to measure surface temperatures of reacting coal particles. Although systems based upon both single and multiple wavelengths have been used, two-color systems are the most often employed. In two-color pyrometry, the brightness temperature of the source is evaluated from a measurement of an emission at two separate and distinct wave lengths. The analysis is based upon the validity of Wien's law for the particular source under investigation. Wien's law can be written in the form (Gaydon and Hurle, 1963):

$$I_\lambda = \frac{2\varepsilon_\lambda A C_1}{\lambda^5} \exp\left(-\frac{C_2}{\lambda T}\right) d\lambda \qquad (1)$$

where

I_λ = intensity of radiation per unit solid angle emitted normal to the surface at wavelength y

ε_λ = emissivity of source at wavelength y

λ = wavelength

A = area

T = absolute temperature of the source

C_1 = first radiation constant

C_2 = second radition constant

The ratio of intensities of the two wavelengths, λ_1 and λ_2, takes the form:

$$R = \frac{\lambda_1^5}{\lambda_2^5} \frac{\varepsilon_2}{\varepsilon_1} \exp\left[-\frac{C_2}{T}\left(\frac{1}{\lambda_2} - \frac{1}{\lambda_1}\right)\right] \qquad (2)$$

where the area and differential wavelength band are assumed constant. If the source is gray; that is, if the emissivity is independent of wavelength, then the temperature can be determined directly from the ratio of intensities of the two wavelengths.

$$T = \frac{C_2\left(\frac{1}{\lambda_1} - \frac{1}{\lambda_2}\right)}{\ell n\left[R\left(\frac{\lambda_2}{\lambda_1}\right)^5\right]} \qquad (3)$$

The application of Equation (3) to a cloud of pulverized coal particles is only valid if several criteria are satisfied. The source must be gray over the wavelength region of interest, λ_1 to λ_2 otherwise errors will be introduced associated with the ratio of $\varepsilon_2/\varepsilon_1$. Limited data are available on spectral output of chars and coals at combustion temperatures. However, it has been suggested that char particles are relatively gray.

When two-color pyrometry is used in a combustion environment, the wavelengths must be chosen to ensure that there is no interference associated with molecular or atomic transitions of the dominant gas-phase combustion products. Spectral emissions associated with carbon dioxide (2.7 and 4.3 um).water vapor (2.5 to 2.9 um), carbon monoxide (4.7 um) and hydrocarbons (discrete lines from 2.7 to 15 um) must be avoided. Although chemiluminescence associated with reactants is weak in comparison to the solid continuum radiation, this can also have an important impact. Bands associated with O_2, N_2, and NO lie in the ultraviolet and visible regions. Spectral lines associated with trace gas-phase products (CH, C_2, OH) may be negligible in comparison to intensity associated with the solid-phase continuum. However, because of the mineral matter contained in the coal, such as sodium, (589.3 nm), potassium, (766.4 and 769.8 nm) and calcium (422.6 nm) even the solid-phase continuum will have discontinuities residing in the visible and near UV regions.

The combustion of pulverized coal can produce relatively large amounts of soot, and because of its nongray nature, it is a potential source of error for any two-color technique. The emissivity of soot has been found (Hottel, 1954) to have approximately an inverse dependence on wavelength in the infrared region, and somewhat larger inverse dependence in the visible region. Analysis of equation (2) with an inverse wavelength dependence of emissivity reveals that the temperature of the soot cloud would be over predicted by up to 10 to 20 percent. Since soot is only one contributor to the cloud emission intensity, its impact is expected to be less than this.

From the above discussion, it is concluded that the success of a two-color particle temperature system is primarily dependent upon the selection of the two wavelengths. They must be separated from any known spectral bands, thus ruling out large regions in the visible and far infrared range. If signal size is a criterion, then the wavelength should be located as near to the maximum on the black body curve as possible. For combustion temperatures of 1500°F, this implies that they are located in the near infrared. Maximum sensitivity of the intensity ratio to temperature is achieved by maximum separation of the wavelengths. However, it is desirable to keep the wave lengths close together in order to avoid changes in the emissivity of the pulverized coal cloud. The two wavelengths, 750 nm and 950 nm, used in this study were selected to satisfy as many of these criteria as possible.

Figure 2.11 shows a schematic arrangement of the two-color particle temperature measurement system used in this study. A water-cooled probe containing a fiber optics light guide was mounted on the side of the burner. The probe acted as a collimator for the fiber optics controlling the field of view. A quartz window on the opposite side of the burner acted as a background to prevent the pickup of radiation from warm walls. Thermal emission from particles passing through the sensing volume was received by the light guide. The fibers were bifurcated within the light guide, and the light signal was thus divided and directed to two lens/filter head assemblies which isolated the wavelengths and directed the light onto independent silicon photodiodes. After amplification, the signals were stored in digital form with a Nicolet digital oscilloscope.

The pyrometer was calibrated against a tungsten strip lamp which, in turn, was calibrated against a disappearing filament pyrometer as discussed in Section 2.2.1. The accuracy of the particular temperature measurement system was assessed by injecting inert 1 um diameter alumina particles and comparing their temperature with that of the combustion products. The data presented in Figure 2.12 indicate that the two-color optical pyrometry system gave temperatures which were in good agreement with the gas temperatures measured with sodium line reversal in the absence of particles. The consistency of the two color temperature measurements of coal particles under rich conditionswith the gas temperature will be discussed further in the results section (Section 3.2.1).

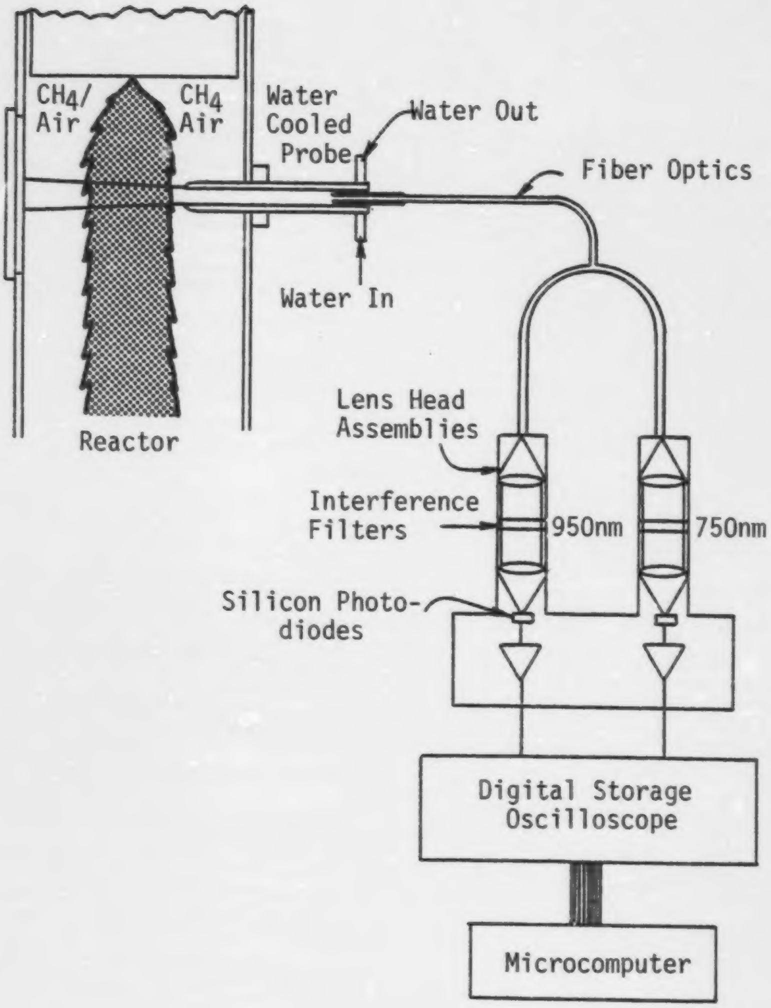

CH_4/
Air
CH_4
Air
Water
Cooled
Probe
Water Out
Fiber Optics
Water In
Reactor
Lens Head
Assemblies
Interference
Filters
950nm
750nm
Silicon Photo-
diodes
Digital Storage
Oscilloscope
Microcomputer

Figure 2.11. Two-Color Pyrometry System.

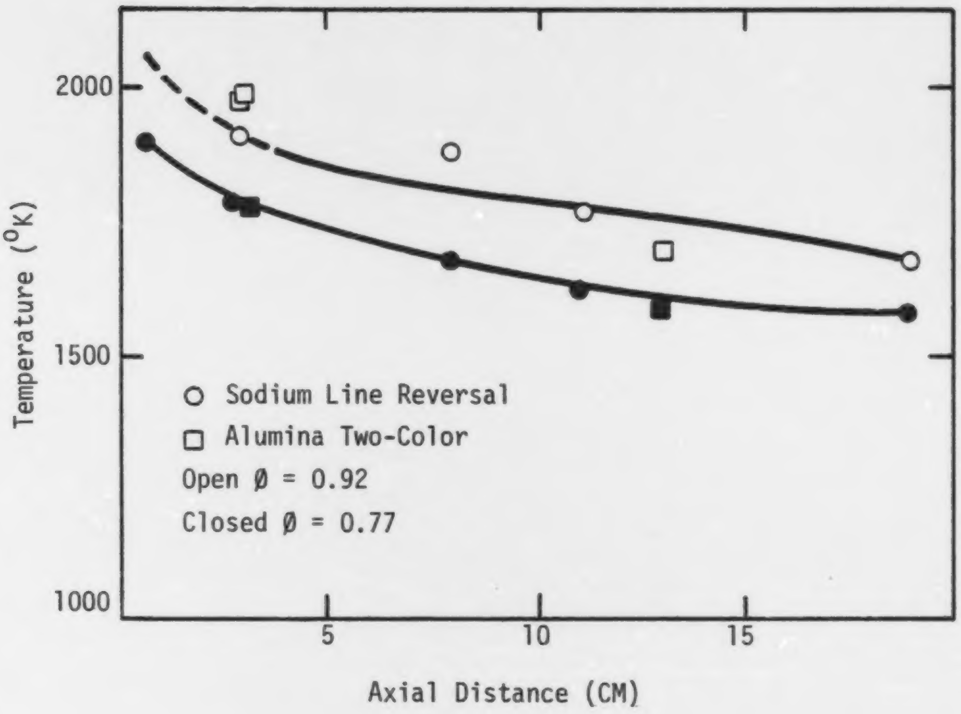

Figure 2.12. Comparison of Gas Temperature Measured by Sodium Line Reversal and Inert Particle Temperatures Measured by Two-Color Pyrometry.

2.2.4 Chemical Analysis

The primary objective of this program was to investigate the physical processes occurring during the high temperature thermal decomposition of pulverized coal and to investigate the interaction of these physical processes with the chemical processes influencing the formation of NO_x and particulate. Because these processes are inherently coupled, there was no attempt to isolate the phenomenon but rather to simulate as closely as possible the environment in a pulverized coal flame. The chemical analysis performed on both the solid and gas phases was designed to link the physical and chemical processes in time and to allow an elucidation of the effects of coal type and size. These analyses were not expected to yield information suitable for interpretation in terms of fundamental rate data but rather were more global in nature.

Several probes were utilized to extract samples from the two phase flame produced when pulverized coal was injected through the hydrocarbon flat flame. The principle probe used for gas and small solid extraction was a double-walled water-cooled probe shown in Figure 2.13. The probe had an outside diameter of 1.6 cm (5/8 in.) and an internal sampling diameter of 0.64 cm (1/4 in.). Internal tubes between the two walls served as pressure taps, water inlets, quench lines, and gas sample extraction lines. Two 0.32 cm (1/8 in.) diameter lines penetrated the inner tube of the probe and could either be used to inject a stream of water to quench the products or to aerodynamically separate the two phase system allowing a portion of the gaseous products to be separated from the solid particles. The operation of this probe was normally with maximum suction so that the entire coal stream was drawn into the probe. In this manner, any radial dependence of properties would be averaged out in a single measurement. Some isokinetic measurements were performed in order to define the radial variation of properties.

The chemical analysis techniques applied to the extracted gas and solid phases are delineated in Table 2-II. The sampling train and procedures were specific to the analysis to be performed:

(1) Continuous on-line measurements of NO, NO_2, CO, CO_2, and O_2 were performed with a sampling train consisting of a heated filter followed by a water dropout through a Thomas teflon lined pump directed to the individual instruments with a splitting manifold;

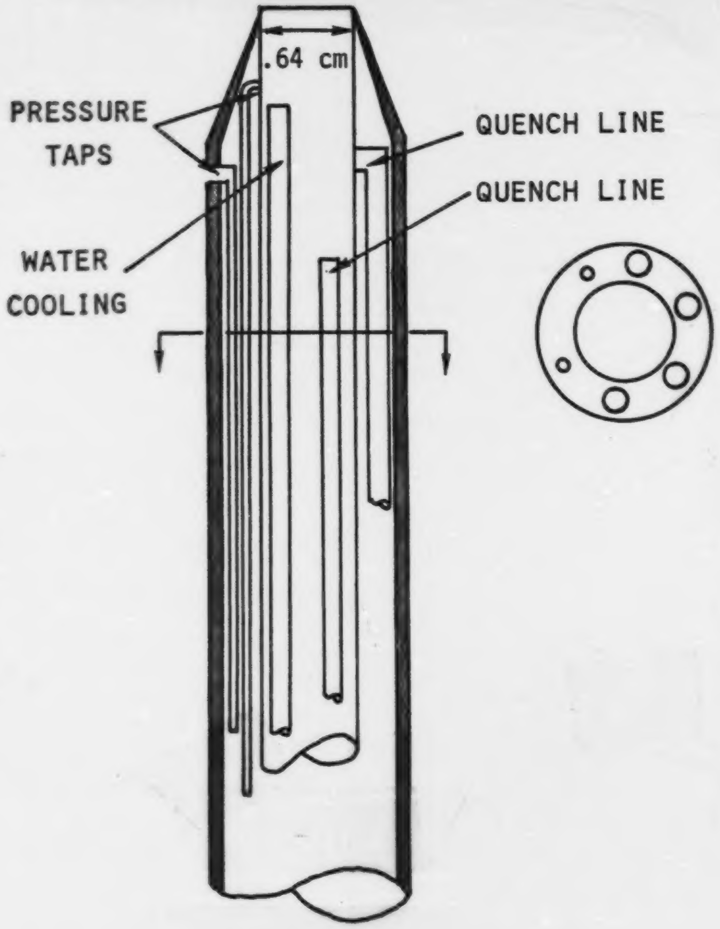
.64 cm
PRESSURE TAPS
QUENCH LINE
QUENCH LINE
WATER COOLING

Figure 2.13. Extractive Probe.

TABLE 2.II

CHEMICAL ANALYSIS TECHNIQUES

Gas Phase	NO, NO_2	TECO Chemiluminescent Analyzer
	HCN, NH_3	Specific ion analysis for ions in bubbler solution of distilled water with Pb CO_3 for sulfur interference removal and Na_2CO_3 as a Ph buffer.
	CO	Beckman NDIR Model 315B
	CO_2	Beckman NDIR Model 315B
	O_2	Taylor Paramagnetic Analyzer Type OA 250
	Hydrocarbons	Perkin Elmer Sigma II Gas Chromatograph with Porapak Q column and FID
Solid Phase	Volatile matter Fixed carbon Ash	ASTM Proximate Analysis
	Carbon Content Hydrogen Content Nitrogen Content	Perkin Elmer Elemental Analyzer 240B
	Sulfur Content	LECO Sulfur Analyzer

(2) Wet chemical analysis for HCN and NH_3 were performed by specific ion techniques on bubblers through which the entire sample stream (particulate and gas phase) was passed. The solution was filtered prior to ion concentration measurements. Measurements were made both with a water quench,using the 1/8 in. internal tube near the entrance of the probe,and without a water quench. The HCN measurements were invariant with the quench while NH_3 concentration measurements increased consistently with the presence of the water quencn; however, in all cases investigated, NH_3 levels were negligibly small.

(3) Gas chromatographic analysis for hydrocarbons were performed on batch samples taken into evacuated stainless steel sample bottles. Because of relatively low solubility of hydrocarbons in water, it was allowed to condense within the bottles without significant loss of measured concentration.

(4) Solid samples were collected in the same manner as described in Section 2.2.2 for structural analysis, i.e., in heated large capacity filters.

2.3. Fuel Selection

The selection of the coals to be studied involved three considerations. The first is that the coals should be selected from the bank of coals currently under investigation within the FCR program in order that the information generated within individual programs can be transferred directly. Also, the coals should span the expected range of behavior, i.e., should adequately cover the rank spectrum. Finally, the coals should be selected with some consideration of the results from other fuel nitrogen screening experiments.

Bench-scale tests from a separate EPA program (68-02-2667) indicated that neither rank nor fuel nitrogen content was sufficient to correlate fuel nitrogen conversion. Figure 2-14 is a plot of the measurements of fuel nitrogen converion versus fuel nitrogen content for a variety of coals burned in a 70,000 Btu/hr (20.5 KW) tunnel furnace. Coals with similar rank and fuel nitrogen content were observed to have widely different fuel nitrogen conversion efficiencies. In particular, the two lignite coals, Buelah, North Dakota and Savage, Montana were of similar rank and chemical composition but had radically different fuel nitrogen conversion efficiency. These coals were selected in

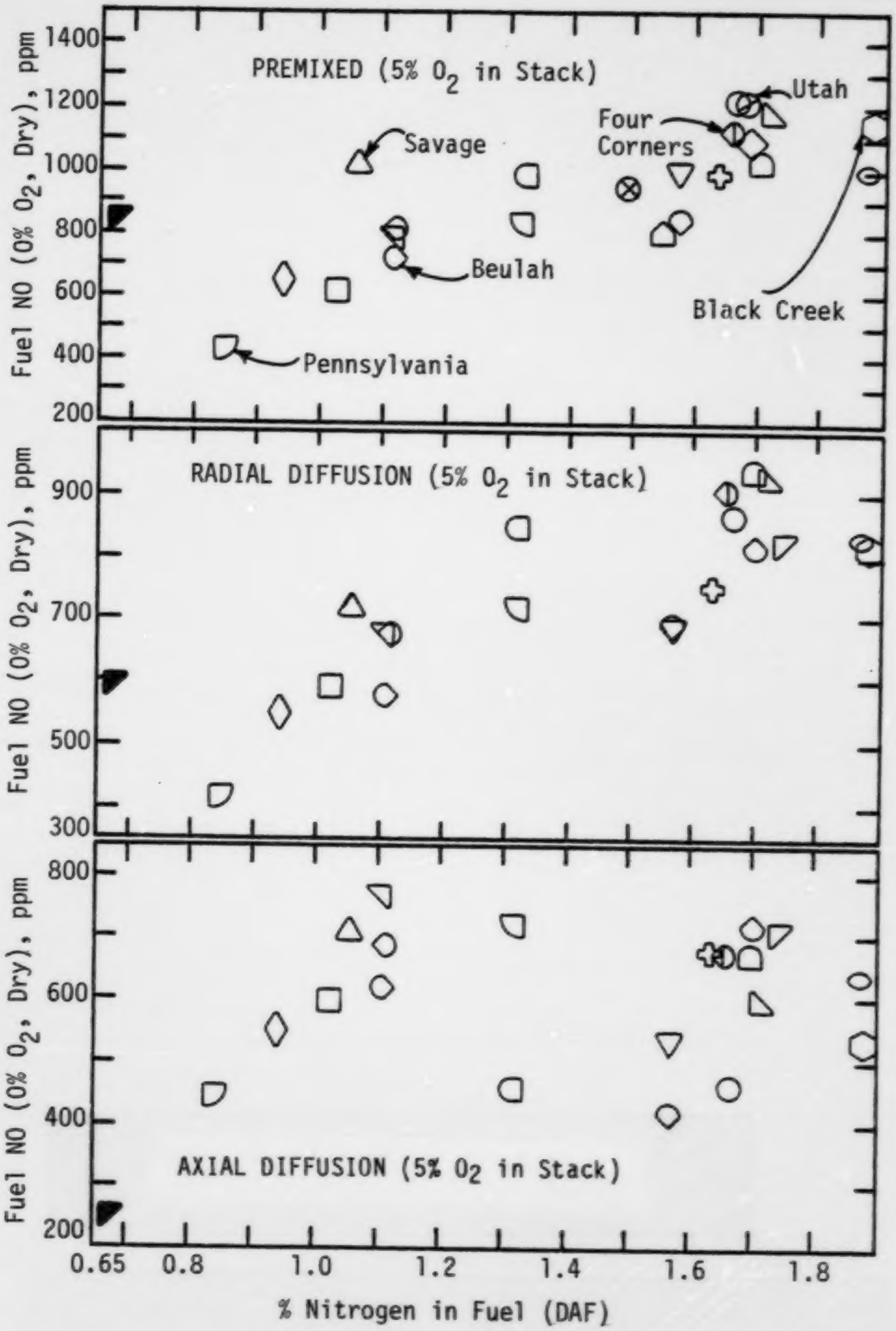

Figure 2.14. Fuel NO as a Function of Fuel Nitrogen Content.

order to investigate whether there were any inherent differences in the physical, chemical or thermal behavior which could result in different fuel nitrogen conversion chemistry.

The coals selected and their chemical composition and rank are listed in Table 2-III. The coals span the rank from lignite to anthracite including two high-volatile, bituminous coals and two lignites. The standard sized samples were prepared by pulverizing the coal and dry sieving for five minutes to obtain the cut between 140 mesh (105 um) and 400 mesh (38 um). Because of the inadequacy of the dry sieving technique, this procedure assured a broad size distribution up to 105 um but without the large quantities of fines associated with normal pulverizer operation. One coal type (Four Corners, New Mexico) was selected to examine the influence of particle size. Aerodynamics classification at Vortec Industries was employed to reduce the base size distribution into size cuts below 40 um, 40 ±4 um, 60 ±6 um, 80 ±8 um and greater than 80 um.

Table 2-III. Coal Analyses

LOCATION	RANK	PROXIMATE ANALYSIS, DRY (WT %)				ULTIMATE ANALYSIS, DRY (WT %)		
		VOLATILE MATTER	FIXED CARBON	MOISTURE (AS RECV'D)	ASH	CARBON	HYDROGEN	NITROGEN
Savage, Montana	Lignite	44.76	47.99	36.36	7.25	64.99	4.04	1.14
Beulah, North Dakota	Lignite	42.82	46.54	33.10	10.64	65.29	3.96	0.99
Black Creek, Alabama	Med. Volatile Bituminous	28.92	66.52	2.25	4.56	82.12	5.21	1.79
Four Corners, New Mexico	High Vol. B Bituminous	40.87	40.50	4.02	18.62	63.49	5.31	1.54
Utah	High Vol. B Bituminous	41.94	48.52	7.41	9.54	72.24	5.75	1.55
Hazleton, Pennsylvania	Anthracite	3.84	87.54	5.46	8.62	84.23	1.78	0.77

3.0 RESULTS

This section deals with the results of the physical, chemical and thermal measurements for all of the coal samples tested. In order to gain a point of reference, the behavior of the 80 um high volatile bituminous coal from New Mexico is discussed first in Section 3.1 including both nominal operating conditions (35 percent excess air flame and matched injection velocities) and variations of particle size, injection velocity and flame stoichiometry. These data are then compared with the results from the other coal types in Section 3.2. Data will also be discussed for a char produced from the baseline fuel.

3.1 The High Temperature Thermal Decomposition and Oxidation of High Volatile Bituminous Coal Particles

The subsequent sectionsfirst describe the physical behavior of high volatile bituminous coals as exemplified by the Four Corners coal and the Utah coal and their decomposition products as they are heated and react. This behavior is linked with the chemical changes that occur to the char and its environment in the next subsection.

3.1.1 Physical Phenomenon

When a coal particle is heated rapidly, it loses mass and the resulting char particle exhibits one of the following:

- its appearance resembles that of the original coal particle;
- it remains the same size as the parent particle but becomes spherical as though it were once molten;
- it swells into an opaque sphere;
- it appears as though some combination of the above had occurred.

In order to better understand the mechanisms involved in the combustion of coal particles, it is important to examine the influence of heating on the particle and the interaction of the reactions of the volatiles and the char on the characteristics of the remaining solid. In this section, results from a series of experiments in which reacting bituminous coal particles were observed are used to define the various regimes associated with thermal decomposition and reaction.

F3-1

Figure 3-1 presents scanning electron micrographs of withdrawn samples and a scaled schematic of the flame produced when burning a sized (80 ±8 μm) high volatile bituminous coal from the Four Corners area of New Mexico in a lean (ϕ = .77) methane/air flame at approximately 1750 K gas temperature. The locations at which samples were withdrawn are shown relative to a length scale. Indicated by the radiation field and the particle structural changes, are the three distinct zones:

- Heat-up (Zone I): This zone is characterized by a relatively short (<10 msec) region with almost no luminosity adjacent to the burner and corresponds to the heat-up of the particles.
- Devolatilization (Zone II): The distinctive feature of this 10-12 cm (∿70 msec) region is the intensity of the thermal radiation. At lower flow rates where single particles could be observed, the particles first become visible at about 1-2 cm as broad bright streaks. The particles which originally were angular in appearance, micrograph A, change into more rounded structures, presumably because of the rounding of sharp edges as the coal softens. The visible surface features which began as small (less than 1 μm), shallow dimples become more extensive. The three extreme particle forms which characterize the early devolatilization process are: (1) essentially impervious particles with limited pore structures similar to the parent coal (for example, micrograph B); (2) particles with single or multiple, large (5-10 μm) blowholes; (3) particles with extensive and somewhat uniform pore structure which are hollow thin shells (for example, micrograph C). The final stages of the devolatilization zone are characterized by the presence of long strands shown in micrographs E and F. These strands can reach lengths of several thousand microns with typical diameters of 5-10 μm. High magnification reveals that these strands are covered by a multitude of distinct particles with diameters less than 500 A. Similar strands have been observed in large-scale turbulent diffusion flames (Szpindler, 1970).
- Oxidation (Zone III): In the third zone, the radiation was limited to fine dim streaks associated with hot char particles. The oxidation zone exemplifies char structures similar to the devolatilization zone; however, only the more substantial structures (G and H) survive fragmentation, and there is a distinct absence of strandular structures except at rich conditions.

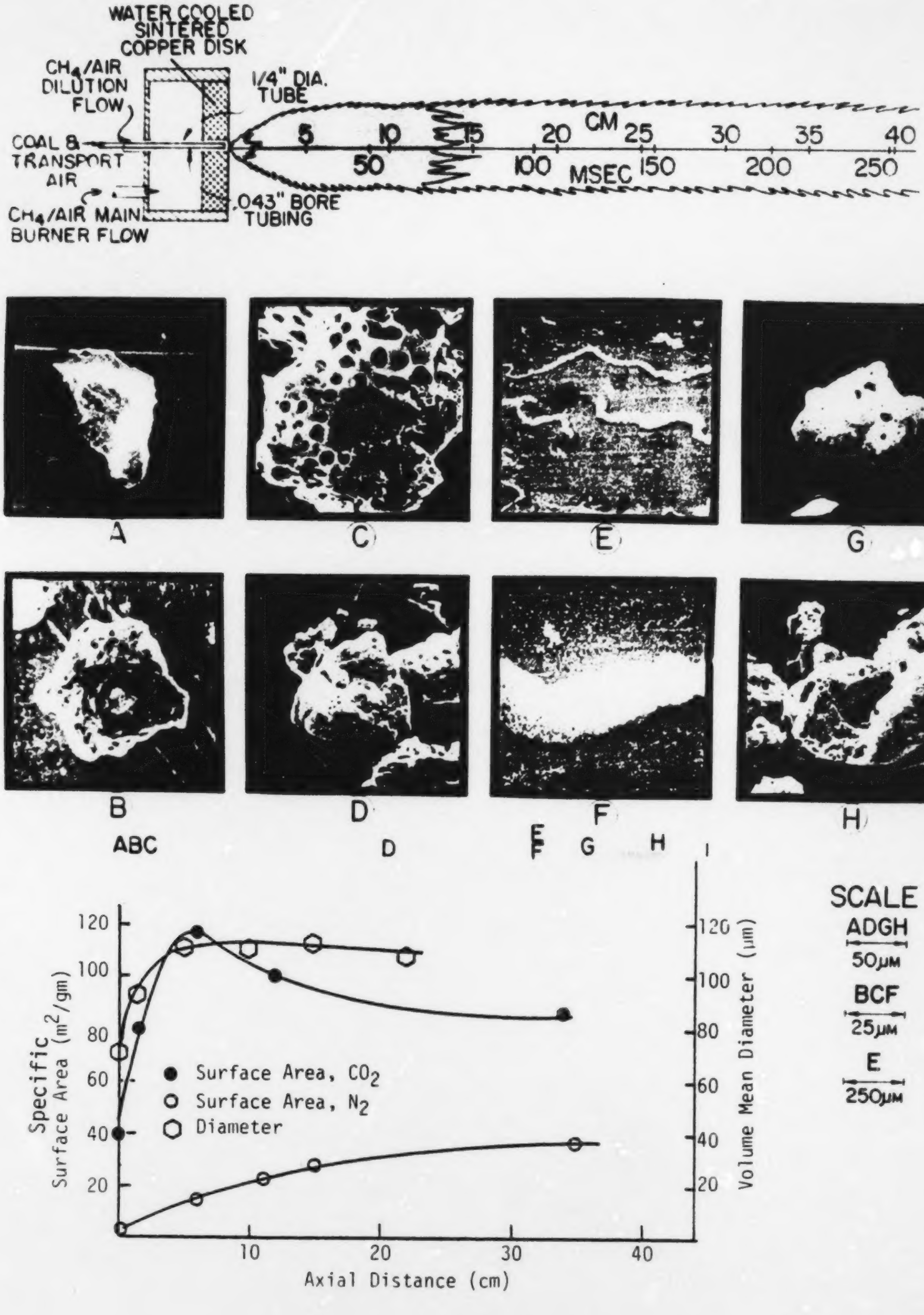

Figure 3.1. Physical Behavior of 80 μm Four Corners, NM, Coal Particles in Lean Methane Air Flame.

Specific surface areas of samples withdrawn from the flame as measured by BET volumetric absorption with both nitrogen and carbon dioxide as the absorbate are also shown in Figure 3-1. Both the nitrogen surface area and the more representative measurements using carbon dioxide (Karr, 1978) were found to increase dramatically through the devolatilization zone. The carbon dioxide surface area declined slightly through the burnout zone.

The changes in the particle volumetric mean diameter parallel the CO_2 specific surface area data, peaking late in the devolatilization zone after about 20 percent of the d.a.f. (dry ash-free) weight is lost. Measurements of the size distribution of the char sample, Figure 3-2, indicate that devolatilization swelling extends the originally narrow distribution to larger diameters. The fragile cenosphere-type structures subsequently fracture and extend the small-size limit before the char burnout zone. The fractured fragments are observed to burn away, while the large structures burn at relatively constant diameters. Since at relatively low temperature and oxygen concentrations, the chemical oxidation rate is rate-controlling (Mulcahy and Smith, 1969); oxygen can penetrate through the particle matrix. Hence, under these conditions, it is not surprising that the char particles burn at constant diameter.

The bituminous Four Corners, New Mexico coal exhibits many of the same behavior patterns described by previous investigators for bituminous coals: swelling (Pohl, et al, 1978), blowhole formation, particle fracture, and the presence of long soot strands (Spzindler, 1970). These structural changes appear to be indicative of the softening of the bituminous coal material and the release of the volatile material. The coupling of the structural changes with the physical aspects associated with the volatile release and the particle thermal behavior is shown more clearly in Figure 3-3. Particle temperatures measured by a two-color pyrometer are presented together with *in-situ* holographs and scanning electron micrographs of impacted samples. The two-color measurements indicate that in the second zone, where the rapid weight loss and the pore development first occur, the particle temperature increases rapidly and peaks approximately 30 msec after injection before declining. The dotted line shown in Figure 3-3 is the temperature of the methane/air combustion products measured by sodium D line reversal in the absence of particles. Thus, these bituminous particles rapidly attain a temperature which exceeds that of the gases into which they are injected. An analysis of this phenomenon and further discussion is supplied in Sections 3.2.1 and 4.3.

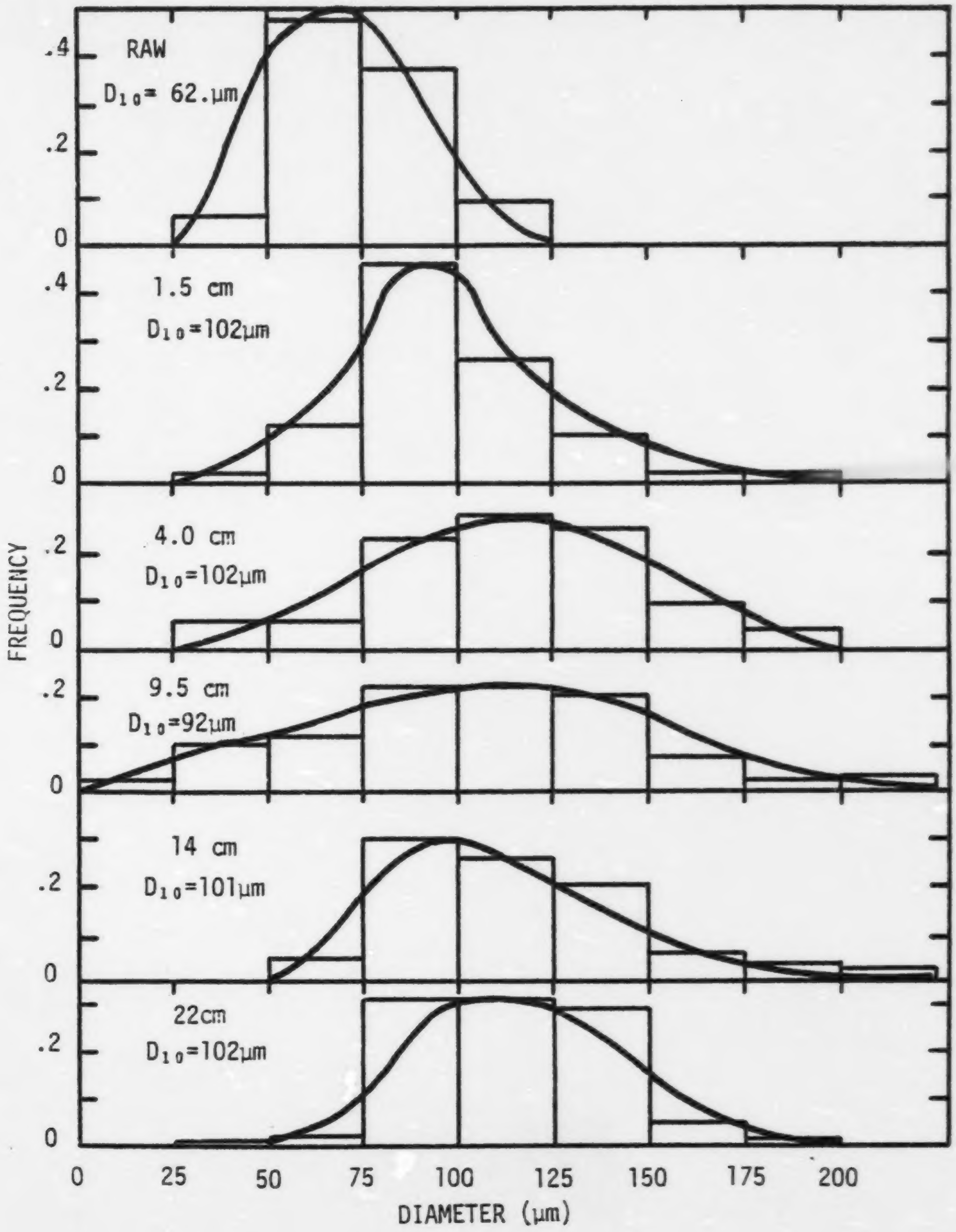

Figure 3.2. Size Distribution Profile for 80 μm Four Corners NM Bituminous Coal in a Lean Methane/Air Flame.

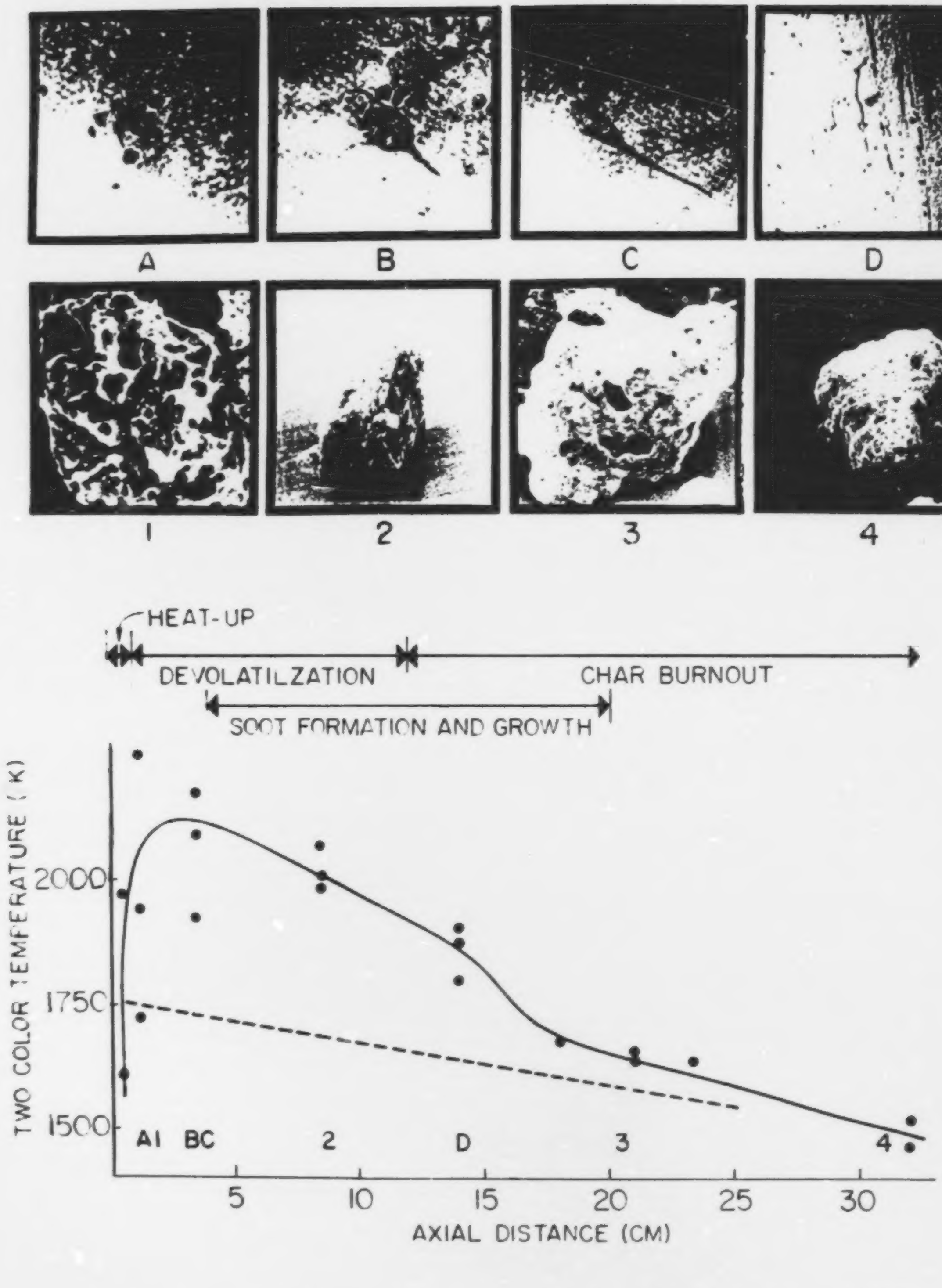

Figure 3.3. Holograms, Micrographs and Particle Pyrometry of 80 μm Four Corners, NM, Coal Particles.

The *in-situ* holograms A, B, and C, which are characteristic of the second zone, illustrate the major observations with this single-frame technique:

- many of the particles are surrounded by a cloud which consists of small (<10 μm) particles;
- most clouds appear to be roughly spherical with an uneven density (hologram A);
- clouds can be drawn out into a trail with the particle still surrounded by a cloud (hologram B);
- in some instances, the char particle and the cloud have been separated (hologram C).

These clouds and trails can be observed by holography because they consist of many small particles. They are believed to result from the secondary pyrolysis of coal volatiles ejected through the pores on the particle surface.

The soot strands which were previously observed in the electron micrographs were first observed in the holograms (D). These are found late in the devolatilization process (Zone II) and appear to be a product of reactions in the fuel-rich volatile cloud.

Several parameters have a significant impact upon the form of the volatile trail accompanying the coal particle. At low injection velocities (i.e., low slip environment) the cloud appears as a spherical envelope around the particle, and high concentrations of soot are observed (see Figure 3-4). At higher injection velocities, the slip between the particle and the gas strips the volatile into the wake of the particle, visually appearing to lower the soot concentration. Under fuel-rich conditions, these trails persist and continue to grow through-out the devolatilization region and only a light slip velocity is required to draw out the trails.

There is evidence suggesting that volatile jetting phenomenon is sufficient to give particles enough momentum to form trails even in a quiescent environment. At low injection velocities, a few particles were observed to jump out of the main particle stream, transverse to the main flow directions. Shadowgraphs of particles in this region were found to have the associated soot trails despite the fact that particles in the center region had envelope clouds.

Under oxidizing conditions, high-speed cinematography (Figure 3-5.) reveals that the cloud grows at a rate of 5 x 10^{-4} cm^3/sec until it reaches a size of

UTAH BITUMINOUS COAL
BASELINE CONDITIONS
(35% Excess Air)
DISTANCE FROM BURNER - 4cm

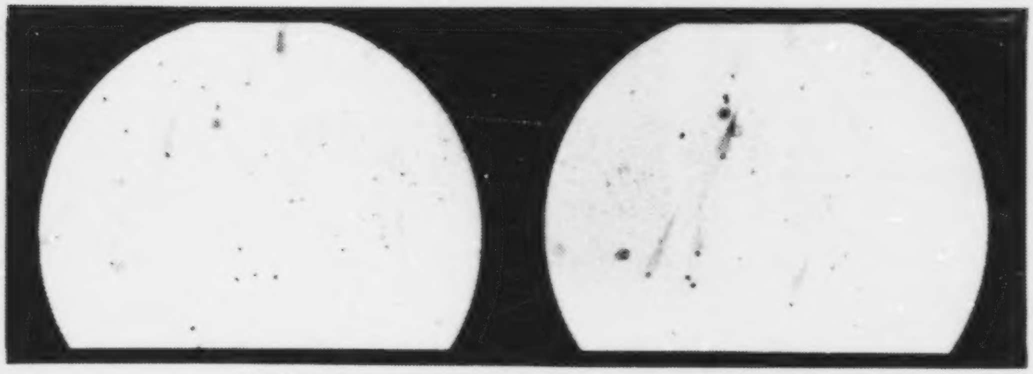

(A) HIGH INJECTION VELOCITY

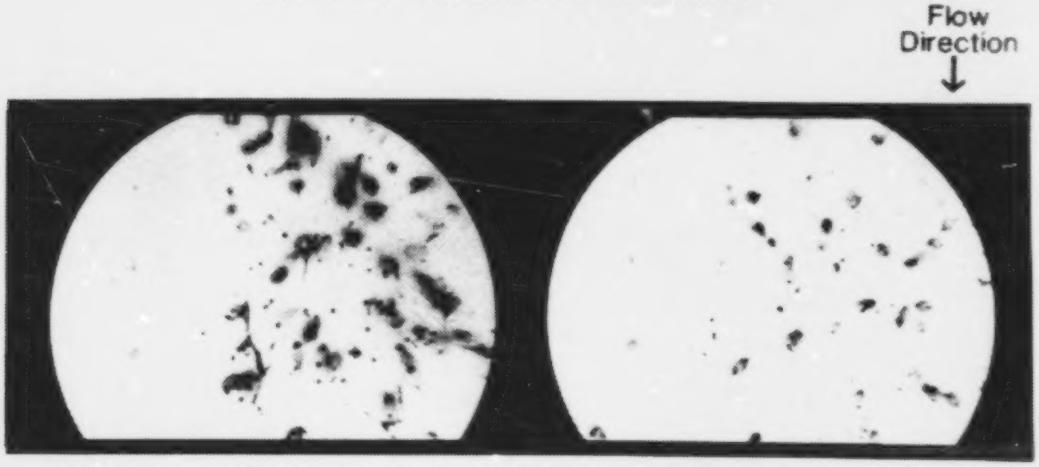

(B) LOW INJECTION VELOCITY

Figure 3.4. Influence of Injection Velocity on Volatile Trail for Utah Bituminous Coal Particles.

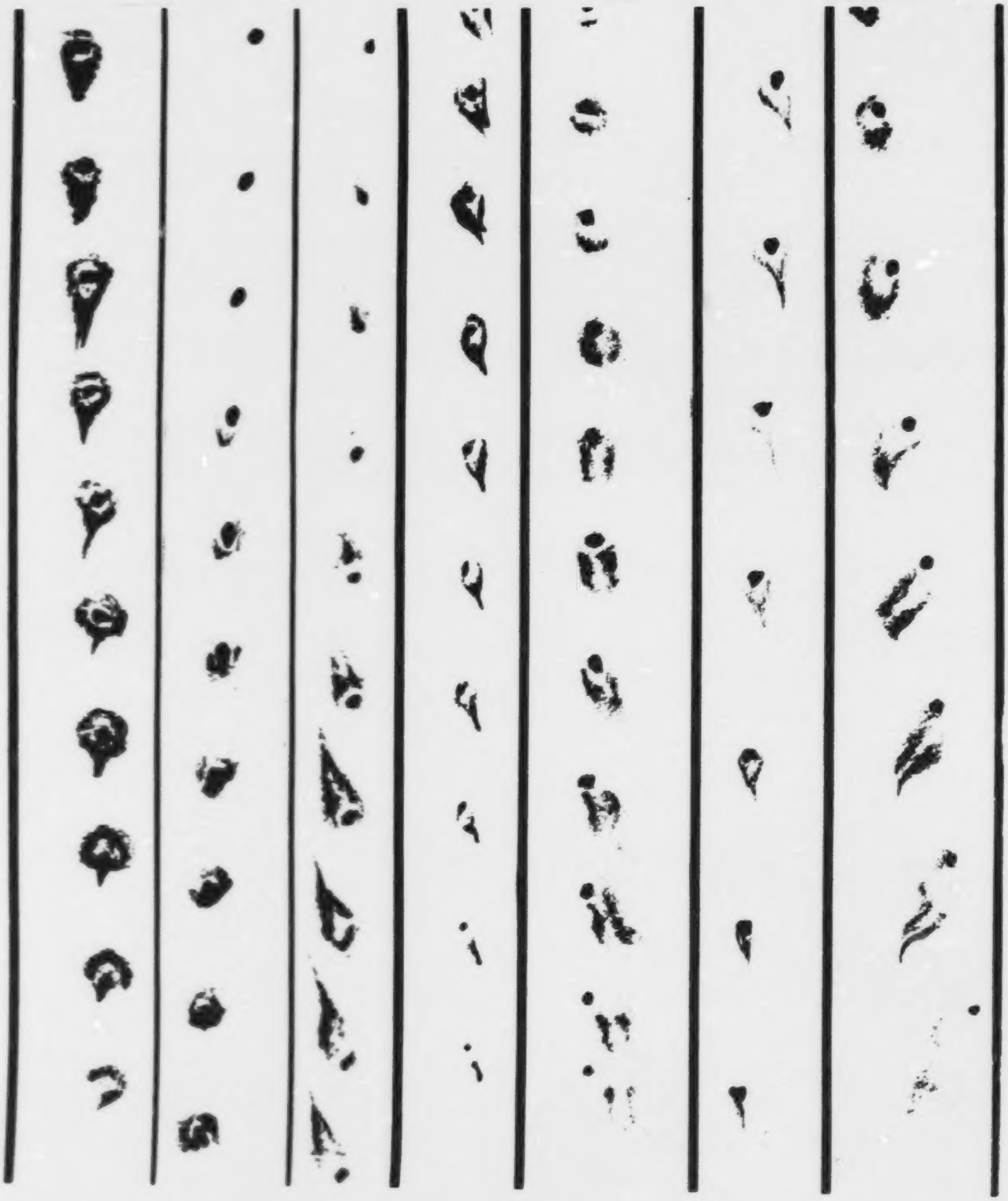

Figure 3.5. High-Speed Shadowgraphs of Reactions 80 μm Bituminous Coal Particles (Speed Between Images ~ 1 msec).

around 300 to 500 μm. This growth rate is consistent with predicted rates using devolatilization rates at similar temperatures (Pohl and Sarofim, 1977). At this point, the oxidation rate of the volatiles is balanced by the volatile evolution and diffusion rate. As the volatile source becomes depleted, the remaining cloud is rapidly oxidized and collapses. A small strand of soot is usually left behind, along with the char particle. Subtle changes in the parent coal particles are also observed during these sequences which last for approximately 10 msec. The initially 80-micron particle swells, the volatile cloud forms, and then both the cloud and the particle contract as the volatiles are depleted.

Figure 3.5 illustrates the sequence of events that occur to the particles as the volatiles are evolved. The most significant observations are:

- all particles do not exhibit precisely the same behavior;
- in many instances, the particle cloud is drawn into a strand which is aligned with the direction of flow. Although the strand normally precedes the particle, there are instances where the strand trails the particle;
- the particle often disengages from its cloud;
- a small number of particles appear to receive an impulse which modifies their direction of flow;
- particles with clouds move slower than particles without clouds;
- some particles disintegrate before the cloud collapses;
- some particles never produce a cloud.

The processes involved with the particle devolatilization are summarized in Figure 3.6. Initially, the particle is heated by convection and radiation and the coal begins to decompose. The particle internal pressure builds up before the volatiles are released and the particle can swell. When the volatiles are released, it might take place initially through a single primary blow hole; but many holes quickly form, and the particle porosity increases as the volatiles are released. The volatile release mechanism is a series of jets from the particle surface which rapidly coalesce a short distance away. At this point, the particle is surrounded by a cloud of gases diffusing into the free stream, and the cloud and the particle can be considered as a micro-system. In the microdiffusion zone near the surface, oxidation reactions

F 3.6

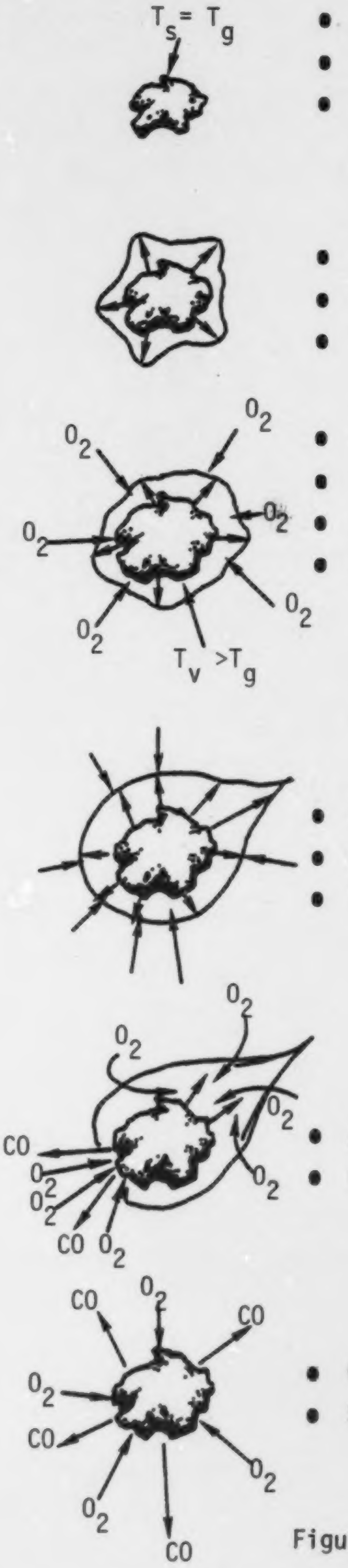

- Particle Heats by Convection and Radiation
- Internal Pressure Buildup
- Particle Swells if Coal Material is Plastic in Nature (Bituminous)

- Blow Holes Form at Weak Points (Bituminous)
- Volatile Release Through Jets
- Volatile Diffuse from Surface

- Particle Porisity Increases as More Volatiles are Released
- Volatiles React with Oxygen Diffusing Inward
- Entire Microsystem Heats Above Bulk Stream
- Soot Formation in Rich Zone

- More Devolatilization due to Increased Temperature
- Steady State Size Dependent on Coal and Size
- Volatile Cloud can be Stripped from Particle

- Asymptotic Volatile
- Cloud Rapidly Collapses

- Char Burnout
- Soot Strand Remains

Figure 3.6. Schematic of Pulverized Coal Combustion Model.

occur and the temperature exceeds that of the free stream. If oxygen cannot significantly penetrate the cloud, pyrolysis reactions form soot and the cloud can be photographed. The amount of volatile release will depend upon the particle size and properties, and the time temperature history. However, at some point the volatile release diminishes, the supply of volatile fuel ceases, and the soot cloud collapses into a strand.

A study of the high-speed movies suggests that, in some instances, the initial volatile jetting is sufficiently violent to throw the particles out of the main stream. However, the main impact of cloud formation appears to be one of retarding the particle velocity due to increased drag or jetting phenomenon. This causes the cloud to precede the particle since the cloud velocity will tend to equilibrate with the free-stream velocity.

Other coal types, and even bituminous coal particles of smaller size, behave strikingly different from the large (80 μm) bituminous coal particles under the same flame-like conditions. The volatile cloud phenomenon and growth of large soot structures are not observed for smaller bituminous coal particles. Observations for 40 μm bituminous particles (Figure 3.7) show few soot strands, clouds, or trails; while 60 μm particles exemplify both but not in the well-developed forms as in the 80 μm case.

3.1.2 Chemical Phenomenon

In this section, the observed chemical processes will be discussed and coupled with the physical mechanism of thermal decomposition. In order to relate the two phenomenon, detailed solid and gas phase composition analyses must be temporarily compared with the physical changes. Of particular interest is the impact of coal size on NO formation, nitrogen intermediates and hydrocarbon species since these were observed to have a major impact on the physical phenomenon.

Figure 3.8 shows the variation of solid composition for the 80 μm bituminous coal from New Mexico. The loss of each component is calculated using the ash as a tracer for the weight loss. Thus, the loss of component A is defined as:

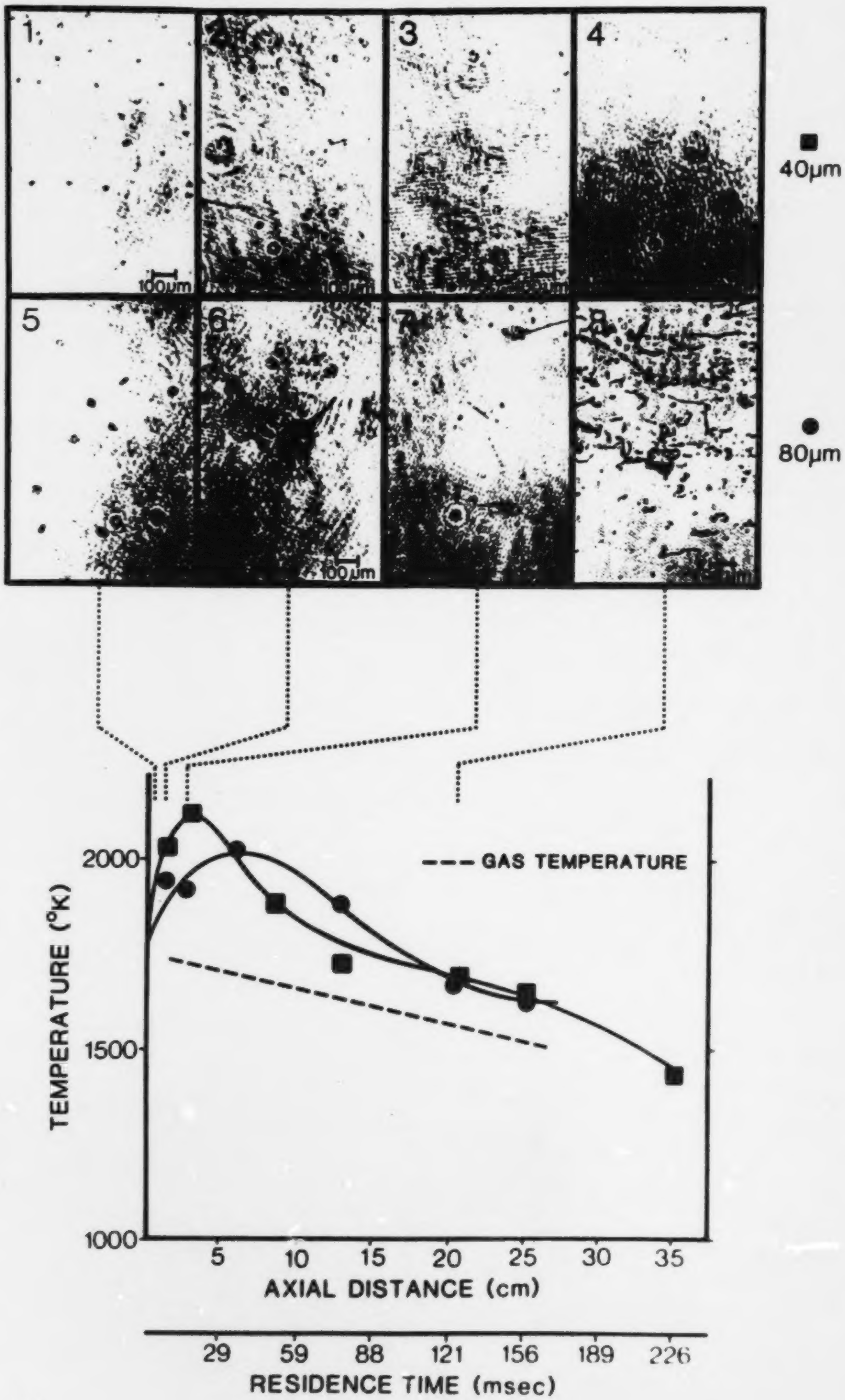

Figure 3.7. Influence of Particle Size on the Thermal and Physical Phenomenon (Four Corners NM Coal)

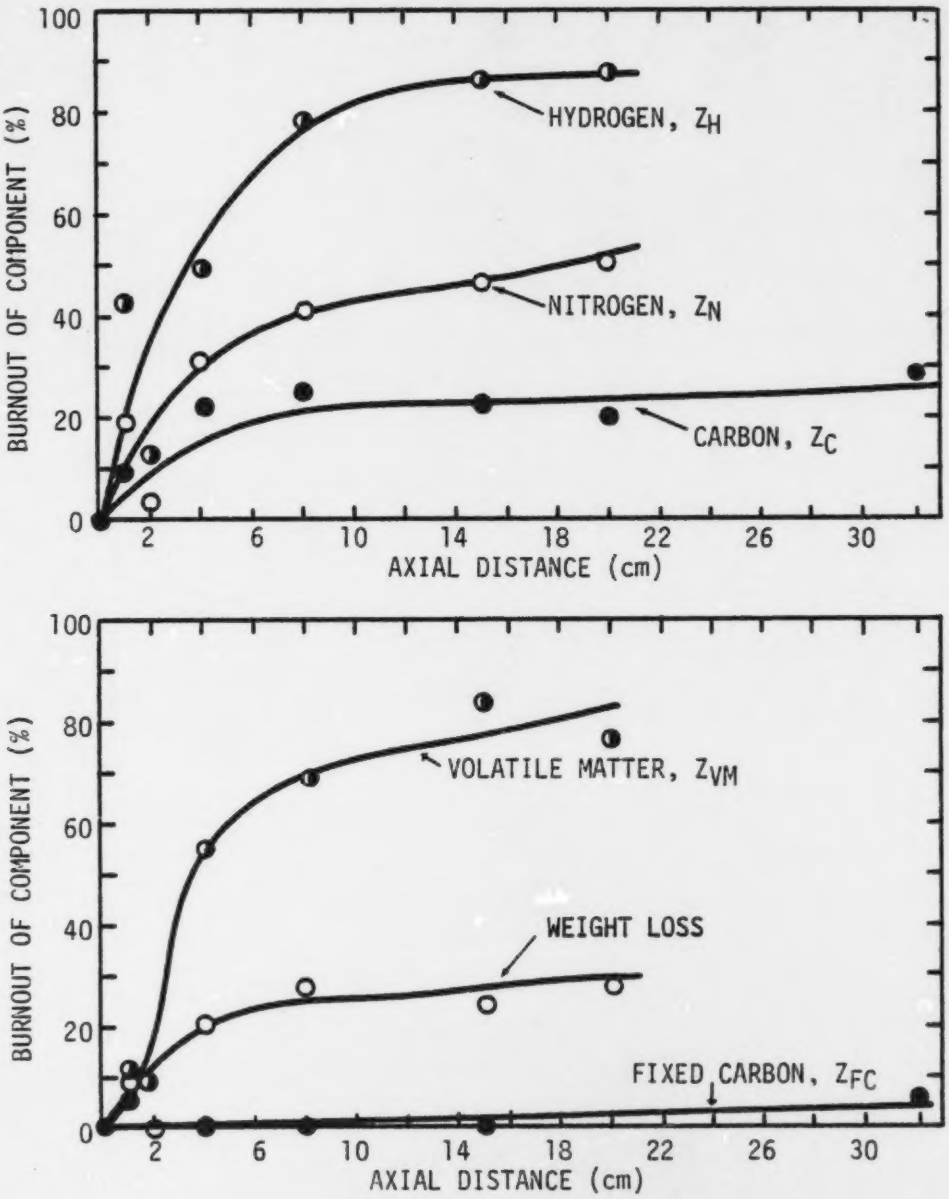

Figure 3.8. Component Burnout Profiles for 80 μm Four Corners NM Bituminous Coal in a Lean CH_4/Air Flame.

temporarily compared with the physical changes. Of particular interest is the impact of coal size on NO formation, nitrogen intermediates and hydrocarbon species since these were observed to have a major impact on the physical phenomenon.

Figure 3.8 shows the variation of solid composition for the 80 um bituminous coal from New Mexico. The loss of each component is calculated using the ash as a tracer for the weight loss. Thus, the loss of component A is defined as:

$$Z_A = 1 - \frac{a}{a_o} \frac{\alpha_o}{\alpha}$$

a denotes the concentration of component A
α denotes the ash concentration
o denotes the initial concentrations

Assuming that the devolatilization zone ends when the hydrogen loss plateaus at 12 cm, which corresponds roughly to the zone definition based on physical observations, the loss of components during devolatilization for the bituminous coal are as follows:

- hydrogen 85 percent
- nitrogen 45 percent
- carbon 22 percent
- volatile matter 75 percent
- fixed carbon less than 2 percent

The volatile matter loss curve is not a true measure of the volatile yield due to the fact that the ASTM yield is not directly related to the yield under combustion conditions. The Q factor (Field et al, 1967) was devised to account for the enhanced yields of volatiles at higher heating rates and lower number densities. The volatile matter loss curve represents only the change in volatile matter content of the solids.

The gas phase composition measurements on the axis of the two phase flame in the thermal decomposition reactor are shown in Figure 3.9. The oxygen from the methane support flame and in the coal transport air are rapidly consumed in the devolatilization zone. All other gas components including NO, CO, HCN and total hydrocarbon peak late in the devolatilization zone. The decline of HCN and CO during the char oxidiation is due to the combination of oxidation, and dilution. The decline in NO can be attributed to gas-phase or heterogeneous reduction and

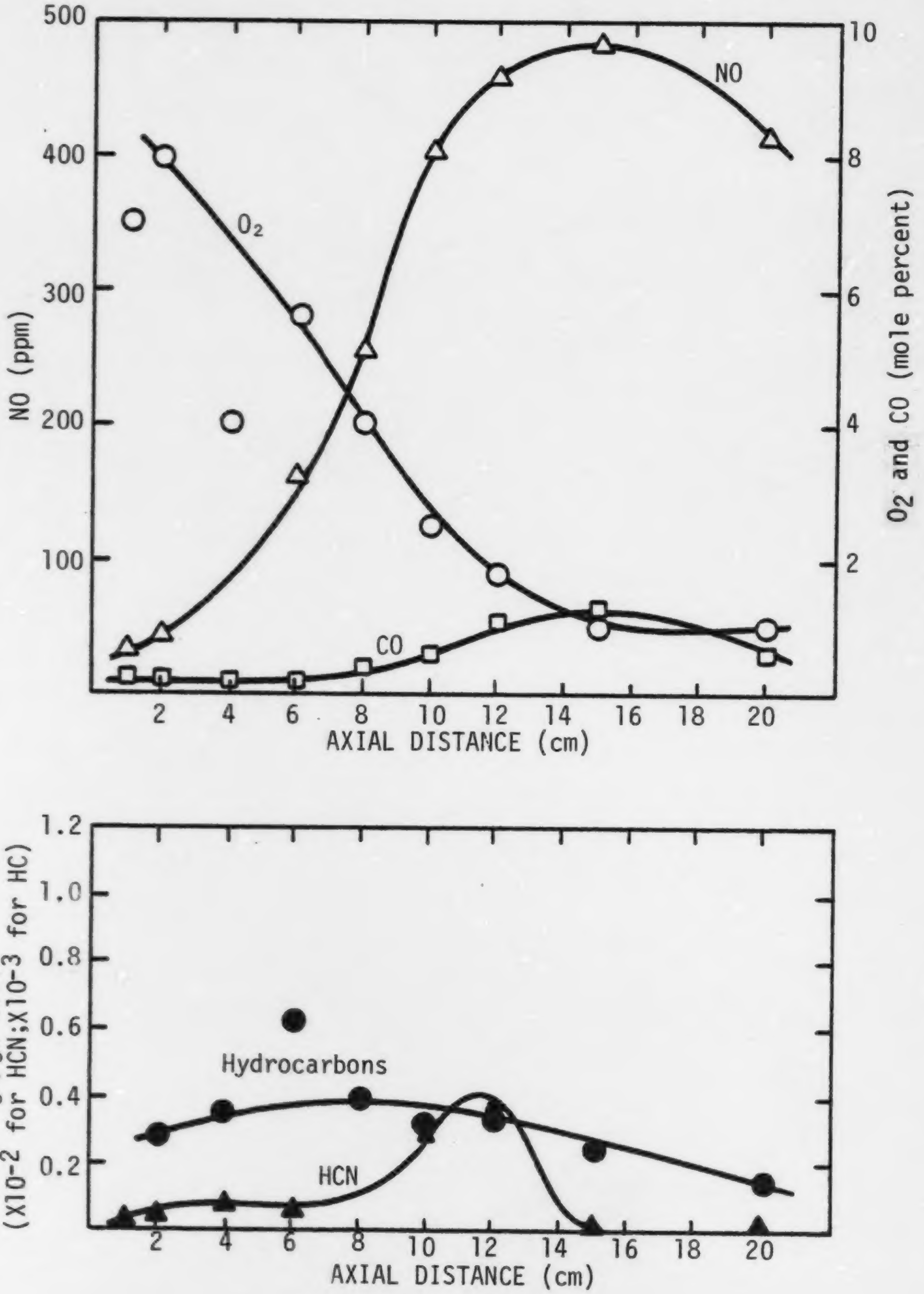

Figure 3.9. Gas Phase Composition Profiles for 80 μm Four Corners N.M. Bituminous Coal in a Lean Methane/Air Flame.

dilution. Little ammonia was measured (<10 ppm), but large amounts of hydrocarbons were found, composed primarily of methane (40 percent), ethylene (22 percent), acetylene (21 percent), propane (12 percent), and ethane (4 percent).

The results obtained with smaller coal particles are more typical of a complete combustion sequence, as shown in Figure 3.10 for the 40 microns Four Corners, New Mexico bituminous coal. The devolatilization process is rapid, with 90 percent of the hydrogen lost in approximately 25 msec (approximately one-quarter of the time required for the 80-micron sample). Sixty percent of the nitrogen is lost in the devolatilization zone, and above 90 percent overall. There appears to be an enchanced yield of nitrogen in the devolatilization zone for the 40-micron sample when compared to the 80-micron sample. Nitrogen is lost at a much slower rate in the char oxidation zone paralleling the carbon-loss rate. The total carbon loss approaches 80 percent at total residence time of 100 msec.

The gas phase composition measurements for the 40 um bituminous coal (Figure 3.11) are different from the 80 um data in several aspects. As expected from the solid phase composition data, nitric oxide and carbon monoxide peak earlier than for the 80 um. Also the peak levels of NO and HCN are higher while the peak levels of hydrocarbons and carbon monoxide are sharply lower.

The absence of volatile clouds and the small amounts of pyrolysis products such as hydrocarbons and carbon monoxide suggest that the volatiles are consumed very rapidly after being released from the coal matrix. For larger particles, the flux of volatiles may be sufficient to shield the surface from oxygen as has been suggested earlier (Howard, 1965), and thus form the volatile cloud. For the 40 um coal sample, the reactions must be occurring very rapidly, perhaps with in the coal structure with simultaneous oxygen attack at the coal surface. These direct observations of the change in decomposition/oxidation modes with changing particle size have far reaching impacts on soot formation and the conversion of fuel nitrogen to nitric oxide.

3.2 The High Temperature Thermal Decomposition and Oxidation of Other Coal Types

The preceding sections discussed the observed physical, chemical and thermal phenomenon associated with nigh volatile bituminous coal particles as they were subjected to simulated flame conditions. Using these results as the baseline behavior, this section will compare the behavior of four other coal types:

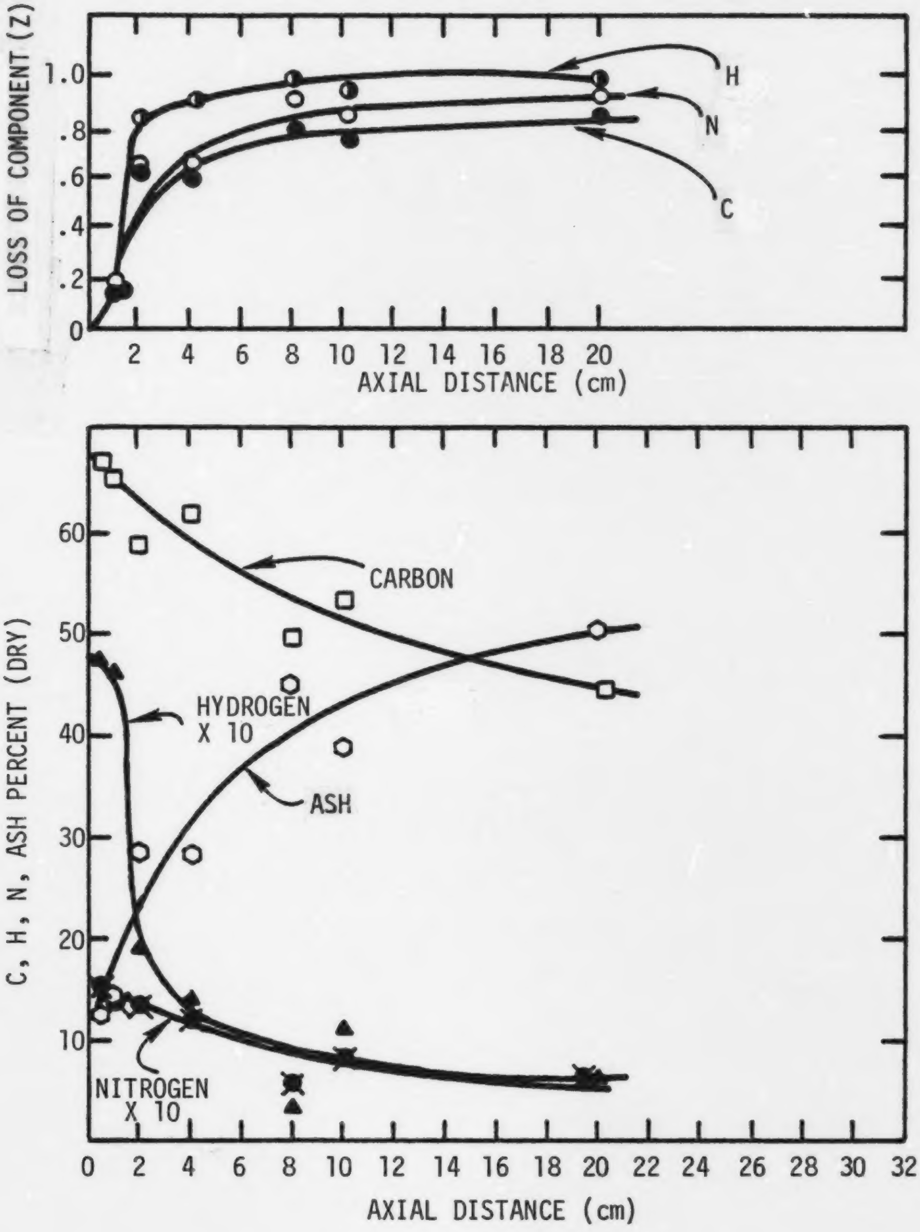

Figure 3.10. Solid Phase Composition Profile - 40 μm Four Corners.

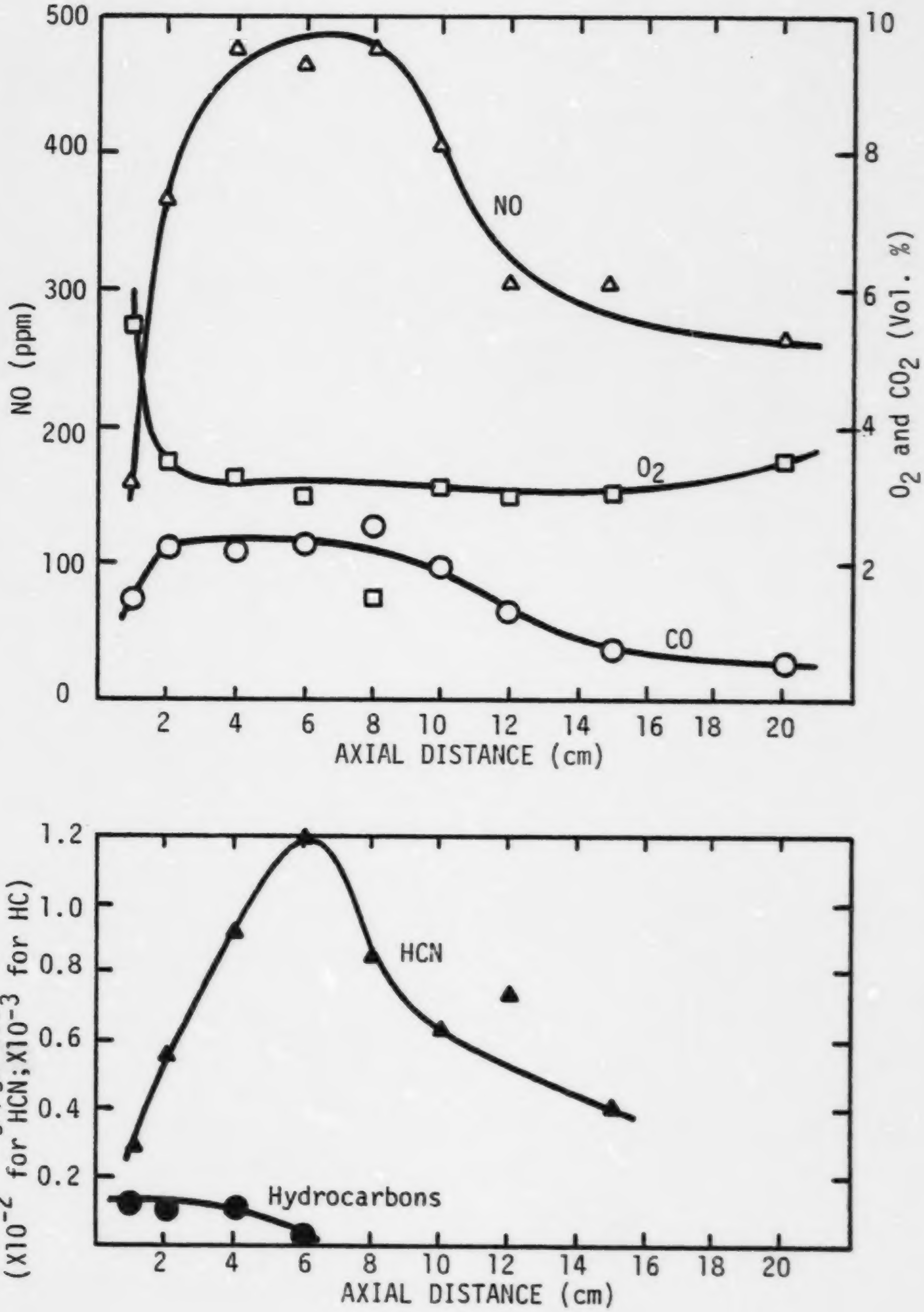

Figure 3.11. Gas-Phase Composition Profiles for 40 μm Four Corners NM Coal in a Lean Methane/Air Flame.

- lignites; one coal from Beulah, N.D. and the other from Savage, Mont.
- anthracite; a coal from Pennsylvania
- bituminous; a coal from Black Creek, Ala.
- Char; a char produced from the high volatile bituminous coal.

3.2.1 Physical Phenomenon

Differences in physical behavior between coal types are to be expected, since even the appearance of the raw coals suggest different physical structures. The morphology of three different pulverized coals are presented in Figure 3.12. Pulverizers used for coal operate on the principal that coal fails in the brittle mode when subjected to a shear force (Karr, 1978). The high-rank anthracite coal is the most crystalline pulverized coal in appearance due to its associated hardness. The operation of the pulverizer appears to break the brittle coal along crystalline planes producing sharp edges and angular structures. The pulverized bituminous coal is also crystalline in appearance, but the edges are not so sharp suggesting that the coal is not as brittle. This malleability causes the pulverizer to produce more rounded particles. Due to the wet nature of lignite, pulverizers which subject the coal to shear tend to make the particles fail plastically (Karr, 1978). The pulverizer crumbles lignite rather than breaking it. The resulting structures are more planar than angular and the surface appears to have deep cracks.

During thermal decomposition, the changes that occur structurally to a Beulah, North Dakota lignite are no less dramatic than for the bituminous coals but are distinct (Figure 3-13). At short residence times, where the bituminous coals have already formed cenospheres, the lignite particles have only slightly changed. These changes are associated with the growth of crevices on the particle surface. The plastic, almost molten, appearance of the bituminous char particle is not a characteristic of the lignite particles which have a dry and flaky appearances. At longer residence times, the distinct particle types can be classified as follows:

- relatively solid particles with cracks;
- high surface area particles with substantial crevice development;
- ultra-high surface area particles with extensive erosion in both pores and crevices.

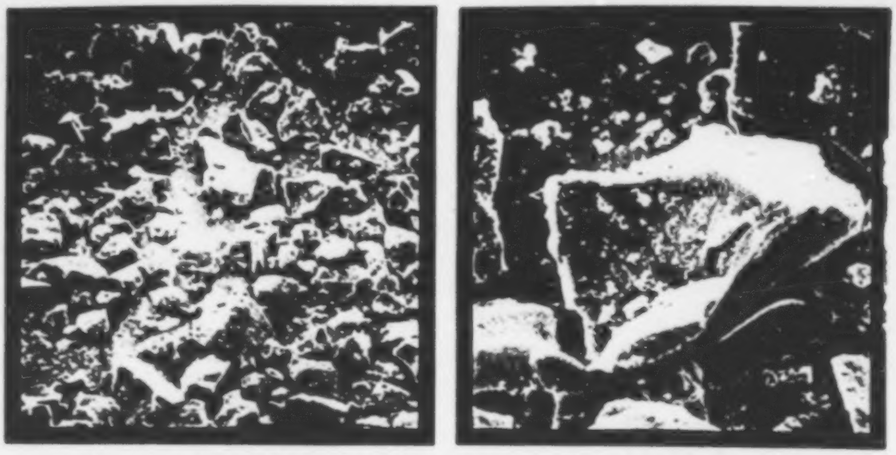

(A) PENNSYLVANIA ANTHRACITE

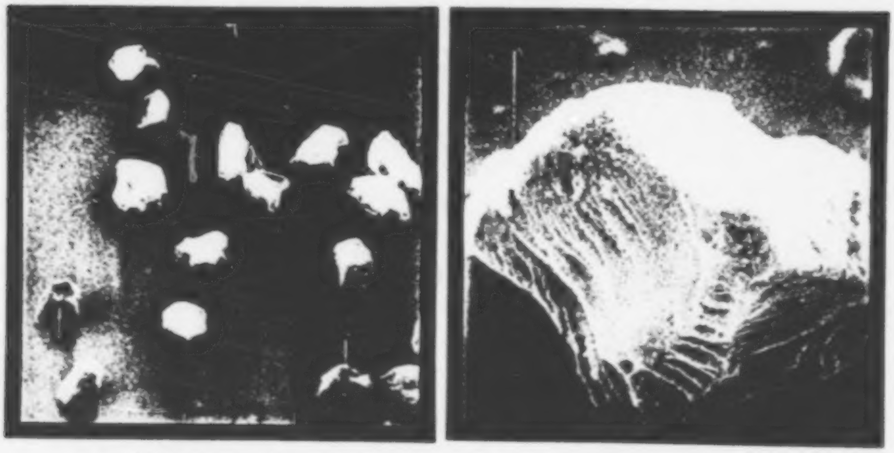

(B) NEW MEXICO BITUMINOUS

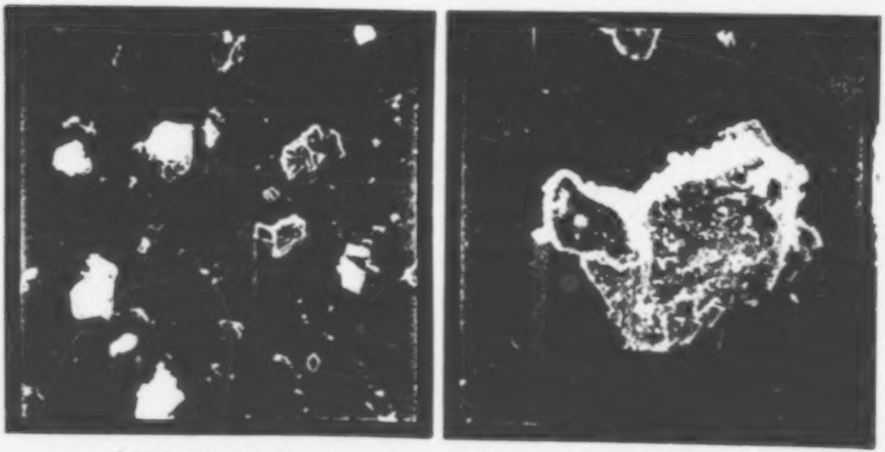

(C) NORTH DAKOTA LIGNITE

Figure 3.12. Scanning Electron Micrographs of Untreated Pulverized Coals.

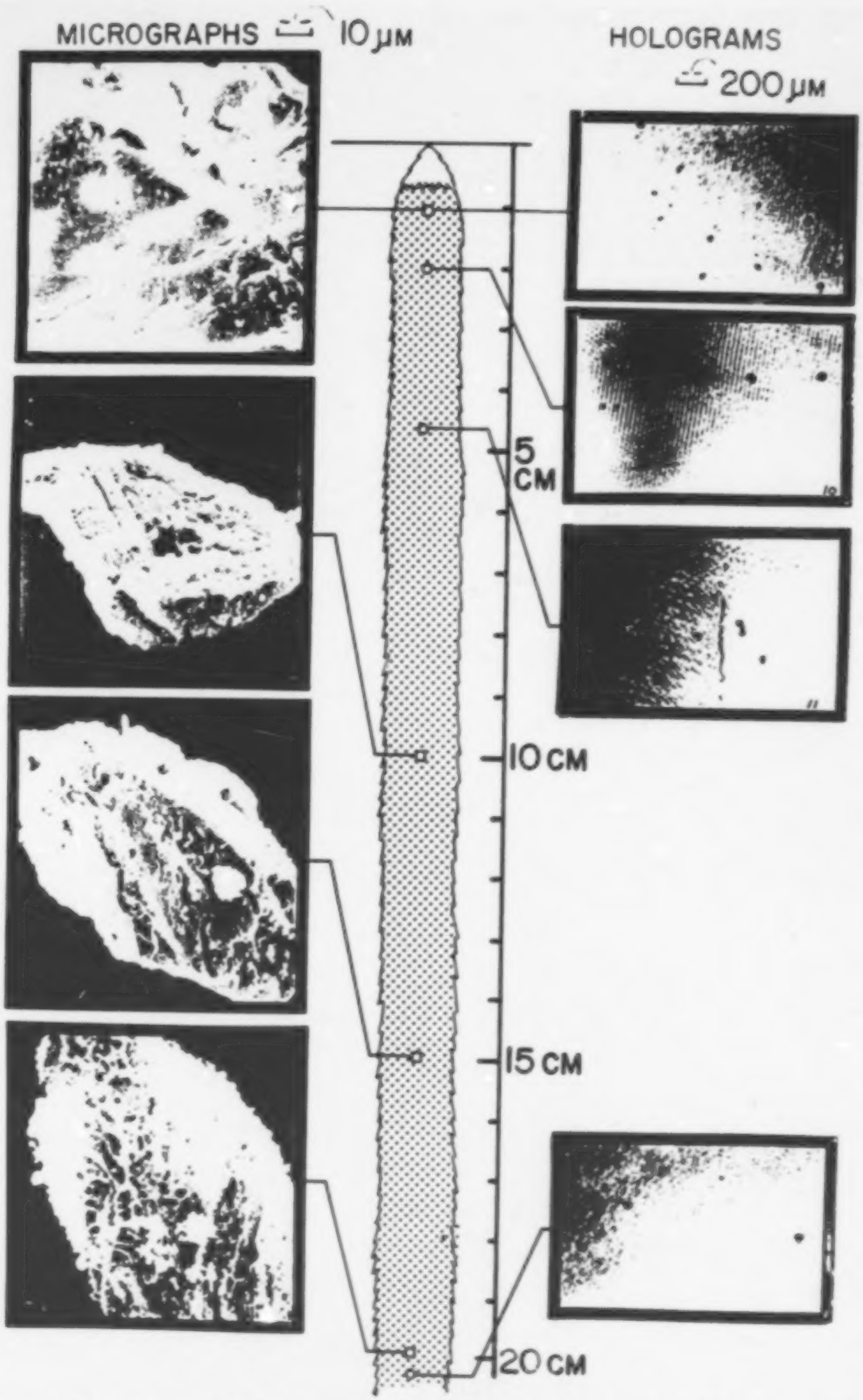
MICROGRAPHS
10 μM
HOLOGRAMS
200 μM
5 CM
10 CM
15 CM
20 CM
10
11

Figure 3.13. Physical Phenomenon Associated With Beulah Lignite Particle Decomposition (CH_4/Air Flame, 35% Excess Air).

Another distinctive feature of lignite coals compared to bituminous particles is the absence of either trail or large soot structure. Holograms of this sample reveal no substantial changes in the lignite particles as they traverse the reactor, and only minimal amounts of larger soot structure under fuel-rich conditions.

The changes in structure of individual lignite particles are revealed by the behavior of the char size and specific surface area. The size change of lignite particles was virtually zero under these combustion conditions as opposed to the gross size changes of bituminous coal particles. On the other hand, the specific surface area (both CO_2 and N_2 shown in Figure 3-14) changed even more dramatically for the lignite than for bituminous. The raw lignite coal was found to have less specific surface area than the bituminous coal. However, the thermal processing produced particles with almost twice the specific surface area of the bituminous coal particles

At the other extreme of coal type, *in situ* measurements (holograms) of anthracite particles exposed to temperatures in excess of 1500 K indicate the anthracite structure does not change after more than 250 ms of high temperature exposure, and there is a distinct absence of both volatile trails and soot even at extremely rich conditions.

A comparison of a number of coal types with chemical properties listed in Table 2-III is supplied by the representative holograms in Figure 3.15. The propensity to form large soot structures and to form visible volatile clouds appears to be strongly dependent on coal type. For the limited number of coals tested, general grouping by rank can be construed with bituminous coals demonstrating both volatile clouds and copious amounts of soot structures. Lignite coals were found to produce only small amounts of soot with no evidence of volatile clouds and anthracite had little tendency to soot.

The propensity to soot of a particular coal could be correlated with the tar yield from the volatiles. This hypothesis is supported by these data since the vacuum pyrolysis data from many of the same coals (Solomon, 1981, FCR Final Report) demonstrates that the bituminous coals have volatiles rich in tars. Lignites, on the other hand, yield only a small tar concentration while anthracites have a small total volatile yield. The absence of a visible vola-

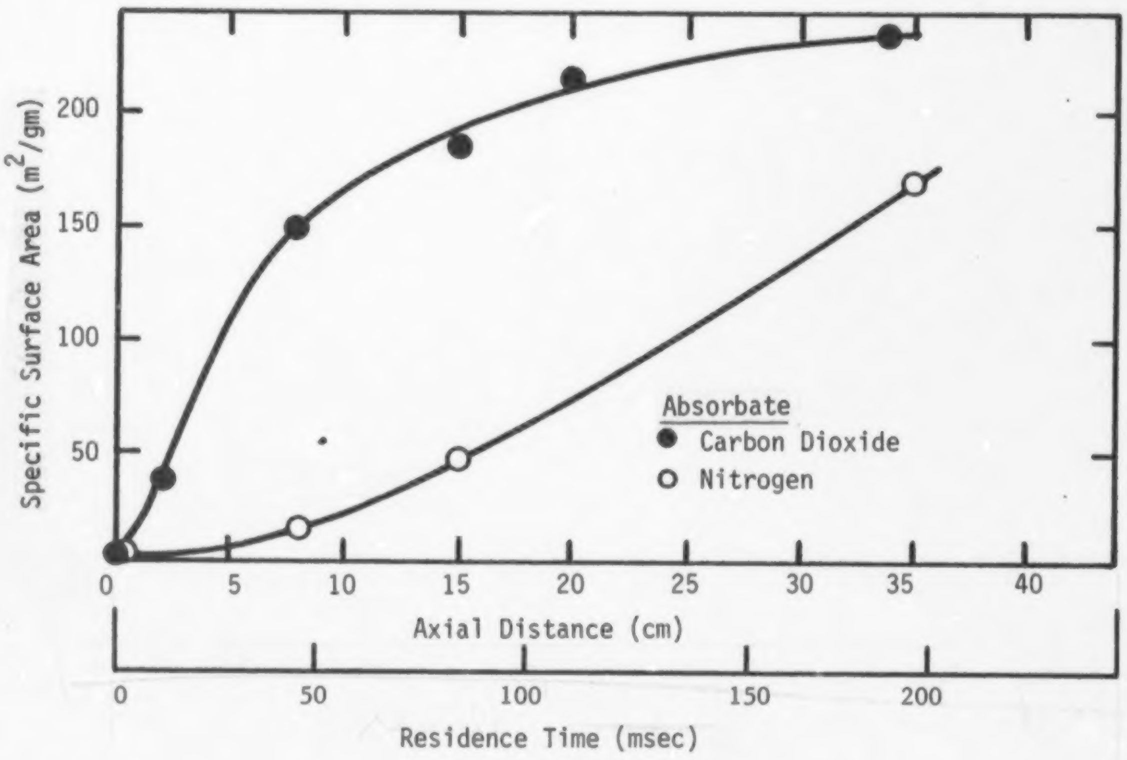

Figure 3.14. Surface Area Changes for Beulah Montana Lignite in Lean Methane/Air Flame.

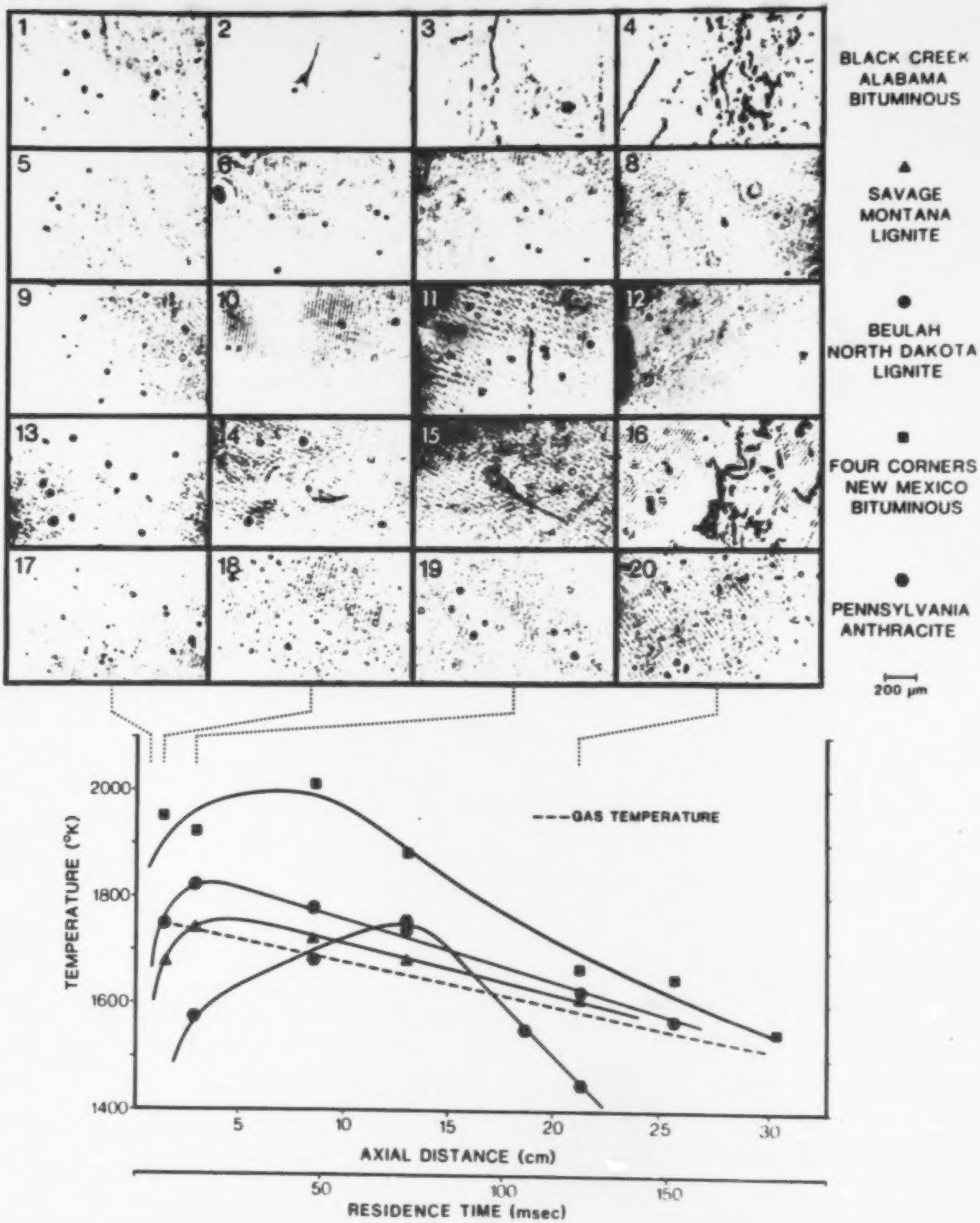

Figure 3.15. The Effect of Coal Type on Physical and Thermal Phenomenon Associated With Pulverized Coal Decomposition.

tile cloud during the lignite thermal decomposition sequence cannot necessarily be construed as a change of mechanism for volatile release and combustion. The clouds may just not be visible to the imaging technique due to the absence of fine particulate within the cloud. Further evidence of cloud formation is required.

3.2.2 Thermal Phenomenon

The relationship between the physical phenomena and the measured particle temperature was shown in Figure 3.3 for the 80 μm Four Corner N.M. high volatile bituminous coal. The particle temperature was found to exceed the gas temperature measured in the absence of particles. This difference was at a maximum in the devolatilization zone where the maximum rate of weight loss occurred and where the particles were observed to produce volatile clouds.

The measured temperature for a low volatile char injected into the same environment was dramatically different from that observed with a high volatile coal. The time/temperature history obtained during the production of this char was essentially the same as that shown in Figure 3.3. However, when the char was reinjected into the reactor, the two-color temperature profile (Figure 3.16) indicated that the char is much slower to ignite and does not attain the same maximum temperature as that observed for the parent coal. The char required almost 9 msec for ignition to occur, almost twice that of the parent coal. The maximum difference between the bulk gas and the two color particle temperature (approximately 85^{o}K) occurred at 20 msec.

Two-color particle temperature measurements for a variety of coal types and sizes are shown in Figure 3.17 and indicate that the behavior can normally be classified by coal rank. All high volatile bituminous coals appear to behave similarly, producing a large temperature overshoot early in the devolatilization zone. Lower rank lignites never attain the extreme temperatures as the bituminous coal. However, they still attain a temperature significantly above the background temperature. For both the lignite coals investigated, the maximum temperature occurs over an extended region (12 to 120 msec). Ignition distances for lignite coals are similar to those of bituminous coals. The anthracite coal is even slower to ignite (ignition distances approximately 30 msec) than the bituminous char.

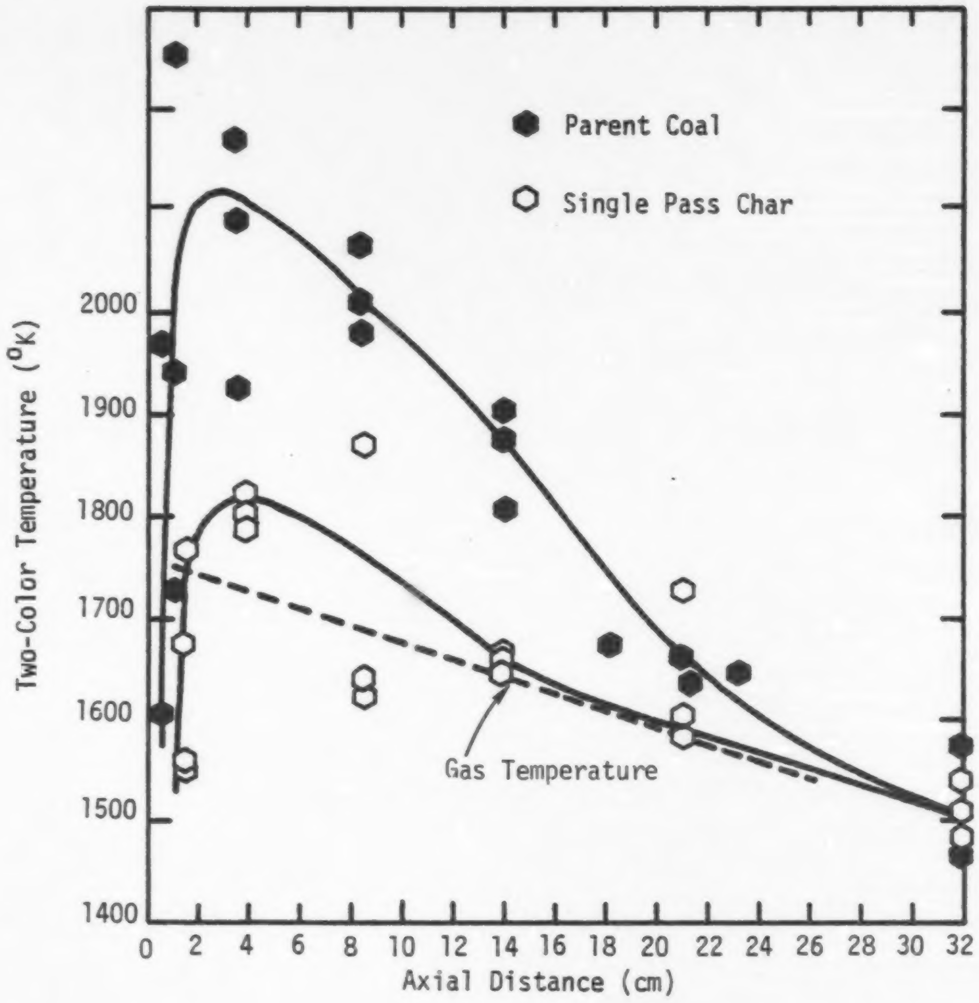

Figure 3.16. Two-Color Temperature Profiles of 80 μm Four Corners NM Bituminous Coal and a Single Pass Char.

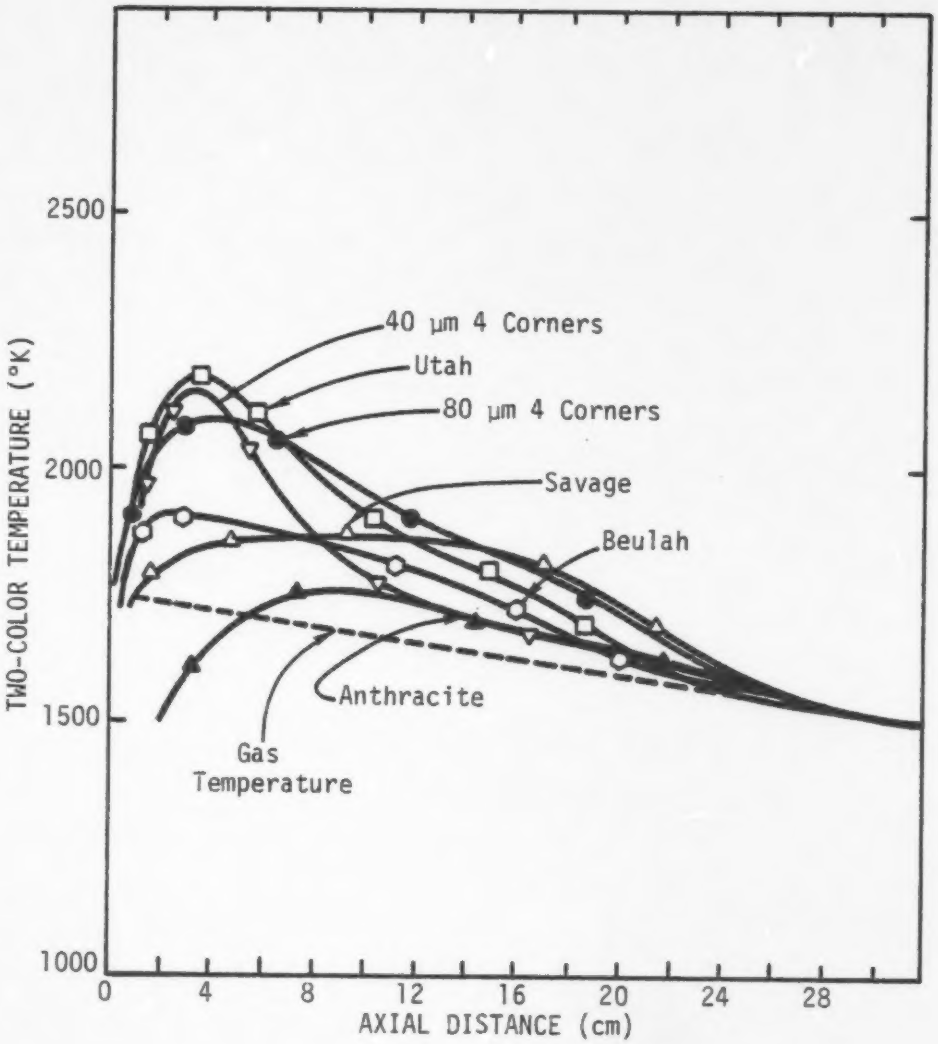

Figure 3.17. Two-Color Temperature Profiles for Pulverized Coal Samples in Lean Methane/Air Flame.

The two-color temperature for each coal appears to be strongly influenced by both the volatile content and the composition of the volatiles. Bituminous coals yield volatiles which are rich in both hydrocarbons and tars with compositions similar to the parent coal (Solomon, 1981). On the other hand, lignites contain a large quantity of water and produce little tar and hydrocarbon and, hence, have a lower volatile calorific value. The extreme behavior is exhibited by char and anthracite which have minimal volatile content. Estimates of the calorific value of the volatiles from the pyrolysis data of Solomon (1981) are shown in Table 3.1, together with the maximum difference between the particle and the gas temperature for each coal. It can be seen that there is correspondence between the volatile calorific value yield and the temperature excess. This is presented graphically in Figure 3.18. T 3.1

Two color measurements of the 80 μm bituminous coal injected into a rich flame using a nitrogen transport fluid, indicate that soot radiation may be influencing the very early behavior. These measurements show the presence of a temperature spike higher than the gas temperature. The spike, which occurs at about 10 msec, is followed by a rapid decline to below the gas temperature. For coals with a high propensity to soot, there may be several regions of behavior as different radiation and combustion modes become dominant. These data indicate that for bituminous coals, the early two color data is biased by soot interference. However, volatile oxidation appears to be the dominant thermal mode during the bulk of the devolatilization zone (Figure 3-19). With the depletion of volatiles, the temperature declines to a level that can be supported by oxidation on the char surface.

The conclusion that volatile oxidation influences the particle thermal behavior supports the hypothesis that during devolatilization, the particle volatile cloud must be considered as a microsystem. Soot was observed with the large particles but not the small particles, and yet the measured particle temperatures were very similar. Thus, the presence of solid particles is not the cause of the increased particle temperature. The results suggest that even the small particles have some thermal coupling between the volatile reaction zone and the particles.

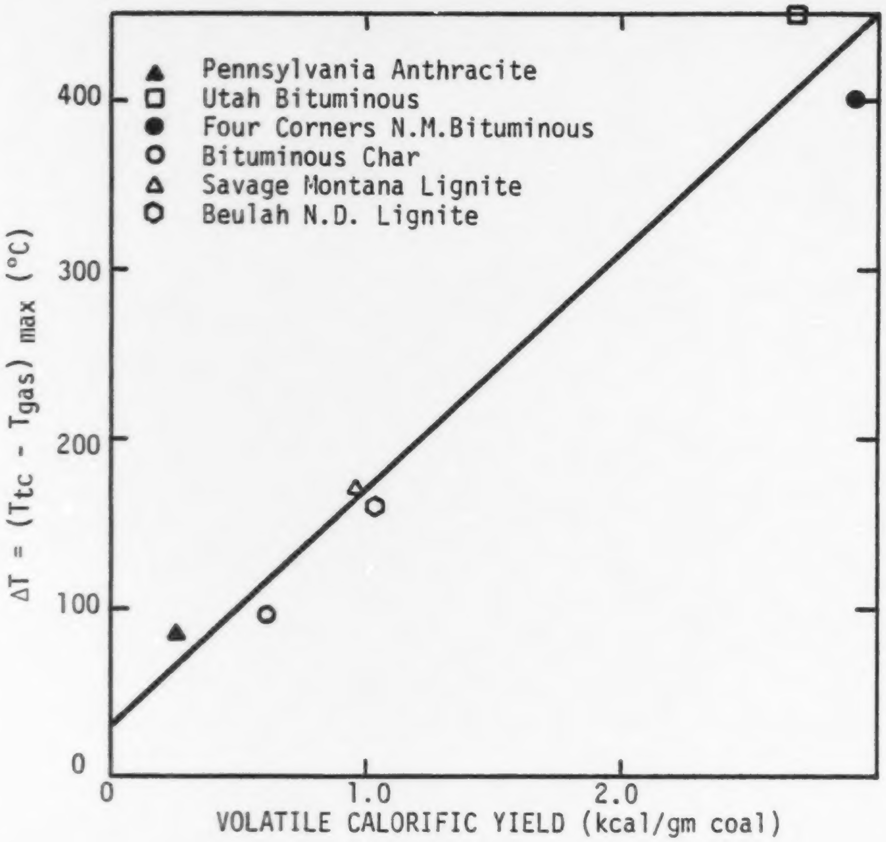

Figure 3.18. Volatile Calorific Yield and Maximum Particle Temperature Excess.

Table 3.I. Volatile Calorific Yields, Temperature Overshoots and Ignition Distance

COAL TYPE	VOLATILE MATTER (% DRY)	MOISTURE (AS REC'D)	$(\Delta T)_{max}$ (^oC)	VOLATILE CALORIFIC YIELD* (kcal/gm COAL)	IGNITION DISTANCE (cm)
Pennsylvania Anthracite	3.84	5.46	85	0.270	5 cm
Bituminous Char	--	--	95	0.61	1.5 cm
Savage, Montana Lignite	44.76	36.36	170	0.95	1 cm
Beulah, N.D. Lignite	42.82	33.10	160	1.03	< 1 cm
Four Corners, N.M. Bituminous	40.87	4.02	400	2.91	< 1 cm
Utah Bituminous	41.94	7.41	450	2.68	< 1 cm

* Estimated from proximate analysis and Solomon volatile composition determined as the lower heating value at a reference temperature of 1750 K.

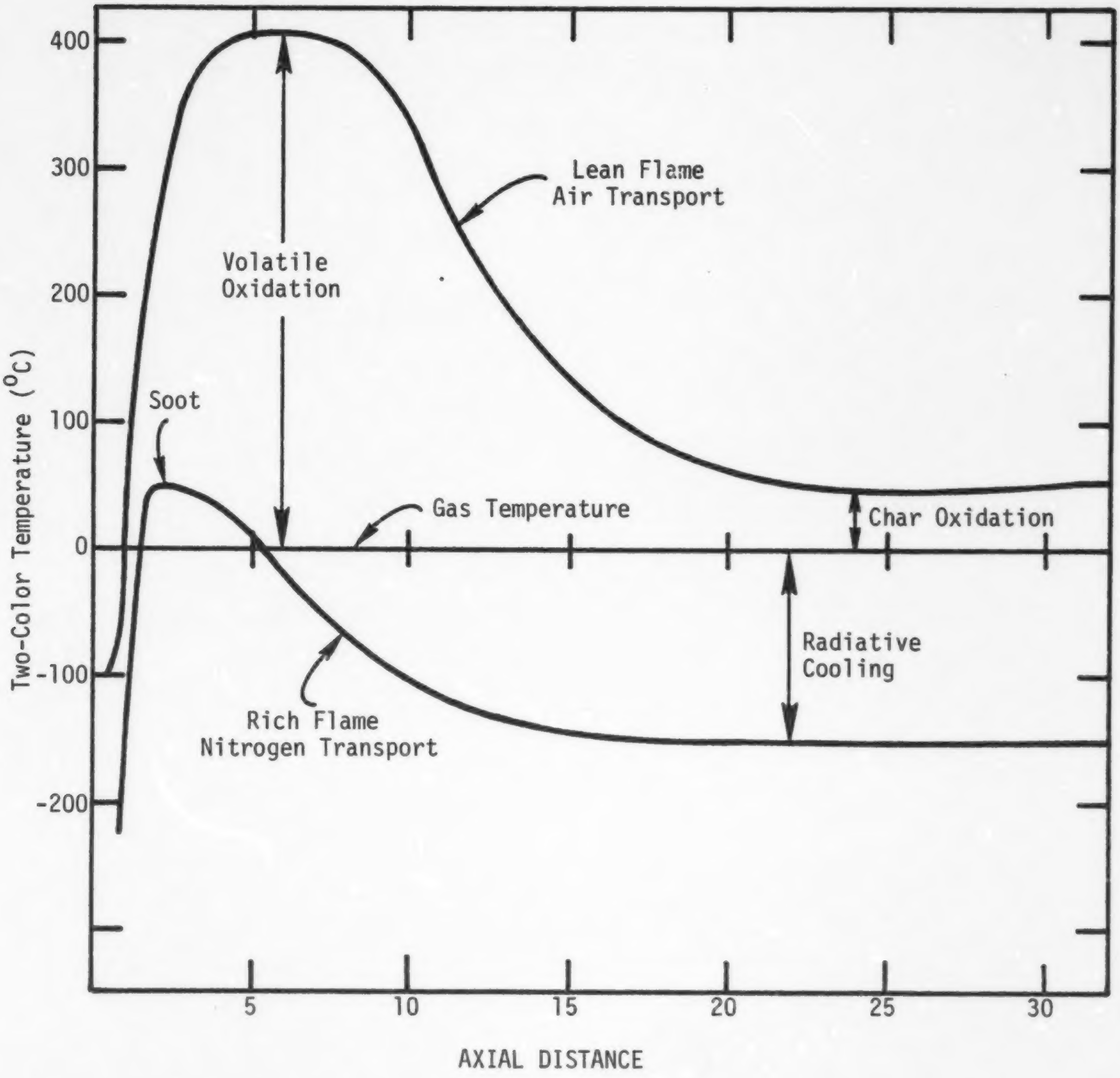

Figure 3.19. Comparison of Two-Color Response With and Without Oxygen Present (Four Corners NM 80 μm).

3.2.3 Chemical Phenomenon

The chemical behavior of reacting high volatile bituminous coal particles as discussed in Section 3.2.1 indicated a well-defined devolatilization zone lasting approximately 70 msec. The chemical evidence for this distinct zone was the sharp decrease in volatile matter and hydrogen content of the solid phase material and a peak in concentration of the predominant volatile species such as HCN, NO, CO and hydrocarbons. These same trends are observed for the Utah high volatile bituminous coal as shown in Figure 3.20 and 3.21.

While bituminous coals are exemplified by the well defined devolatilization zones, lignites appear to decompose more slowly. These coals lose volatile content throughout the entire reactor residence time. Figure 3.22 illustrates this fact with the Beulah lignite. Losses of carbon and nitrogen occur almost linearly with time, while hydrogen is exponential only at early residence times. Total nitrogen loss exceeds 85 percent for this sample, compared to approximately 60 percent for the bituminous coals of similar size. The rate of evolution of hydrogen is still faster than those of nitrogen and carbon. Similar trends are exemplified by the Savage Montana lignite as shown by the solid phase composition data in Figure 3.23.

Gas phase measurements for the Beulah lignite sample (Figure 3.24) indicate little volatile species such as hydrocarbons, carbon monoxide or hydrogen cyanide. However, peak levels of nitrogen oxides are only about 20% lower than for the bituminous coals.

Two low-volatile samples, a Pennsylvania anthracite and a char produced from the 80 μm Four Corners bituminous coals, behaved quite differently from each other. The anthracite solid composition changed very little down the entire length of the reactor. However, the single-pass char which was produced by collecting solid at 20 msec, loses large amounts of its remaining hydrogen, nitrogen, and carbon when it is reinjected (Figure 3.25). The distinguishing feature between the component burnout profiles of the char and its parent coal is the similarity between carbon and nitrogen loss rates for the chars. Also, the gas phase composition measurements for the single-pass char yielded almost no volatile species (HC, HCN, CO, NH_3) while the NO peaked at about 300 ppm.

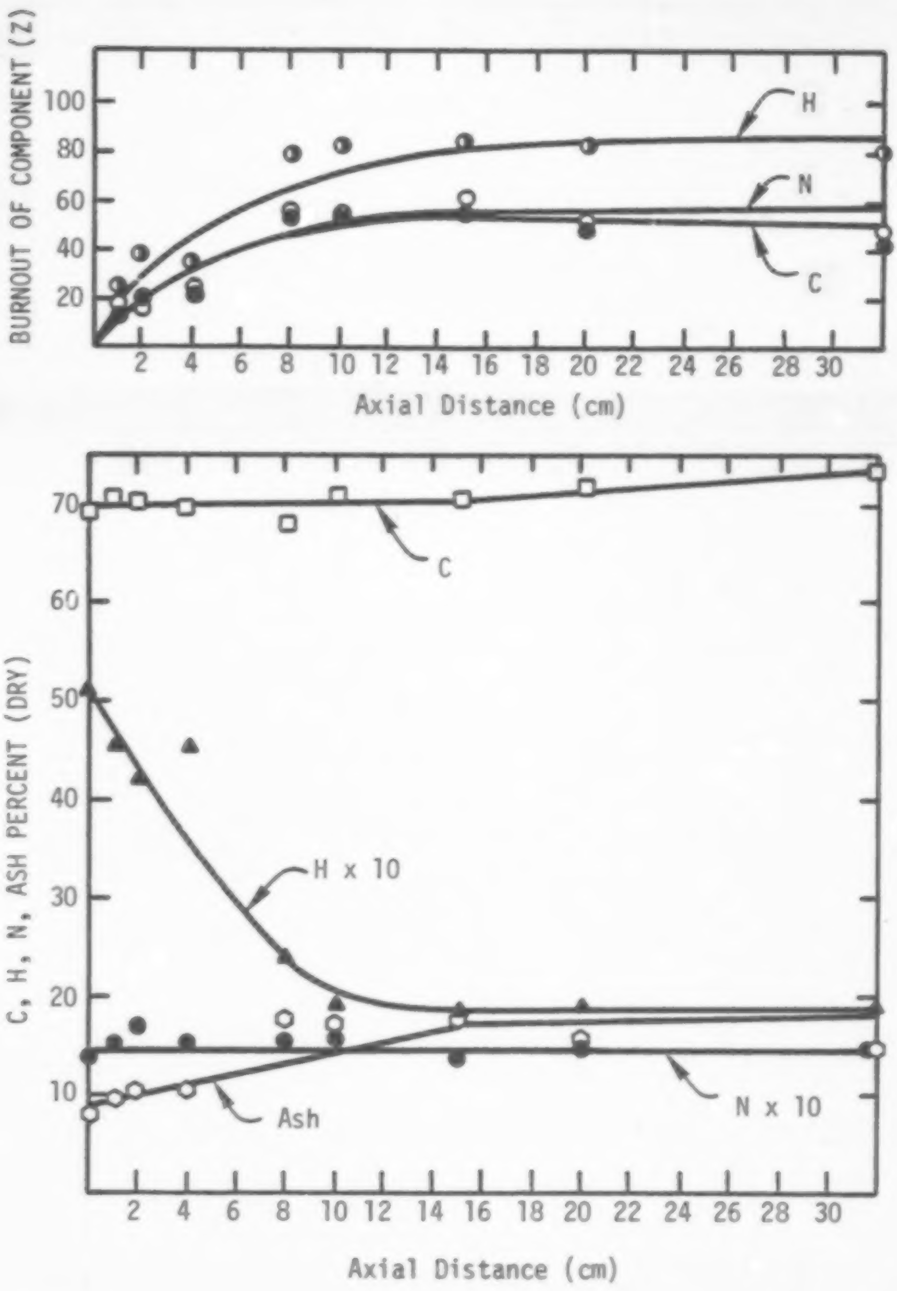

Figure 3-20. Solids Composition Profile - Utah Bituminous

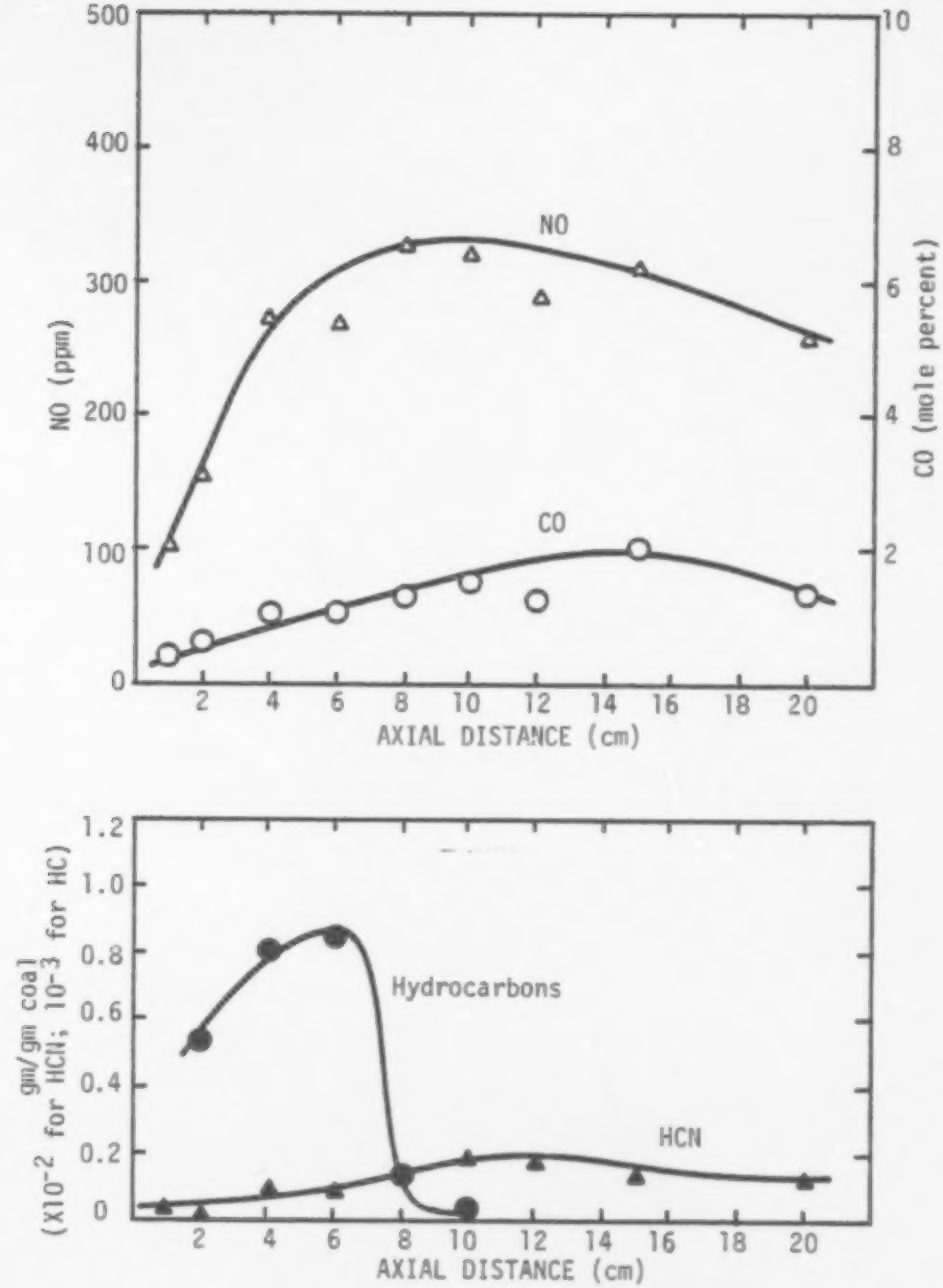

Figure 3.21. Gas Phase Composition Profile for Utah Bituminous Coal in a Lean Methane/Air Flame.

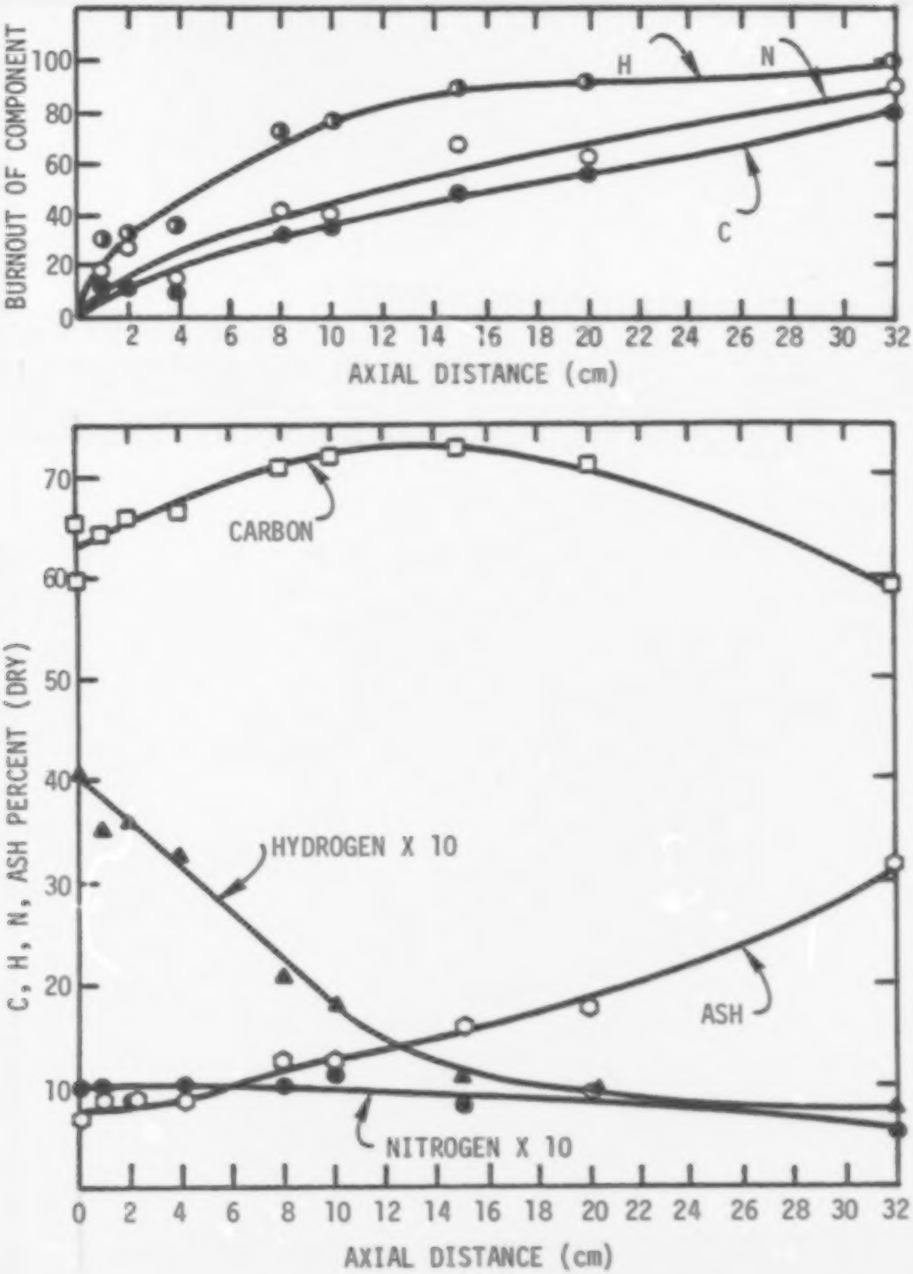

Figure 3-22. Solid Composition Profile - Beulah Lignite.

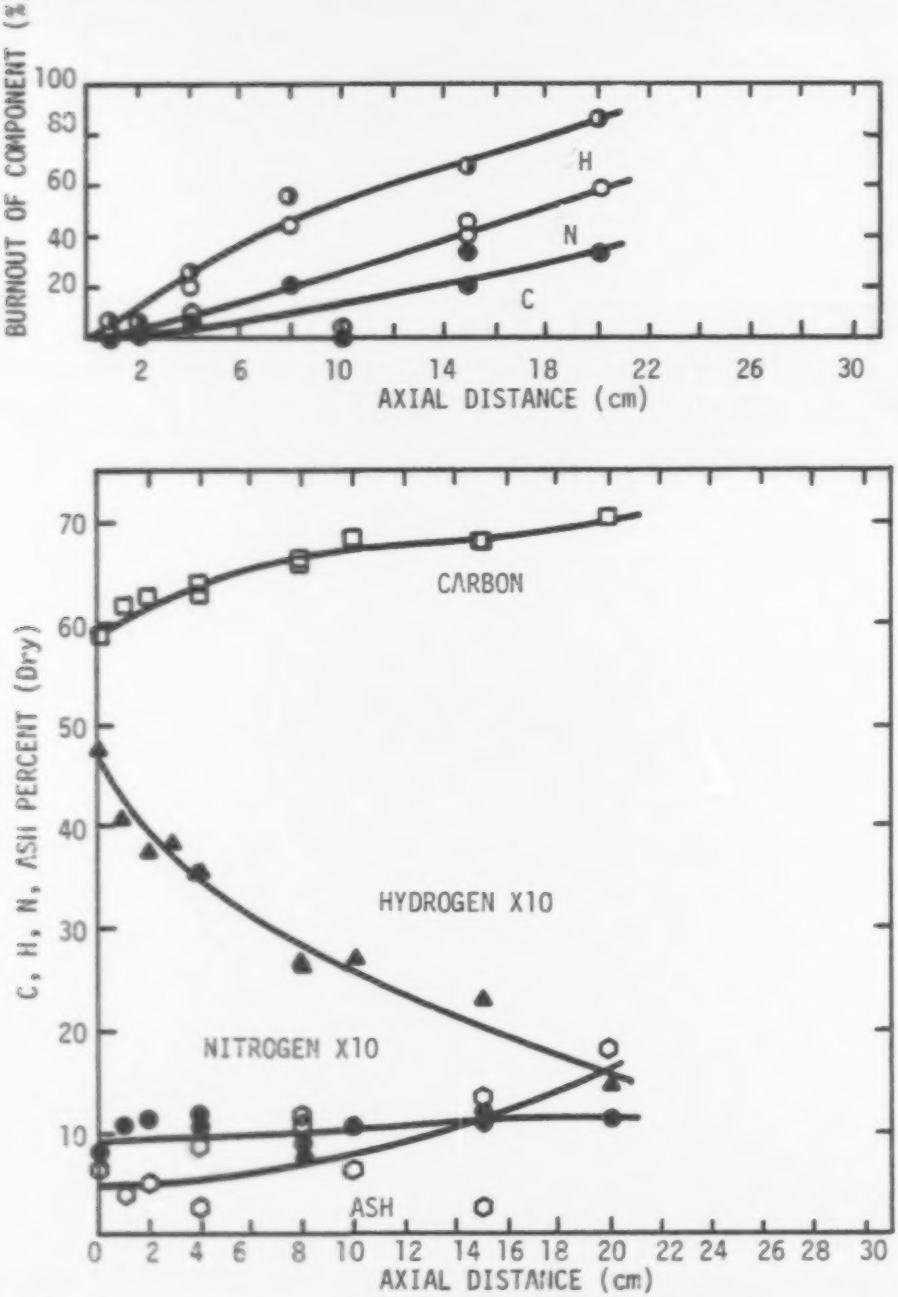

Figure 3.23. Component Burnout and Elemental Analysis Profiles for Savage Montana Lignite in a Lean Methane/Air Flame.

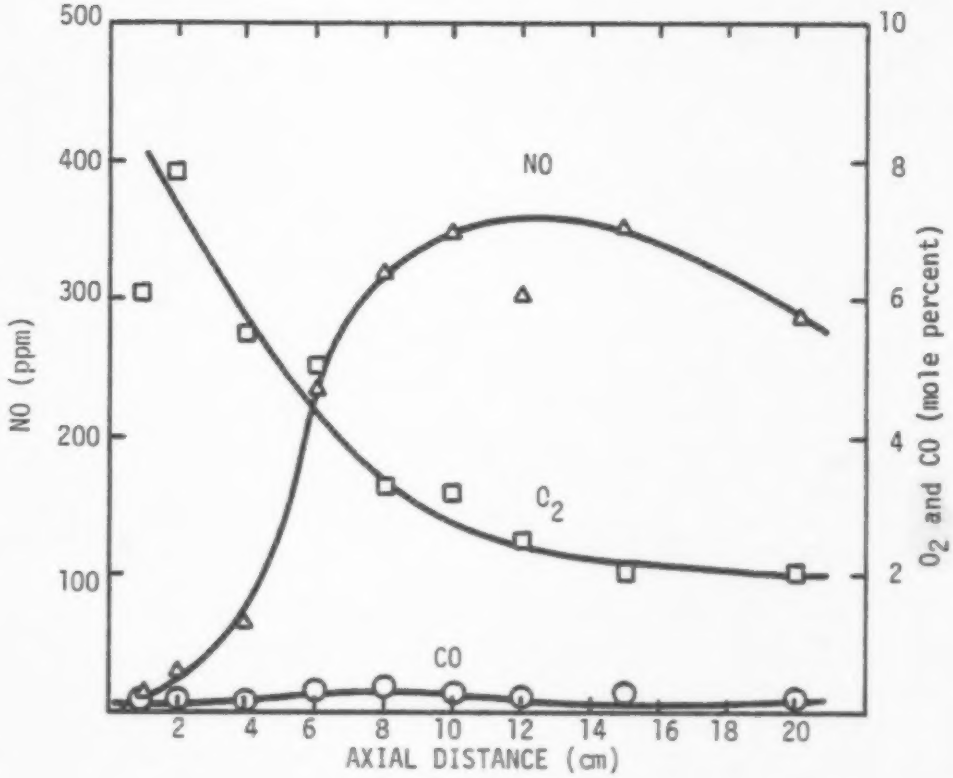

Figure 3.24. Gas-Phase Composition Profile for Beulah ND Lignite in a Lean Methane/Air Flame.

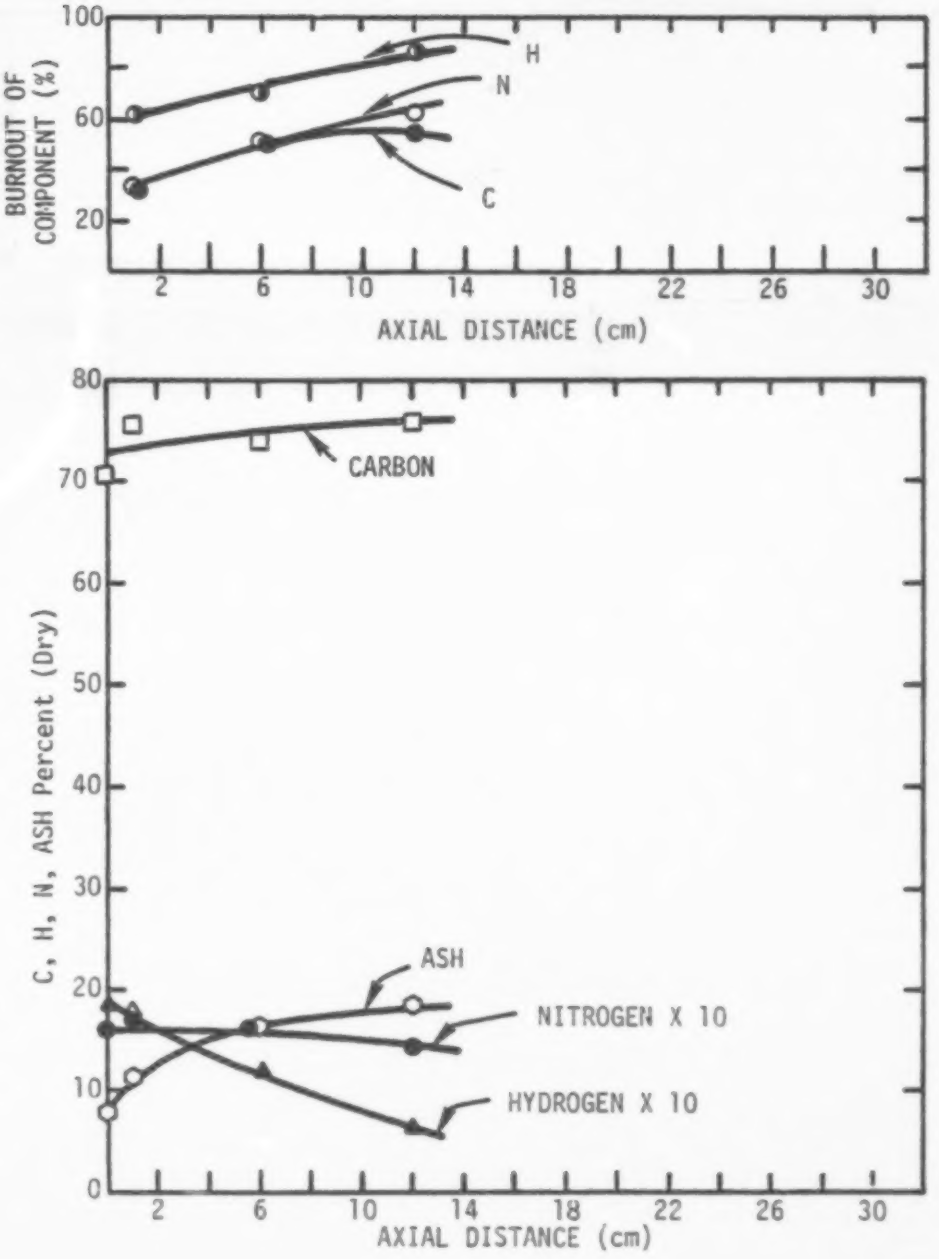

Figure 3.25. Component Burnout and Elemental Analysis Profiles for Single Pass Four Corner NM 80 μm Char in Lean Methane/Air Flame.

A comparison of the magnitude and location of the peak concentrations of selective volatile species is given in Table 3.II for the coals tested. Several notable differences exist which shed some light of the impact of fuel type and size. For example, a comparison of the data indicate the following:

- smaller particles have suppressed levels of hydrocarbons, comparable levels of volatile NO, and higher levels of HCN;
- lignites yield little HCN in comparison to bituminous coals and only negligible amounts of hydrocarbons;
- lignite volatile NO is lower than for bituminous coals;
- low volatile samples (char and anthracite) yield negligible amounts of volatile hydrocarbons or HCN; however, volatile NO for the char is significantly higher than for the anthractie.

When these data are compared with the thermal and physical data from preceding sections for the same coal samples, a consistent mechanism of the coupled thermal decomposition process can be delineated. This speculative mechanism along with a computer model of the process will be discussed in the next section.

Table 3.II. Peak Levels and Positions of Volatile Species

Coal Sample	CO		NO		HCN		HC	
	Peak Level (%)	Peak Location	Level (ppm)	Location (cm)	Level gm/gm coal	Location (cm)	Level (gm/gm coal)	Location (cm)
Four Corners, N.M. 80 µm Hv bit.	1.5	15	460	15	$.40 \times 10^{-2}$	12	$.4 \times 10^{-3}$	8
Four Corners, N.M. 40 µm Hv bit.	2	5	480	7	1.2×10^{-2}	6	$.1 \times 10^{-3}$	2
Utah Hv bit.	2	15	350	9	$.10 \times 10^{-2}$	12	.85	6
Beulah N.D. Lignite	<.2	8	350	12	$<10^{-3}$	*	$<10^{-4}$	*
Savage Mont. Lignite	.5	8	320	6	0.15	12	$<10^{-4}$	*
Pennsylvania Anthracite	.2	10	90	*	$<10^{-3}$	*	$<10^{-4}$	*
Four Corners, N.M. 80 µm char	<.1	10	310	14	$<10^{-3}$	*	$<10^{-4}$	*
Four Corners, N.M. 80 µm with Nitrogen Carrier	1.0	9	400	8	1.5×10^{-2}	8	NM	NM

* No Maximum observed

NM - Not Measured

4.0 SUMMARY AND DISCUSSION

4.1 Soot Formation

One of the more striking results to arise from the *in situ* visualization techniques is the copious amounts of soot that can be formed in the close vicinity of reacting coal particles. The amount of soot formed as qualitatively observed by the photography techniques was found to be strongly dependent on several variables:

(1) Coal Type. The high volatile bituminous coals and bituminous coals in general, have extremely high propensity to soot, while other coal types (lignites, anthracites and chars) have demonstrated little tendency to soot. A general ranking based on the coals tested in this program would be

high volatile bituminous → bituminous → lignite → bituminous char → anthracite

Since the soot first appears in the devolatilization zone, it is not surprising that the low volatile samples are of the lowest soot ranking. However, the sooting tendency must also be related to the composition of the volatiles. Pyrolysis studies of these same coals (Solomon, 1981) indicates that the bituminous coal volatiles are rich in hydrocarbons and tars which are highly aromatic. The volatiles from the same lignite coals on the other hand were composed mostly of CO, CO_2 and H_2O with relatively little tar or hydrocarbons. These same conclusions can be drawn from the gas phase measurements in the devolatilization zone (see Table 3.II). Significant levels of hydrocarbons were measured only for the bituminous coals. These hydrocarbons are expected to be the precursors to soot formation and to increase the reaction temperature (Haynes and Prado, 1981). Therefore, the tendency to soot is expected to be directly related to the concentration of these species.

(2) Coal Size. A close examination of the holograms and shadowgraphs taken of reacting small bituminous coal particles (40 μm) has revealed no examples of sooty volatile clouds despite the very strong sooting tendency of larger particles of the same coal. This result suggests strong coupling between the physical and chemical mechanisms of coal decomposition and a change in the decomposition

mechanism with particle size. The data lend support for a mechanism by which oxygen can be screened from the particle surface by the flux of volatiles. This sets up a microdiffusion system in which volatiles can react under fuel rich conditions to produce soot. However, smaller particles produce a smaller flux of volatiles which can allow oxygen to penetrate to the particle surface (Howard and Essenhigh, 1967). The volatiles from small particles then react under effectively lean conditions which can suppress soot formation. If this physical mechanism is valid, it is expected to influence other chemical reactions such as volatile fuel nitrogen conversion to NO_x.

(3) Aerodynamic Environment. Particles which were injected into the combustor at a higher velocity were found to produce long drawn out volatile trails (see Figure 3.4) which visually appeared to have lower soot concentrations than in the spherical clouds associated with lower injection velocities. The transition in the volatile cloud shape with the relative particle/gas velocity, from an envelope to a wake, suggests an analogy with evaporating oil droplet behavior (Sjorgren, 1978; Nakanishi, et al 1981). For single oil droplet flames, it has been found that soot yield will decrease as the flame makes the transition from envelope to wake due to increased microscale mixing of the evaporated material with the bulk stream. This phenomenon needs to be quantified for pulverized coal in terms of the influence of temperature, particle size, and oxygen concentration.

4.2 Coal Nitrogen Behavior

The fate of fuel nitrogen and the formation of fuel NO in bench scale reactors and long turbulent diffusion flames are discussed in Chapter 9 and Chapter 10 respectively of the EPA monograph (Sarofim et al, 1981). Much of the gas phase and solid phase composition data presented in this report are strikingly similar to the in-flame measurements performed on the IFRF turbulent diffusion flames (Michel and Payne, 1981, FCR final report) despite the dramatic scale difference from 1 gm/min to 3700 gm/min of coal. This report supplies fundamental information to help interpret some of the bench scale results, particularly the differences in coal type and the impact of particle size.

Figure 4.1 demonstrates the difference between the various component loss rates for the Four Corners coal. It is clear that nitrogen loss is not strictly a devolatilization process nor a char oxidation process but is somewhat intermediate. Figure 4.2 shows the nitrogen yield (i.e., the nitrogen lost from the coal expressed as gm of nitrogen as NO per gm of original coal or char) for all the solids tested. Their behavior can be grouped by coal rank and size. There appears to be major differences between the yields from bituminous and lignite coals. Initially, the rate of nitrogen evolution is highest for bituminous coals, which corresponds to the fact that the nitrogen in these coals are highly volatile. At times greater than approximately 70 msec, the bituminous coals demonstrate a lower nitrogen loss rate than the lignite samples.

The dependence of nitrogen evolution on particle size is dramatic. The small bituminous coal yields 90 percent of its total nitrogen in less than 100 msec. The entire decomposition and oxidation sequence is compressed for this sample with almost 80 percent of the carbon lost in a traverse of the reactor. The nitrogen loss rates derived by Pohl and Sarofim (1976) for approximately 40 μm bituminous coal particles in a pyrolysis experiment were used to calculate the burnout of nitrogen using the measured two-color particle temperature data. The remarkable agreement between the measured and predicted data burnout curves is shown in Figure 4.3. The 80 μm particles attain the same temperature and yet their nitrogen yield is almost half that of these small particles.

Stack NO measurements for the small size coal sample demonstrated a very strong dependence of NO produced from the coal on the coal feed rate. The conversion efficiency of fuel nitrogen lost from the solid to NO is determined from the particulate composition profiles and the stack NO measurements and can vary from approximately 100 percent at low rates to almost 20 percent at medium flow rates (see Figure 4.4). Single particle conversion efficiencies are defined as the extrapolated conversion efficiency to zero coal flow. These data imply that the single particle conversion efficiency for 40 μm particles is very high, suggesting almost complete oxidation of the nitrogen volatiles to NO under oxidizing conditions in the volatile cloud/particles microsystem. Reducing conversions at higher coal flow rates probably occur because the devolatilization process is so rapid that the free stream contains high nitrogen species concentrations and low or zero oxygen concentrations. The high levels of HCN measured under nominal conditions is indicative of the rapid devolatilization rate. A single particle conversion efficiency (extrapolation to zero coal flow) for the 80 μm Four Corners bituminous coal particles based on the nitrogen loss is

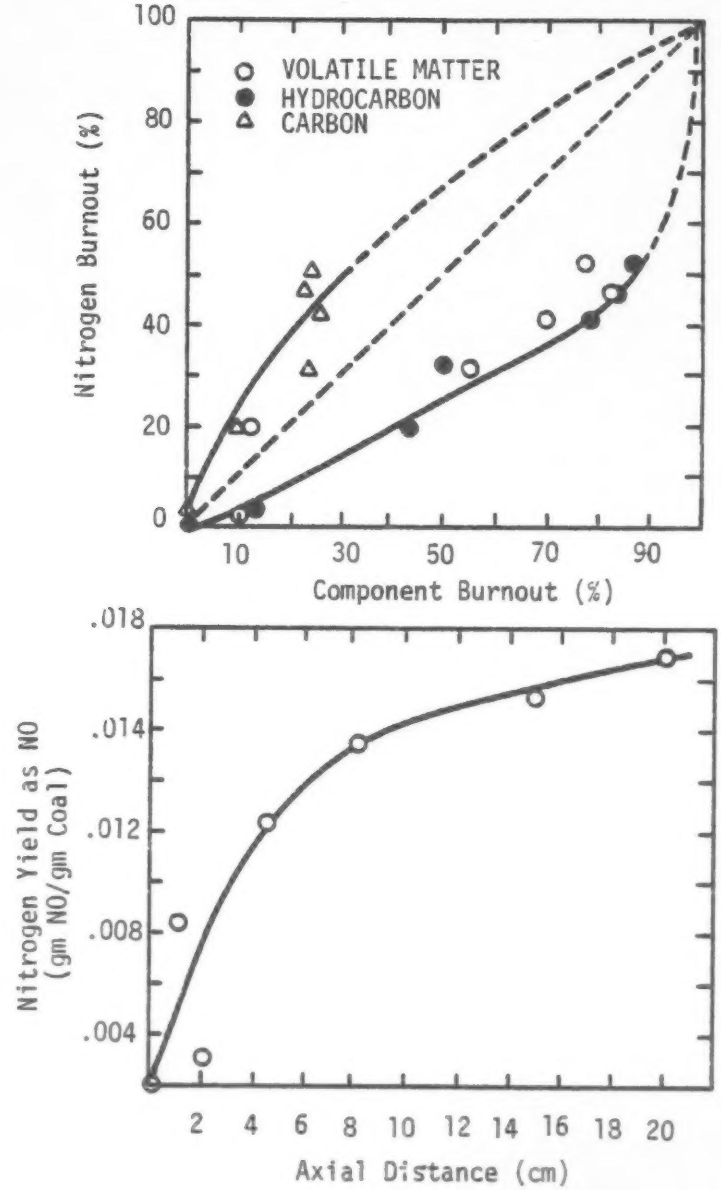

Figure 4.1. Nitrogen Burnout and Yields for 80 μm Four Corner NM Coal in a Lean CH_4/Air Flame.

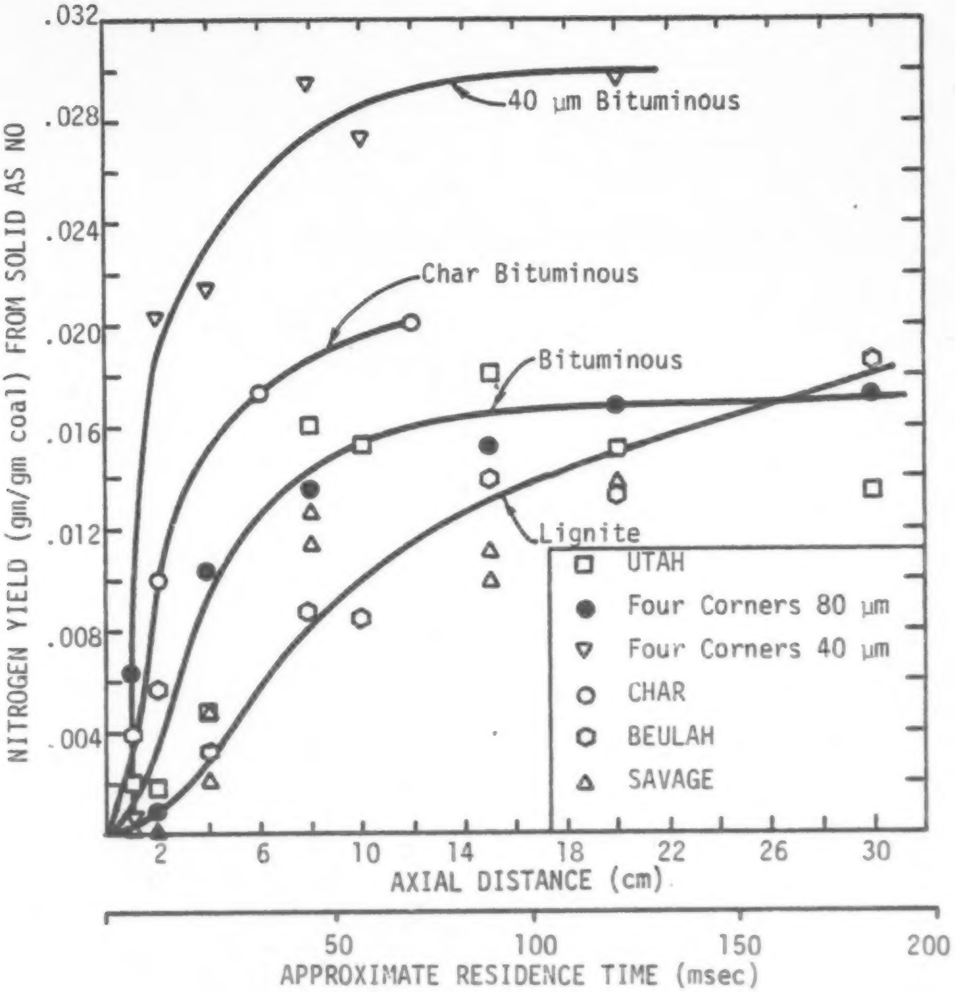

Figure 4.2. Nitrogen Yield Profiles as NO Based on Solid Phase Composition Measurements.

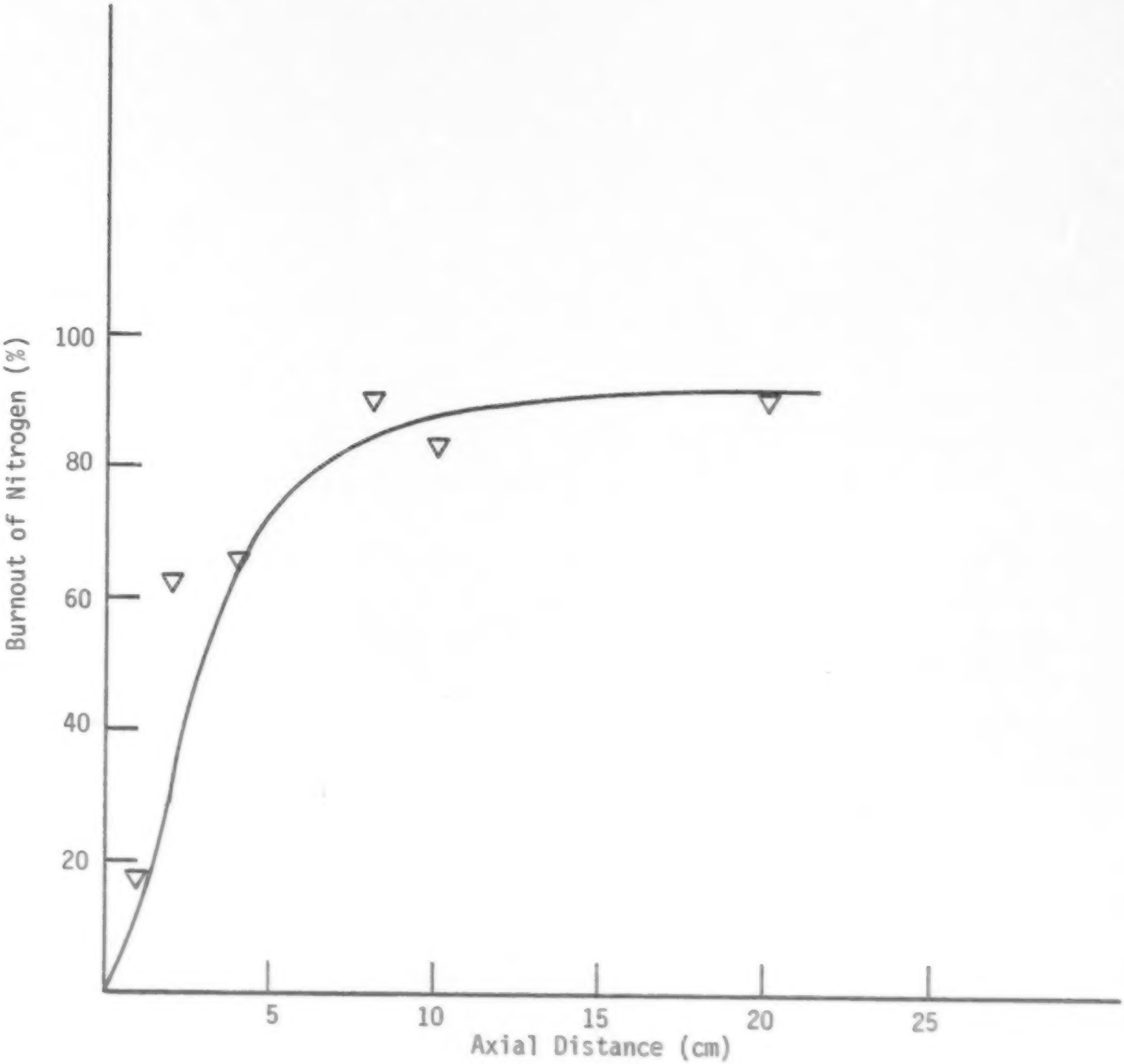

Figure 4.3. Predicted Nitrogen Burnout Profile from Particle Temperature History and Nitrogen Pyrolysis Correlation (Pohl and Sarofim, 1976) for 40 μm Four Corners, N. Mex. Coal.

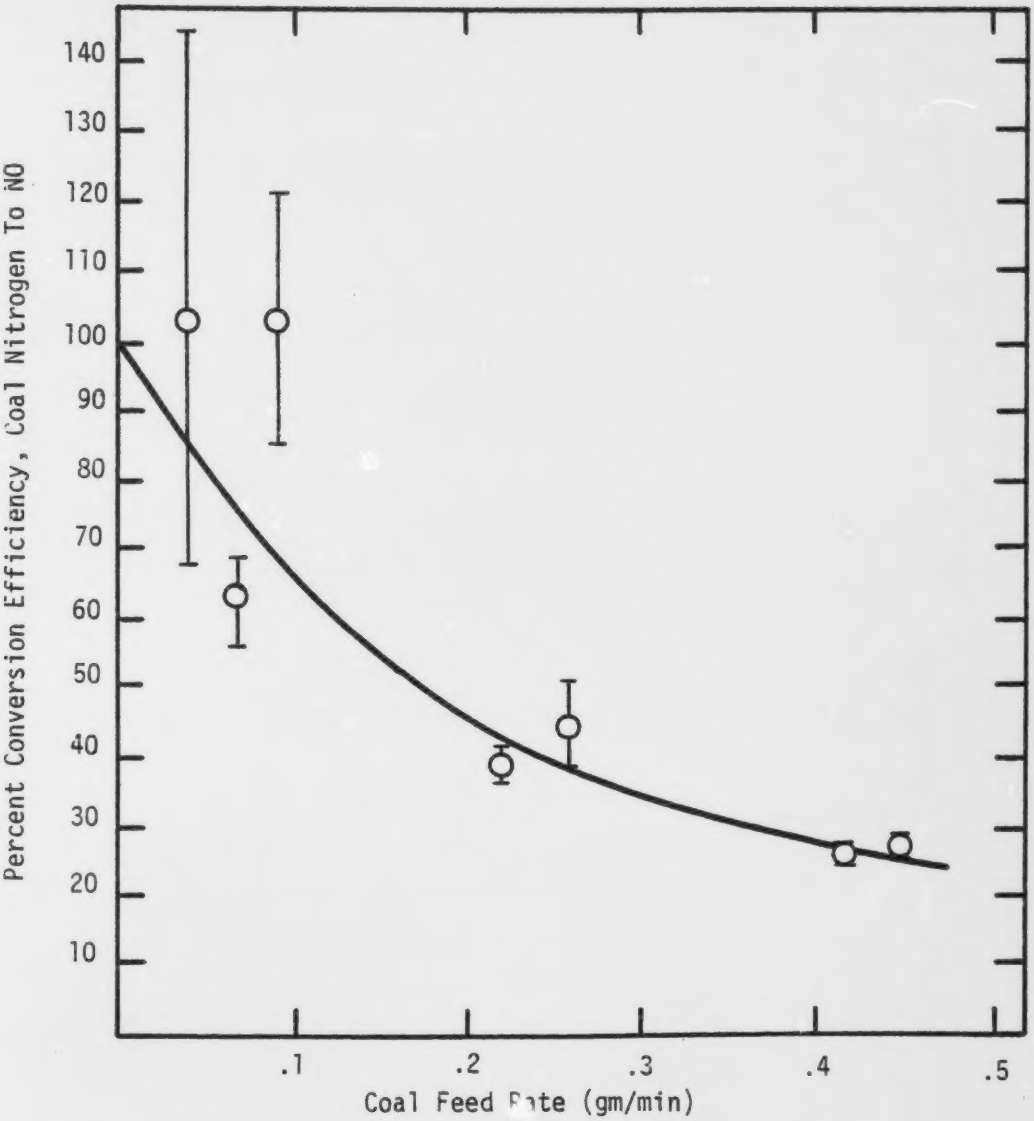

Figure 4.4. Influence of Coal Feed Rate on Conversion Efficiency of Coal-Nitrogen to NO for 40 μm Four Corners NM Coal.

approximately 65 percent. This suggests that even when the oxygen concentration of the free steam is high, the thickness of the cloud around the larger particle prevents oxygen penetration. Thus, the cloud is fuel rich and the production of molecular nitrogen from the volatile fuel nitrogen species will be favored. These results are in agreement with bench scale results on the impact of coal particle size on fuel nitrogen conversion (Chen et al, 1981).

In the bench scale reactor studies, fuel NO emission was found to depend to some extent upon total fuel nitrogen content (see Figure 2.14 and Chen et al, 1981). However, coals of similar nitrogen content could yield very different fuel nitrogen conversion efficiencies. This was found to be the case for the Beulah and Savage lignites. The extrapolated single particle conversion efficiency based on the total nitrogen loss for Beulah lignite (as determined from exhaust NO measurements) was only 40 percent and yet the measured efficiency for the Savage lignite was 60 percent. Both coals had similar solid composition and burnout profiles, and hydrocarbon concentrations were low for both coals. The only distinguishing features were the presence of higher levels of HCN and CO with the Savage coal.

4.3 Modeling Volatile Oxidation

The observations of the existence of a volatile envelope cloud for bituminous coal particles suggests the possibility of modeling volatile oxidation as a spherical diffusion flame. This conceptual picture should be acceptable at least for the restricted case where the particle and gas have no relative velocity. At higher relative velocities, the volatile cloud may be stripped from the particle and react remote from the particle surface. However, under zero slip conditions, the steady state behavior can be treated as a diffusion of volatiles outwards from the coal surface and the subsequent reaction of volatiles with the oxygen diffusions towards the surface. The reaction of the volatiles in the boundary layer surrounding the particle then defines the volatile cloud extent.

The simple model to be used here is designed to explore some of the physical observations made concerning the impact of coal type and size. The model makes use of the diffusion flame computer code developed by Kau and Tyson (1981, FCR final report) which was cast in spherical coordinates. The boundary conditions at the surface of the particle were used to control the volatile composition and volatile evolution rate. The volatile composition based on the pyrolysis data of

Solomon (Solomon, 1981) was used to designate the composition boundary layer condition assuming a linear devolatilization rate. The gradient was set using only a characteristic devolatilization time which is taken to be 10 msec from the baseline conditions.

Two other boundary conditions which deserve comment are the oxygen level and the temperature conditions. It is assumed that any oxygen reaching the particle surface is rapidly consumed, i.e., the oxygen boundary condition is set to zero. The temperature, on the other hand, was allowed to seek an equilibrium level at the surface by setting the gradient to zero just at the surface. This effectively eliminates the particle itself as a heat source of sink. This is a specific assumption of the model and is only strictly true if there is no surface reaction and the particle temperature has equilibrated with the local gas temperature. The coupling of the cloud temperature with the particle temperature whether by radiation to and from the sooty cloud or by conduction has not yet been fully explored.

Figure 4.5 shows the predicted distribution of XN species surrounding the particle. The calculations which utilize the chemical kinetics delineated in the FCR final report Volume 1 indicate the sphere of activity is approximately 500 μm which is similar to the soot cloud diameter observed with the high speed cinematography. Figure 4.6 demonstrates the impact of the devolatilization time on the temperature profile, and the oxygen and methane concentration profile. The predicted center line temperature or equilibrated particle temperature at a devolatilization time of 10 msec is consistent with the measured particle temperature in the devolatilization zone. The increase in the devolatilization time is seen to decrease the volatile flux and thus oxygen will penetrate to the particle surface and the hydrocarbon concentration will fall off abruptly. An extrapolation of these observations to soot and NO_x formation would suggest that higher devolatilization rates (i.e., shorter devolatilization times) could dramatically increase soot and decrease the conversion of volatile fuel nitrogen to NO_x due to the increased residence time in the rich zone.

The predicted impact of particle size is shown in Figure 4.7 for the high volatile bituminous coal. The major predicted difference between the two sizes is the penetration of oxygen to the surface of 40 μm particles and

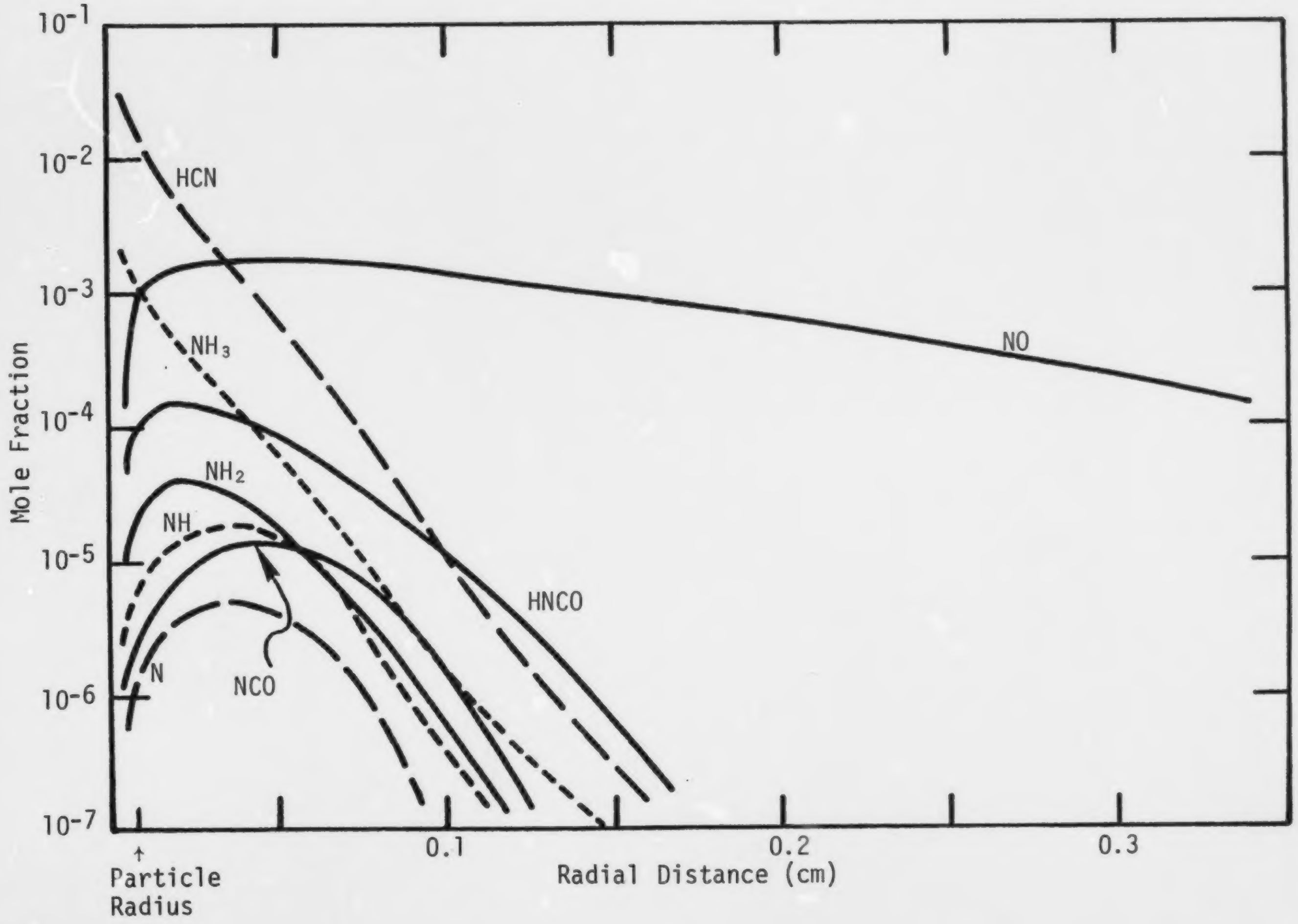

Figure 4.5. Σ(XN) Speciation for 80 μm Bituminous τ = 10 ms.

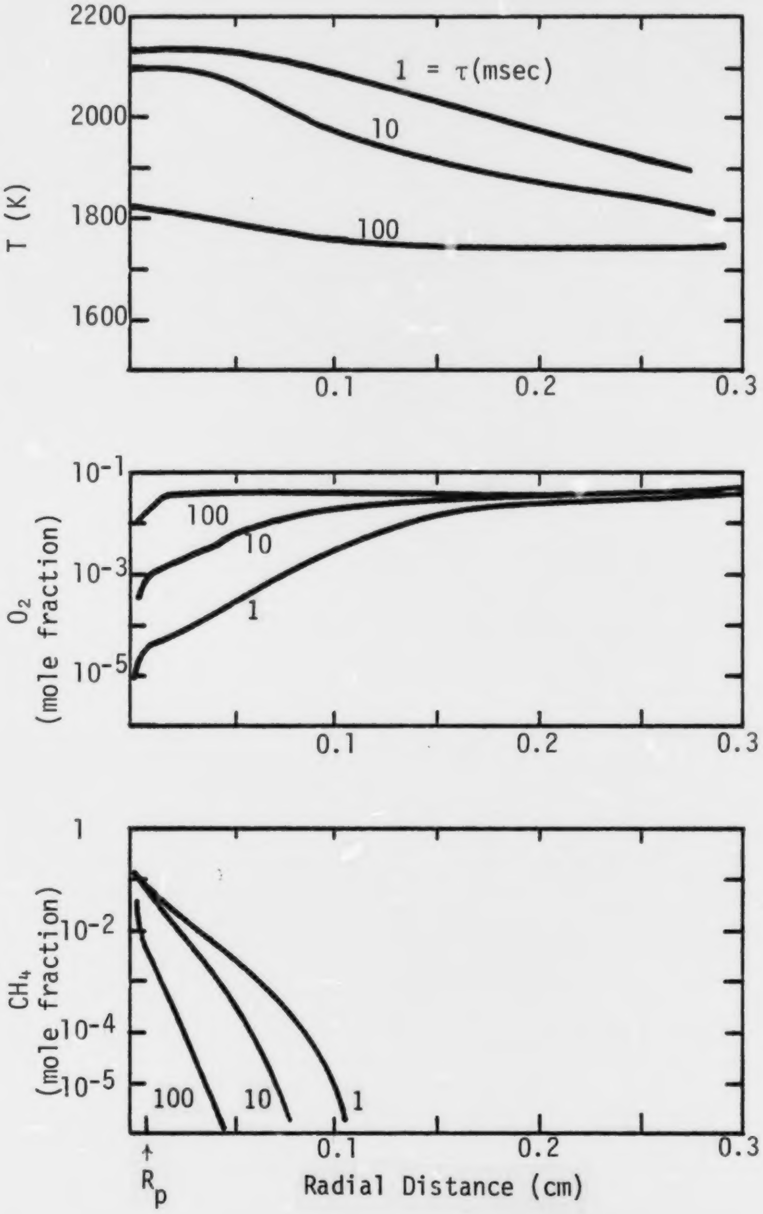

Figure 4.6. Predicted Cloud Temperature, O_2 Profile and CH_4 Profile for Spherical Diffusion Flame as a Function of Devolatilization Time, τ for 80 μm Particles.

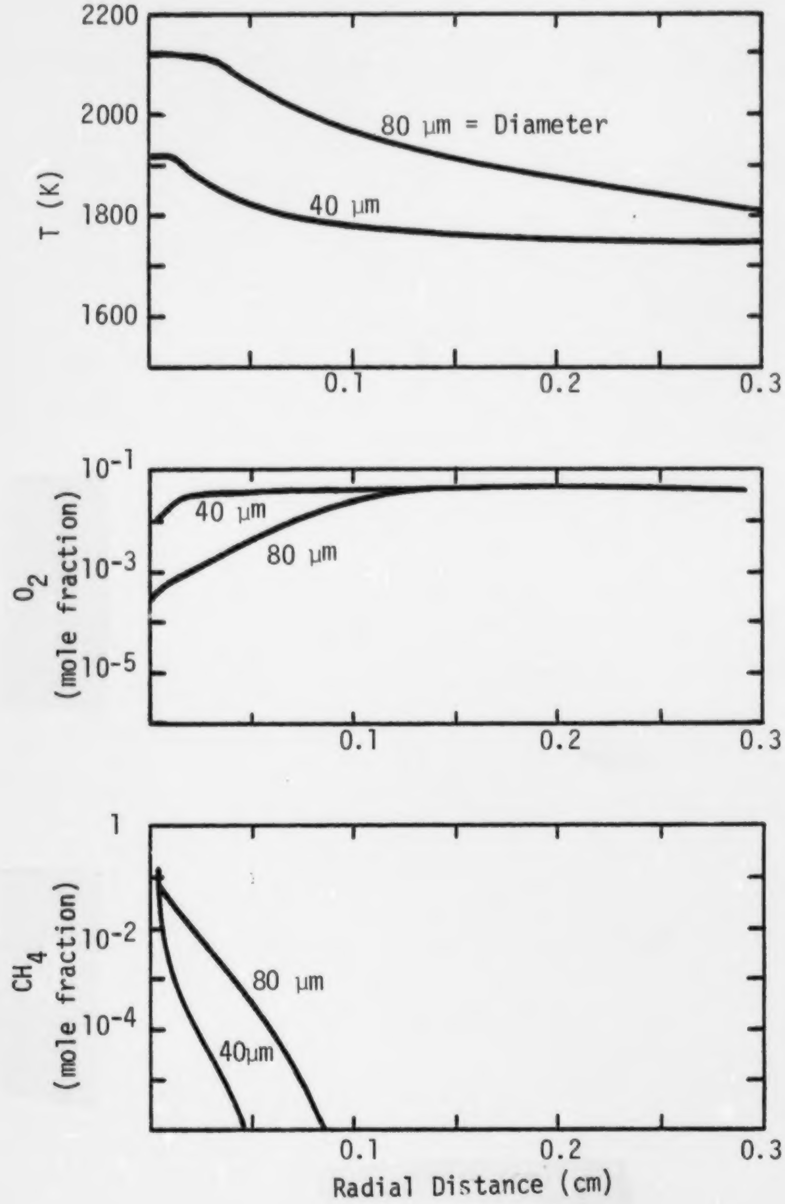

Figure 4.7. Predicted Behavior for Bituminous Coal Particle Cloud as a Function of Particle Size.

the extent of the volatile cloud for 80 μm particles. These results are consistent with the observation of no visible volatile clouds for the 40 μm high volatile bituminous coal. However, these calculations do not allow for the change in the devolatilization time with particle size. The 40 μm coal would be expected to devolatilize more quickly and therefore somewhat counteract the size difference. Nonetheless, the calculations demonstrate a clear trend with size that is consistent with the physical observations. The cloud temperature for the 40 μm particles was predicted to be lower than for 80 μm particles in contrast to two color pyrometry measurements which indicated similar peak temperature. This discrepancy indicates the inability of the simplified model to correctly handle the heat transfer coupling between the cloud and the particle or the radiative cooling of the microsystem.

Other factors are seen to have strong influences on the microsystem combustion behavior. In particular, increased oxygen concentration in the bulk stream can act to suppress the extent of the volatile cloud (Figure 4.8). On the other hand, the bulk gas temperature has little influence on the cloud extent but strongly influences the particle temperature (Figure 4.9). The influence of coal type is demonstrated in Figure 4.10 for the bituminous and lignite coals at a relatively large devolatilization time. The trends are consistent with previous observations; i.e., the particle temperature is higher for the bituminous, and oxygen penetration is larger for the lignite coal. The magnitude of the effects is magnified for faster devolatilization rates.

The mathematical model correctly predicts many of the variables and trends associated with the oxidation of volatiles in the devolatilization zone. This indicates that the phenomenological model developed throughout this report on the thermal decomposition and oxidation of pulverized coals at high temperature is a plausible mechanism.

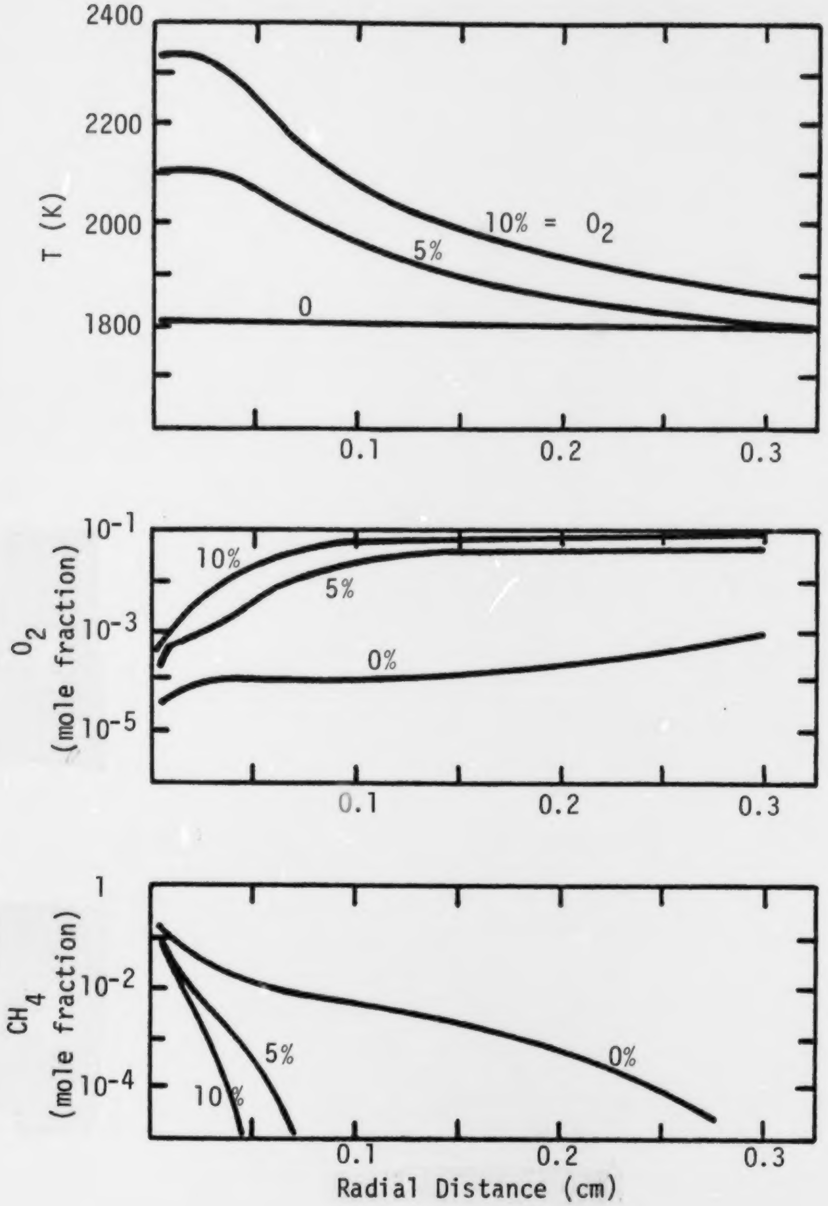

Figure 4.8. Predicted Cloud Behavior for 80 μm Bituminous Particles as a Function of Free-Stream Oxygen Concentration (τ = 10 msec).

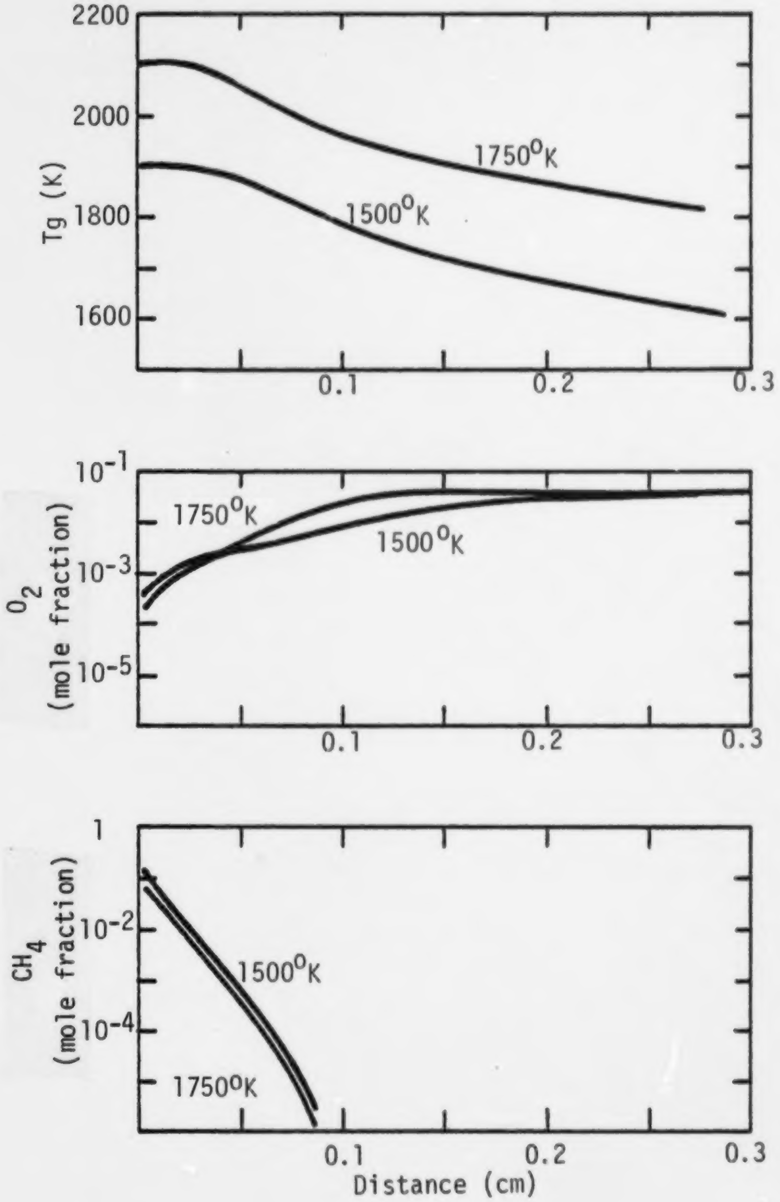

Figure 4.9. Predicted Thermal and Chemical Profiles for 80 μm Bituminous Particles as a Function of Gas Temperature (τ = 10 msec).

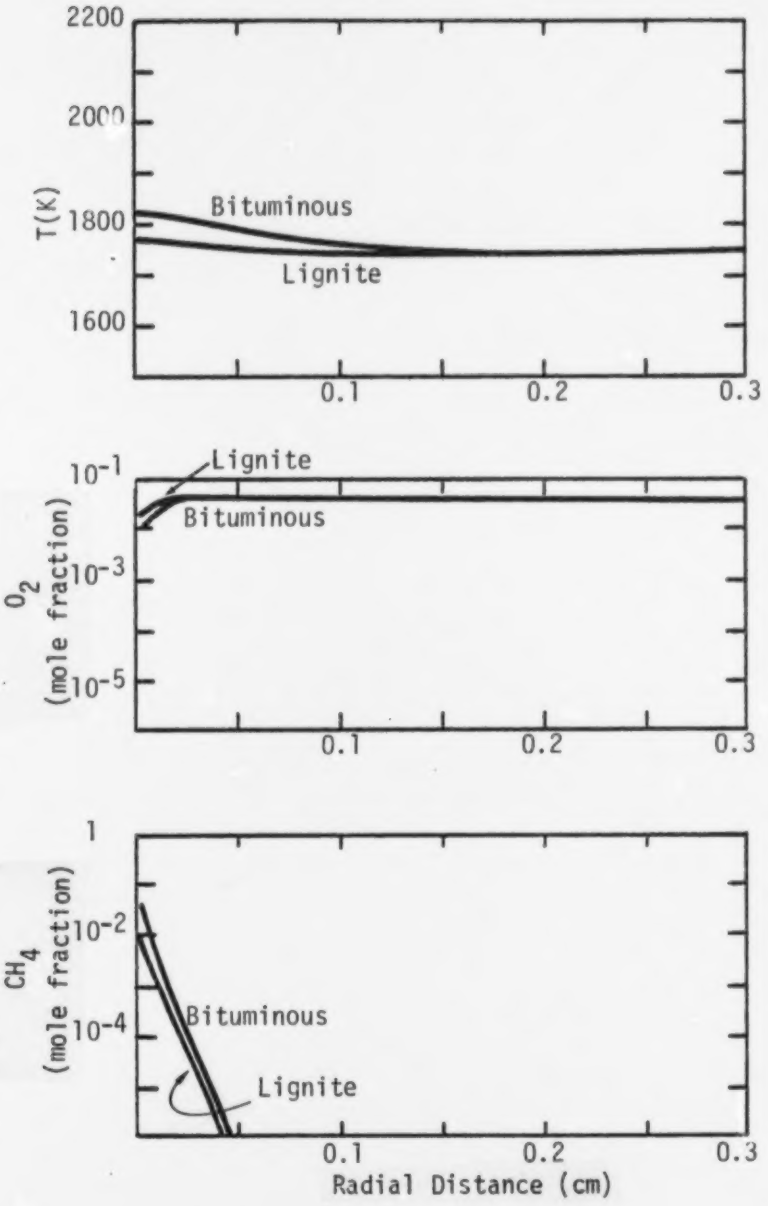

Figure 4.10. Predicted Profiles for Bituminous and Lignite Clouds With Devolatilization Time of 100 msec.

5.0 RECOMMENDATIONS FOR FUTURE WORK

There are a variety of areas which require further exploration. Some of these arose due to lack of time to complete all of the tasks initially specified and others arose during the program as a result of some of the results. Areas which appear to require particular attention are as follows:

IGNITION. The mechanisms of pulverized-coal ignition is still uncertain. Because of the relative importance of this parameter, not only to fuel nitrogen processing but to flame stability, it should continue to be explored.

SOOT FORMATION. Copious amounts of soot were observed to be formed by pulverized-coal particles in the devolatilization range. Also, the magnitude of the soot produced appeared to be strongly dependent upon many of the controllable parameters including stoichiometry, particle size, coal type, and slip velocity. These observations require quantification if the controllable parameters are to be used for the control of soot emissions. Further, there is a need to identify the levels and types of polycyclic aromatic hydrocarbons being produced.

TEMPERATURE RESPONSE. The time/temperature history has been found to be important to all aspects of the fuel nitrogen chemistry sequence. However, little is known concerning the actual particle temperature response in large-scale flames. Hence, one particular program that should be initiated is the application of two-color pyrometry techniques developed in this program to large-scale flames.

COAL PARTICLE DECOMPOSITION MODEL DEVELOPMENT. This study has indicated the importance of the microscale phenomenon occurring during the thermal oxidation of coal particles. Also a simplified model has been used to predict many of the observed phenomenon. However, a comprehensive model incorporating much of the currently available information of coal reaction chemistry and physics would be an extremely powerful predictive tool. Some aspects of the physical phenomenon need to be explored more fully. In particular, the heat transfer coupling on thermal feedback between the volatile cloud and the parent coal particle needs to be investigated.

CHAR NITROGEN CONVERSION TO NO_x. Still little is known about what factors influence the conversion of char nitrogen to NO_x. Since this may be the limiting factor for advanced NO_x reduction concepts, it is of considerable importance if further advances are to be made. One possibility is to take advantage of the diagnostics utilized and developed in this program to study the combustion of char. Of particular interest is how the first-stage processing influences the char properties and how they, in turn, influence the oxidation of the char and the conversion of char nitrogen. The ultimate goal of the program would be to find conditions of minimum conversion of char nitrogen and maximum burnout rate.

6.0 REFERENCES

Alternkirch, R.A., R.E. Peck, and S. L. Chen, 1978. Powder Technology, 20, 189.

Eckert, E.R.G. and R.M. Drake, 1972. Analysis of Heat and Mass Transfer, McGraw-Hill, New York.

Field, M.A., D.W. Gill, B.B. Morgan and P.G.W. Hawksley, 1967, Combustion of Pulverized Coal, British Coal Utilization Research Association, Leatherhead, England.

Gaydon, A.G. and I.R. Hurle, 1963. The Shock Tube in High-Temperature Chemical Physics, p. 177, Reinhold Publishing, New York.

Hamor, R.J. and I.W. Smith, 1971. Fuel, 50, 394.

Hottle, H.D., 1954, Radiant Heat Transmission, in W.H. McAdams (ed.), Heat Transmission, 3d ed., Chap. 4, McGraw-Hill Book Company, New York.

Howard, J.B. and R.H. Essennigh, 1967a. Ind. Eng. Chem. Proc. Des. Dev., 6, 74.

Howard, J.B. and R.H. Essenhigh, 1967b. Eleventh Symposium (International) on Combustion, p. 399, The Combustion Institute, Pittsburgh, PA.

Howard, J.B., 1965. Mechanism of Ignition and Combustion in Flames of Pulverized Bituminous Coal, Ph.D. Thesis, Pennsylvania State University.

Kau, E., and T. Tyson. "Mathematical Modeling of Microscale Combustion of a Coal Particle", Volume IV, Part II of this report series.

Karr, C., (ed.), 1978. Analytical Techniques for Coal and Coal Products, Academic Press, New York.

Michel, J. and R. Payne. "Detailed Measurement of Long Pulverized Coal Flames for the Characterization of Pollutant Formation", Volume IIa, Part II of this report series.

Mulcahy, M.F.R. and I.W. Smith, 1969. Rev. Pure and Appl. Chem, 19, 81.

Nakanishi, K., T. Kadota and H. Hiroyasu, 1981. Comb. Flame, 40, 247.

Pohl, J.H. and A.F. Sarofim, 1976. The Sixteenth Symposium (International) on Combustion, p. 491, The Combustion Institute, Pittsburgh, PA.

Pohl, J.H., H. Kobayashi and A.F. Sarofim. 1978. Western States Sectional Meeting of The Combustion Institute, 78-12, Boulder, CO.

Sjorgsen, A., 1975. The Fifteenth Symposium (International) on Combustion, The Combustion Institute, Pittsburgh, PA, p. 1957.

Freihaut, J.D., and D.J. Seery. "Method for Characterization of Coal During Thermal Decomposition", Volume IIb, Section I of this report series.

Szpindler, G. a D., 1970. "Studies of the Combustion Rate and Structure of Pulverized Fuels Burned in the C.15 Trails of the IFRF. Part 1. Microscopic Examination of the Structural Changes in the Solid Particles in a Pulverized Bituminous Coal Flame", CSIRO Investigation Report 381R, Sydney Laboratory, Chatswood, Australia.

Trolinger, J. and M.P. Heap, 1979. Appl. Optics, 18, 1757.

7.0 ACKNOWLEDGEMENTS

The authors wish to acknowledge the invaluable contributions of Pat Sampson in the conduct of the experiment; the encouragement and support of W. S. Lanier, the Project Officer; and T. J. Tyson , the Technical Director of the FCR program. The holocamera and technical support was provided by Spectron Development Laboratories. The interpretation of the data was aided by discussions with A. F. Sarofim, D. W. Pershing, and J.O.L. Wendt.

II. DETAILED MEASUREMENT OF LONG PULVERIZED COAL FLAMES FOR THE CHARACTERIZATION OF POLLUTION FORMATION

Prepared by:

J. Michels and R. Payne

International Flame Research Foundation

Prepared for:

Energy and Environmental Research Corporation
18 Mason
Irvine, CA 92714

TABLE OF CONTENTS

Section Page

SUMMARY II-1

1.0 INTRODUCTION II-2

1.1 Background II-2
1.2 Objectives and Scope of the Work II-3

2.0 EXPERIMENTAL CONDITIONS II-5

2.1 Input Variables II-5

2.2 Furnace Boundary Conditions II-9
2.3 Measurements and Instrumentation II-13

3.0 EXPERIMENTAL RESULTS II-16

3.1 Flame Output and Furnace Boundary Conditions . . . II-16
3.2 Aerodynamic Conditions II-18
3.3 Gas Temperatures and Sampled Components II-29
3.4 Pollutant Formation II-31

4.0 FURTHER EVALUATION OF RESULTS II-92

4.1 Mixing Factor and Degree of Oxidation II-92
4.2 Burn-Out Degree of Sampled Solids II-93
4.3 An Attempt to Correlate Nitrogen Burnout With the Total Concentration of Nitrogen Species II-94
4.4 Influence of Coal Size Distribution and Composition II-94

5.0 CONCLUSIONS II-105

6.0 REFERENCES II-107

7.0 TABLES OF FLAME POINT DATA II-108

8.0 PHOTOGRAPHS OF FLAMES II-123

LIST OF FIGURES

Figure Page

1 Double Concentric p.f. Burner for LCF Trials (EPA/EERC) . II-10

2 Primary Jet Temperature Along the Axis of the Coal Pipe . II-11

3 Schematic of the IFRF Furnace nr 1 . . . . II-12

4-1 Incident Radiation at the Furnace Side Wall and Average Wall Temperatures, Flame A1 . . . . II-19

4-2 Incident Radiation at the Furnace Side Wall and Average Wall Temperatures, Flame B1 . . . . II-20

4-3 Incident Radiation at the Furnace Side Wall and Average Wall Temperatures, Flame A2 . . . . II-21

4-4 Incident Radiation at the Furnace Side Wall and Average Wall Temperatures, Flame A4 . . . . II-22

4-5 Incident Radiation at the Furnace Side Wall and Average Wall Temperatures, Flame B2 . . . . II-23

4-6 Incident Radiation at the Furnace Side Wall and Average Wall Temperatures, Flame B3 . . . . II-24

5-1 Hubbard Probe Measurements of the Flow Boundaries II-25

5-2 Hubbard Probe Measurements of the Flow Boundaries II-26

6-1 Measured Axisymmetric Stream Lines, Flame A1 . . . . . . II-28

6-2 Measured Axisymmetric Stream Lines, Flame B1 . . . . . . II-28

7-1.1 Axial Temperatures, Flame A1 . . . . II-35

7-1.2 Radial Temperatures, Flame A1 . . . . II-36

7-1.3 Radial Temperatures, Flame A1 . . . . II-37

7-1.4 Radial Temperatures, Flame A1 . . . . II-38

7-1.5 Isotherms (°C), Flame A1 . . . . II-39

7-2.1 Axial Gas Concentrations, Flame A1 . . . . II-40

LIST OF FIGURES (Continued)

Figure Page

7-2.2 Radial Gas Concentrations, Flame Al II-41

7-2.3 Radial Gas Concentrations, Flame Al II-42

7-2.4 Radial Gas Concentrations, Flame Al II-43

7-3.1 Axial Nitrogen Oxide Concentration, Flame Al II-44

7-3.2 Radial Nitrogen Oxide Concentration, Flame Al II-45

7-3.3 Radial Nitrogen Oxide Concentration, Flame Al II-46

7-4.1 Axial Ammonia and Hydrogen Cyanide Concentrations II-47

7-4.2 Radial Hydrogen Cyanide Concentrations, Flame Al II-48

7-5 Flame A_1 Mixing Factor (M_2) and Degree of Oxidation (N) . . . II-49

8-1 Axial Temperatures, Flame A_2 . . . . II-50

8-2 Axial Gas Concentrations, Flame A_2 . . . . II-51

8-3 Axial Nitrogen Oxide Concentration, Flame A_2 . . . . II-52

8-4 Axial Ammonia and Hydrogen Cyanide Concentrations, Flame A_2 . II-53

8-5 Flame A_2, Mixing Factor (M_2) and Degree of Oxidation (N) . . II-54

8-6 Flame A_2, Burnout of Solids II-55

9-1 Axial Temperatures, Flame A_4 . . . . II-56

9-2 Axial Gas Concentrations, Flame A_4 . . . . II-57

9-3 Axial Nitrogen Oxide Concentration, Flame A_4 . . . . II-58

9-4 Axial Ammonia and Hydrogen Cyanide Concentrations, Flame A_4 . II-59

9-5 Flame A_4, Mixing Factor (M_2) and Degree of Oxidation (N) . . II-60

9-6 Flame A_4, Burnout of Solids II-61

LIST OF FIGURES (Continued)

Figure Page

10-1.1 Axial Temperatures, Flame B1 . . . . II-62

10-1.2 Radial Temperatures, Flame B1 . . . . II-63

10-1.3 Radial Temperatures, Flame B1 . . . . II-64

10-1.4 Radial Temperatures, Flame B1 . . . . II-65

10-1.5 Isotherms (°C), Flame B1 . . . . II-66

10-2.1 Axial Gas Concentrations, Flame B1 . . . . II-67

10-2.2 Radial Gas Concentrations, Flame B1 . . . . II-68

10.2.3 Radial Gas Concentrations, Flame B1 . . . . II-69

10-2.4 Radial Gas Concentrations, Flame B1 . . . . II-70

10-3.1 Axial Nitrogen Oxide Concentration, Flame B1 . . . . II-71

10-3.2 Radial Nitrogen Oxide Concentration, Flame B1 . . . . II-72

10-3.3 Radial Nitrogen Oxide Concentration, Flame B1 . . . . II-73

10-3.4 Radial Nitrogen Oxide Concentration, Flame B1 . . . . II-74

10-4.1 Axial Ammonia and Hydrogen Cyanide Concentrations, Flame B1 . II-75

10-4.2 Radial Hydrogen Cyanide Concentrations, Flame B1 . . . . II-76

10-4.3 Radial Hydrogen Cyanide Concentrations, Flame B1 . . . . II-77

10-5 Flame B1, Mixing Factor (M_2) and Degree of Oxidation (N) . . II-78

10-6 Flame B1, Burnout of Solids II-79

11-1 Axial Temperatures, Flame B2 . . . . II-80

11-2 Axial Gas Concentrations, Flame B2 . . . . II-81

11-3 Axial Nitrogen Oxide Concentrations (Flame B2) II-82

11-4 Axial Ammonia and Hydrogen Cyanide Concentrations, Flame B2 . II-83

LIST OF FIGURES (Concluded)

Figure		Page
11-5	Flame B2, Mixing Factor (M_2) and Degree of Oxidation (N).	II-84
11-6	Flame B2, Burnout of Solids	II-85
12-1	Axial Temperatures (Flame B3)	II-86
12-2	Axial Gas Concentrations (Flame B3)	II-87
12-3	Axial Nitrogen Oxide Concentration (Flame B3)	II-88
12-4	Axial Ammonia and Hydrogen Cyanide Concentrations (Flame B3)	II-89
12-5	Flame B3, Mixing Factor (M2) and Degree of Oxidation (N).	II-90
12-6	Flame B3, Burnout of Solids	II-91
13	Comparison Between Measured Total and Expected Fuel Nitrogen Species Concentrations	II-95
14a	Average Particle Size Distribution of the Input Coal . .	II-96
14b	Ash and Volatile Distribution of the Input Coal as a Function of Particle Size	II-96
15	Particle Size Distributions Across the Coal Jet	II-98
16-1	Ash and Volatile Distribution Across the Coal Jet as a Function of Particle Size (Flame A1)	II-99
16-2	Ash and Volatile Distribution Across the Coal Jet as a Function of Particle Size (Flame B1)	II-100
17	Particle Size Distributions Along the Axis	II-101
18.1	Ash and Volatile Axial Profiles in Individual Size Fractions, Flame A1	II-102
18.2	Ash and Volatile Axial Profiles in Individual Size Fractions, Flame B1.	II-103

LIST OF TABLES

Table Page

1 Average Coal Analysis Over the "LCF" Trials Period . . . II-6

2 Flame List for the "LCF" Trials II-7

3 Flame Output Data II-17

4 Measured Peak Temperatures, Concentrations, and Their Axial Positions II-34

5 Flame A1 . . . . II-109

6 Flame A2 . . . . II-114

7 Flame A4 . . . . II-116

8 Flame B1 . . . . II-117

9 Flame B2 . . . . II-121

10 Flame B3 . . . . II-122

SUMMARY

This report describes the results of an experimental program carried out at the IFRF Research Station for EERC.

The purpose of this work was to characterize a number of "long" coal flames with regard to pollutant formation, and in particular for the evolution of fuel nitrogen species, in order to provide data for the validation and possible further development of mathematical models of nitrogen oxide formation.

Six "long" coal flames have been produced with the same burner and under similar boundary conditions. The differences between these flames were mainly due to air and fuel input velocities and temperatures which have a direct effect on the mixing characteristics and the coal heating rates. A comprehensive set of data is given in both graphical and tabulated form. Despite the many difficulties encountered in making measurements in such flames, particularly for sampling in regions of high temperature and solid concentrations, the consistency between the various measurement is generally good. Nevertheless, no attempt has been made to give a detailed interpretation of these data as this was beyond the objectives of this report.

Indications are that globally the combustion is controlled by mixing and that the influence of fuel kinetics is basically the same in all cases. In particular, NH_3 concentrations were always very low, while HCN was found to form very rapidly and in large amounts.

More detailed evaluation of these data is still required for a quantitative interpretation of fuel nitrogen conversion to HCN and to NO. Also, further experimental work in this area should possibly include the effect of variable fuel kinetics with the use of different coals and vitiation of the combustion air and the effect of furnace scale.

1.0 INTRODUCTION

1.1 Background

The projected future increase in the use of coal, particularly for industrial and utility steam generation, has in recent years further stimulated research work on all aspects of coal combustion with a current special emphasis on areas relating to the control of noxious emissions. While work has progressed on all fronts, from small bench-scale studies aimed at understanding the fundamental details of heterogeneous combustion through large-scale demonstrations of current technology, our ability to satisfactorily integrate the fundamental information into prediction procedures for complete combustion systems is still limited. This is particularly true in the transfer of new technology from the laboratory to full-scale systems, where the effect of scale can be important and where little is known at present, particularly with respect to coal combustion.

At the present time a number of individual laboratories and research groups are actively engaged in projects directed towards the understanding of basic coal combustion phenomena. Major areas of study include chemical kinetics, heterogeneous processes (including fuel nitrogen conversion), and transport processes for modeling flames, and NO_x formation, with much detailed work concerning coal devolatilization, volatile gas and char combustion and emission formation [1]. From the results of such studies there is a wealth of fundamental information available, derived mainly on small-scale systems, which is currently being used in the interpretation of data from pilot- or full-scale combustion systems and in the identification of advanced burner concepts.

In many cases, however, the basic data is (of necessity) obtained in situations where, for example, the chemistry is uncoupled from the fluid dynamics and turbulence. While such an approach is generally acceptable when determining rate constants, it is not acceptable in the prediction of stationary combustion systems where the kinetics and the flow field are coupled. Similarly, many prediction procedures are usually only compared to one experiment or set of data, where ideally a range of experiments covering several different geometries or scales is required. A direct transfer of results from one system to another is, therefore, often very difficult and a full validation of fundamentally-derived approaches applied to real combustion systems requires very detailed information of at least the time mean local properties. In complicated large-scale combustion systems such detailed information is, however, difficult and expensive to obtain and is for these reasons very often not available.

In view of the above statements and considering the present status of knowledge of heterogenous combustion phenomena, which is now extensive and is continually developing, it is believed that a useful role could be served, both in the validation and further development of current approaches, by the generation of detailed experimental data from large (realistic) scale combustion systems. Such data, if obtained under well-defined aerodynamic and boundary conditions and in relatively simple coal-fired configurations, could provide a useful basis for the rationalization of fundamental experimental results from different sources and for the validation of prediction procedures.

Industrial pulverized coal flames can be classified in two general groups. Wall-fired boilers, both single and opposed wall, utilize flames whose characteristics are dominated by the flow field close to the burner. The second group of flames are produced with completely axial flow and have a high fineness ratio. These long turbulent diffusion flames are typical of corner, arch and turbo-fired boilers and tend to be inherently low producers of NO. However, the physical parameters controlling NO formation, the effects of scale and the practical lower limits of NO emission achievable with this type of flame have not been defined. As part of the FCR program, EER has developed a mathematical model of a long pulverized coal flame which includes detailed finite rate kinetics describing the fate of fuel-bound nitrogen. Unfortunately, there appears to be a lack of information with which to validate the model and also define its weaknesses.

1.2 Objectives and Scope of the Work

The purpose of this program was to utilize state-of-the-art measuring techniques to characterize in detail a number of long pulverized coal flames under well-defined input and boundary conditions.

Measurements in these flames included the determination of local gas and solids compositions and concentrations, temperatures, and radiative and aerodynamic characteristics in sufficient detail that the data can be used for the validation of prediction procedures both for the global combustion process and for specific phenomena relating to coal particle combustion. This characterization can aid model development as well as providing information which will be of direct value to other EPA programs.

The work reported here is restricted to measurements of pulverized coal flames with all axial flow and the use of a very simple double concentric, parallel flow burner system. Such burner systems produce "long" flames which are far-field dominated and where the heat release is protracted. While such flames exhibit the real characteristics of certain classes of furnace flames, the results are more amenable to analysis, and a knowledge of mean residence time could provide the necessary link between the flow field and the reaction kinetics.

An optional second phase of work has been proposed, to extend the program beyond the simple flames of this type, and to include the possibility for measurements on a different furnace scale. The future planning for this second phase should be based upon experimental and theoretical results of the present work.

2.0 EXPERIMENTAL CONDITIONS

2.1 Input Variables

- Coal type (table 1)

The coal chosen for this study was a high volatile bituminous coal. This choice was made for a number of reasons, e.g.:

- stable ignition can be achieved with such coal over a wide range of burner velocities and temperatures;
- a high volatile level is a characteristic of many US coals;
- the ash content is sufficiently low to minimize deposition on heat transfer surfaces.

Coal from the Saar region of Germany represented a convenient source for IFRF and its composition lies in the range of typical US coals. The coal was prepared and milled on-site in the IFRF plant which provides for a batchwise operation and in which the main element is a ball-mill. For the above coal a normal p.f. size distribution was approximately 30% > 75 μm, with a gradient of unity in a Rosin-Rammler distribution. The coal was additionally dried down to a moisture content of approximately 2%.

- Selected input variables (table 2)

Prior to this work, a comprehensive study of the IFRF literature available on the types of flame envisaged had been carried out with a particular consideration for conditions obtained with a high volatile, low ash coal. For this type of coal, the devolatilization and ignition behavior is known to play an important role on NO_x formation through the evolution of both fixed and volatile nitrogen in oxidizing or reducing atmospheres.

For the long diffusion type coal flames employed in this study, the flame variables believed to be of primary interest were ignition distance and burnout length. Both parameters may be expected to influence overall emissions of NO_x through the different fuel-air mixing histories required to produce different flames, particularly the extent of premixing prior to ignition, and through the effective overall combustion intensity within the flame volume itself. In the selection

Table 1. Average Coal Analysis Over the "LCF" Trials Period

Volatiles	32.0 ± 1	% weight	(dry)
Ash	7.6 ± 1	"	

Elementary analysis

C	74.65	"	"
H	4.70	"	"
N	1.12	"	"
S	0.85		
O	11.08	"	"
	92.4		

Low calorific value	31	MJ/Kg	"
Stoichiometric air requirement	9.744	Kg/Kg	"

of appropriate flame input conditions a review was made of previous IFRF coal flame studies in order to identify the most important burner variables having an influence on fuel-air mixing history. Attention was focused primarily on the trials C10, C11, C12 and C15 [2-5] which used burners of the double concentric type and in which a coal with 35-37% volatile matter and 6-8% ash was used. Analysis of results from these studies showed that the secondary air velocity (or axial momentum) is the major parameter influencing the type of flame formed. With flames with a large (>20 m/s) secondary air velocity, and where the ratio of primary to secondary momentum is low, the momentum of the secondary air jet results in a rapid entrainment of hot combustion products and ignition of the coal jet occurs at or close to the burner exit. When secondary velocities are low (<10 m/s) results show that a relatively high primary stream momentum is required in order to produce stable flames. In such cases the ignition front is normally detached from the burner.

In this present series of trials, a primary interest was therefore to investigate the effect of fuel air mixing on the fate of coal nitrogen species. To this end a series of flame conditions was selected for which the measured input values are listed on Table 2. These flames are classified into two basic types depending upon the input values:

- flames with a high (≥25 m/s) secondary air velocity and where the primary/secondary momentum ratio is low. These flames are referred to as type 'A' and were normally ignited at the burner.
- flames with a low (10 m/s) secondary air velocity and with a high primary/secondary momentum ratio. These flames are referred to as type 'B' and have a slightly lower total burner momentum than type 'A' and are generally characterized by delayed ignition.

Within these two basic classes of flames various other input variables were applied in order to change mixing and ignition characteristics. For approximately constant total momentum and primary/secondary momentum ratios (achieved by adjusting steam velocities) the percentage of air supplied as primary air was increased (flame A1 vs flame A4

Table 2. Flame List for the "LCF" Trials

Flame	A1	A2	A4	B1	B2	B3
Coal mass flow (kg/h)	212	220	219	212	228	220
Total air mass flow (kg/h)	2319	2394	2442	2334	2533	2440
Primary air ratio (% total)	11.0	25.1	25.2	18.6	19.9	34.0
Secondary air						
. Mass flow (kg/h)	2064	1794	1827	1900	2030	1610
. Temperature (°C)	490	490	475	500	300	470
. Velocity (m/s)	25.1	25.1	28.4	9.6	10.6	12.5
Primary air						
. Exit temperature (°C)	150	315	220	190	130	350
. Exit velocity (m/s)	21.9	30.8	17.4	40.7	41.1	29.7
. Total momentum (N)	17.2	19.5	18.4	12.4	14.4	14.3
. Primary/secondary momentum ratio	0.20	0.56	0.28	1.44	1.39	1.55
Burner diameters (mm)						
. primary	70.3	107.1	132	70.3	70.3	132
. secondary	260	260	260	399	342	342

and flame B1 vs flame B3). In the case of the type A flames, one condition was investigated in which the primary/secondary momentum ratio was increased, all else remaining unchanged (flame A2 vs flame A4), and one additional condition was investigated in which the air preheat temperature was reduced (flame B2 vs B1).

In all cases the total thermal input was kept constant at 2.1 MW and the nominal excess air was 10%. A general impression of overall flame form can be seen in the flame photographs (Section 8.0).

A simple double concentric burner was used, which is shown on fig. 1, where both primary and secondary ducts were interchangeable. The relationship between burner configurations, input conditions and flame form can be understood from the information presented in table 2 and the flame photographs.

In the design of the burner it was felt necessary to keep the last burner part (length of 1 m) as smooth as possible for the establishment of both primary and secondary flow uniformity. Also, the latter part of the coal injector was not insulated in order to facilitate burner changes and to prevent too great a step causing a flow disturbance close to the exit. As a result of this the coal pipe (stainless steel) was subject to back radiation from the flame and the primary jet was therefore heated prior to the exit. In order to quantify this effect, measurements of primary jet temperature were carried out along the centerline with a bare thermocouple, and the results are shown on fig. 2. The primary air exit temperatures reported on table 2 were obtained by extrapolating those lines with help of the measured flame temperature profiles (section 3.3).

2.2 Furnace Boundary Conditions

The trials were carried out in the IFRF furnace nr. 1, which is a refractory tunnel furnace of approximate dimensions 1.9 x 1.9 x 6.25 m. This furnace, shown schematically on fig. 3, was cooled by 6 fixed loops in the last 2.2 m and by 12 straight pipes arranged 3 by 3 in the first half of the furnace. The latter could be removed in order to facilitate furnace cleaning and also to speed up the furnace heating periods at night and after weekends. The amount of heat extracted by this cooling load was relatively low and generally in the range 31-36% of the

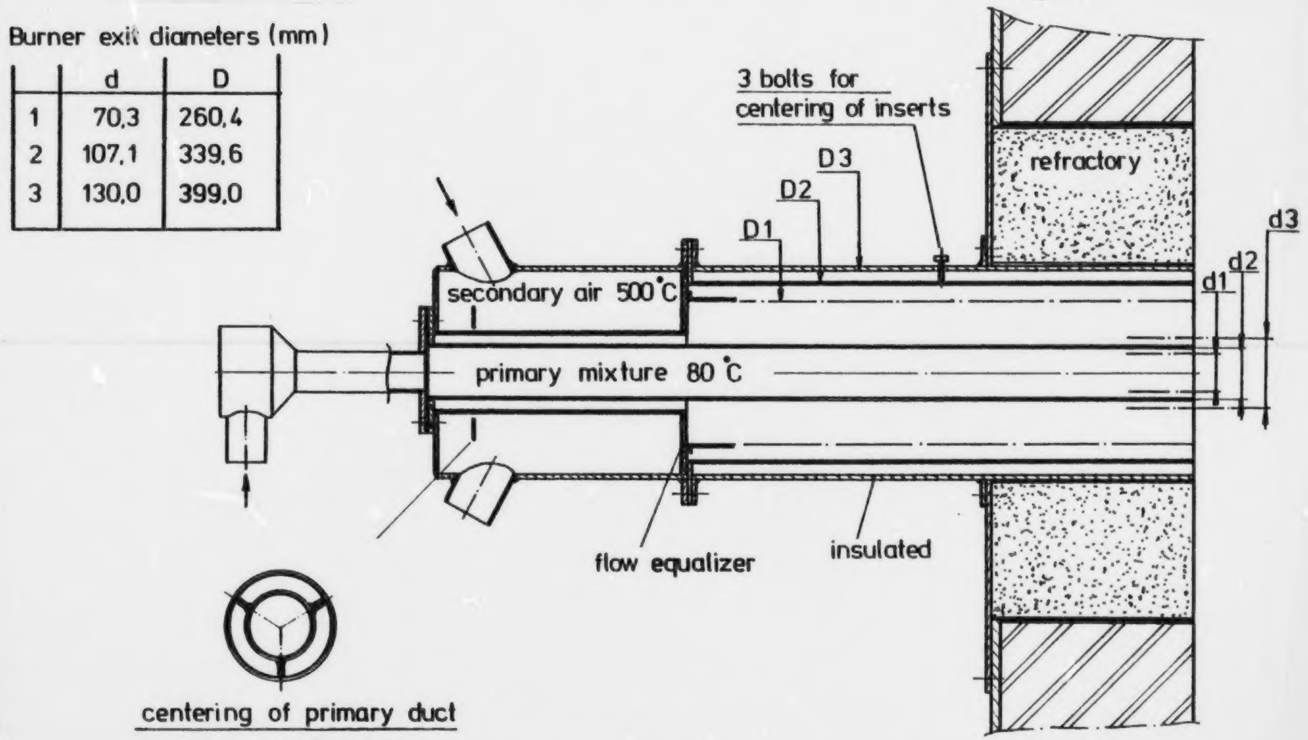
3 bolts for
centering of inserts
refractory
D1
D2
D3
d1
d2
d3
secondary air 500°C
primary mixture 80°C
flow equalizer
insulated
centering of primary duct

Burner exit diameters (mm)

	d	D
1	70,3	260,4
2	107,1	339,6
3	130,0	399,0

Figure 1. Double Concentric p.f. Burner for LCF Trials (EPA/EERC).

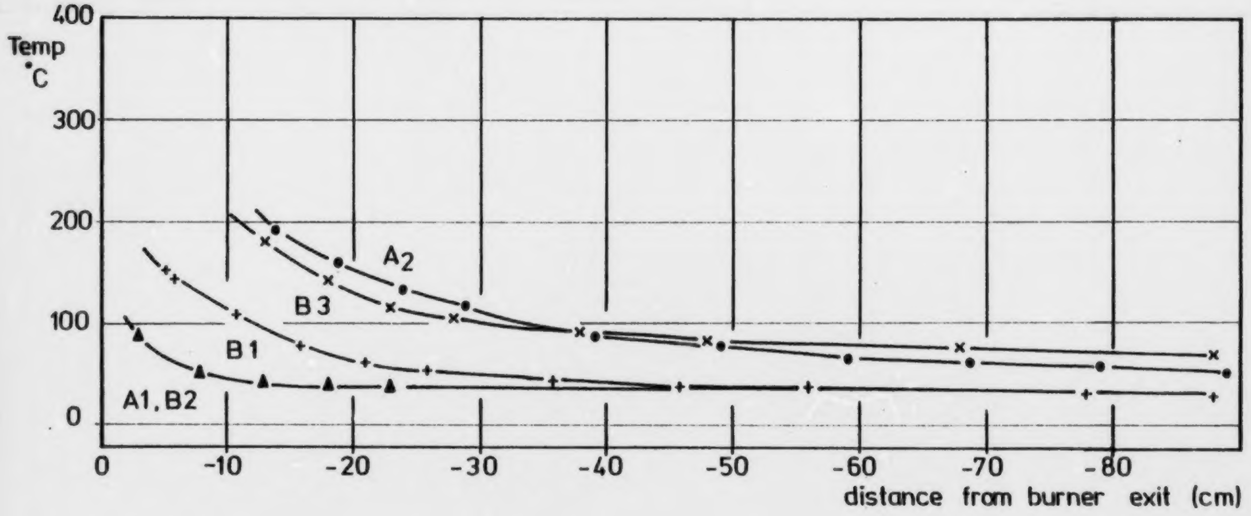

Figure 2. Primary Jet Temperature Along the Axis of the Coal Pipe.

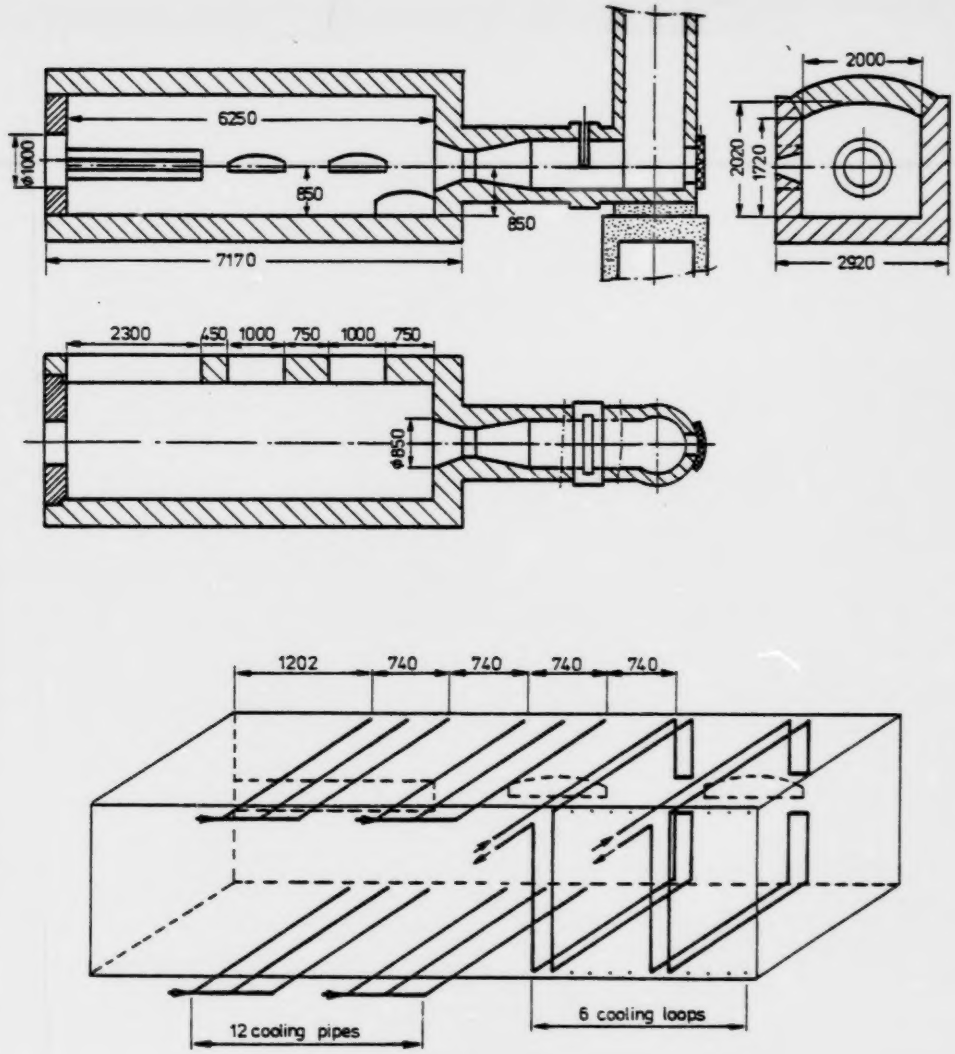
6250
φ1000
850
850
7170
2000
2020
1720
2920
2300
450
1000
750
1000
750
φ850
1202
740
740
740
740
12 cooling pipes
6 cooling loops

Figure 3. Schematic of the IFRF Furnace nr 1.

heat input so that a flue gas temperature in excess of 1200 C could be obtained.

The furnace wall temperatures were reasonably stable for all flame conditions, with, however, a tendency to increase slowly with time as a result of ash deposition and building up. In order to minimize this effect, periodic cleaning of the furnace was carried out, approximately every four hours.

2.3 Measurements and Instrumentation

Measurements have been carried out during a three week period and on a two shift, five days a week basis. The furnace was also operated at nights for temperature maintenance and this gave the possibility to finalize the measurement program during a few night shifts whenever this was necessary.

The measurements consisted of:

- the routine input measurements with monitoring all air and fuel input variables and sampling coal every day to check upon coal composition and fineness;
- the normal output measurements with standard IFRF instrumentation. A heated quartz probe, with heated sampling line (teflon) followed by a glass wool filter was used for flue gas sampling (for the species O_2, CO_2, CO, NO_x).

A normal solid sampling "A" probe was used to collect flue gas solids. This probe is a water cooled (thermal quench) system in which particulate material is removed in a sintered bronze filter integrated into the probe sampling head. Sampling is carried out under isokinetic condition. This and other sample probe designs are discussed in Reference 9.

In-Flame Measurements

In-flame sampling represented the major objective of this study and it was proposed to carry out mapping in the coal flames involved.

Detailed mapping of flames A1 and B1 was carried out involving both axial and radial profiles throughout the horizontal plane of the burner centerline. Characterization of the other flames was only made along the axis.

Because of the nature of the flames selected, a large proportion of the measurements needed to be made in regions of high temperature and reduced oxygen concentrations. This presented a number of difficulties both in terms of probing techniques and in the functioning of analytical equipment [6].

These difficulties were fully appreciated and every effort was made to ensure the accuracy, representativeness and repeatability of the results. Also, some of the sampling system requirements for different components were incompatible, and this has necessitated separate measurements with different instruments.

The following in-flame measurements have been made:

Temperature

Measurements of local gas temperature using a standard water-cooled suction pyrometer equipped with a Pt-Pt/Rh thermocouple and ceramic radiation shields.

Gas-Velocity

By means of a water-cooled Prandtl probe coupled with the use of a Hubbard probe to define quickly the forward/reverse flow boundaries.

Gas Composition

Sampling by type B water-cooled filter probe (equipped with a quartz wool filter) and gas-chromatographic analysis for the species O_2, CO_2, N_2, H_2, CH_4 and higher hydrocarbons. It was possible to cross-check the results by means of the on-line flue gas analyzers.

NO

Also sampling with a type B water-cooled filter probe and analysis with a (TECO) chemiluminescent analyzer equipped with a stainless steel converter. Both "shower" (water quench) probe and steam cooled probes were also used to check upon the validity of the measurements in the high temperature regions of the flames.

NH_3, HCN

Measurement of NH_3 and HCN was carried out via a wet chemical method involving absorption in a KOH solution and the use of ion selective electrodes [7]. For this method, the sample was sucked at a maximum flow rate of 21/min during 12 min 30 sec through a 3 m steam heated line and is absorbed in a bubbling bottle containing a KOH solution (pH comprised between 13 and 14).

Immediately after the collection of all the samples, NH_3 was measured with a NH_4^+ sensitive glass membrane electrode which has a Nernstian response in this region of pH, following the equation:

$$E = Eo+ - S.\log [NH_3]$$

The measurement of CN- is then carried out after removal of sulfur (HSO_3-, SO_4--) with cadmium carbonate which is soluble in a solution containing CN- of NH_4+: cadmium sulfate is formed and precipitates.

The CN- ion-sensitive electrode is an Ag_2S mixed crystal electrode (solid state electrode) where the available Ag+ is governed by Nernst law within the range 10^{-5} - 10^{-1} M.

Solids

Local solids sampling was carried out by means of conventional water-cooled filter probes. Wherever possible, isokinetic sampling was used (based on earlier velocity measurements) to determine the local solids concentration (g/m^3) and to provide a solids sample for later detailed analysis (3 g per sample). Also, simultaneous measurement of gas concentrations was carried out with the flue gas analyzers, to ensure the repeatability of the previous gas concentration measurements and the representativeness of solid sampling.

Radiation

A knowledge of radiation characteristics is important for prediction procedures concerning the total combustion system. The distribution of total radiant heat flux (kW/m^2) incident at the furnace side-wall was determined by means of an ellipsoidal radiometer probe.

Analysis of Solids Samples

Post-experimental analyses carried out concerned largely the sampled solids. These were processed at the Research Station for:

- sieve analysis, for flames A1 and B1 only, and along the first two meters of the flame axis;
- volatile and ash fractions, including those of the sieved samples.

A portion of each sample was also sent to an external laboratory for elementary analysis including carbon, hydrogen and nitrogen (Kjeldahl technique for N-content).

A full description of IFRF measuring techniques and instruments can be found elsewhere [8, 9].

3.0 EXPERIMENTAL RESULTS

This section includes all measured data presented in the form of tables and graphs for the six flames investigated. It must be stressed that it is not the intention here to provide an extensive discussion of the results but mainly to make those results easily available in a coherent and comprehensive form. Therefore, following a general introduction on the main features of these flames based upon input-output measurements, in-flame measurements will be briefly and comprehensively described. Also, figures for in-flame measurements (7-12) are organized on a flame by flame manner and in a constant order, so that references to figure numbers will not be necessary.

Measured flame data have also been tabulated (section 7) where the tabulation includes all relevant repeat measurements and intermediate point data, and derived flame properties.

3.1 Flame Output and Furnace Boundary Conditions

Photographs of the six flames produced are shown at the end of this report. All the type "A" flames, obtained with a secondary air velocity above 25 m/s, were ignited at the edge of the coal injector as expected and it can be seen that ignition proceeds along the core of the coal jet (2 to 3 jet diameters). Flame B3 was also surprisingly ignited at the burner despite the large primary air ratio (34% of total air flow) which may be due to the high primary temperature already mentioned (fig. 2).

Flames B1 and B2 presented a visible ignition distance of 0.8 to 1.0 m which was very stable throughout the measurement period.

The important output data (averaged) are shown on Table 3; the definition of excess air "from chimney" has been defined through the relation:

$$e_{ch} = \frac{A^*}{B+D-P}$$

where A^* = oxygen available
B = oxygen needed
D = reacted oxygen
P = oxygen originating from coal

and thus takes account of all flue gas components.

It can be seen that the NO-emissions are mainly a function of the flame type (i.e., attached or detached) and do not depend so much upon the input variables; detached flames having higher NO-emissions as normally expected. Furnace boundary conditions can be expressed in terms of wall temperatures and

Table 3. Flame Output Data

	A1	A2	A4	B1	B2	B3
Excess air(% stoich.)						
"From input"	12	12	14	13	14	14
"From chimney"	9	9	9	9	10	9
Visible ignition distance (m)	0	0	0	0.8-1.0	0.8-1.0	0
Visible flame length (m)	4.8	5	4.5	6	6	5.5
Stoichiometric mixing length (m)	2.8-3.3	4.4	3.4	4.8	4.6	3.15
Flue gas O_2 %	1.75	1.8	1.8	1.85	1.9	1.8
NO ppm	270	280	250	380	430	320
temp. °C	1230	1270	1250	1220	1300	1260
Measured heat extracted (KW) (± 50 KW)	670	680	730	650	600	620

arriving radiation at the furnace walls; this is shown on fig. 4, where the profiles of wall and roof temperatures represent time averages made throughout the measurement periods. Moreover the wall temperatures have been smoothed using measured points on top and bottom of the furnace wall (right hand side wall).

In addition, the wall temperature profiles of flame A1 obtained in the first measurement period (including measurement of radiation) have also been plotted, in order to explain the relatively low radiation measured for this flame (peak 257 kW/m^2) compared to the other "attached" flames (peak 330-340 kW/m^2).

In fact, during the first measurement period, the ash layer in the furnace was not completely established and thus the wall temperatures had not yet reached a maximum; also, by virtue of the T^4 law for radiation, a relatively small difference in wall temperature has resulted in the large displacement of radiation observed.

It can be noted that the averaged wall temperatures of flame B1 and the corresponding radiative fluxes are also lower than for the other flames. In this case, too large a deposition of ash has been deliberately avoided in order to prevent any change of wall temperature (within ± 30°C), because it appeared that the ignition distance could otherwise vary significantly; in particular, for temperature variations in excess of 50°C (relative to average), unstable ignition was observed, with periodic "flash-back" towards the burner exit.

This phenomenum was not found for flame B2 despite the high wall temperatures attained. The measured heat extracted by the cooling system and the flue gas temperatures (table 3) indicate also similar differences between the various flames, if exception can be made of the effect of flame length and position of radiation peaks.

3.2 Aerodynamic Conditions

The limits of forward and recirculated flows measured with a Hubbard probe are shown on fig. 5; these indicate that attached flames have very similar aerodynamic characteristics, the first two meters being comparable to a round free jet (with half angle of 7-8 degrees). Flame B1 (and probably flame B2) also seem to present a reduced entrainment rate and jet angle.

Velocity measurements have been made for flame A1 and B1 only. It must be noted that such measurements are very difficult in flame regions with high solid

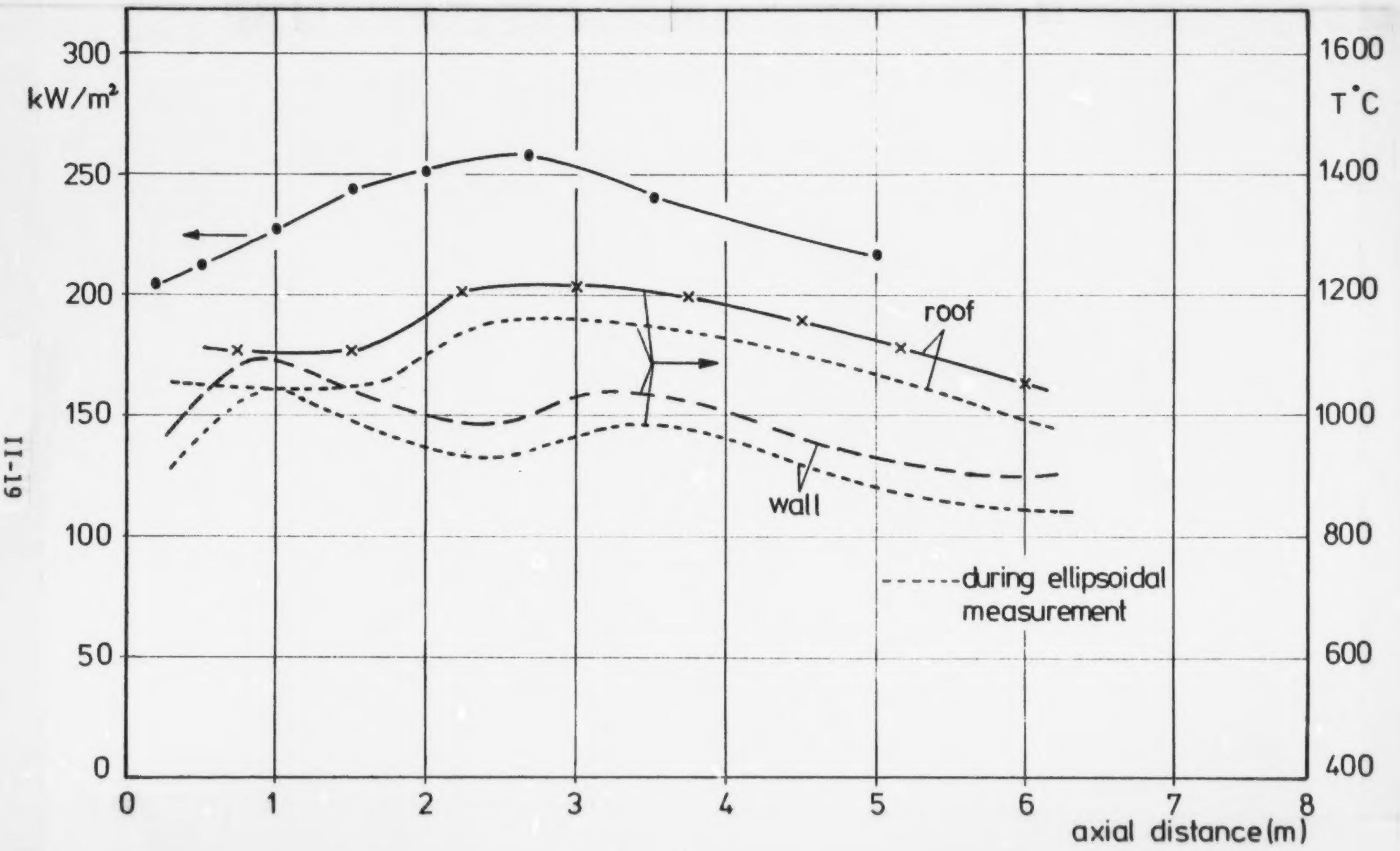

Figure 4-1. Incident Radiation at the Furnace Side Wall and Average Wall Temperatures, Flame A1.

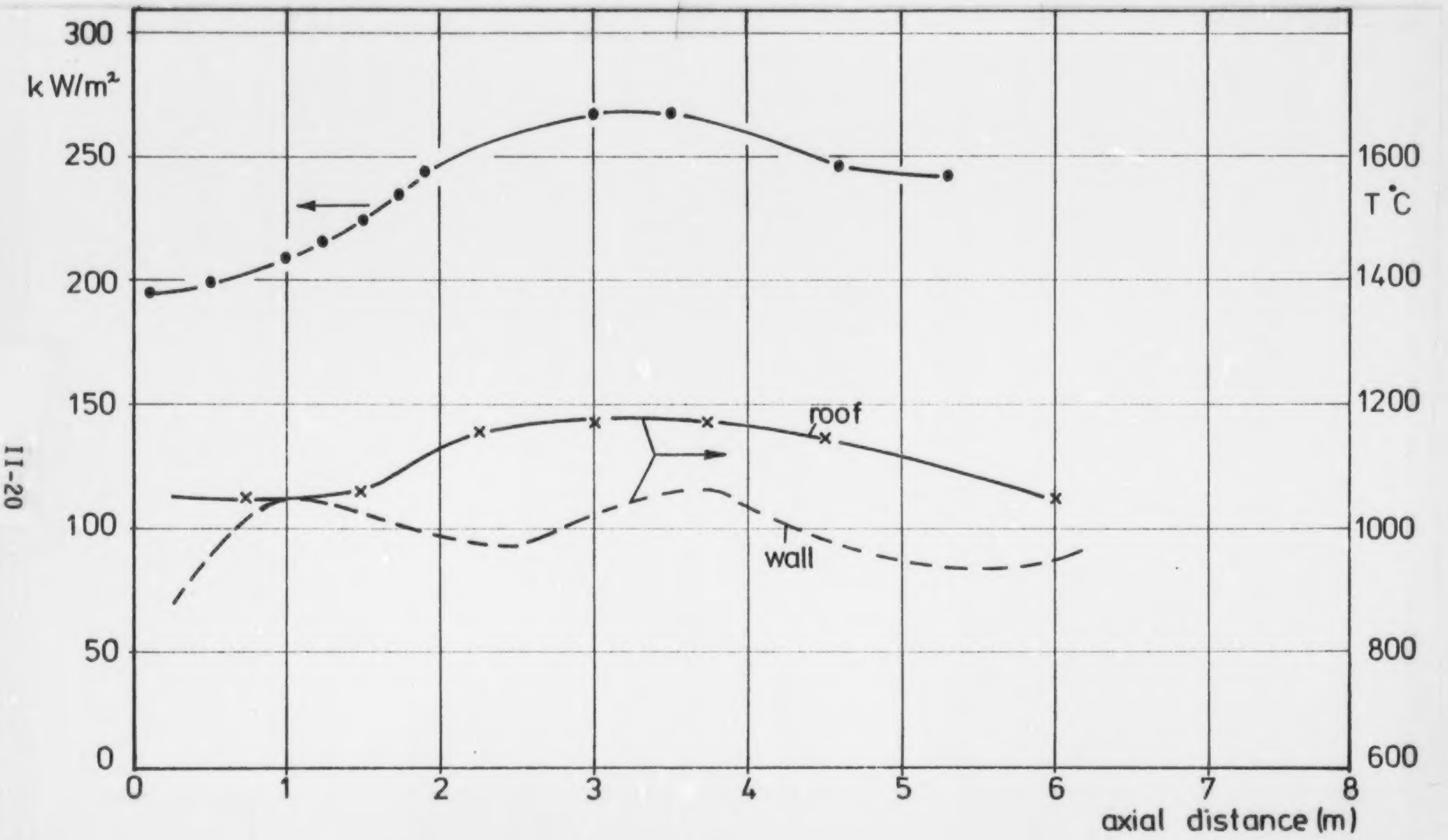

Figure 4-2. Incident Radiation at the Furnace Side Wall and Average Wall Temperatures, Flame B1.

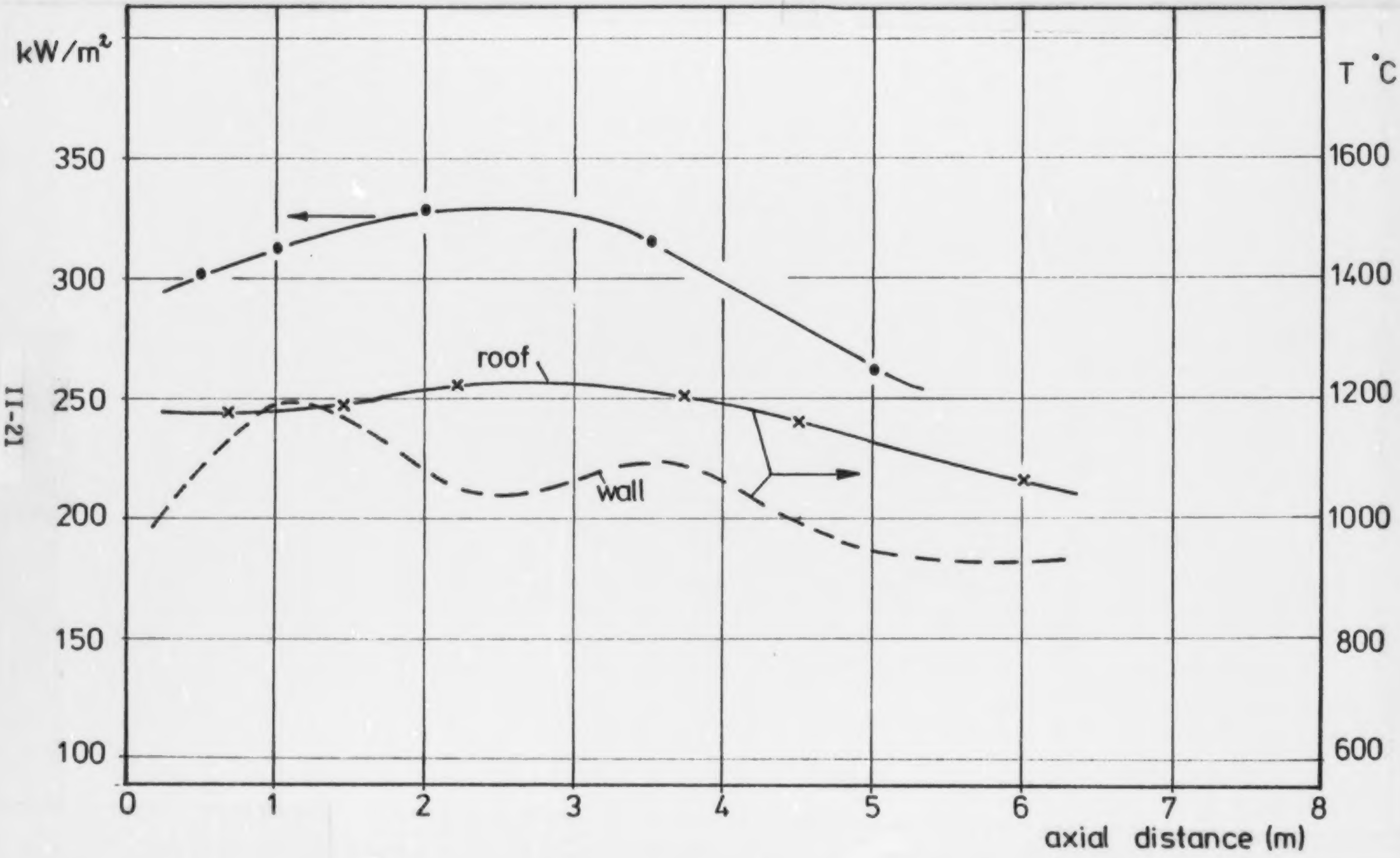

Figure 4-3. Incident Radiation at the Furnace Side Wall and Average Wall Temperatures, Flame A2.

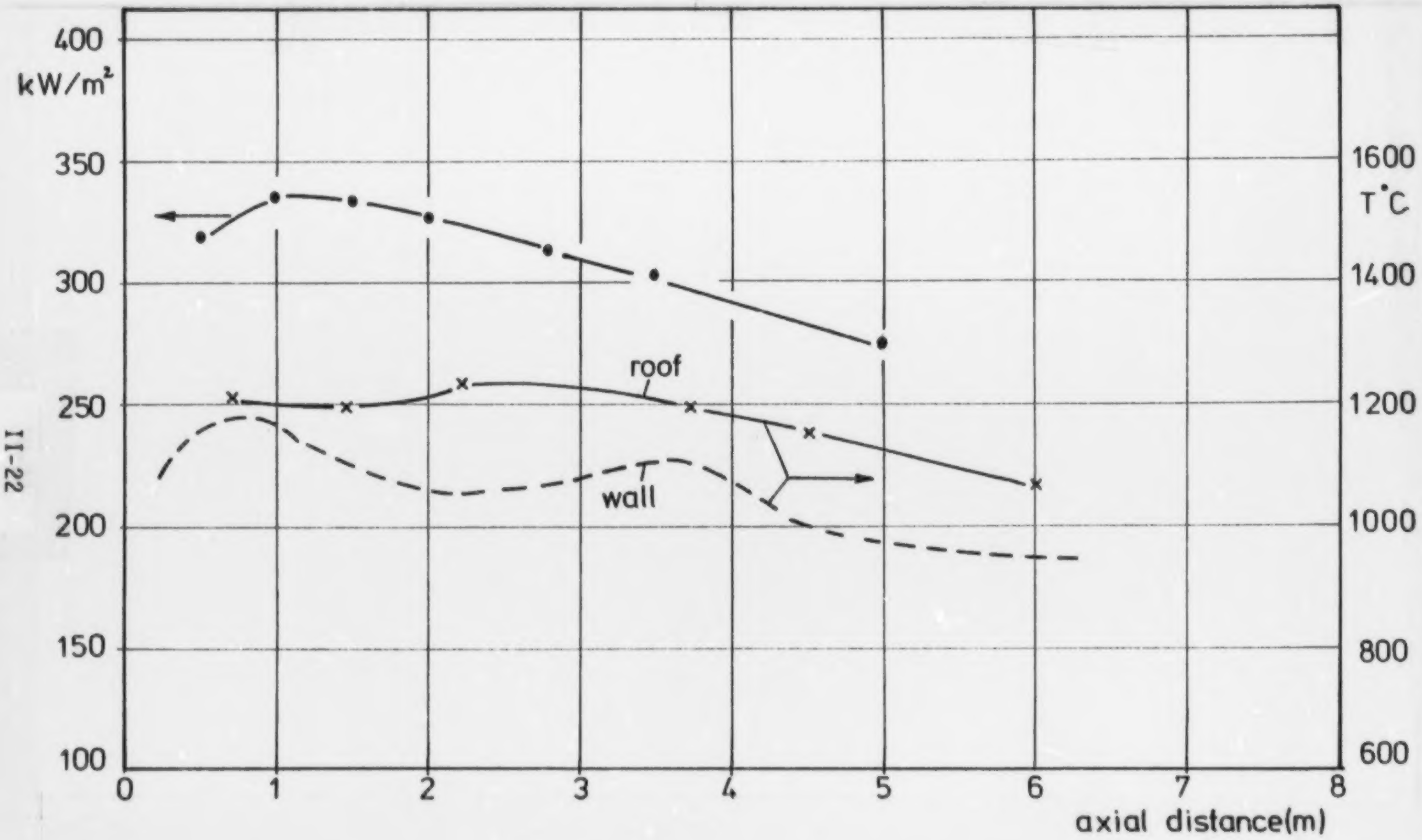

Figure 4-4. Incident Radiation at the Furnace Side Wall and Average Wall Temperatures, Flame A4.

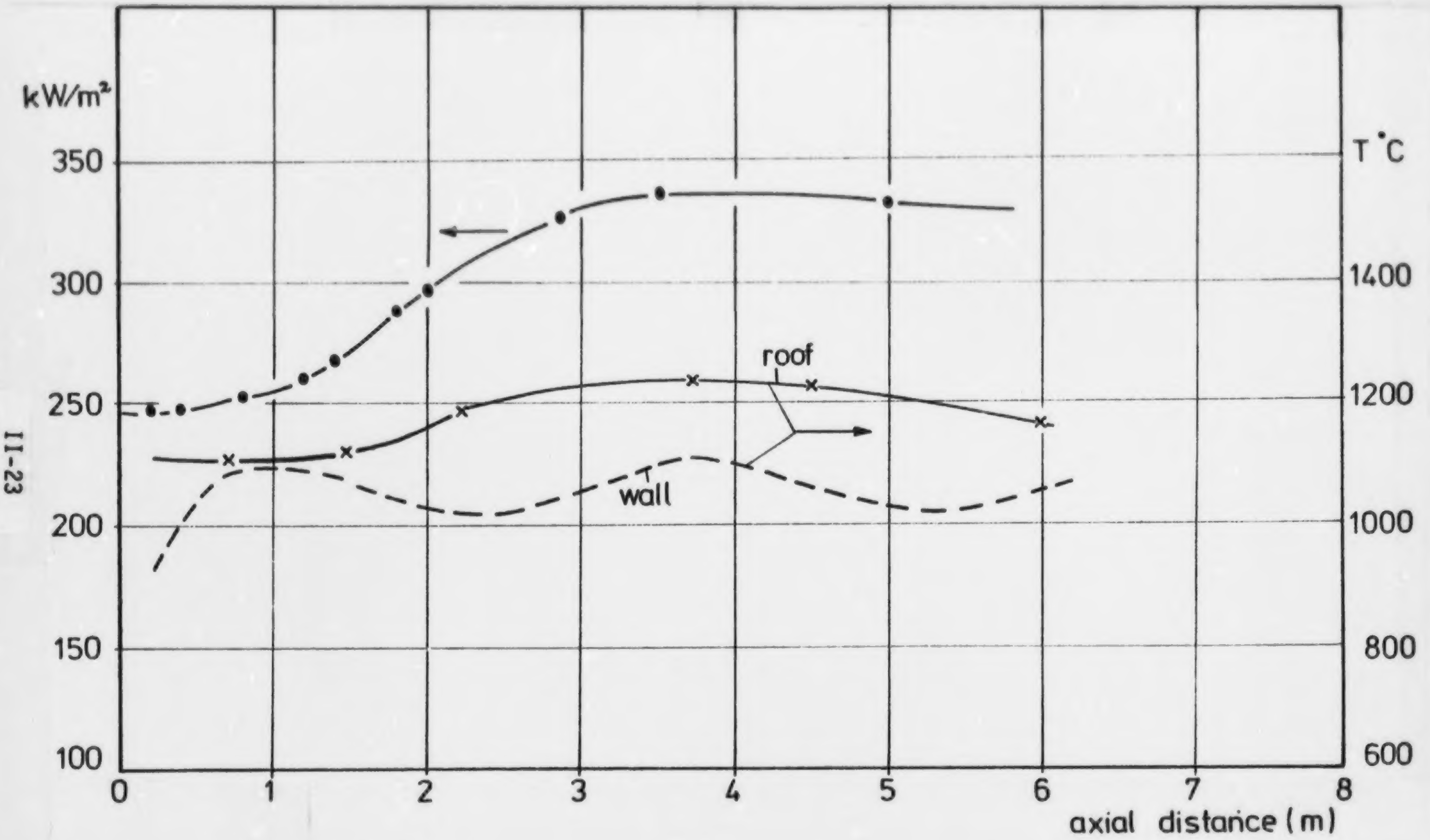

Figure 4-5. Incident Radiation at the Furnace Side Wall and Average Wall Temperatures, Flame B2.

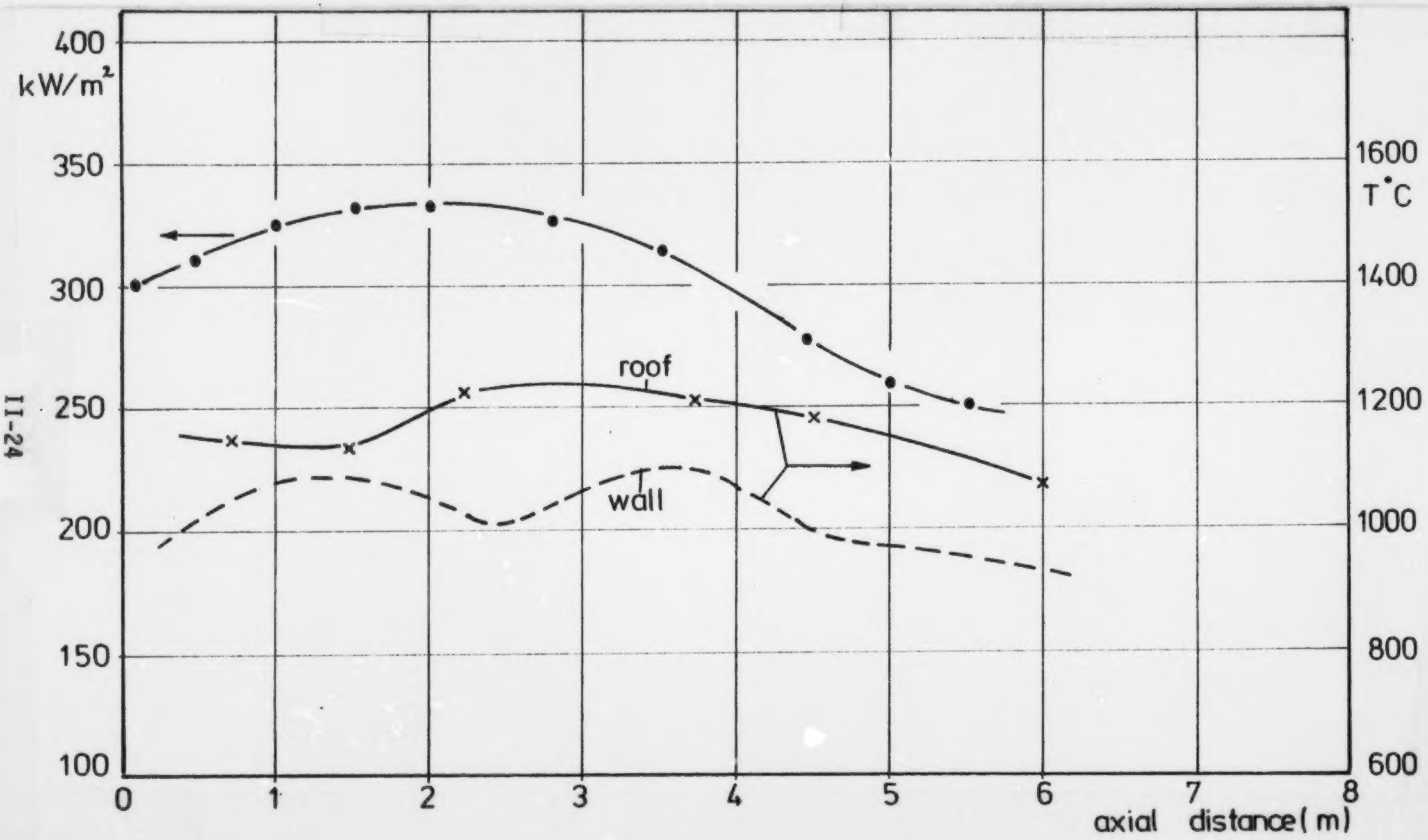

Figure 4-6. Incident Radiation at the Furnace Side Wall and Average Wall Temperatures, Flame B3.

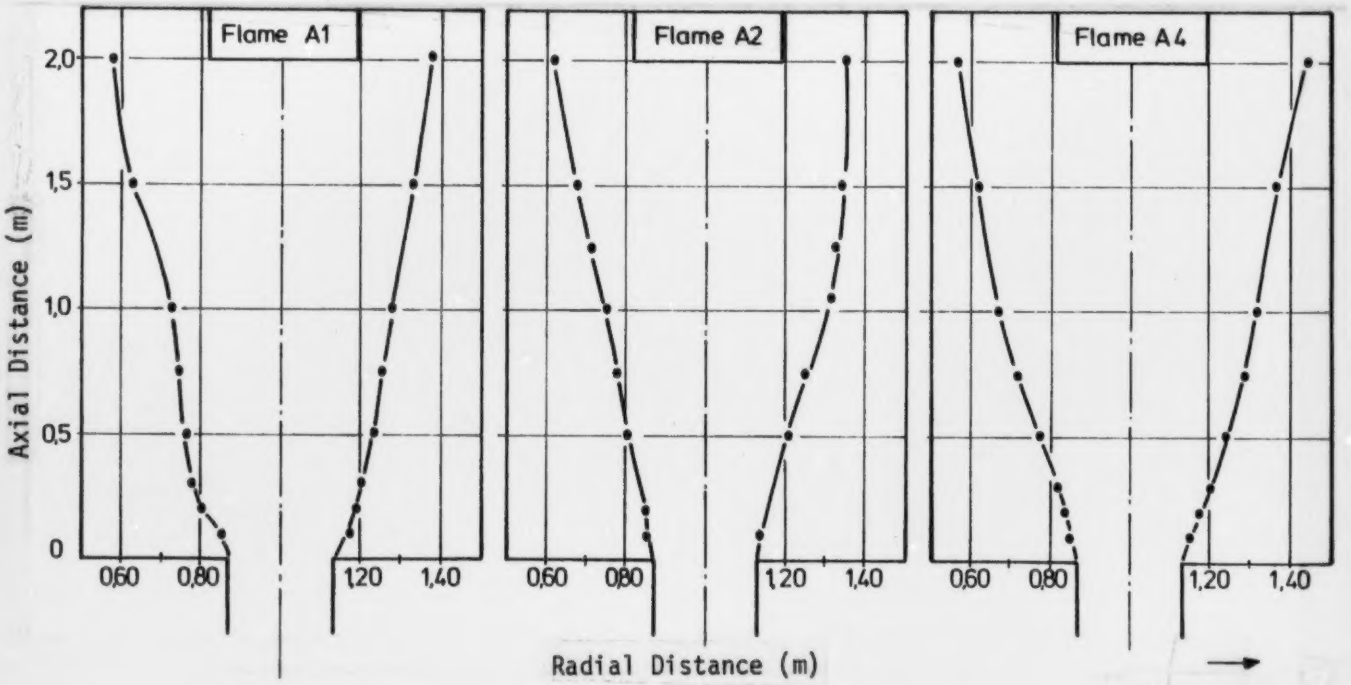

Figure 5-1. Hubbard Probe Measurements of the Flow Boundaries.

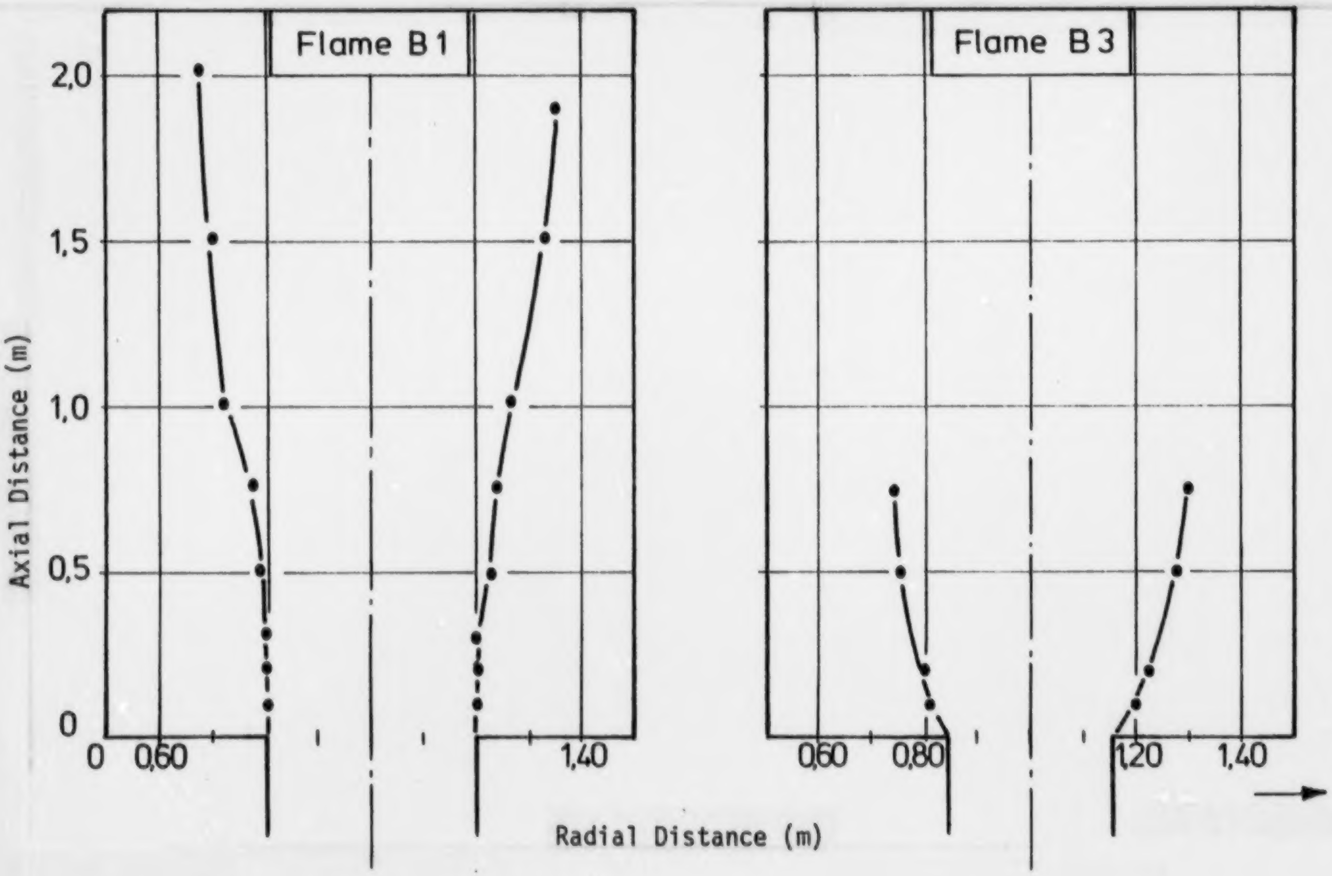

Figure 5-2. Hubbard Probe Measurements of the Flow Boundaries.

concentrations and temperatures due to the large "turbulent" fluctuations and the impossibility to carry a time integration of the signal for a period longer than four seconds.

Moreover, in the calculation of velocity, account must be taken of the total density (gaseous plus solid phases); in the early region of the coal jet, correction for solids may thus be quite large (in excess of 20%) and difficult to assess since the accuracy of measured solid concentrations is, in this region, subject to errors (see later).

Velocity data of flame A1 and B1 are included in the tables (section 7) and have further been used for the calculation of integrated mass flows across circular sections of the flames, defined as:

$$\psi_{(r)} = 2\pi \int_0^r y \cdot \rho \frac{273}{273+t} \cdot Va \cdot dy$$

with $\psi_{(r)}$ - integrated mass flow at radius r (kg/s)
ρ - local density (total (kg/m^3)
t - local temperature (°C)
Va - local axial velocity (m/s)

Lines of constant ψ, equivalent to stream lines for axisymmetric jets, are shown in figs. 6.1 and 6.2 with the normalized stream function ψ/ψ_o as a parameter (ψ_o is the total input mass flow rate).

The boundary conditions (burner exit and wall) are rather well verified for flame A1, and the Hubbard profile (thin line) corresponds approximately to the limit of the forward flow. For flame B1 however, the line $\psi/\psi_o = 1$ extends beyond the forward flow region, which could indicate that the air flow profiles are not axisymmetric. It is known that for this type of flame, with a low secondary air velocity, the buoyancy effects can become important and result in a downward motion of cold secondary air in the first part of the furnace, followed by an upward motion in the second part after mixing with hot recirculated products; this is certainly the case for flame B1 since the level of oxygen concentration measured in the recirculation zone were found to be in the range 7.5-8% up to an axial distance (A.D.) of 3 m, which corresponds to an excess oxygen of 53-60%.

Nevertheless, the velocity of the coal jet was high enough so that the flame zone itself was axisymmetric; in this case the "recirculation" of air could be treated as for tertiary air introduction through the furnace walls.

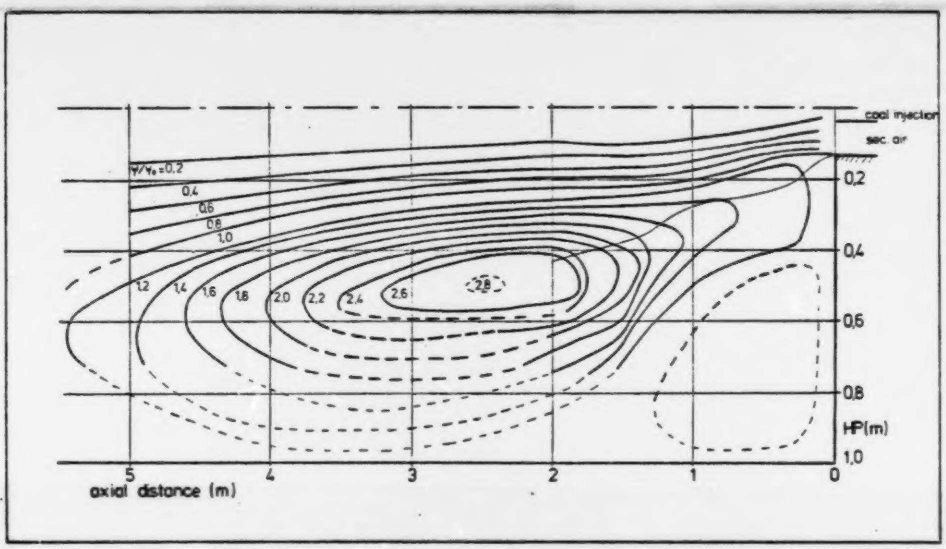

Figure 6-1. Measured Axisymmetric Stream Lines, Flame A1.

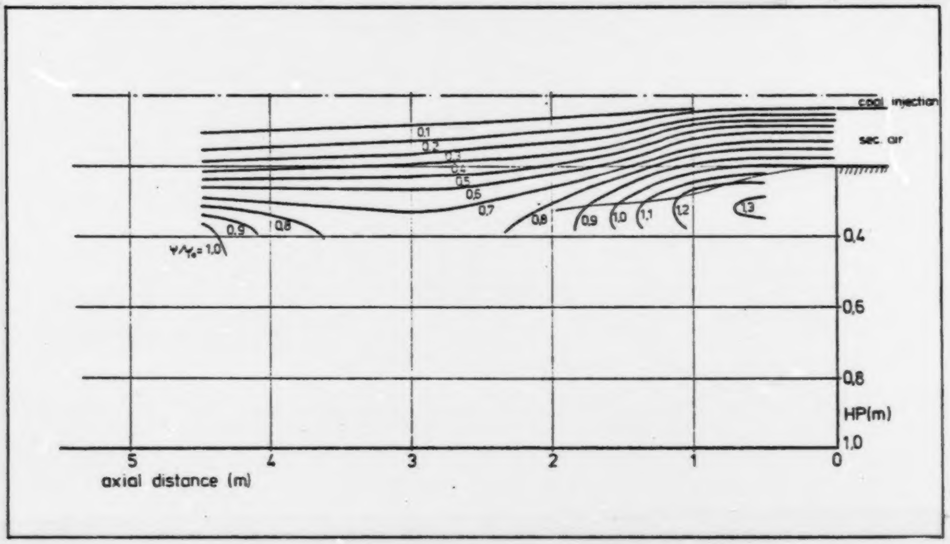

Figure 6-2. Measured Axisymmetric Stream Lines, Flame B1.

3.3 Gas Temperatures and Sampled Components

An overview of all the results indicates that the differences between the flames are mainly a function of the mixing characteristics, and that fuel kinetic effects are basically the same for all conditions.

In the early part of the flame, the dominant mechanism is obviously the heating rate of the fuel/air jet which is shown to depend principally upon flame type:

- For B1 and B2, with delayed ignition, the heating rate is relatively small up to the ignition point, i.e. up to axial distance of 1 m, where gas temperature is in the range 500-600°C; thereafter the temperature rise is very fast and comparable to that of A2, A4 and B3.
- For the attached flames ignition is also delayed on the axis, as can be inferred from other measurements (e.g. gas and solid composition). The axial ignition temperature is found in the range 500-600°C. Classification of these flames in terms of axial heating rate, °C/s (from burner exit to ignition point) is shown in the following table where the coal velocity is assumed to be constant and equal to input.

Flame	B3	A4	A1	A2
ignition delay at 600°C (m)	.10	.24	.32	.28
ΔT (0-xi) (C)	250	380	450	285
$\Delta T/\Delta t$ (10^4 C/s)	7.4	4.5	3.5	2.5

Beyond the ignition point, these flames present similar or higher temperature gradients, except flame A1, where the combustion seems to be more rapidly limited by the lack of oxygen (see gas concentration graphs). Thus the axial temperature peak of flame A1 is 2 m downstream from the burner compared to about 1 m for the other attached flames.

Isotherms have been drawn for flames A1 and B1 (see graphs) and these confirm the general features already discussed. In particular, the "recirculation zone" of flame A1 is shown to be practically isothermal whereas that of flame B1 is subject to the effect of dilution with a colder stream. Also, the core ignition pattern is clearly visible between the 500-600°C isotherms.

Temperature measurements up to the ignition point have generally been carried out after removal of the inner shield of the pyrometer and without suction. Despite the care taken to eliminate flame attachment problems and the effect of longitudinal heating of the shield in these regions (e.g. through the flame boundaries), the accuracy of the measurement is not better than $\pm$ 50 C.

The same general trends can be observed from gas composition measurements. It is here instructive to note that the position of the CO-peak (and minimum of O_2) is quite close to the temperature peak ($\pm$ 20 cm) except for flame A1 where it is found significantly earlier. The same applies for the hydrogen peak with the same exception of flame A1. For the detached flames all the concentrations peaks were found to coincide even better with that of temperature which seems to indicate also that devolatilization is very fast and quasi-local. Hydrocarbons other than CH_4 were generally not present in detectable amounts and it was decided not to carry out a systematic detection in order to save on the analysis time. Also, and for the same reason, gas chromatography was only carried out in the first part of the flame, since conventional analyzers could be used with confidence in the other regions where CO-levels were always low.

Sampling of gases and solids was perhaps one of the most difficult tasks, especially in the regions of primary interest, that is where ignition of coal particles has just started; in some places, and particularly for flame A1 which was more heavily loaded with solids (c.f. table 2), periodic coking at the probe tip has prevented the collection of sufficient amounts of samples. This was partially solved for solid sampling through periodic removal of the probe tip.

Another associated problem was that of partial gasification of the coke deposits, immediately noticed on the analyzers by a regular increase of CO and also NO levels. Repeated measurements and cross checks of data from other probes have fortunately prevented potential errors of this nature.

A third type of problem could sometimes occur at gas temperatures in excess of 1500°C with partial devolatilization of the solid samples already collected in the bronze filter. This generally necessitated the use of a sampling flow rate lower than isokinetic in such regions in order to ensure adequate quenching.

Isokinetic sampling was also not possible in the first part of the coal jet since this would have necessitated the reduction of the tip diameter or an increase of the nominal pump capacity (7 l/min), both solutions being incompatible with the B probe design.

Therefore, solid concentrations measurements made in the highly loaded regions had to be corrected for sampling velocity: the correction factor was merely taken as the ratio of sampling to actual velocity with the assumption that the particles do not follow the stream lines but keep their original trajectories; from previous IFRF work, this assumption was found to be realistic for relatively large particles [9].

Moreover, such corrections did not require a good accuracy since they were only needed for a more realistic calculation of mixing factor and degree of oxidation (see section 4.1). Since gas velocities were only measured for A1 and B1 these had to be used for the other flames (of same type), after normalizing with jet input velocities.

The axial lengths of the flames where corrections had to be made, are indicated in section 7.

3.4 Pollutant Formation

The measurement of NO, NH_3, HCN was the major objective of this work and necessitated separate measurements with different probes as described in section 2.

The major difficulty encountered was due to the existence of very large gradients in both axial and radial directions as can be seen on the graphs. Such gradients, associated with high turbulent fluctuations, should in principle require the use of much smaller probes or, as an alternative solution, to sample within a constant control volume with, therefore, a constant probe geometry. This was not the case here but, although the space averaging effect of the various probes may be different, it is believed that the degree of fineness should be sufficient for understanding and modelling of the basic phenomena.

The peak concentration level of NO was found to be between 500 ppm and 600 ppm and the position of this peak corresponded quite well with that of flame temperature, except for A1 where it occurs together with the hydrogen peak. Beyond this point the decay of NO seems to be mainly due to dilution effects, and perhaps to a lesser extent to secondary reduction by CO.

Regarding the measurement of NH_3 and HCN, it can be noted that the latter was found in large amounts but that NH_3 concentrations did not generally exceed 30 ppm, except for flame A1 (peak at 74 ppm NH_3). Also NH_3 is seen to occur before HCN when it was detected in a significant amount (>10 ppm).

The small amount of NH_3 observed was at first believed to be due to the use of "basic" solutions in the bubblers of the sampling train, but the use of neutral and acid bubblers, alone and in various combinations failed to produce different results. Other reasons for this might be:

- a too fast reaction of NH_3 in the control volume itself or at the probe tip because of the high flame temperatures;
- further reaction of NH_3 along the stainless steel sampling tube. This should however be of only minor significance due to the low tube temperature which was steam cooled (temp. around 150 C).

Thus it can be concluded that either there was effectively very little NH_3 in the flames or that the reaction mechanisms for the destruction of NH_3 were too fast compared to its residence time across the flame fronts.

The HCN profiles are seen to be very steep and, here again, the existence of such gradients may lead to a difficult interpretation of the absolute levels recorded. The sampling technique was also checked for this measurement by placing different numbers of bubblers in series. For the highest concentrations recorded always less than 10% of the HCN was found in the second bubbler, while in the third, concentrations were negligible.

The steep gradients in HCN were especially apparent in the case of narrow flame jets, e.g., A1, B1, B2 obtained with the smallest coal injector, where the amplitude of the HCN peak could fluctuate quite significantly. These variations are mainly due to the steep radial gradients as can be seen on the graphs of A1 and B1.

For flame A1 these radial gradients are negative after complete establishment of the flame (A.D. $\geq$ 1 m) and correspond to the existence of opposite gradients of temperature, oxygen and NO concentrations.

For flame B1, these radial gradients are negative as well but the axis of the flame seems to be at a small angle relative to the burner axis. Temperature profiles indicate an angle of circa 2 degrees (10 cm at A.D. = 3 m) while concentration profiles indicate half of this value, and this is also true for velocities.

This effect is very important for the HCN concentrations and is the reason for the dotted line on the axial profile of flame B1 (HCN max.). Nevertheless, such effects were of less importance for the other flames since they were significantly wider (A2, A4, B3) and it was observed that a small displacement of the probes in the radial direction did not affect so much the measured temperatures and gas concentrations as for flame B1.

Measured peak levels of temperature, CO, H_2, NO and HCN are given in Table 4 together with their axial positions; it is interesting to note that there is a good correspondence between CO and HCN peak positions with due regard for the smoothness of CO profiles and associated discrepancy of peak position. There is not however a clear correlation between NO and HCN peak positions which may not be surprising since NO and HCN are seen to form simultaneously and conversion from one to the other is possible in both directions, plus the eventuality of evolution toward molecular nitrogen.

A final interpretation of such results will therefore need to use more sophisticated treatments based on simplified theoretical calculations and/or mathematical models.

At this stage of the evaluation it is however possible to see that for the type "A" flames there is some agreement between the axial heating rate ($^{o}C/s$) already defined and the amplitude of the HCN peak which vary in opposite directions (the order being A4-A1-A2).

Table 4. Measured Peak Temperatures, Concentrations and Their Axial Positions.

	A1	A2	A4	B1	B2	B3
Temperature (°C)	1450	1430	1500	1600	1470	1520
Position (m)	2.0	1.0-1.5	1.0-1.2	1.75	2.0	1.0
CO (%)	9.6	7.5	9.0	10.0	15	6.5
Position	1.1	1.0-1.5	0.85	1.9	1.8	1.2-1.5
H_2 (%)	2.4	4.0	8.3	4.8	12.5	3.1
Position (m)	1.4	1.5	0.60	1.75	1.75	1.5
NO (ppm)	460	500	540	620	600	580
Position (m)	1.5	1.1	0.80	1.8-2.0	2.0	1.2
HCN (ppm)	3000	4060	1600	2950	1115	2720
Position (m)	1.15	1.3	0.9	1.75	2.0	1.2
HCN + NO (ppm)	3440	4440	2110	3280	1715	3300
Position (m)	1.15	1.3	0.9	1.75	2.0	1.2

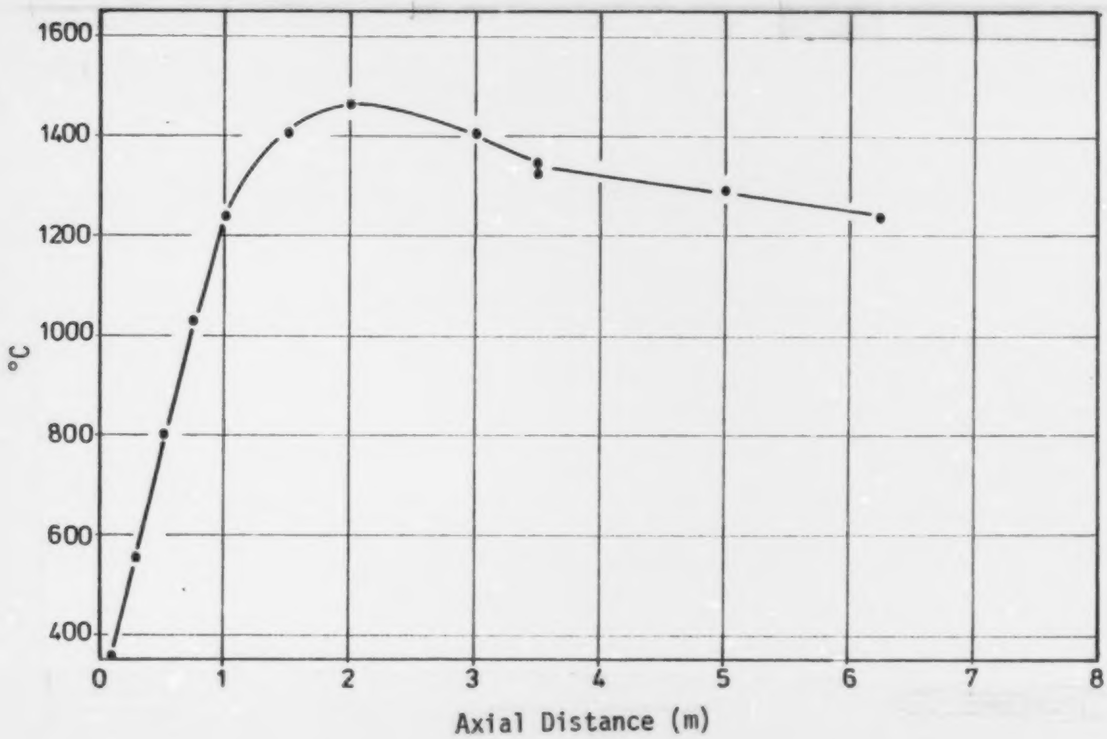

Figure 7-1.1. Axial Temperatures, Flame A1.

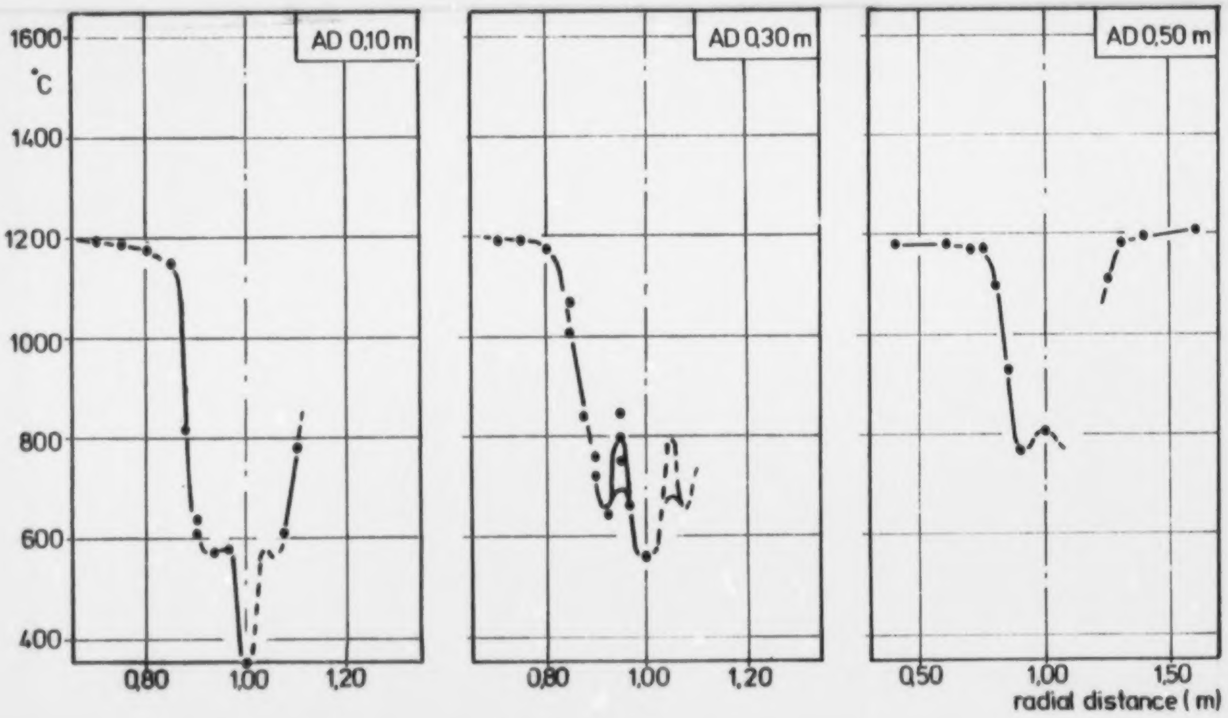

Figure 7-1.2. Radial Temperatures, Flame A1.

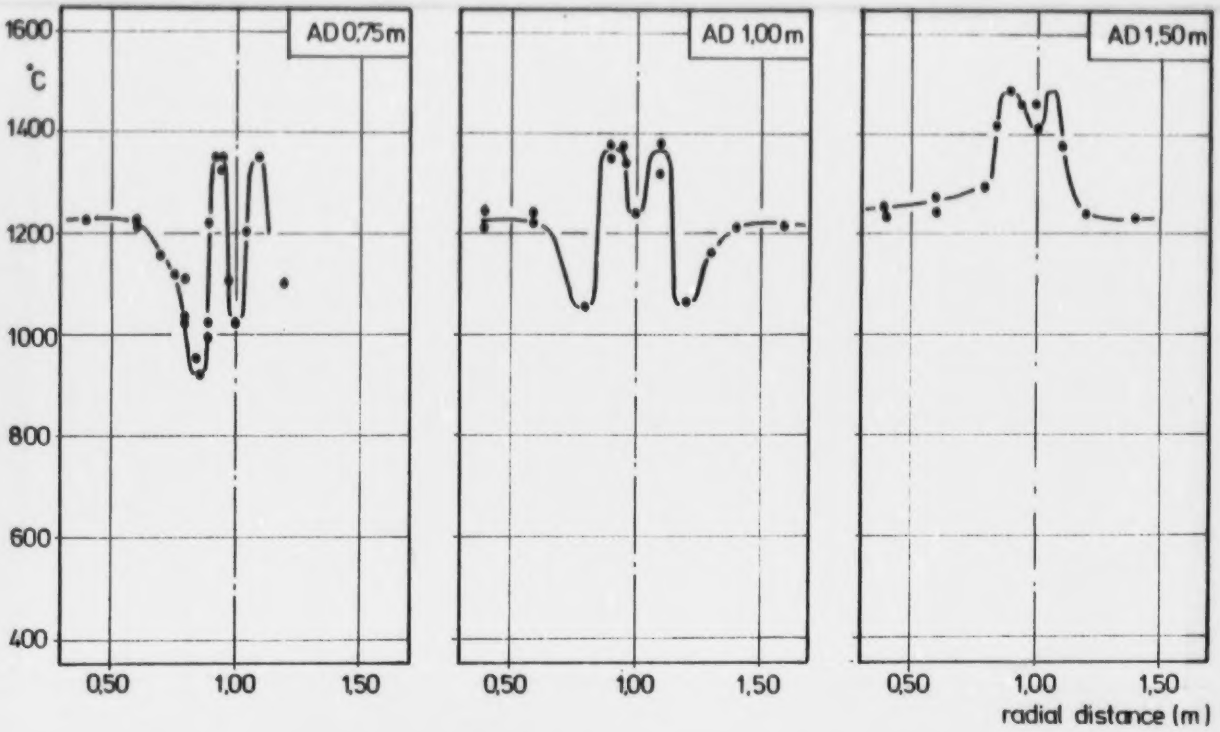

Figure 7-1.3. Radial Temperatures, Flame A1.

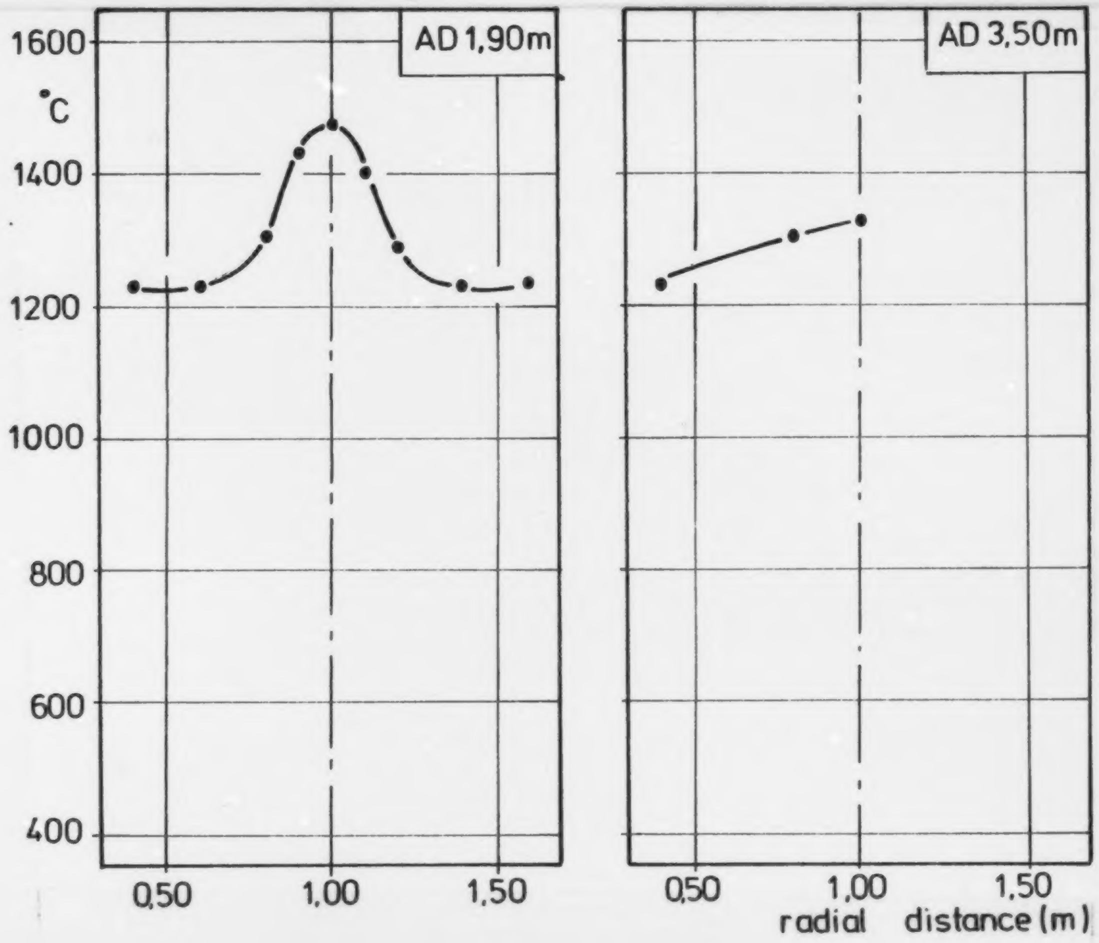

Figure 7-1.4. Radial Temperatures, Flame A1.

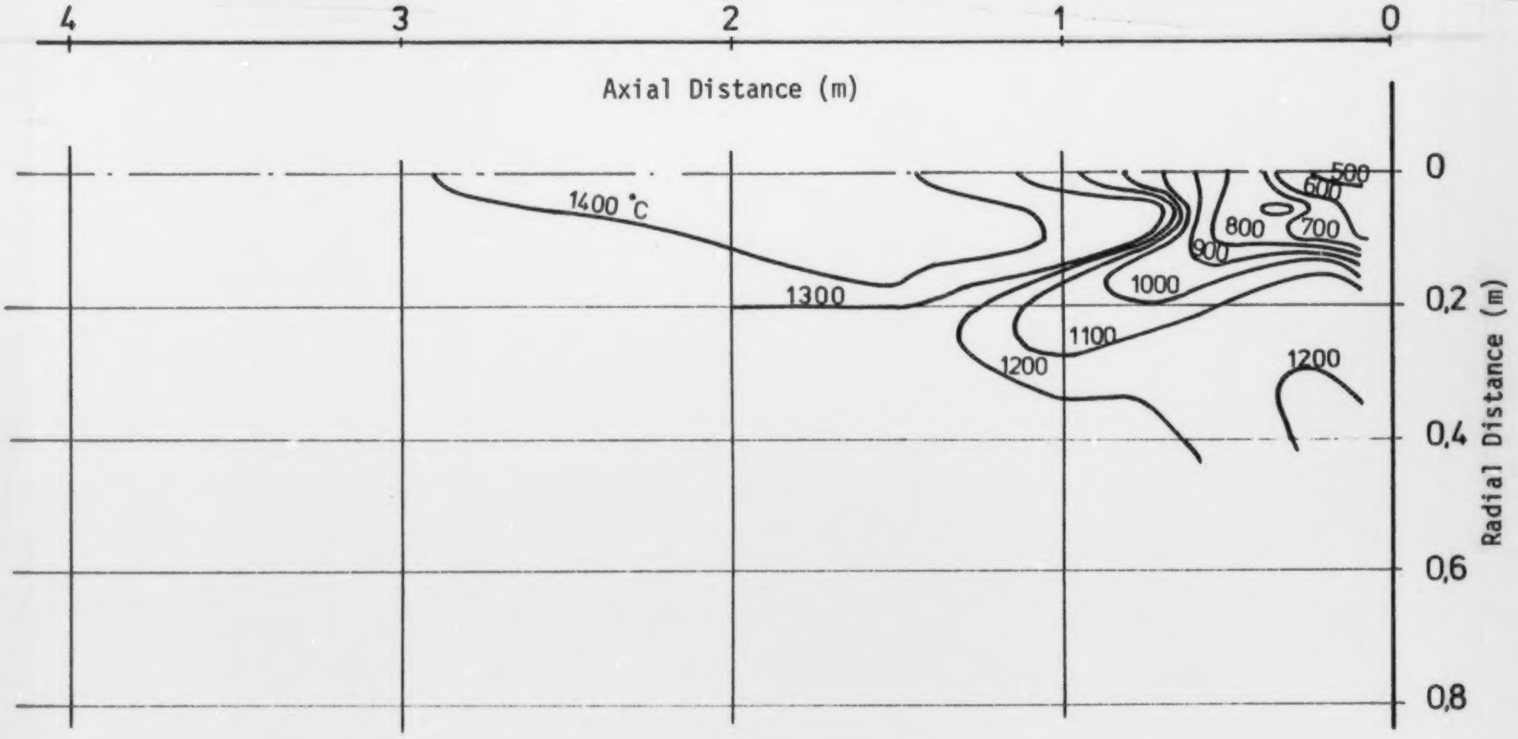

Figure 7-1.5. Isotherms (°C), Flame A1.

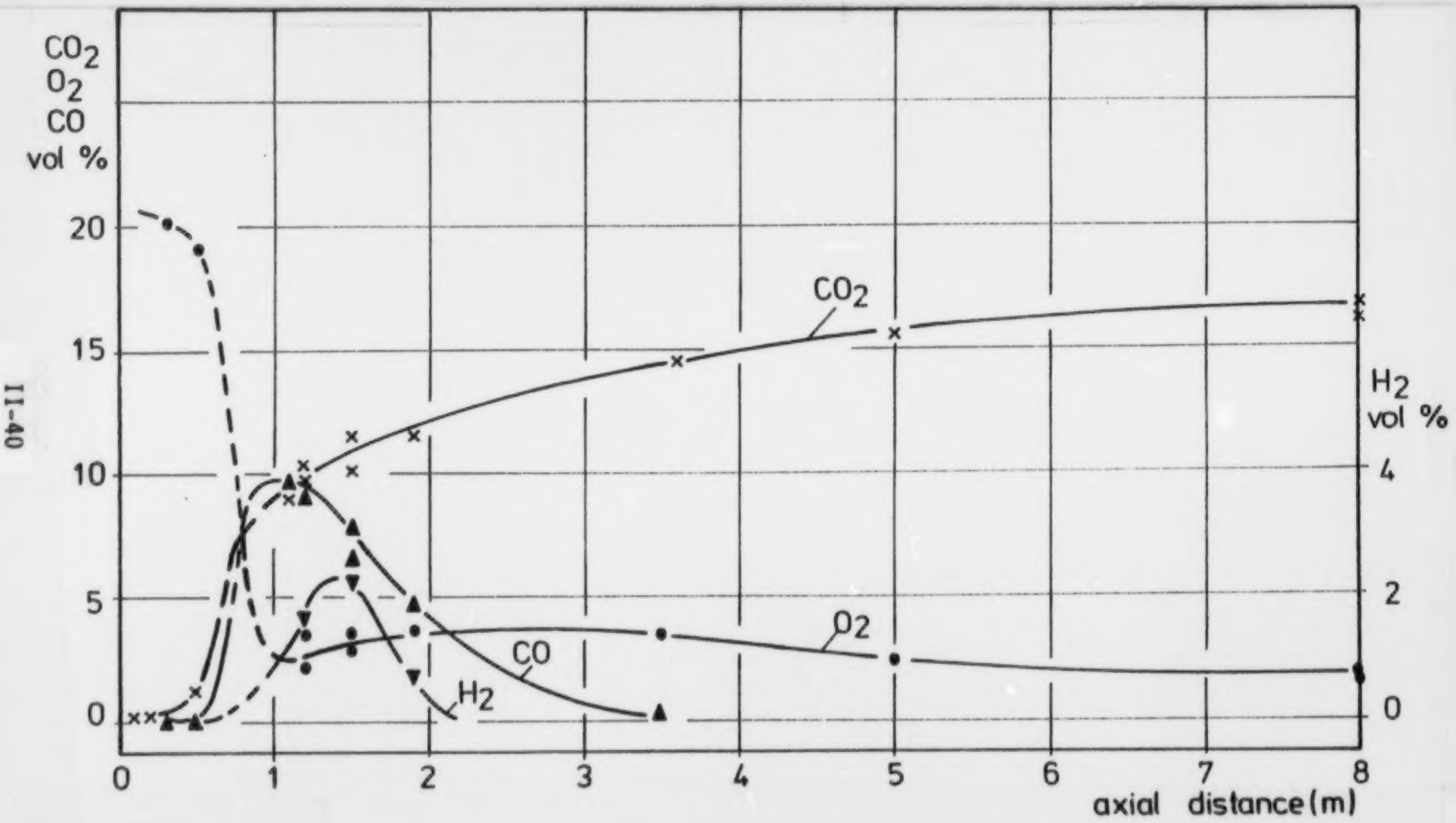

Figure 7-2.1. Axial Gas Concentrations, Flame A1.

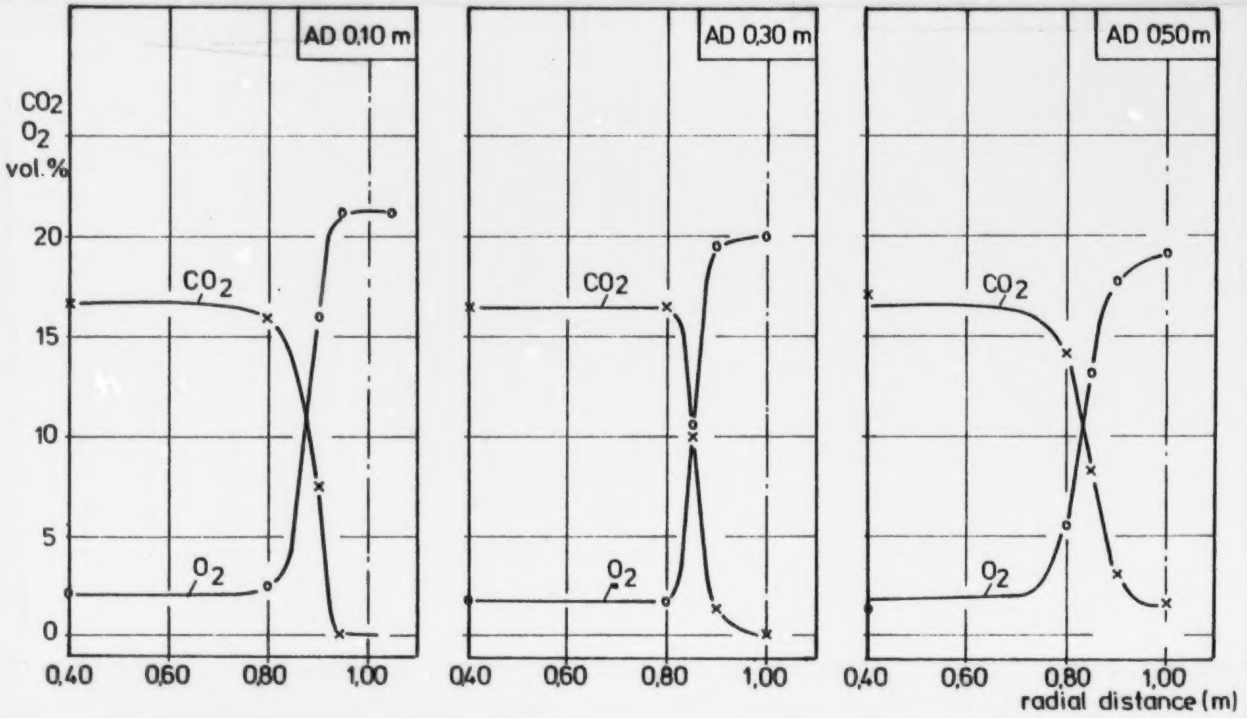

Figure 7-2.2. Radial Gas Concentrations, Flame A1.

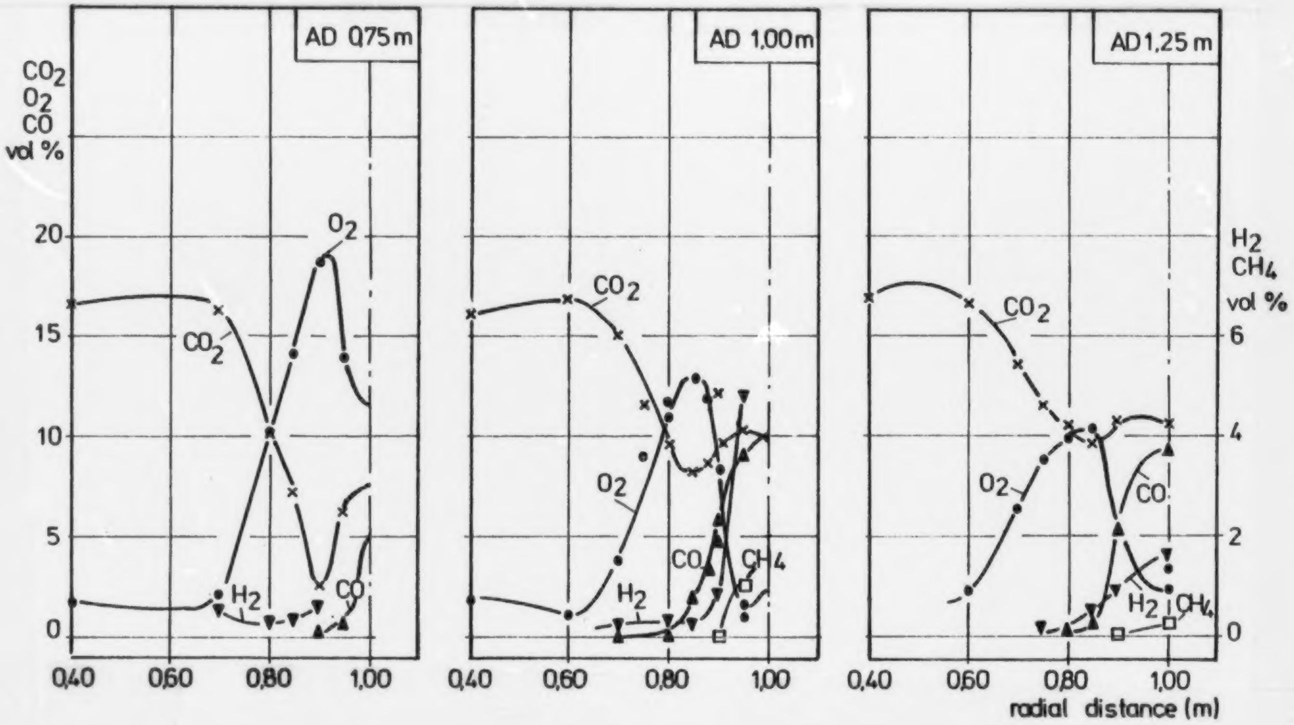

Figure 7-2.3. Radial Gas Concentrations, Flame A1.

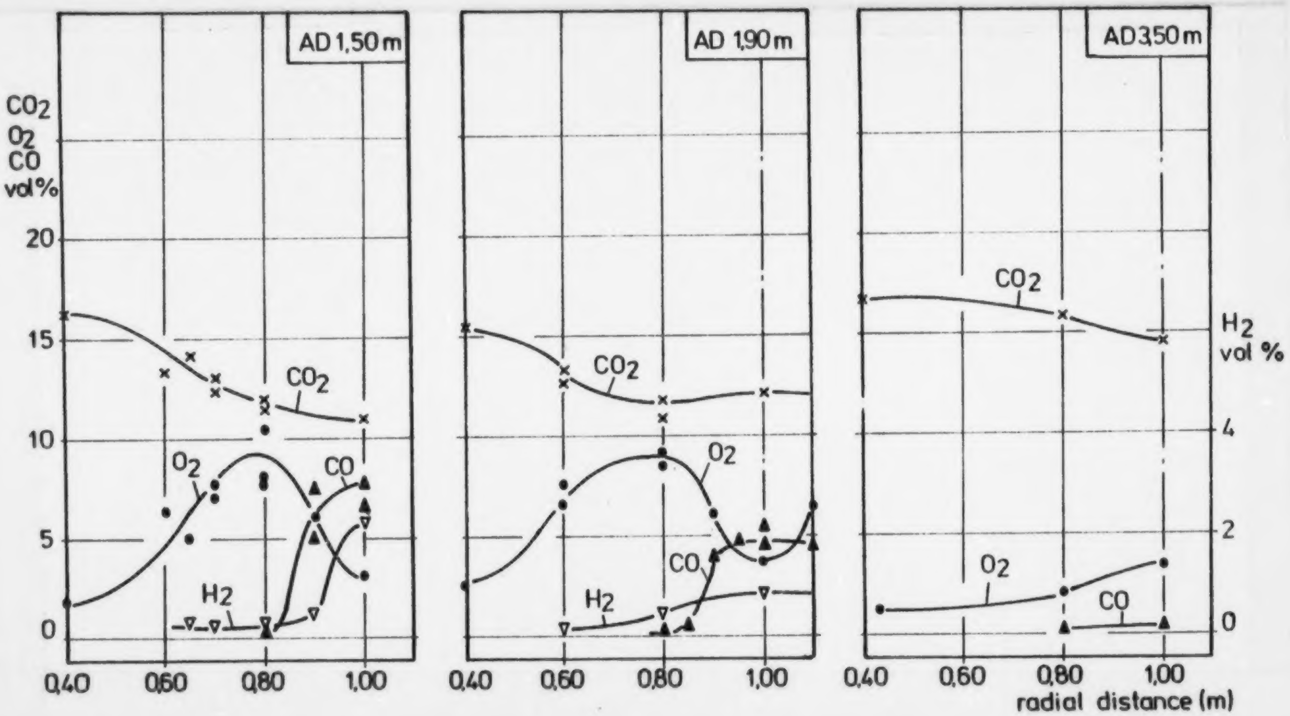

Figure 7-2.4. Radial Gas Concentrations, Flame A1.

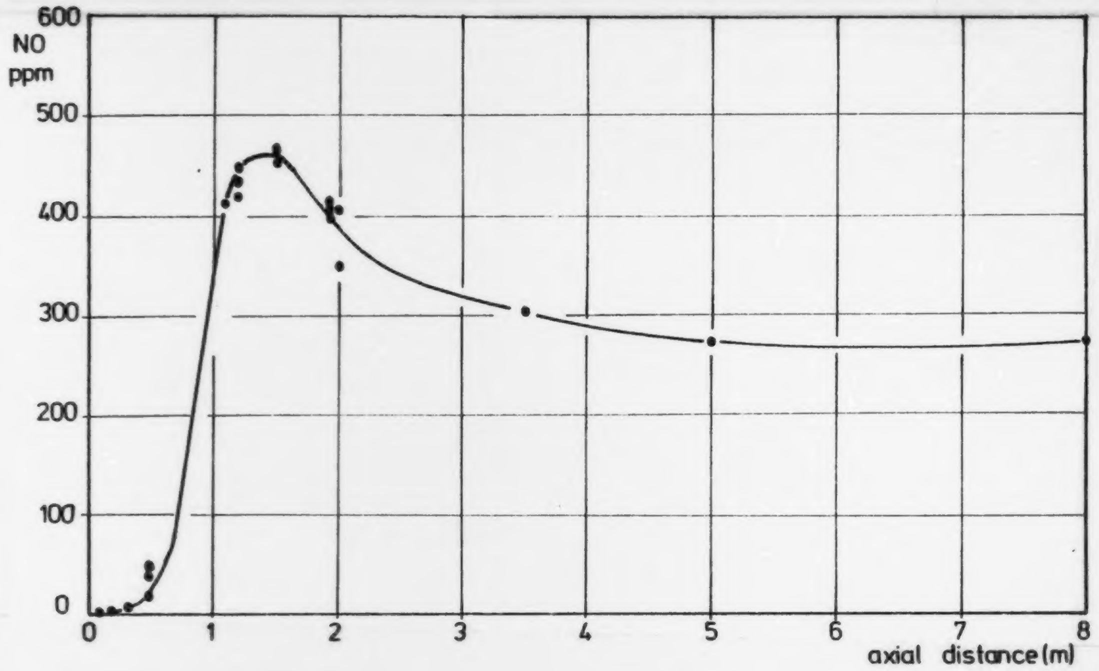

Figure 7-3.1. Axial Nitrogen Oxide Concentration, Flame A1.

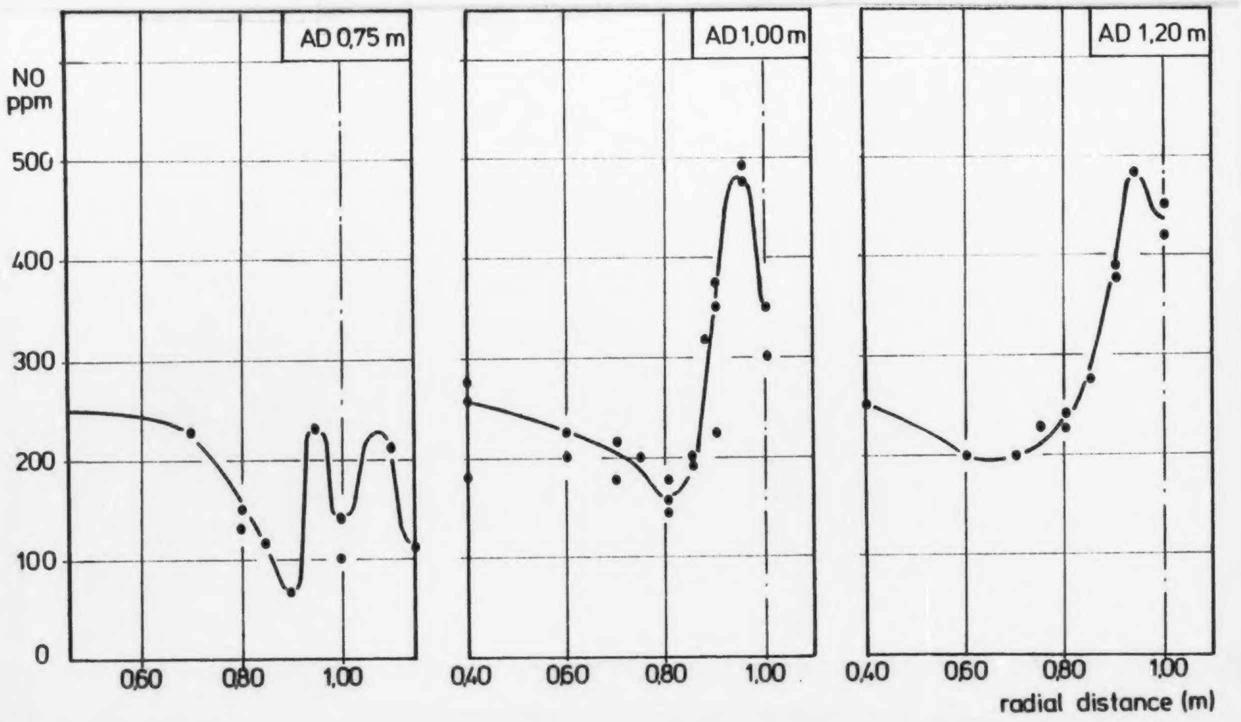

Figure 7-3.2. Radial Nitrogen Oxide Concentration, Flame A1.

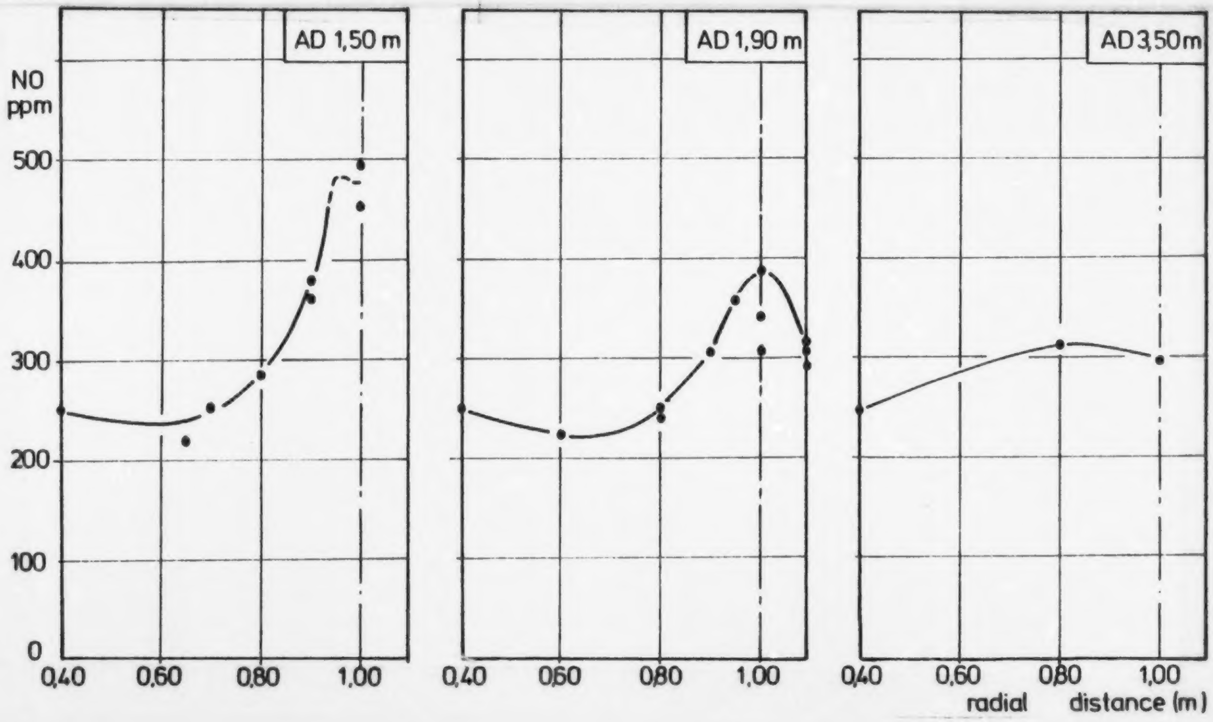

Figure 7-3.3. Radial Nitrogen Oxide Concentration, Flame A1.

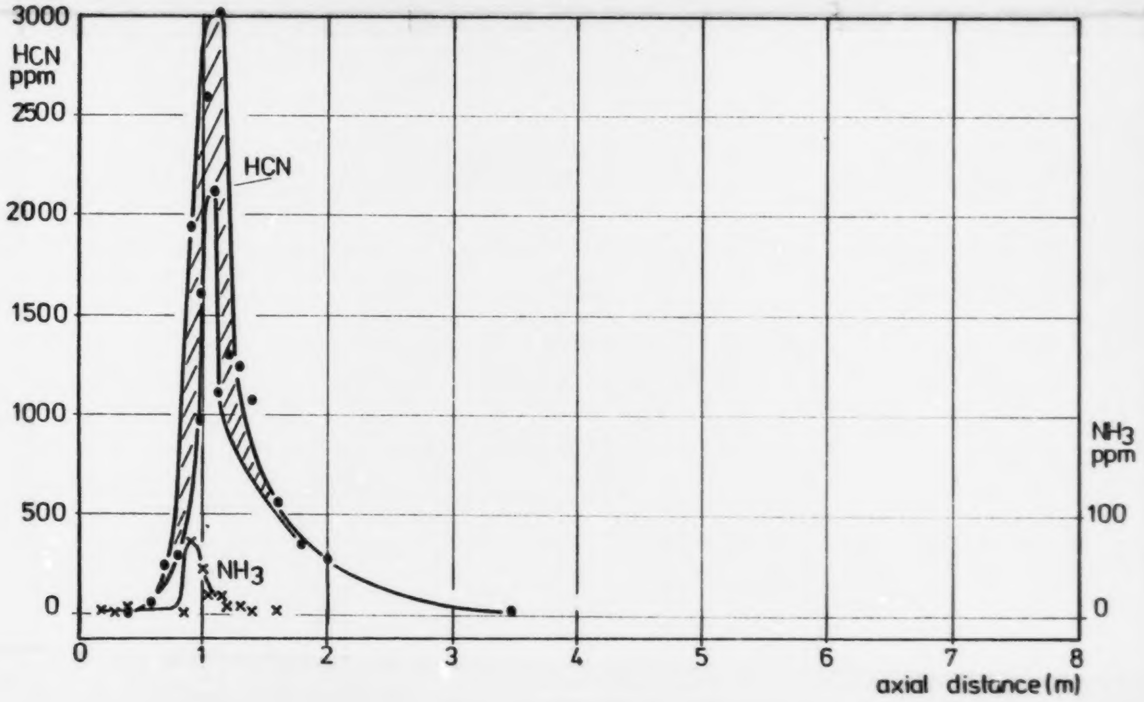

Figure 7-4.1. Axial Ammonia and Hydrogen Cyanide Concentrations, Flame A1.

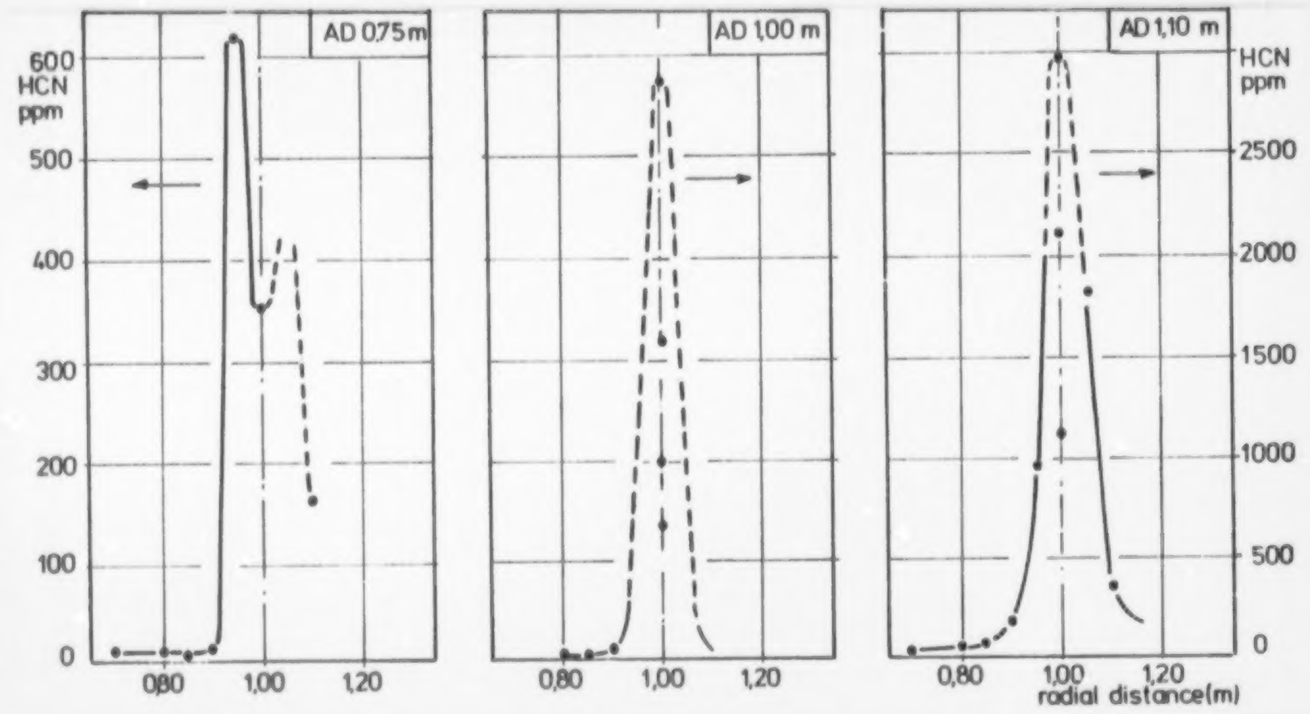

Figure 7-4.2. Radial Hydrogen Cyanide Concentrations, Flame A1.

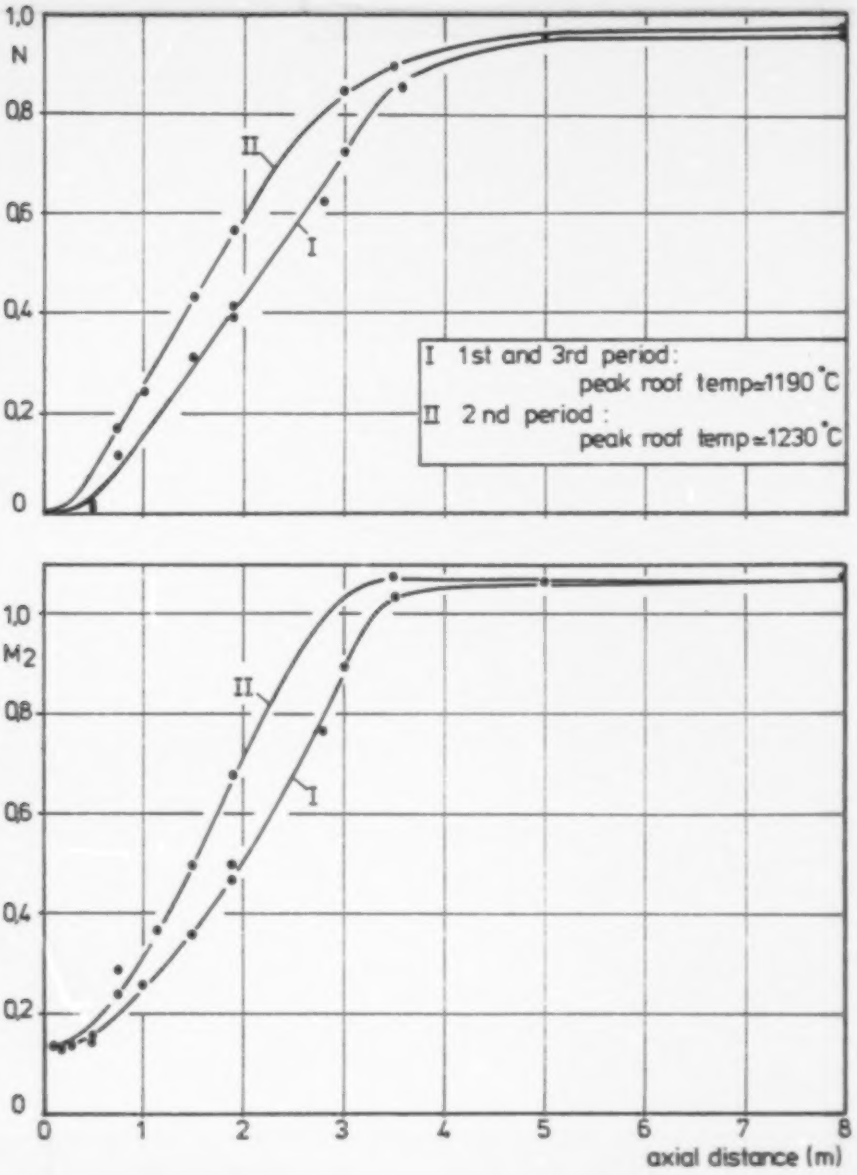

Figure 7-5. Flame A1, Mixing Factor (M_2) and Degree of Oxidation (N).

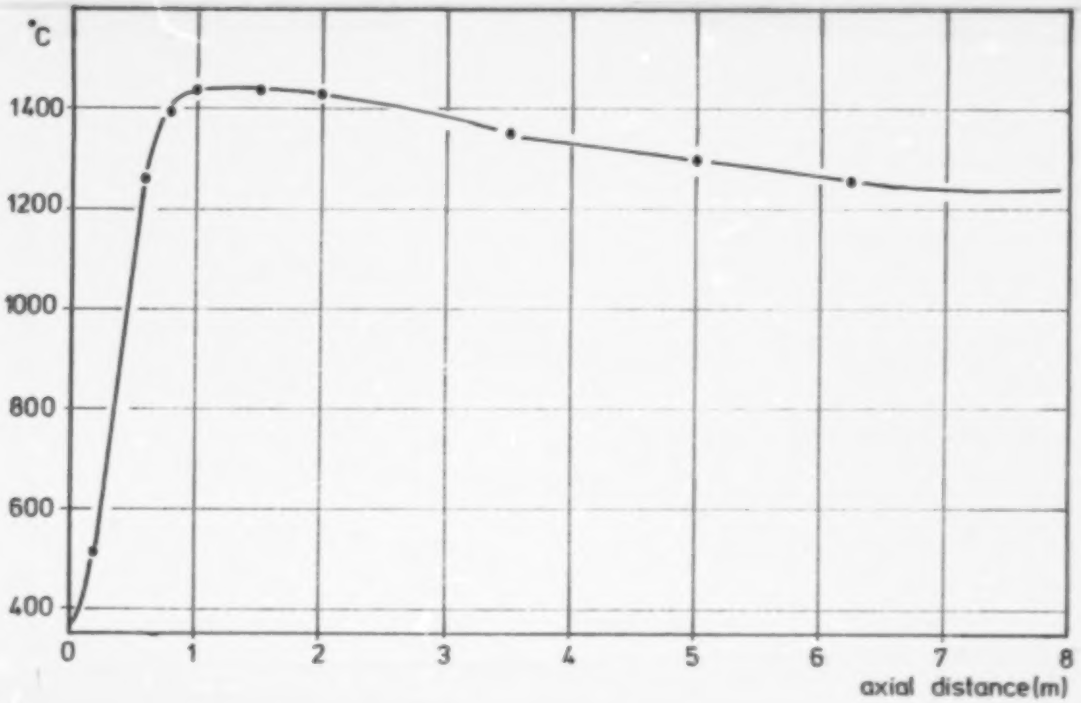

Figure 8-1. Axial Temperatures, Flame A2.

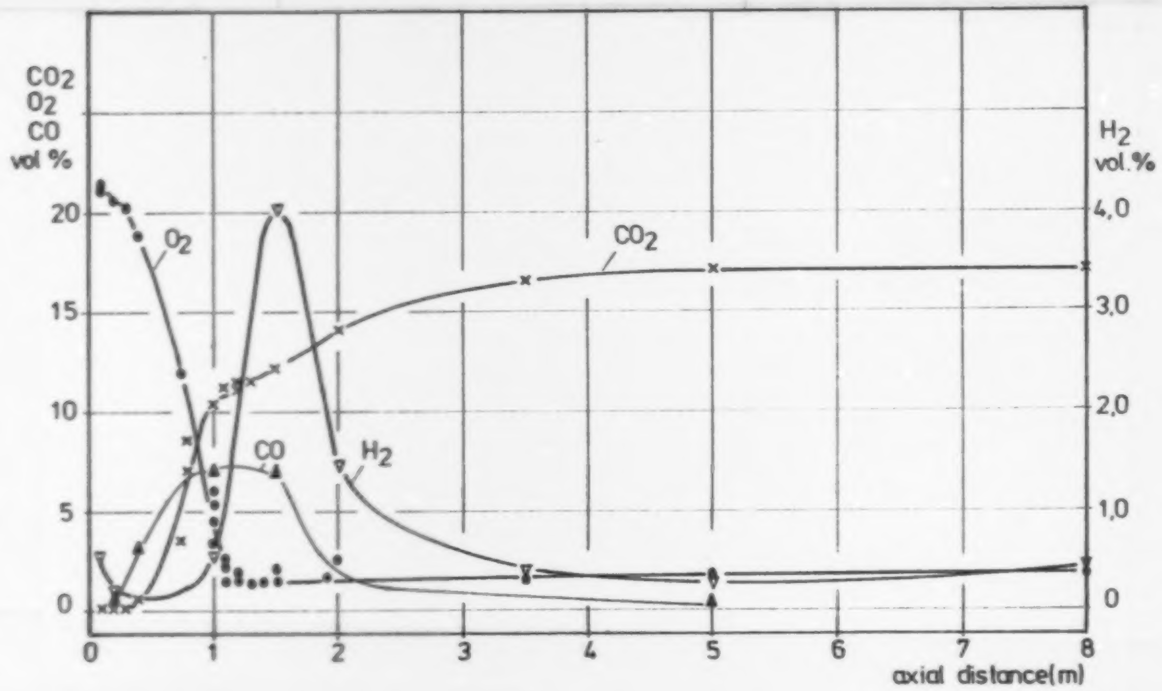

Figure 8-2. Axial Gas Concentrations, Flame A2.

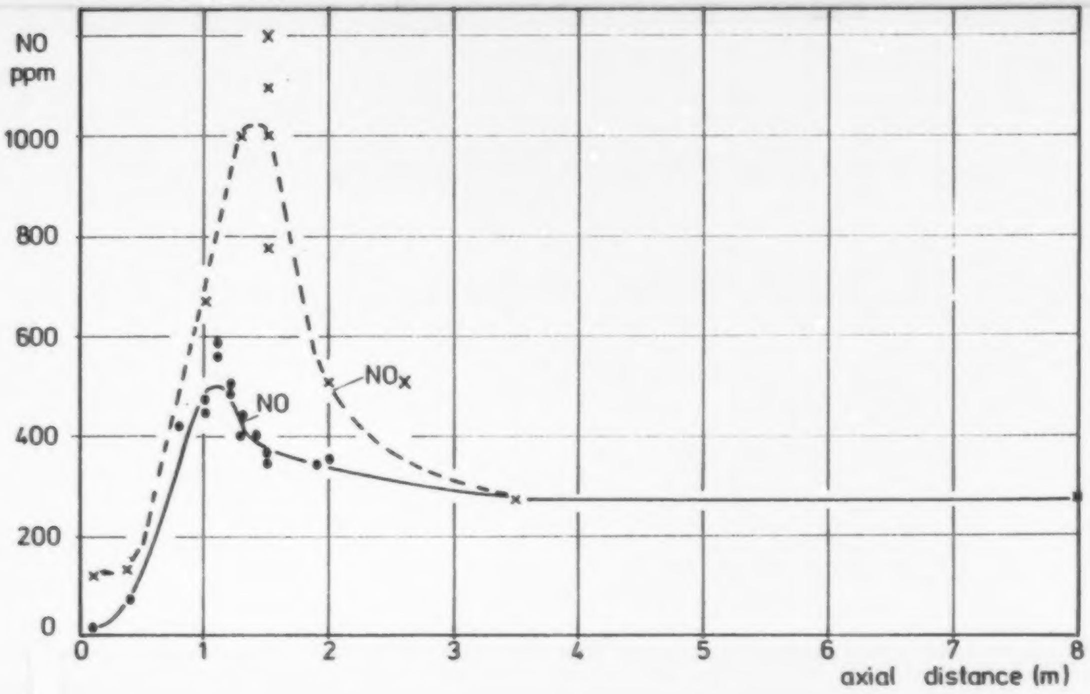

Figure 8-3. Axial Nitrogen Oxide Concentration, Flame A2.

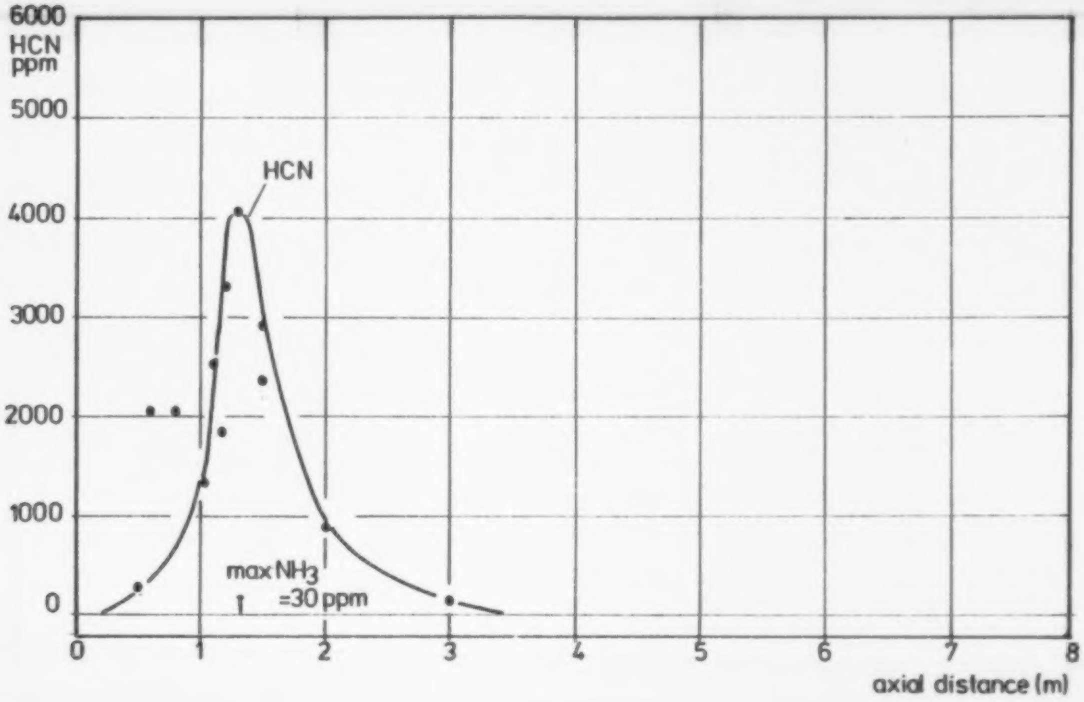

Figure 8-4. Axial Ammonia and Hydrogen Cyanide Concentrations, Flame A2.

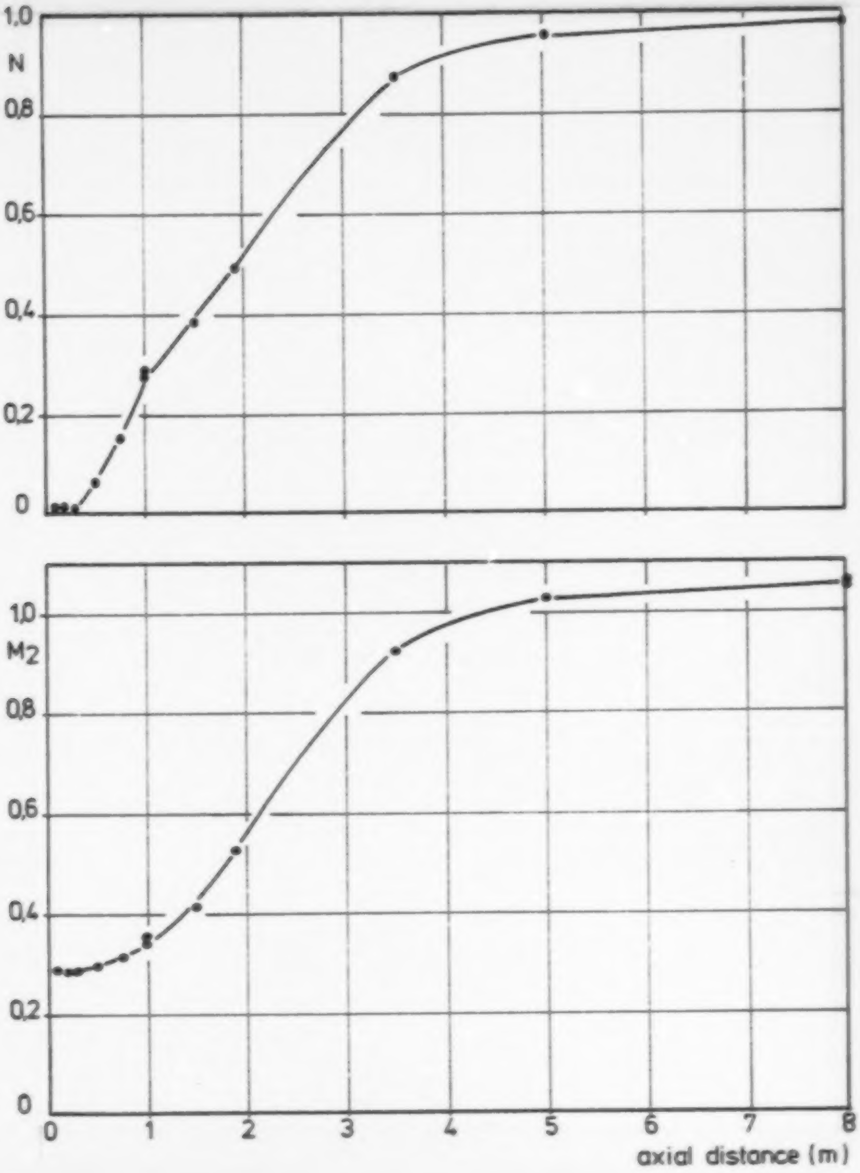

Figure 8-5. Flame A2, Mixing Factor (M_2) and Degree of Oxidation (N).

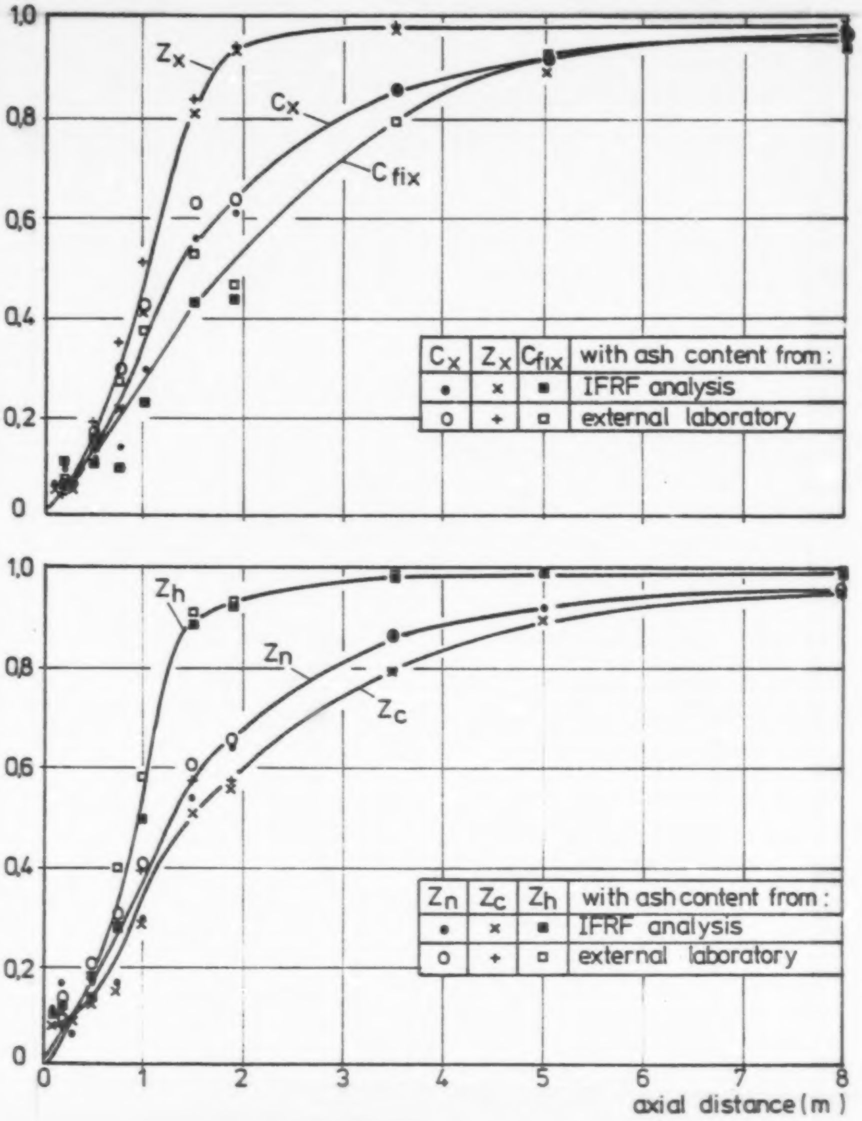

Figure 8-6. Flame A2, Burnout of Solids.

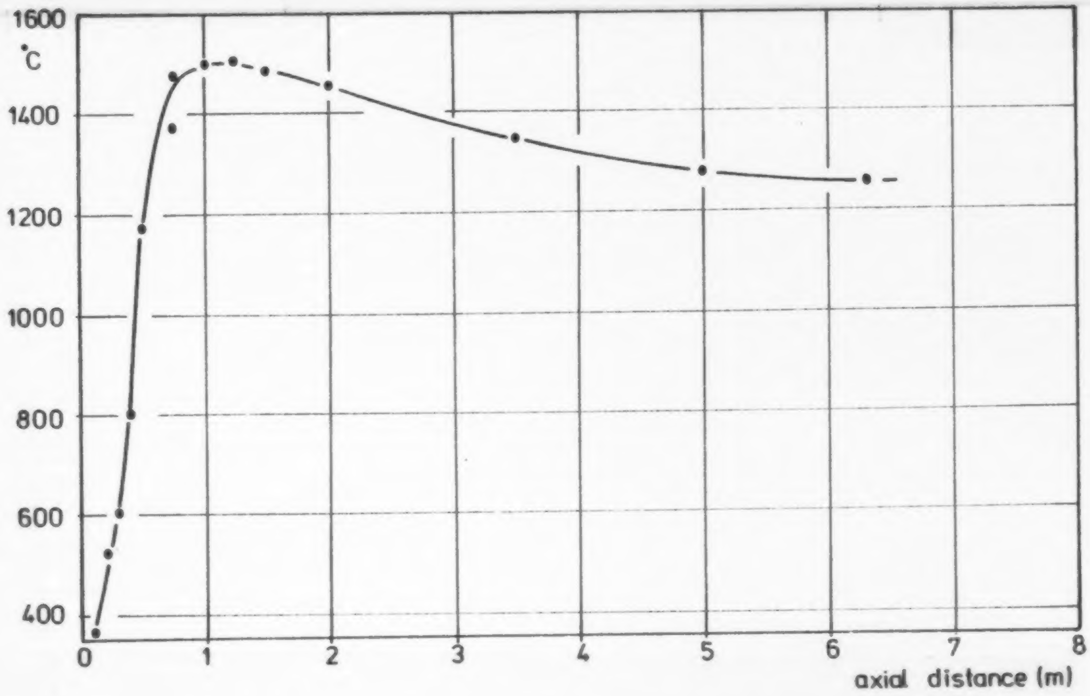

Figure 9-1. Axial Temperatures, Flame A4.

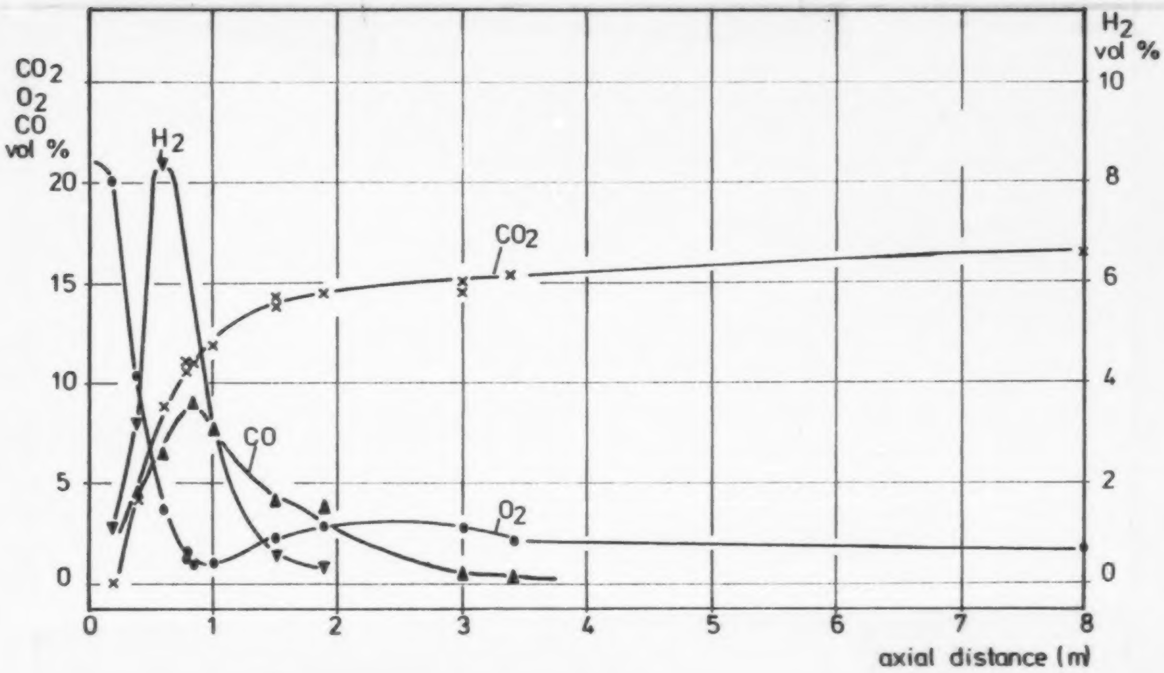

Figure 9-2. Axial Gas Concentrations, Flame A4.

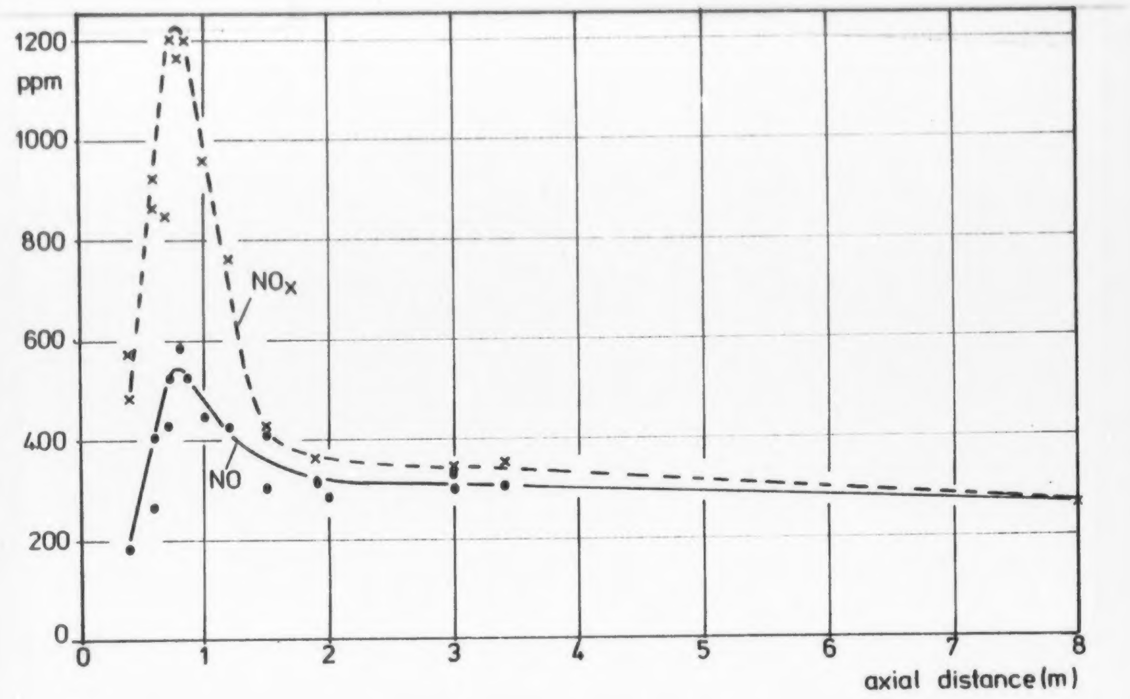

Figure 9-3. Axial Nitrogen Oxide Concentration, Flame A4.

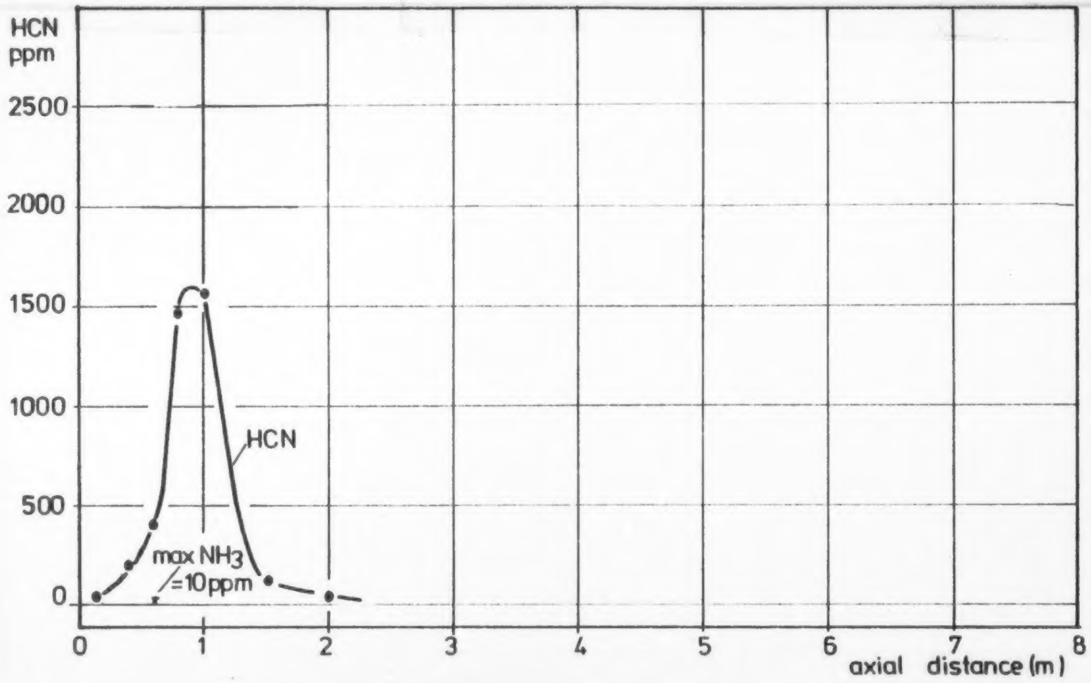

Figure 9-4. Axial Ammonia and Hydrogen Cyanide Concentrations, Flame A4.

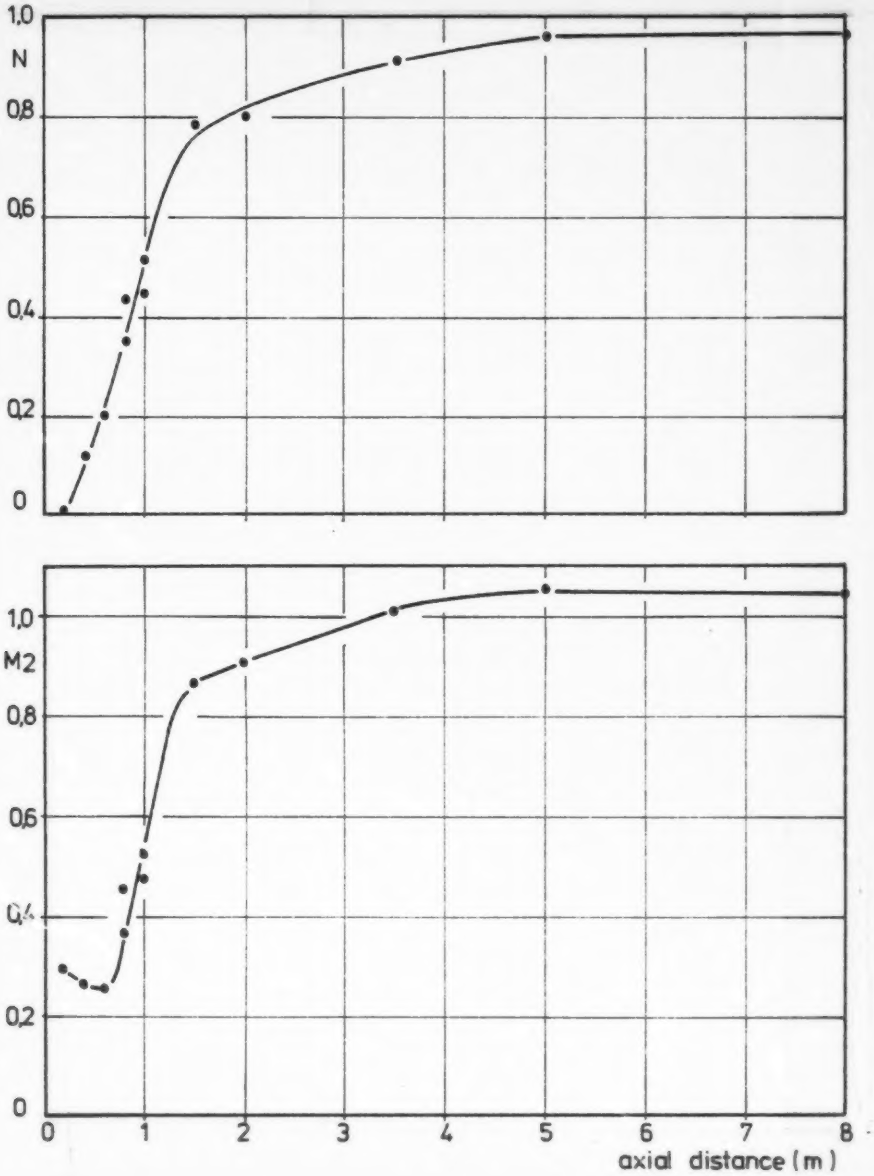

Figure 9-5. Flame A4, Mixing Factor (M_2) and Degree of Oxidation (N).

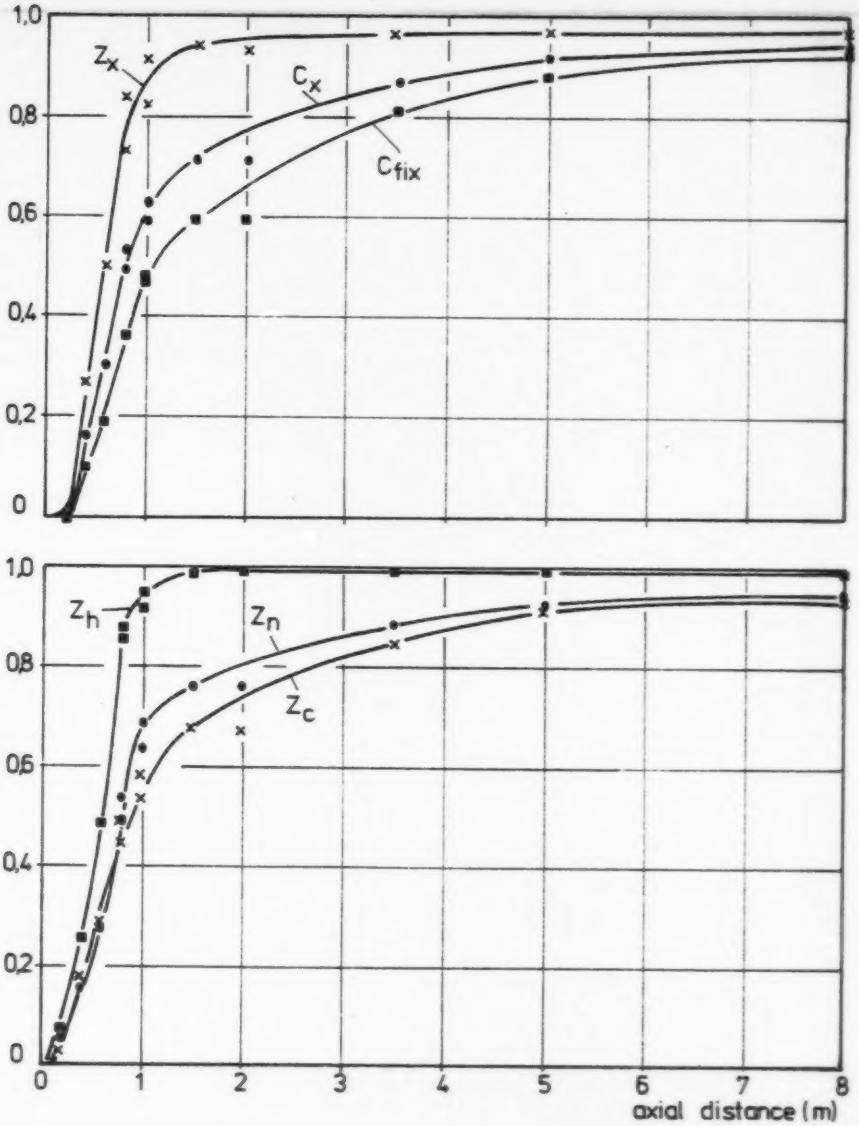

Figure 9-6. Flame A4, Burnout of Solids.

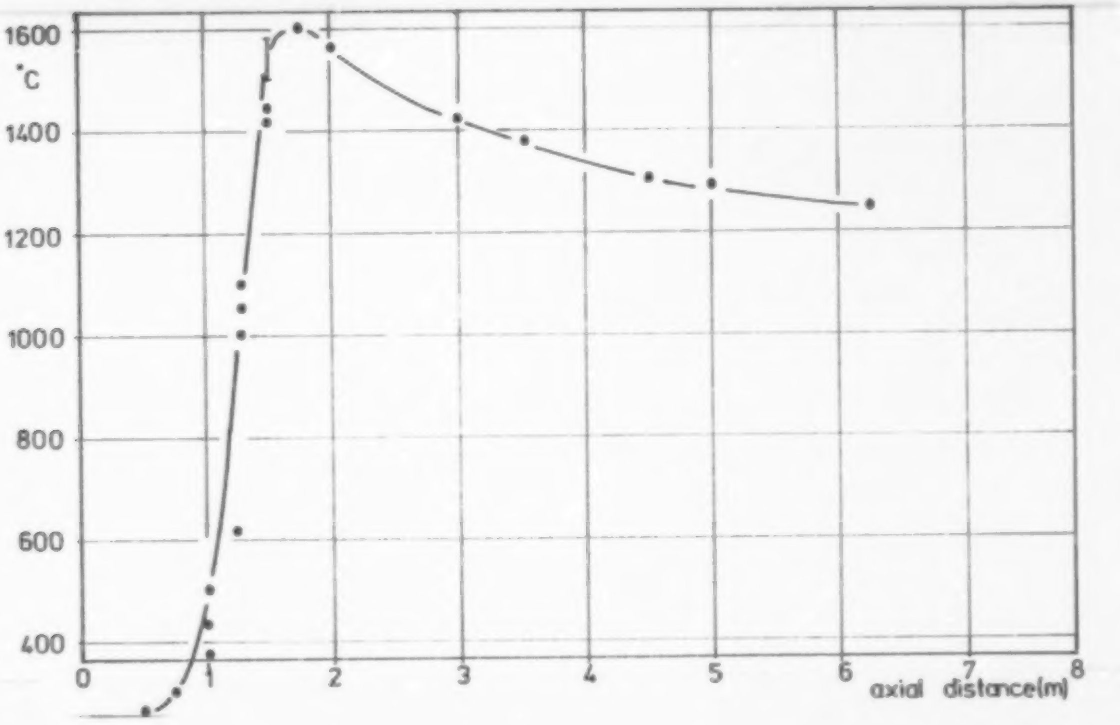

Figure 10-1.1. Axial Temperatures, Flame B1.

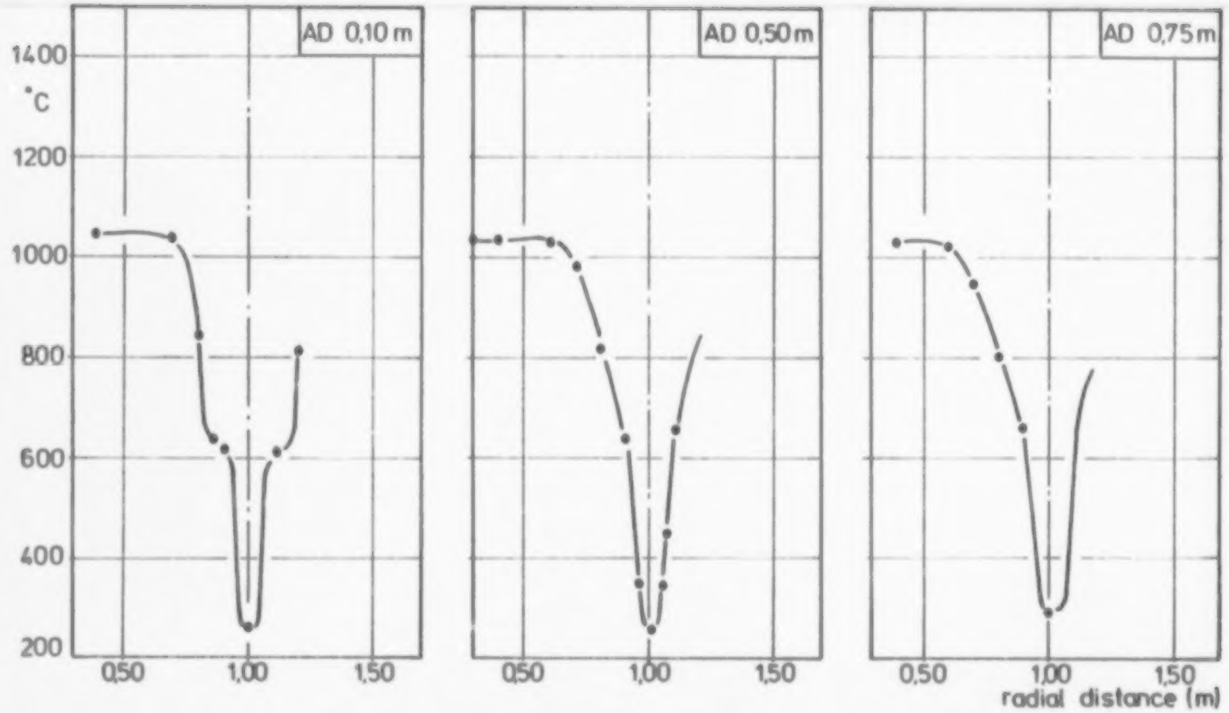

Figure 10-1.2. Radial Temperatures, Flame B1.

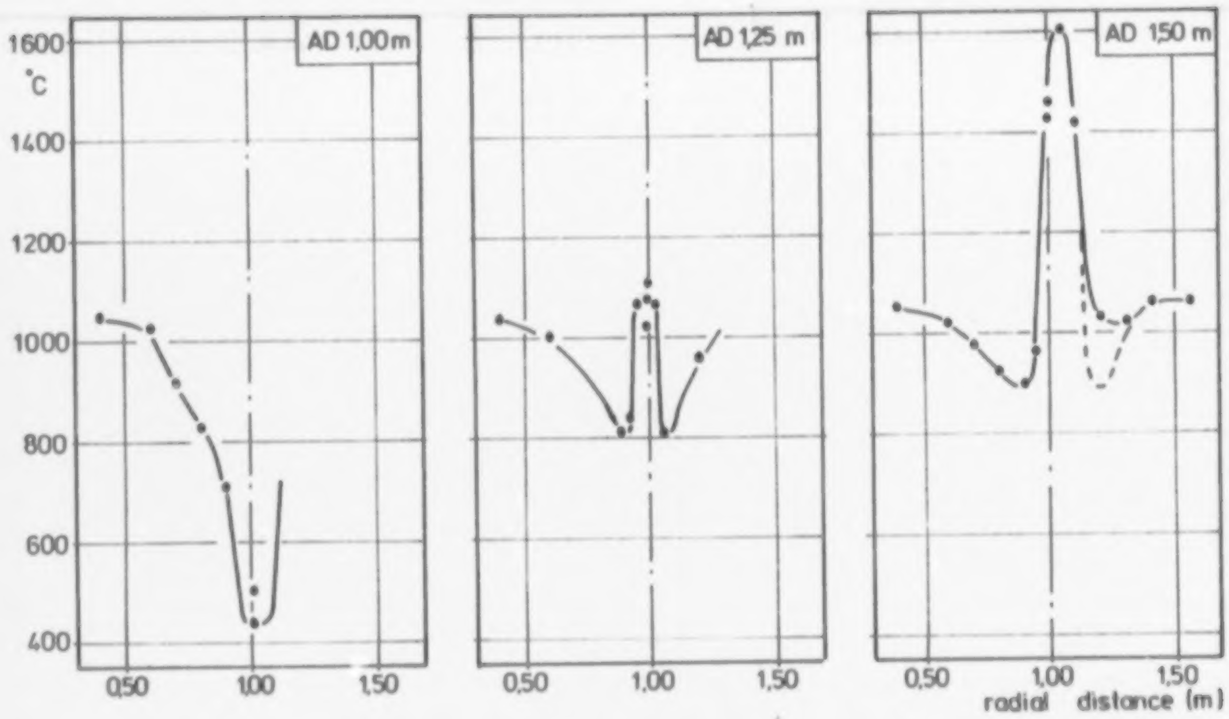

Figure 10-1.3. Radial Temperatures, Flame B1.

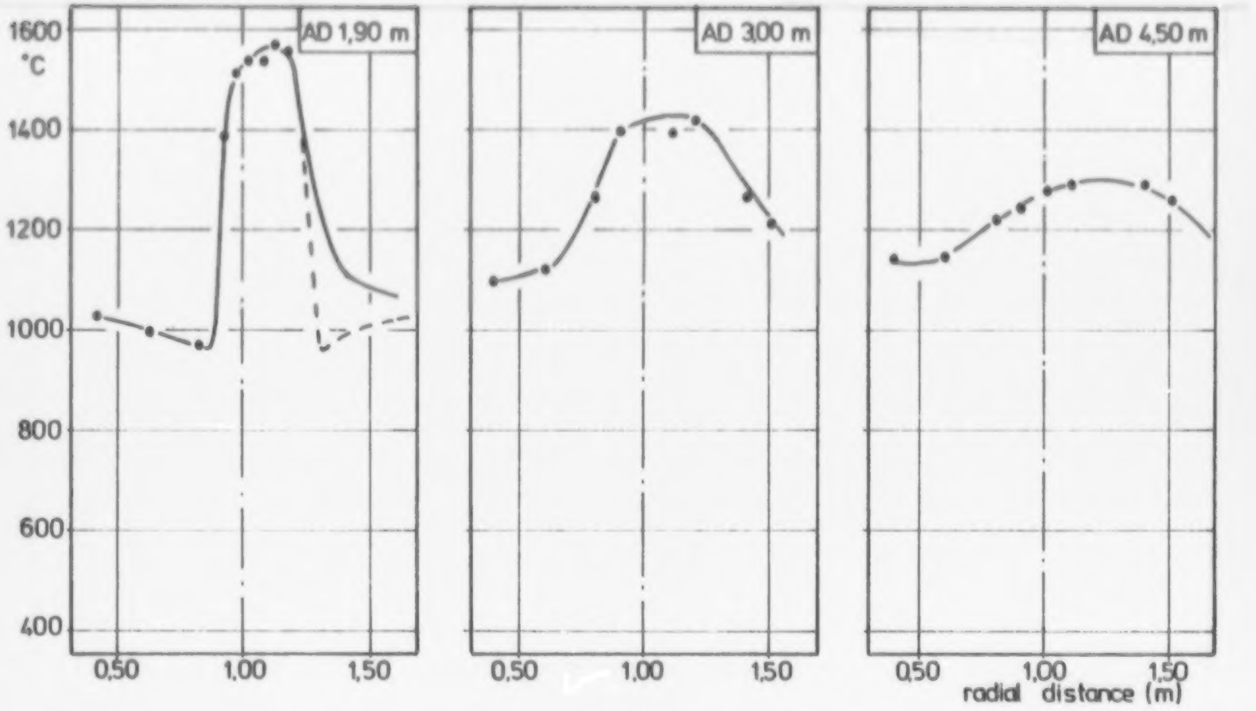

Figure 10-1.4. Radial Temperatures, Flame B1.

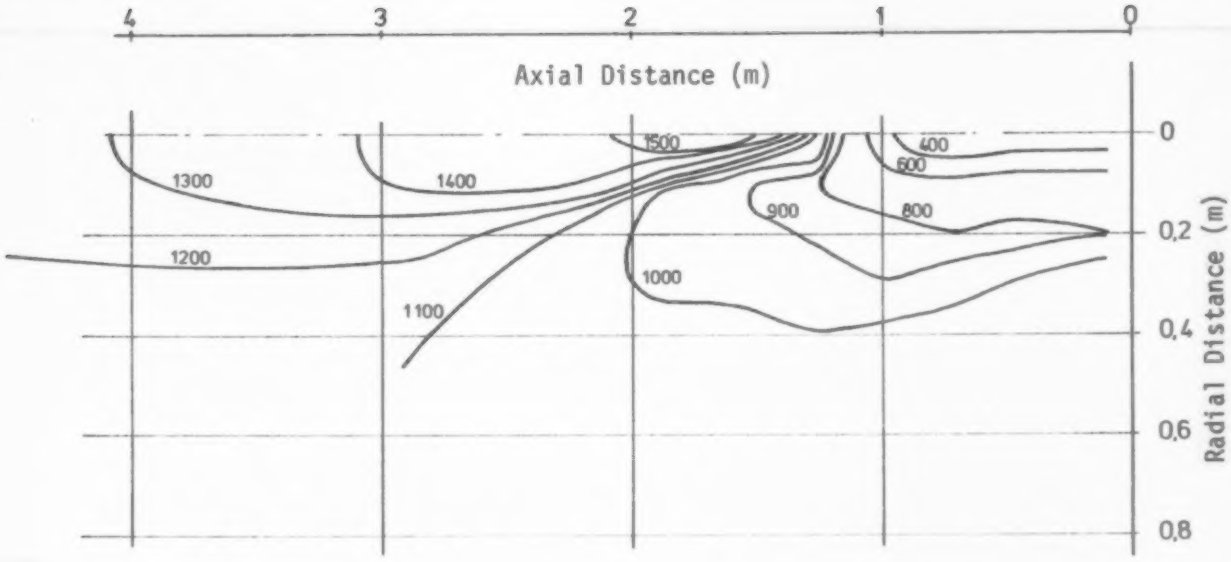

Figure 10-1.5. Isotherms (°C), Flame B1.

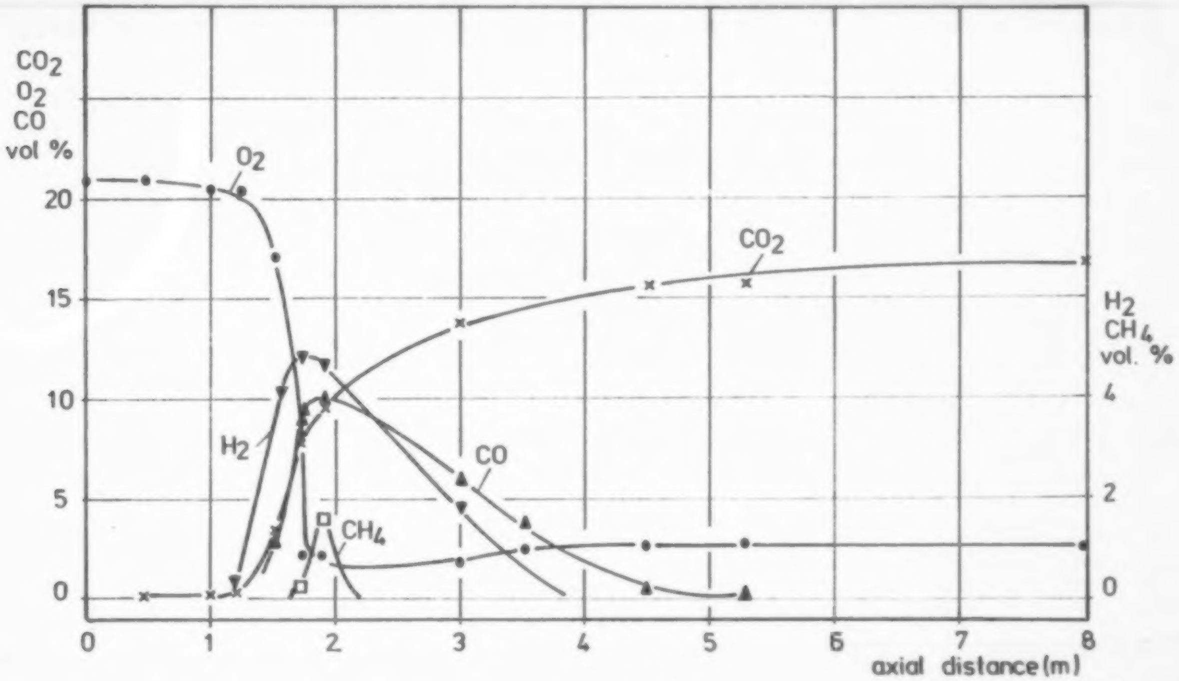

Figure 10-2.1. Axial Gas Concentrations, Flame B1.

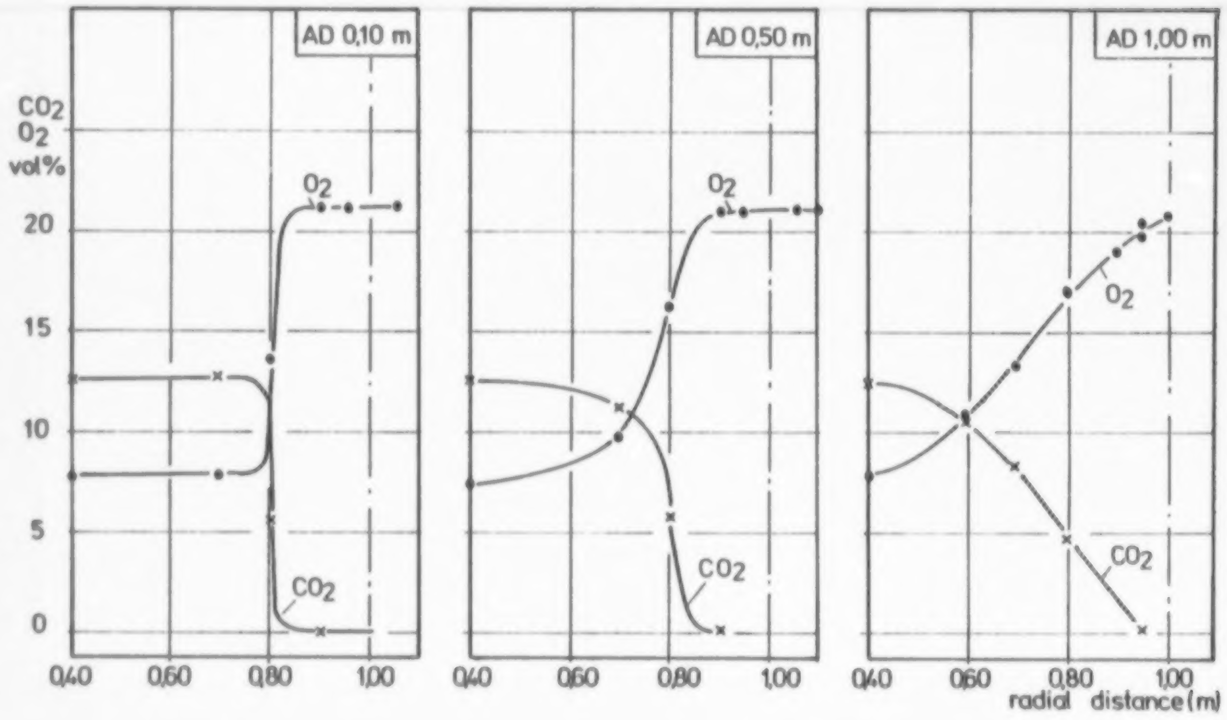

Figure 10-2.2. Radial Gas Concentrations, Flame B1.

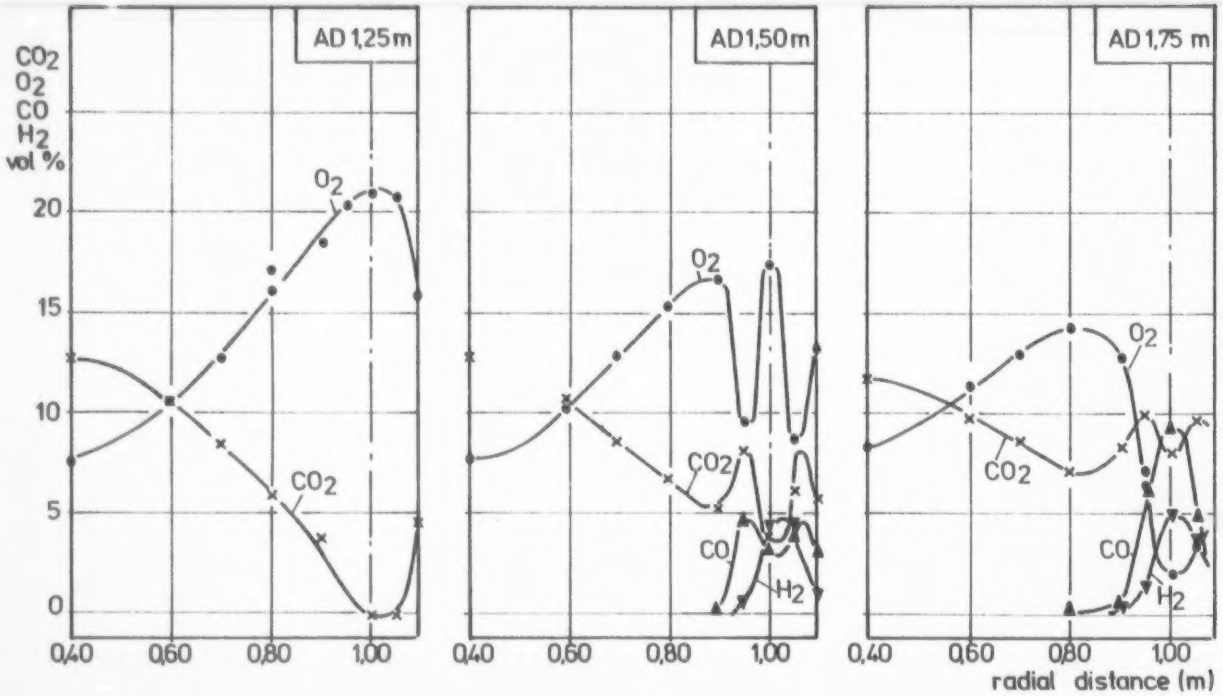

Figure 10-2.3. Radial Gas Concentrations, Flame B1.

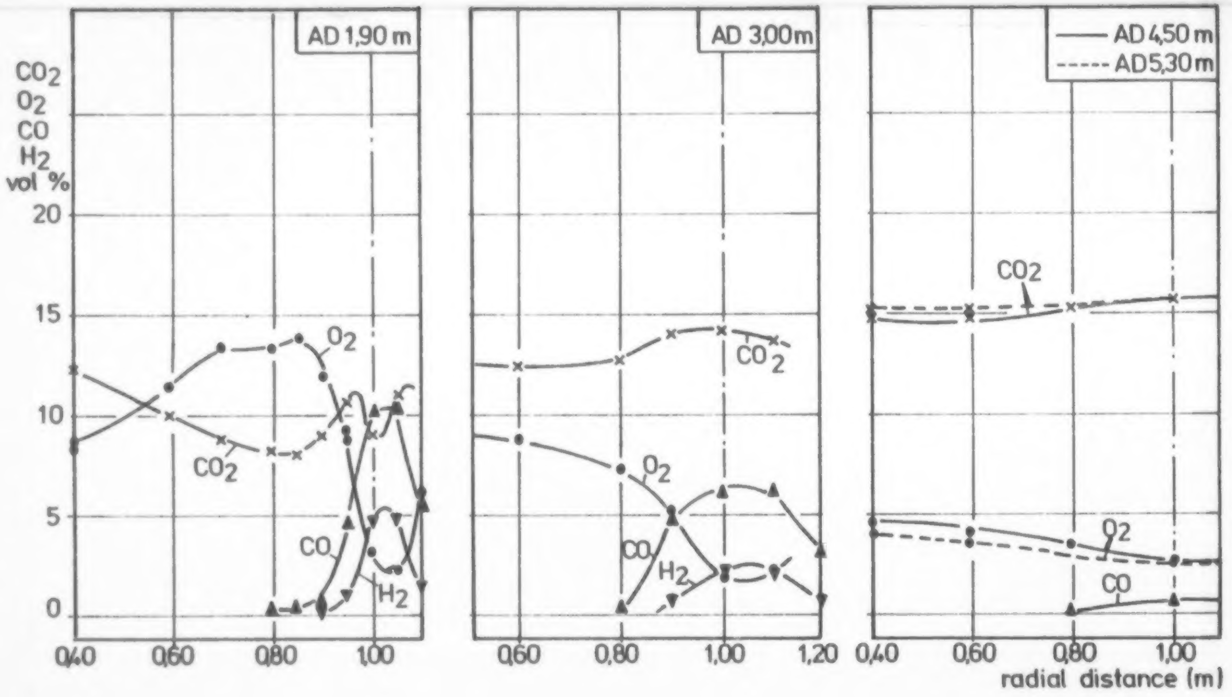

Figure 10-2.4. Radial Gas Concentrations, Flame B1.

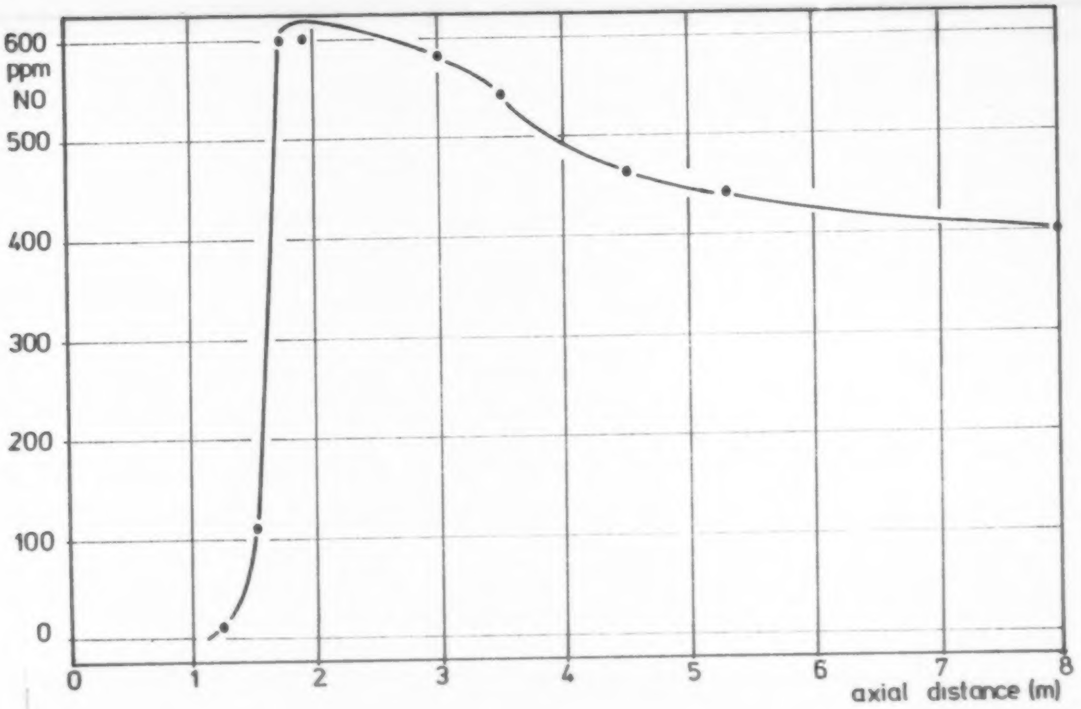

Figure 10-3.1. Axial Nitrogen Oxide Concentration, Flame B1.

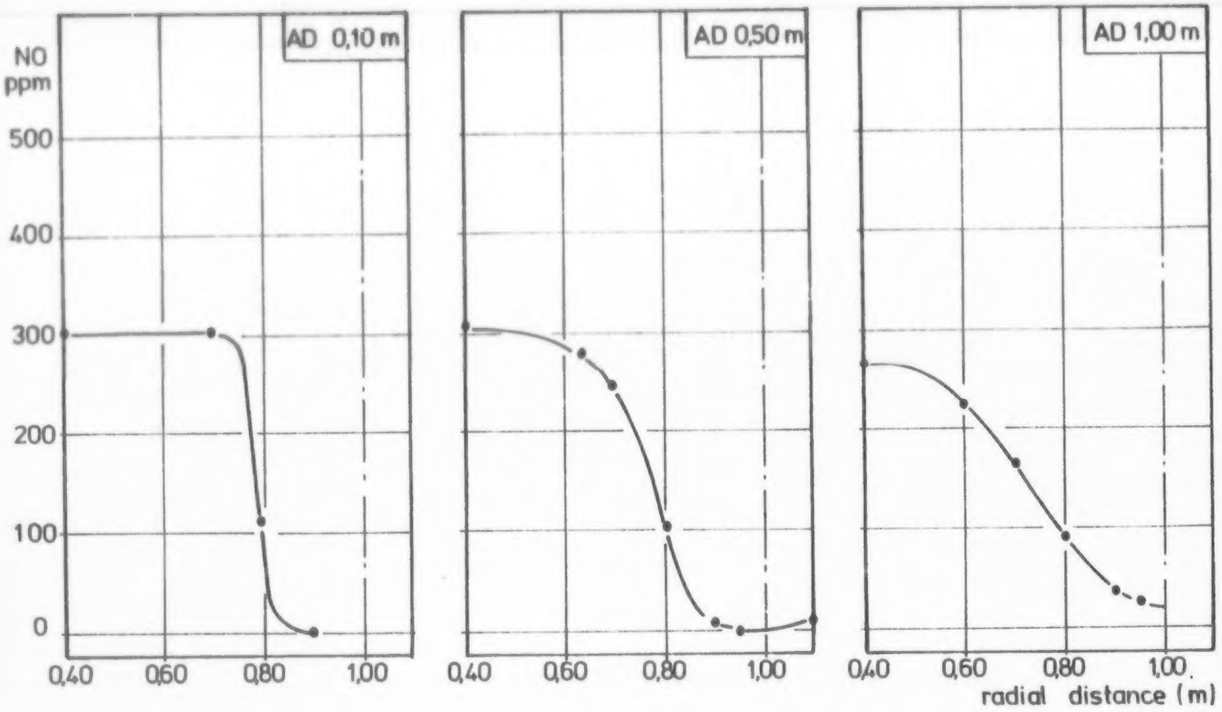

Figure 10-3.2. Radial Nitrogen Oxide Concentration, Flame B1.

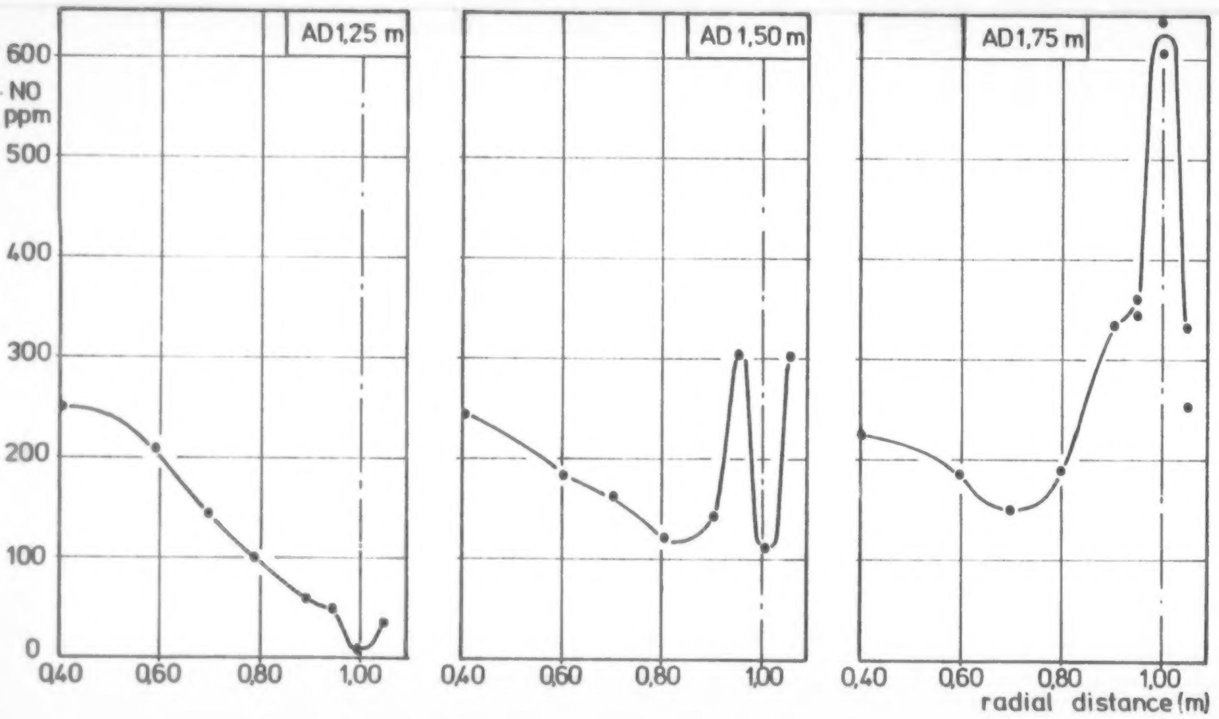

Figure 10-3.3. Radial Nitrogen Oxide Concentration, Flame B1.

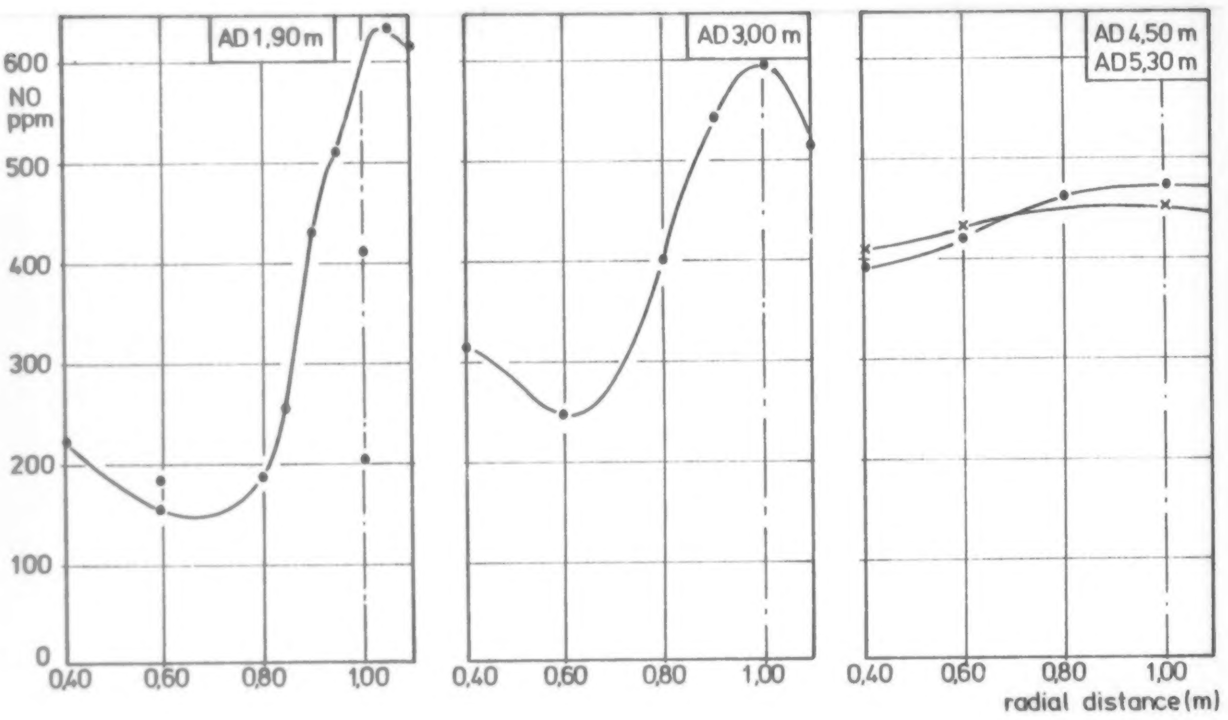

Figure 10-3.4. Radial Nitrogen Oxide Concentration, Flame B1.

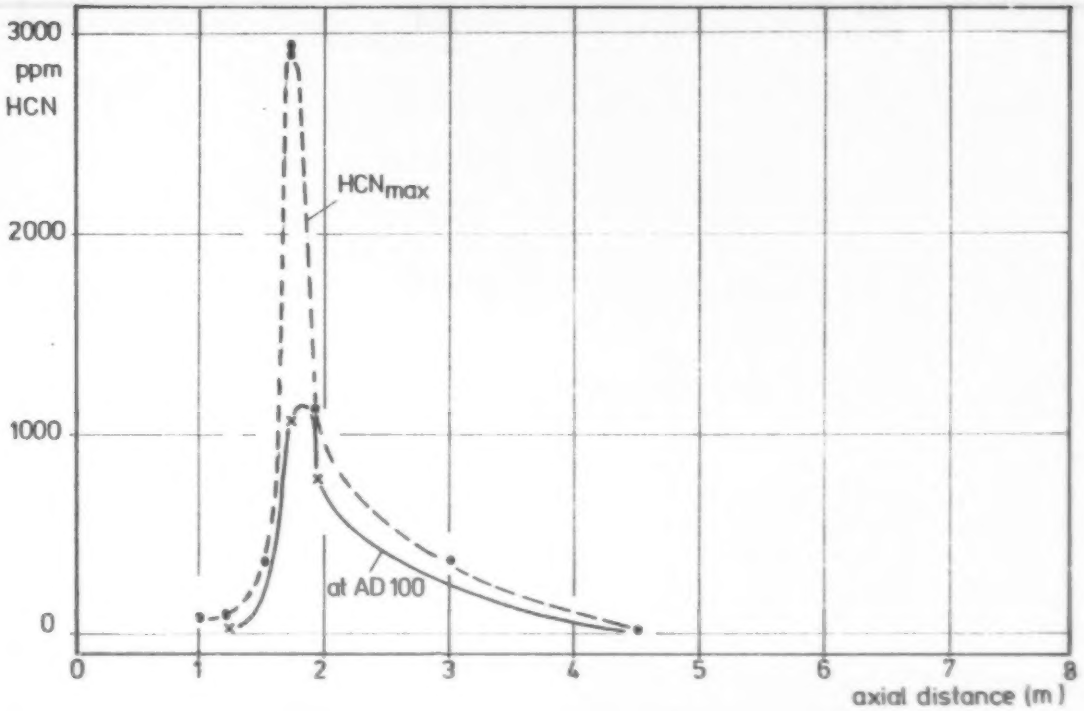

Figure 10-4.1. Axial Ammonia and Hydrogen Cyanide Concentrations, Flame B1.

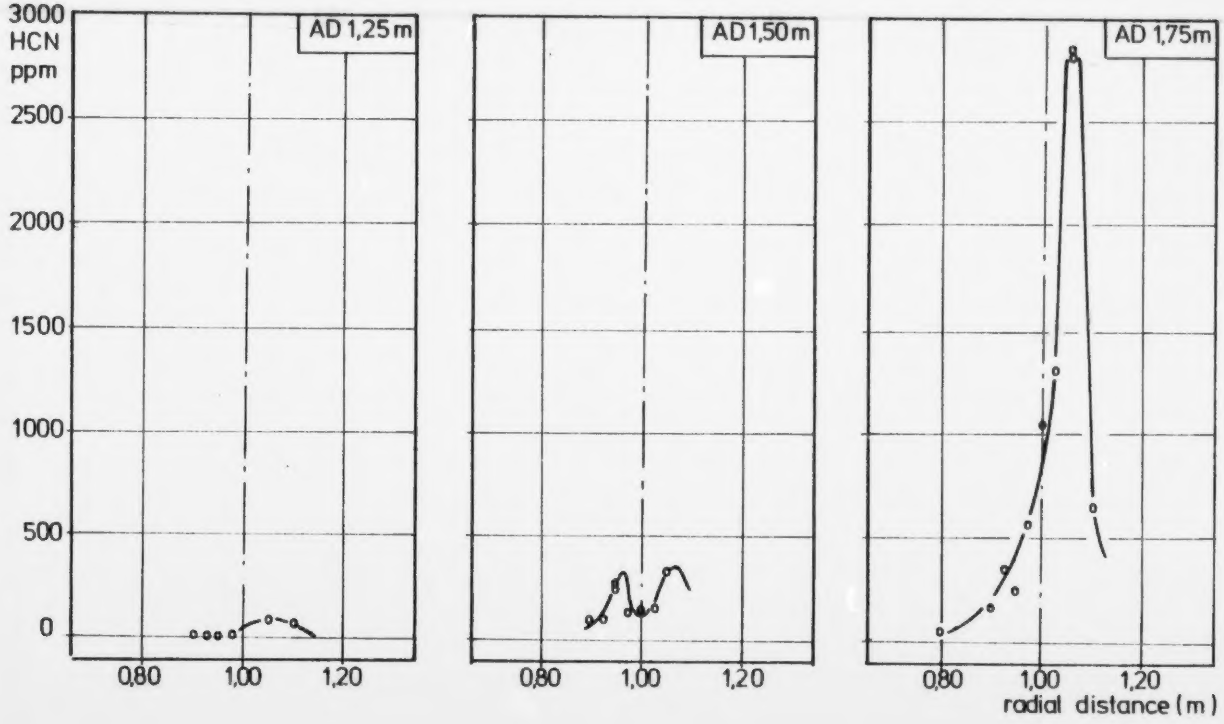

Figure 10-4.2. Radial Hydrogen Cyanide Concentrations, Flame B1.

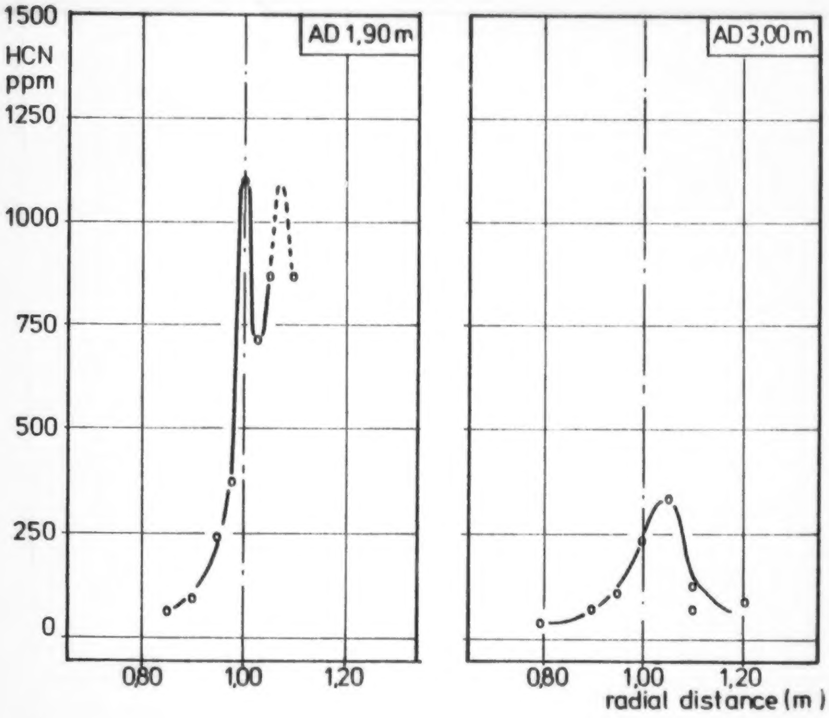

Figure 10-4.3. Radial Hydrogen Cyanide Concentrations, Flame B1.

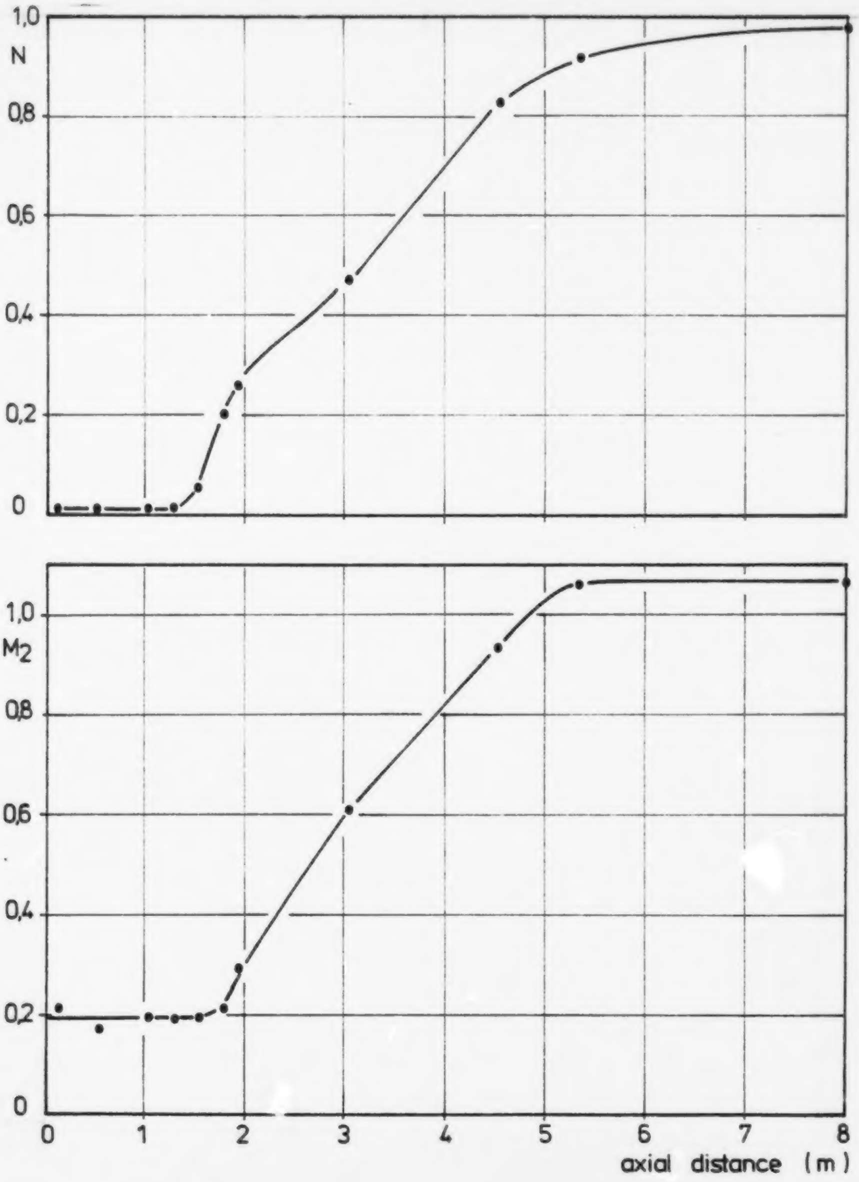

Figure 10-5. Flame B1, Mixing Factor (M_2) and Degree of Oxidation (N).

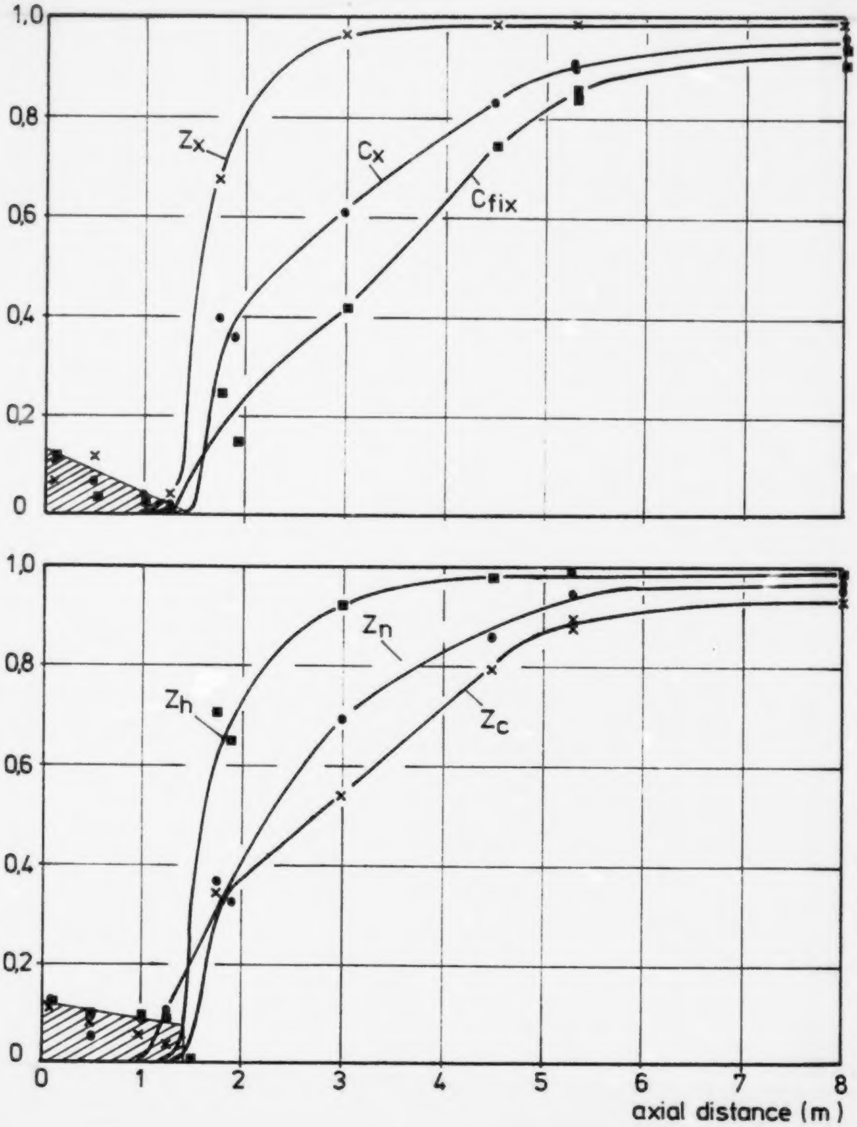

Figure 10-6. Flame B1, Burnout of Solids.

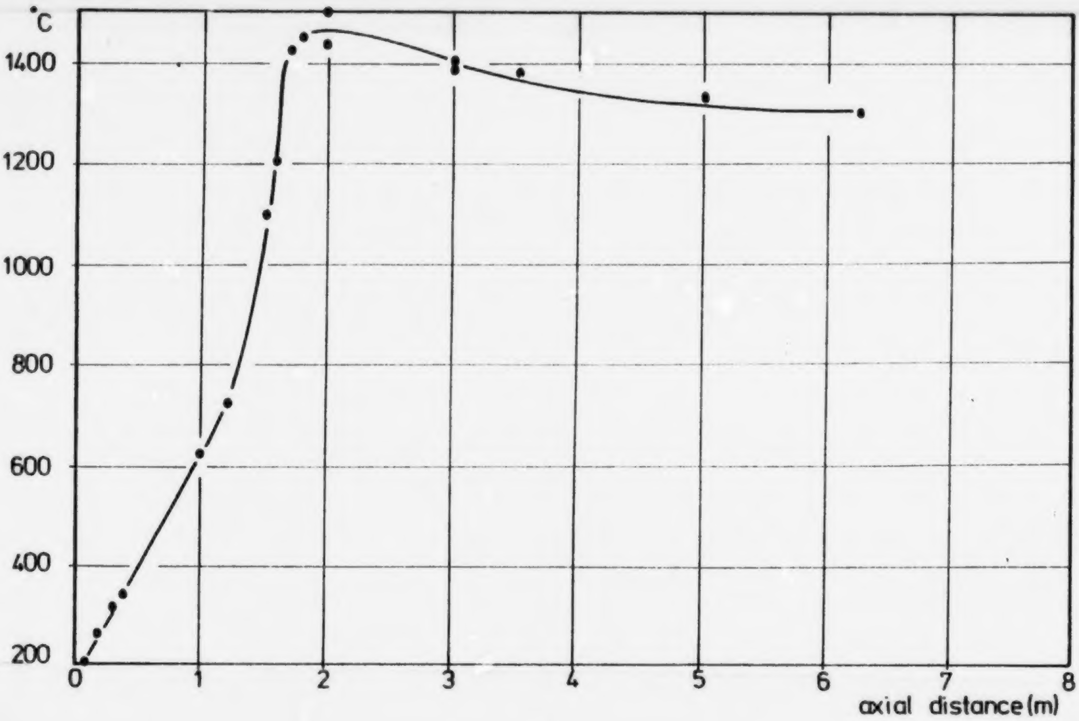

Figure 11-1. Axial Temperatures, Flame B2.

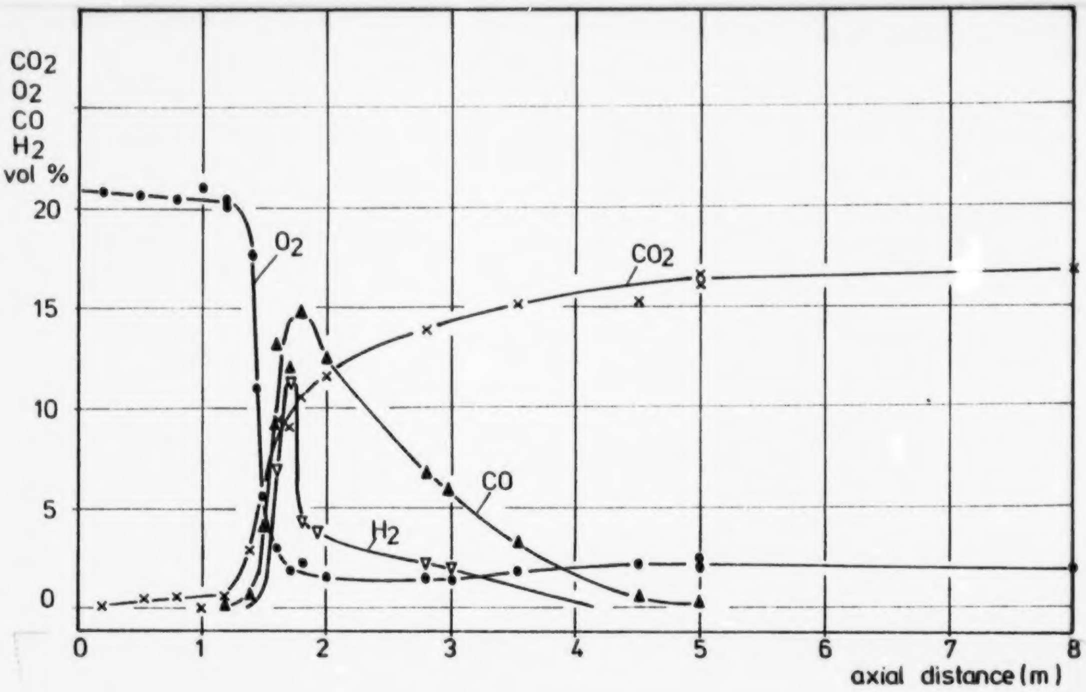

Figure 11-2. Axial Gas Concentrations, Flame B2.

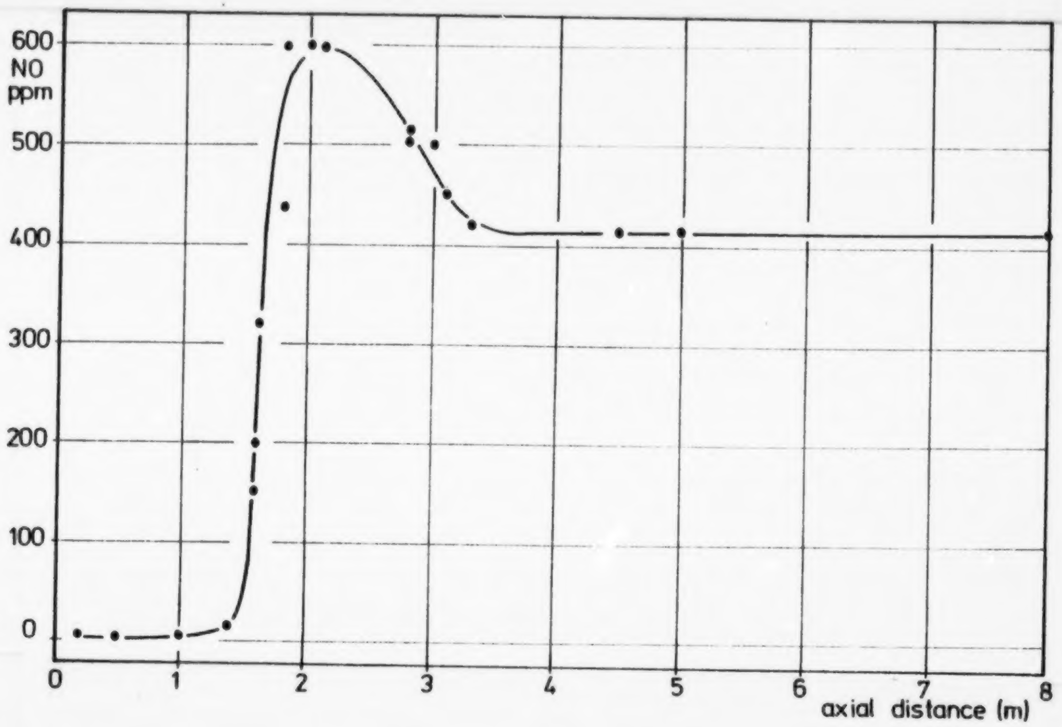

Figure 11-3. Axial Nitrogen Oxide Concentrations (Flame B2).

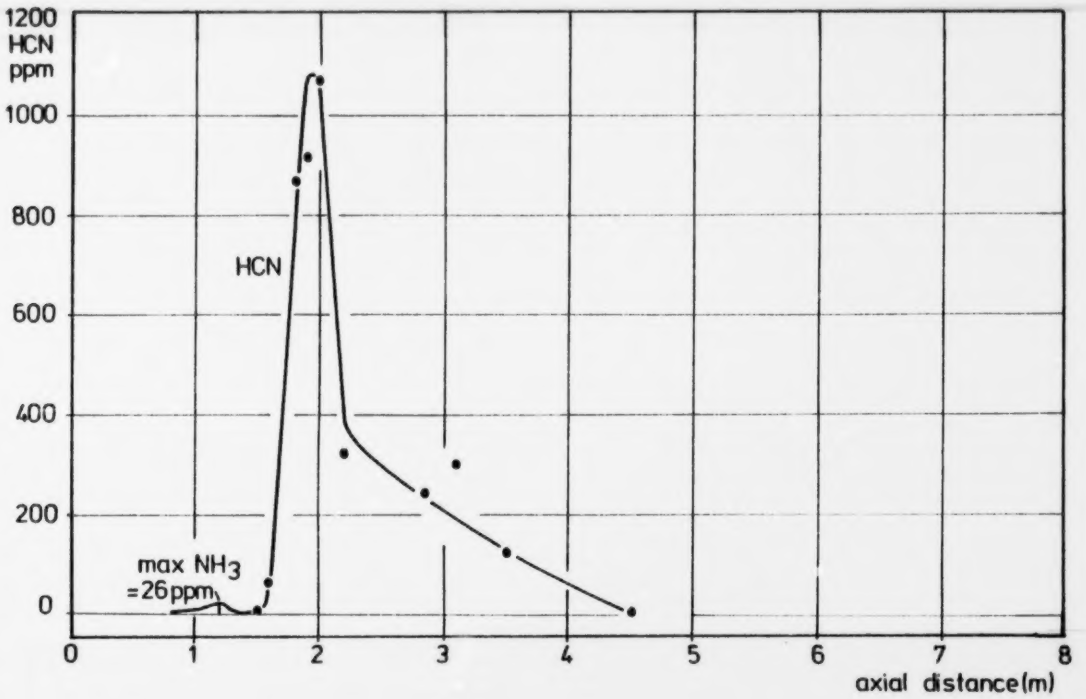

Figure 11-4. Axial Ammonia and Hydrogen Cyanide Concentrations, Flame B2.

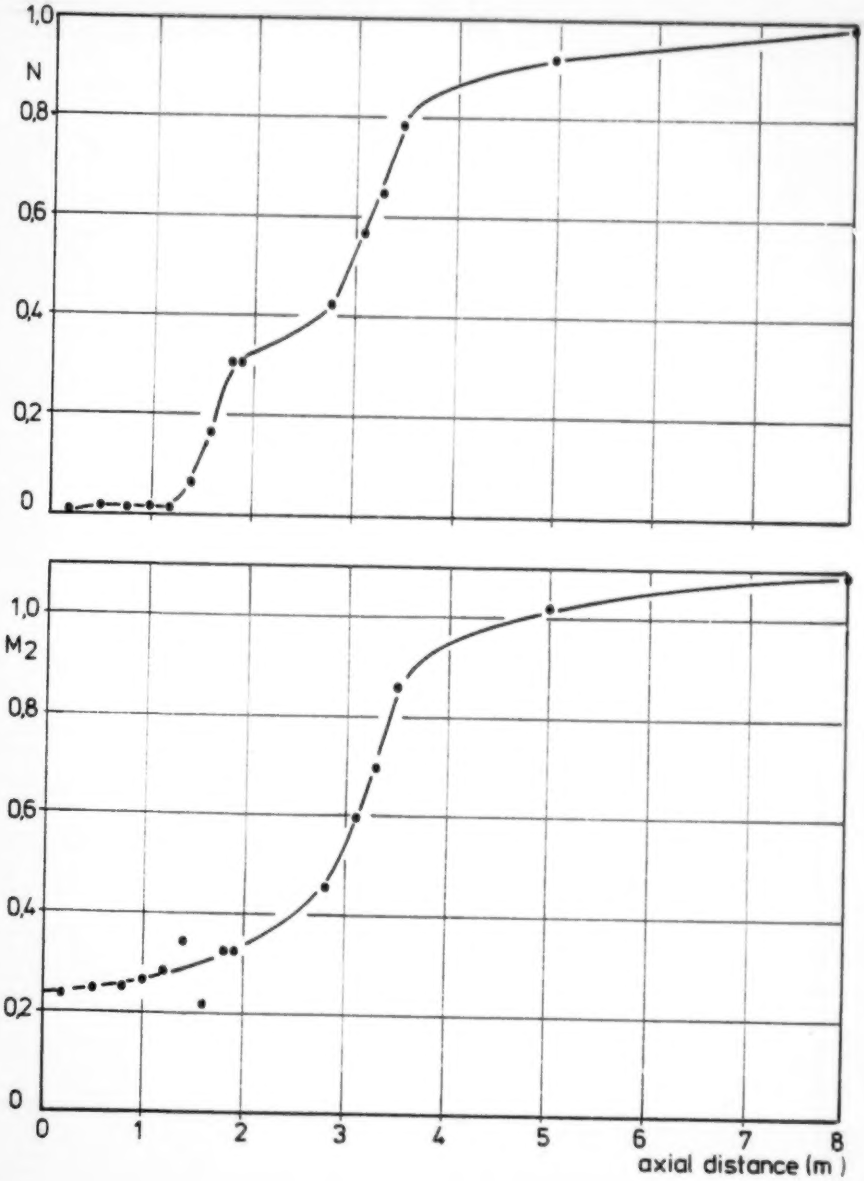

Figure 11-5. Flame B2, Mixing Factor (M_2) and Degree of Oxidation (N).

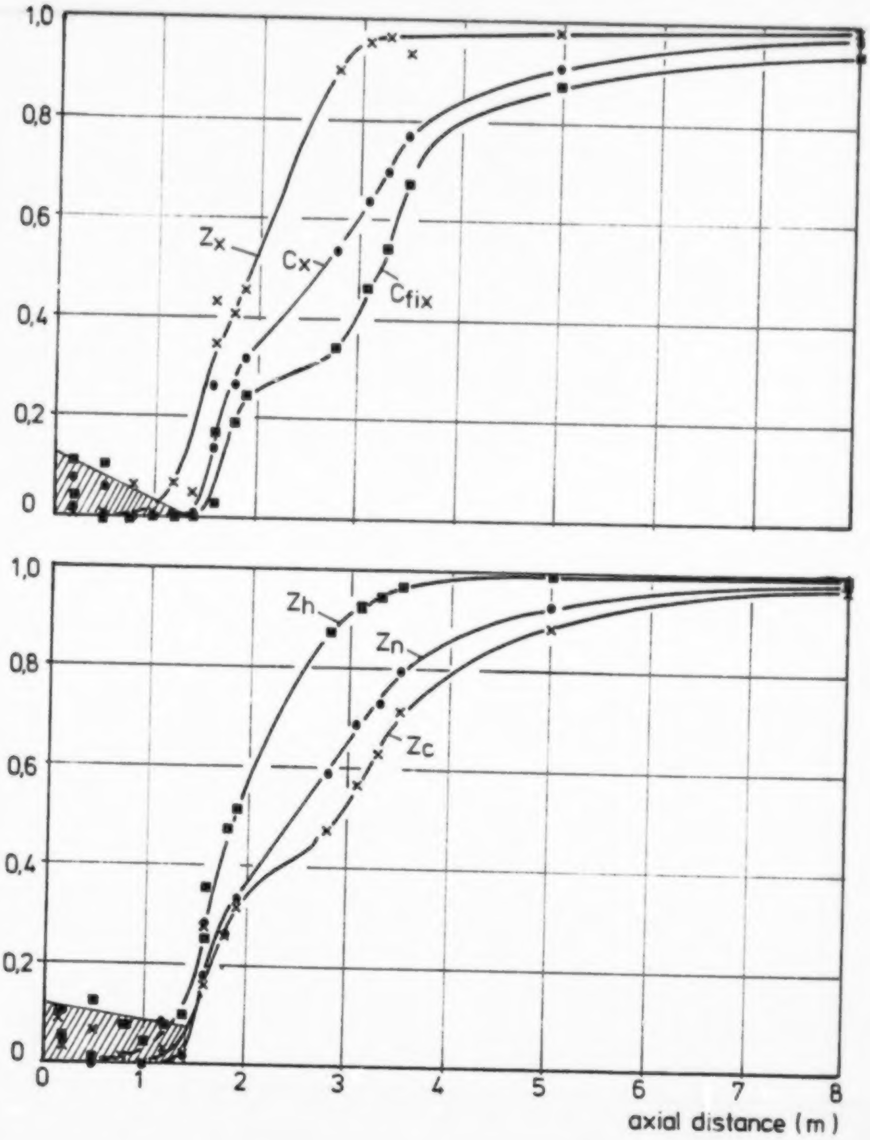

Figure 11-6. Flame B2, Burnout of Solids.

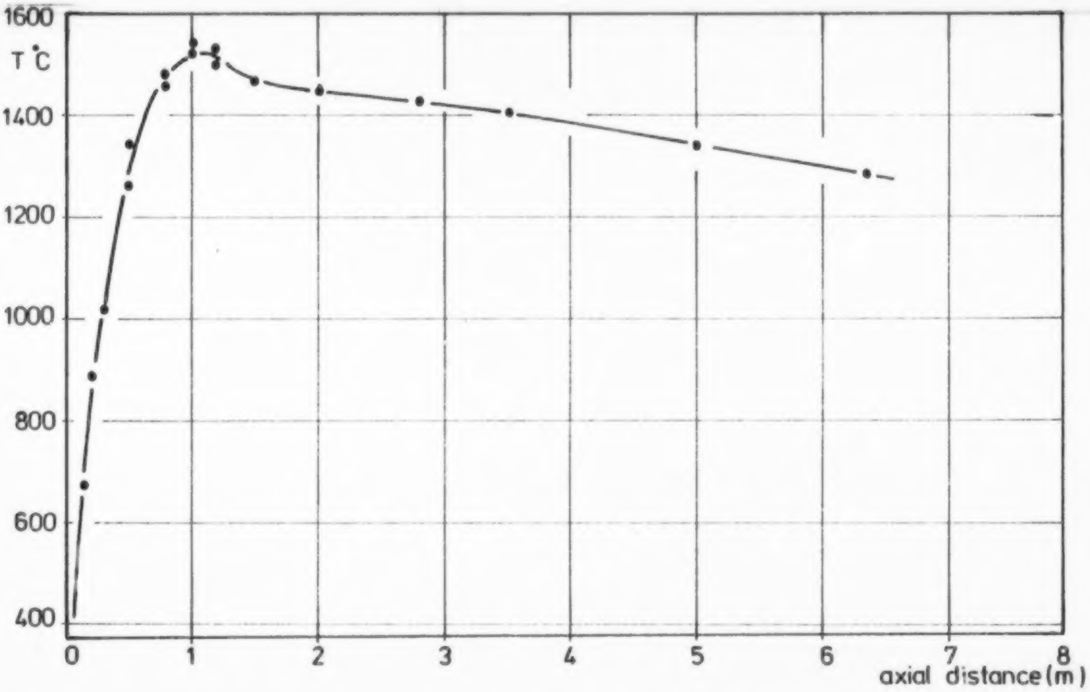

Figure 12-1. Axial Temperatures (Flame B3).

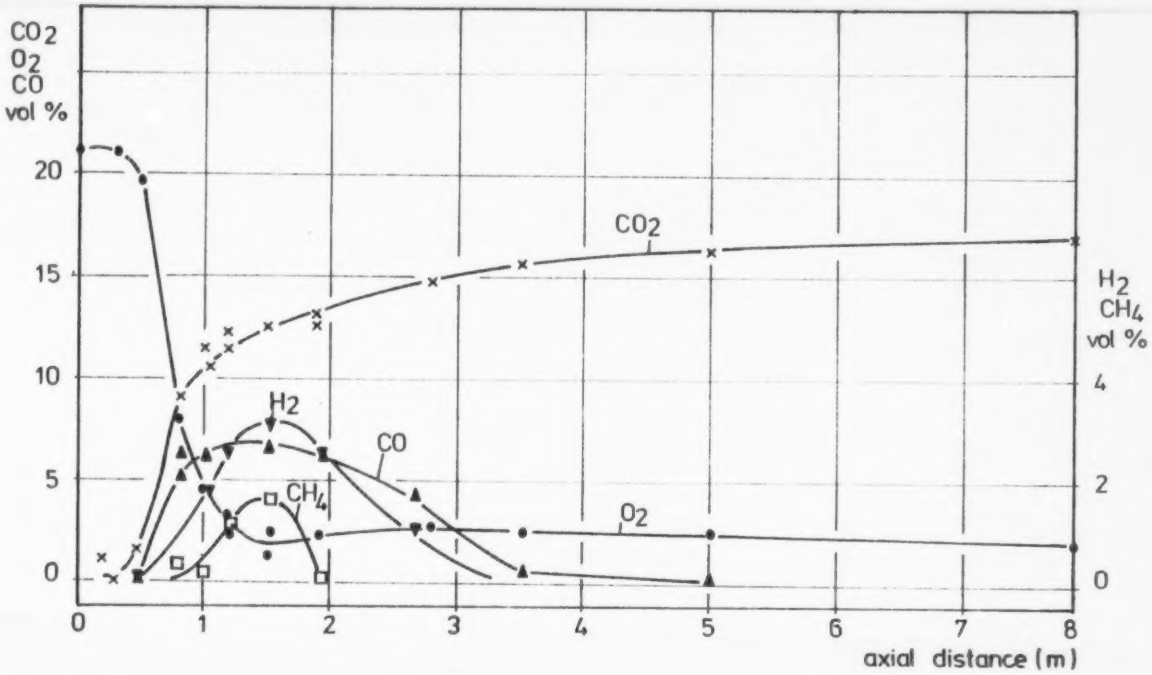

Figure 12-2. Axial Gas Concentrations (Flame B3).

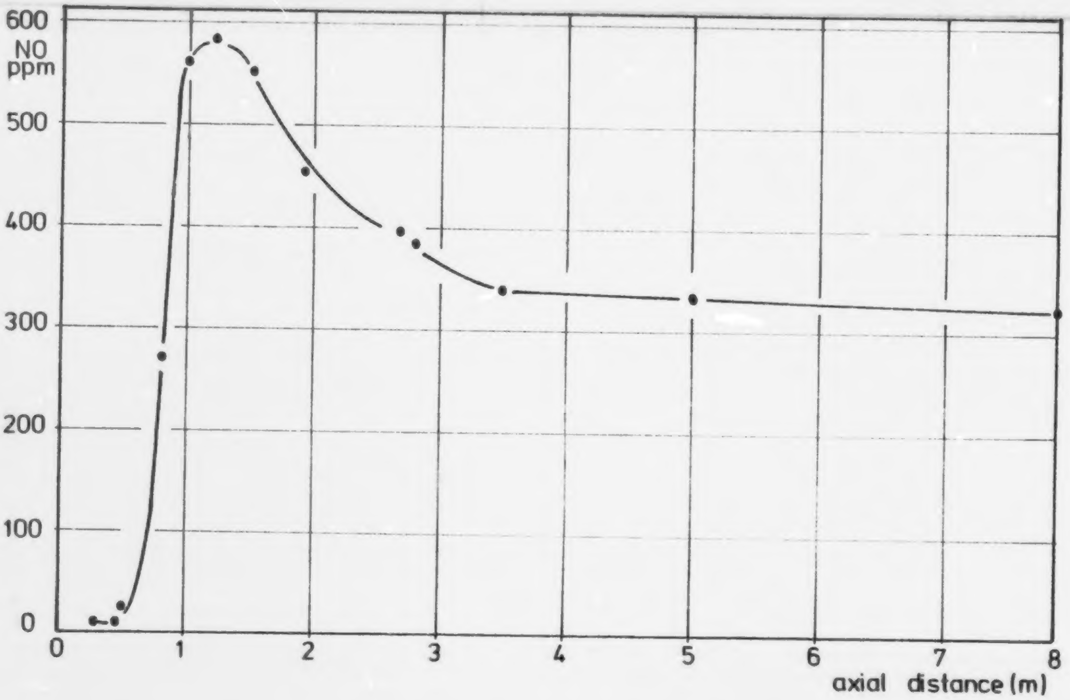

Figure 12-3. Axial Nitrogen Oxide Concentration (Flame B3).

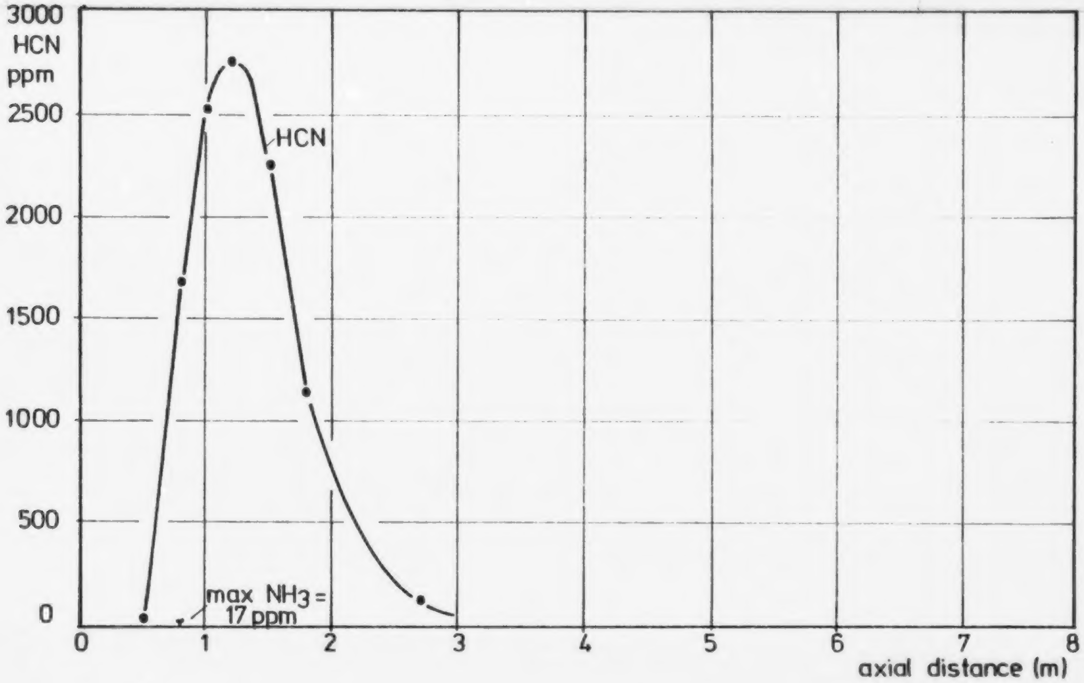

Figure 12-4. Axial Ammonia and Hydrogen Cyanide Concentrations, (Flame B3).

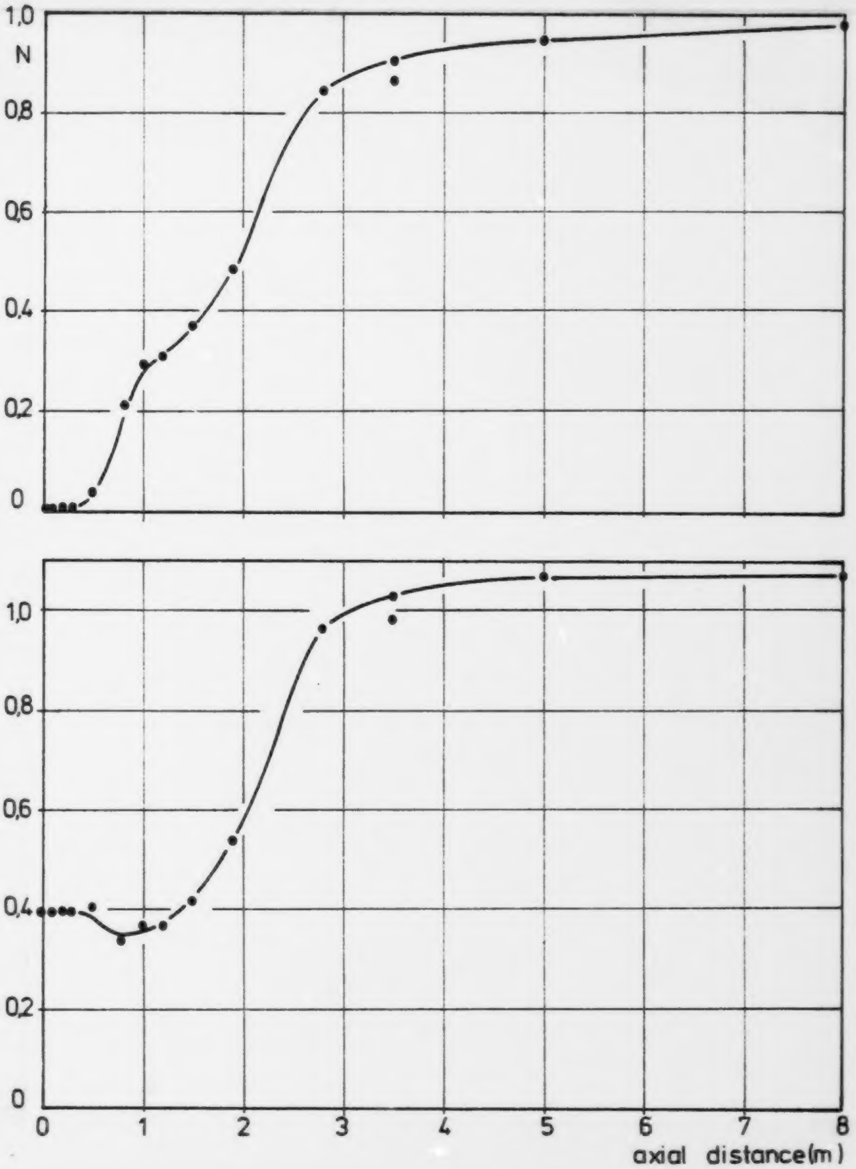

Figure 12-5. Flame B3, Mixing Factor (M_2) and Degree of Oxidation (N).

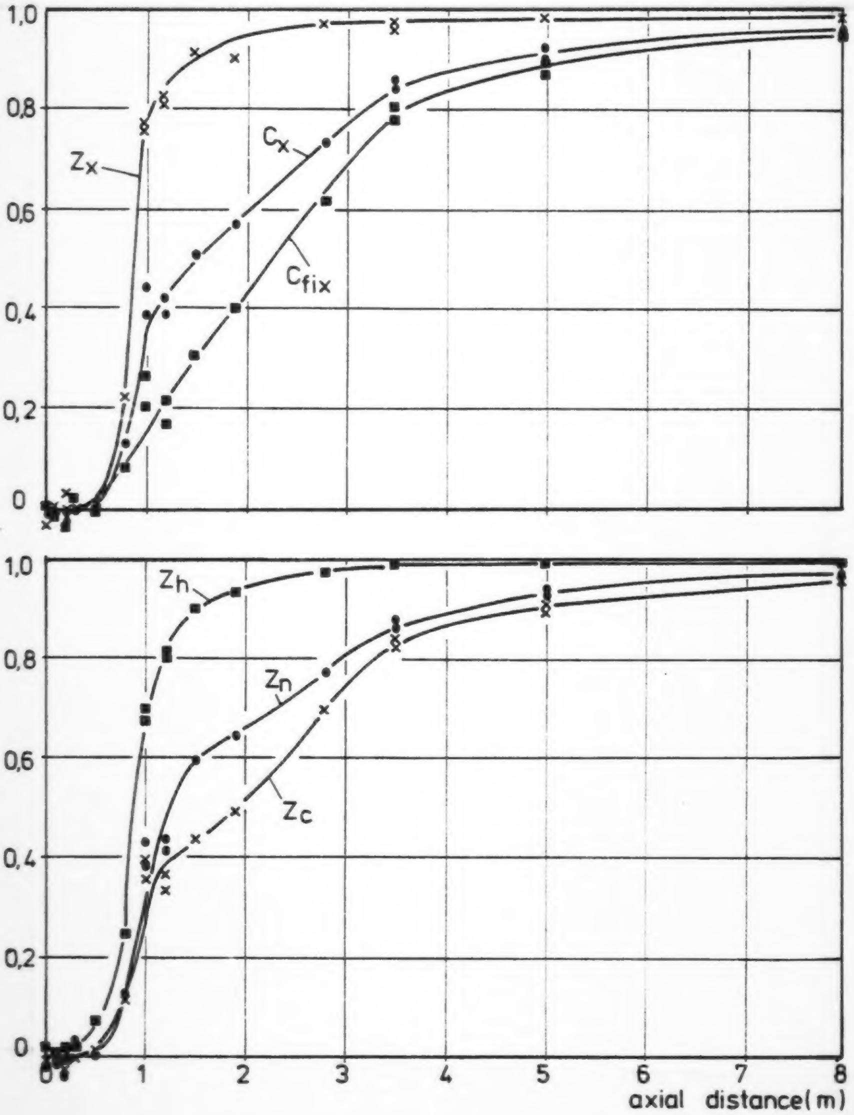

Figure 12-6. Flame B3, Burn-out of Solids.

4.0 FURTHER EVALUATION OF RESULTS

A standard evaluation of the experimental data has been made and is presented as part of the tabulated results (section 7) where definitions of the various quantities are also given. Axial profiles are included in the flame by flame sets of graphs (7-12) (see end of section 3).

4.1 Mixing Factor and Degree of Oxidation

The stoichiometric oxygen/fuel mixing factor (M2) is a convenient way to express globally the state of a given flame control volume in terms of relative oxygen and fuel availability. The value of M2 at the burner exit should always be equal to the stoichiometric premixing ratio. This is true within the variation due to coal composition at this point relative to average (Table 1).

The value of M2 at the chimney is slightly lower than the overall air/fuel ratio (about 2%) and this reflects in fact the presence of incompletely burnt solids.

The degree of oxidation (N) expresses globally the state of the oxygen-fuel reaction and it can be seen that it is always lower than M2 as normally expected with pulverized coal combustion.

It can be seen that the visible flame length (Table 3) always corresponds very well with a 95% degree of oxidation; however there is no evident correlation with the stoichiometric mixing length (M2 = 1) which is certainly a strong function of fuel and air axial velocities (or residence time).

The measurement of solid concentration in the early part of the coal jet may be somewhat inaccurate, as already discussed, and leads to a certain discrepancy in the M2 values; this could be the reason for the decreasing value of M2 in this region for flame A4 and B3. Another reason for this could be attributed to the decreasing availability of oxygen due to volatile formation, and it can be noticed (Table 4) that flame A4 had the earliest hydrogen peak.

The data of flame A1 are seen to depend quite significantly upon the furnace boundary conditions and this could only be attributed to the change of wall temperature (about 40 C) and radiation flux as already mentioned (section 3.1). The repeatability of the measurements has nevertheless been checked and demonstrated through comparison between 1st and 3rd measuring periods under identical wall temperature conditions. Also, whenever it is relevant, the various tabulated data (section 7) correspond together with regard to the different periods.

4.2 Burn-Out Degree of Sampled Solids

Burn-out of combustibles, volatiles, fixed carbon, elementary carbon, hydrogen and nitrogen have been calculated from the analysis of solid samples and the average input coal analysis (see section 7 for definitions and tabulated data). The axial profiles are seen to be quite consistent with previous observations.

In particular the total burn out (C_X) is found in the range 90-94% at the visible flame length; there is little evolution after this point and up to the 94-96% chimney value.

The first region of the flame is associated with a linear devolatilization rate (i.e. Z_X) after the axial ignition point. Also, the Z_X profiles maintain their slope up to the position of the hydrogen concentration peak, and somewhat further (e.g. A4, B1, B2). It is interesting to note that the hydrogen and volatile burn out profiles are quite similar while those of elementary carbon and nitrogen follow the total burn out evolution.

The discrepancies observed between point data arise from several factors:

- In the early part of the coal jet the ash content of solids is always very close to that of the input coal and the difference varies therefore significantly with local ash values (the repeatability of ash content is within 1% on average). A better characterization of these effects is given in the following section.
- On some occasions a systematic difference was noted between the two different ash analysis carried out (IFRF and external laboratory). Wherever the latter analysis seemed as accurate (or more) the value has been given in the tables (see section 6); in particular, it was consistently higher for flame A2 and this effect is shown on the graphs.
- In addition to these factors, the influence of boundary conditions is also reflected here for flame A1, but to a lesser extent than for the mixing factor and degree of oxidation.

4.3 An Attempt to Correlate Nitrogen Burn Out with the Total Concentration of Nitrogen Species

The best possible method for a better understanding of the results in terms of fuel nitrogen evolution would be to make a total nitrogen balance at every "location" in the flame. This is, however, quite complex here, and requires some modeling of the flame aerodynamics to isolate dilution from reaction effects.

Moreover the evolution of fuel nitrogen towards molecular nitrogen, which can only be assessed by difference, can also be very large. In fact for full conversion of the fuel nitrogen one would expect a fuel NO concentration of 2200 ppm at the chimney, which is 5 - 9 times the measured value. An attempt to quantify this effect within the flames has been made using the gaseous carbon concentration ($Cg = CO_2 + CO + CH_4$) as a reaction tracer as follows:

From the expected flue gas concentrations with an excess air of 10%, the total concentration of reacted fuel nitrogen may be approximated by

$$\Sigma \text{ N expected} = \frac{(CO_2 + CO + CH_4) \text{ Flame}}{16.7} \cdot \frac{Z_n}{Z_c}_{\text{ flame}} \cdot 2200 \text{ (ppm)} \cdot$$

Comparisons between this quantity and the total nitrogen concentration measured ($HCN + NO + NH_3$) is shown on fig. 13.

There is a qualitative agreement only, i.e. between the positions of expected and measured peak concentrations. The graphs indicate that beyond this peak, the decay of measured nitrogen (mainly HCN) must be due to a great part, to evolution towards molecular nitrogen. Because of that, quantitative agreement is obviously not possible but it is however worth mentioning that the two flames having significantly lower peak values than expected (A4, B2) are also those with the highest hydrogen peak (Table 4).

4.4 Influence of Coal Size Distribution and Composition

The granulometry of the input coal and the corresponding ash and volatile content of the six sieved fractions is shown on Figures 14 a and b. The size distribution follows well a Rosin-Rammler law for the fraction above 63 μm; the coal fineness corresponds to 32% > 75 μm with an exponent of 1.1 (slope).

The ash and volatiles contents are shown to depend on particle size both varying in opposite direction with about 44% decrease of ash content and 20%

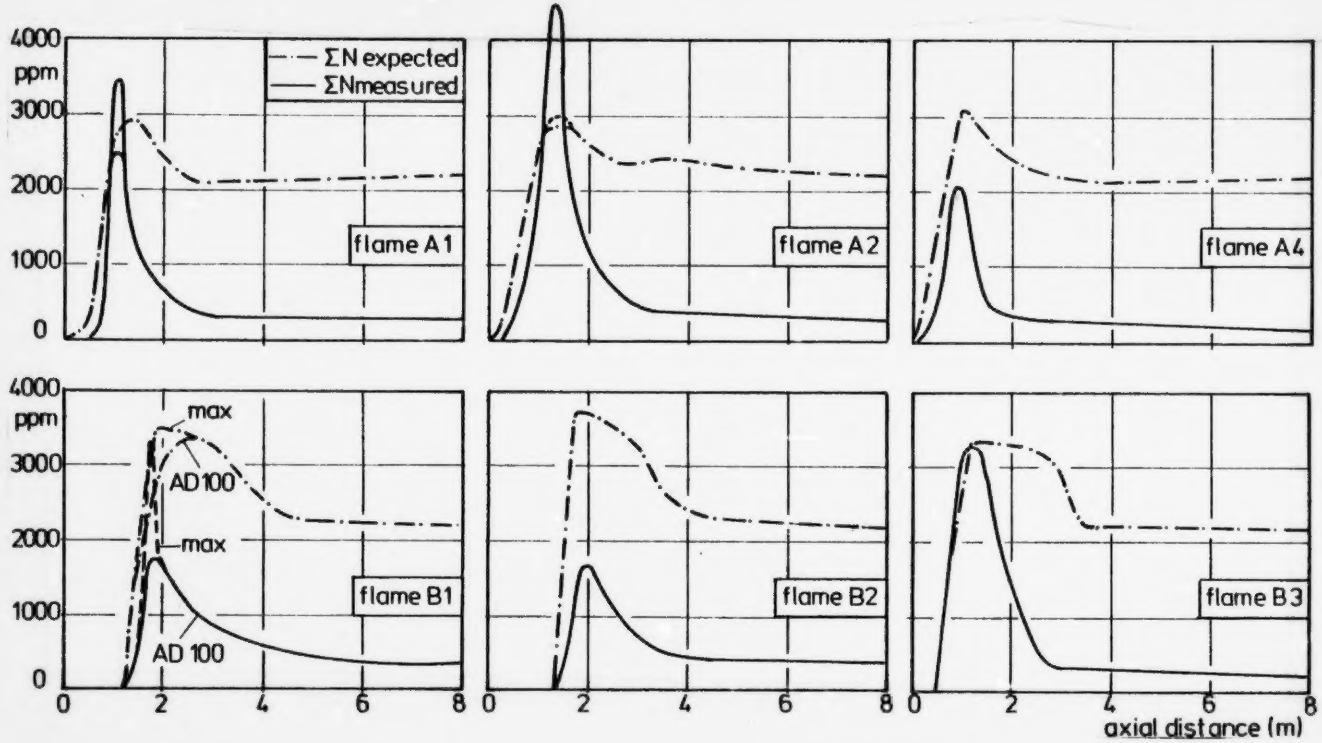

Figure 13. Comparison Between Measured Total and Expected Fuel Nitrogen Species Concentrations.

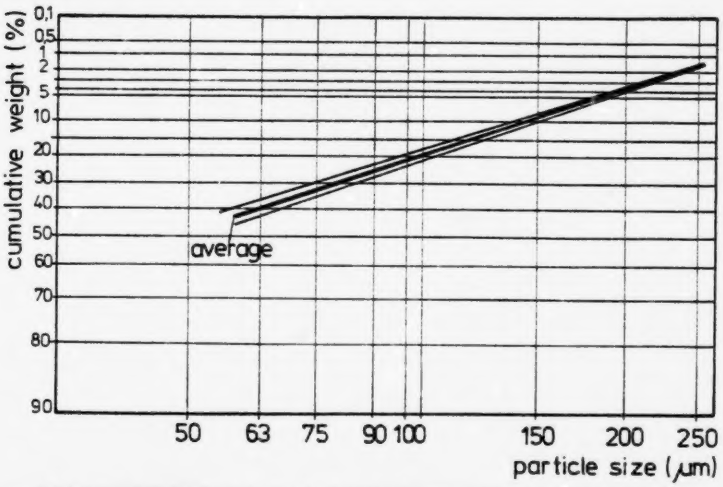

Figure 14a. Average Particle Size Distribution of the Input Coal.

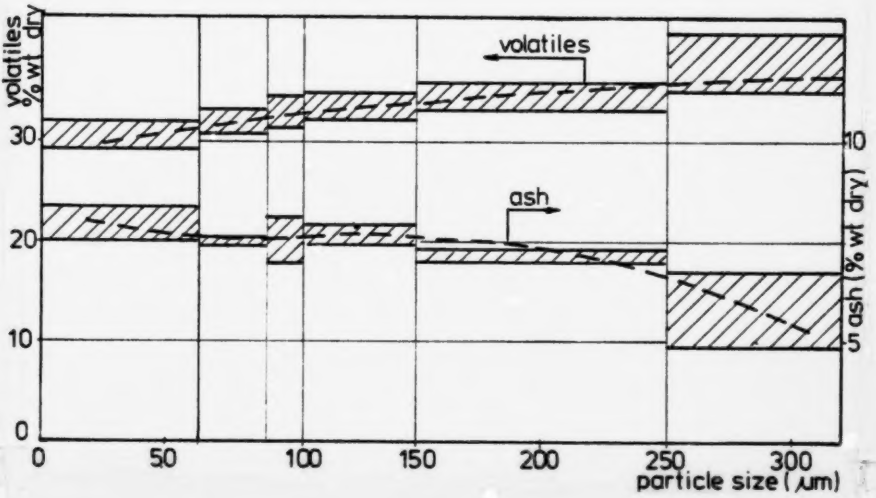

Figure 14b. Ash and Volatile Distribution of the Input Coal as a Function of Particle Size.

increase of the volatile content from fine to coarse particles. However, the ash distribution seems to be quite flat up to 150 μm and corresponds more or less to the level of the average input coal (7.6%); this is not the case of the volatile content which varies more steadily with particle size.

The influence of these variations was examined for flame A1 and B1 in the same way, by sieving the samples (when sufficient quantity was available) and analyzing each size fraction for ash and volatiles.

Checking the analysis against that of the total sample could thus be achieved as well and good agreement was found in general. Size and composition distributions are shown on figs. 15-18 and several comments can be made:

- The size distribution is not constant across the coal jet (A.D.=0 for A1, A.D.=0.10 m for B1) and it seems that coarser particles are found close to the axis of the jet than at its boundaries (these are 3.5 cm from the axis). It must be noted however that the sampling velocities here were lower than 7 m/s and thus far from the isokinetic conditions, but this did not apparently affect the results since the slopes of the size distributions are quite close to unity and that a shift (compared to input coal) to coarser particles is only found for flame B1 (A.D. 0.10 m). The consistency of ash and volatile variation with particle size is also evidenced inside the coal jet, taking account of weighing and analysis accuracy.
- The fineness of the samples collected is seen to increase along the flame axis (up to the point where the quantity of sample was still sufficient). This may correspond to the larger weight loss of smaller particles which are seen to have a faster devolatilization and combustion rate. However, a clear identification of this effect is only possible 40-50 cm from the axial ignition point.

  Other effects are certainly also present due to individual particle size changes as a result of swelling, sintering, exploding and possible agglomeration inside the probe. In particular, swelling and coking was very important for flame A1 at an axial distance of 0.75 m.

  Such effects explain to some extent the discrepancy of global ash and volatile content found before, due both to particle size and non-uniform behavior of individual particles as a function of their size.

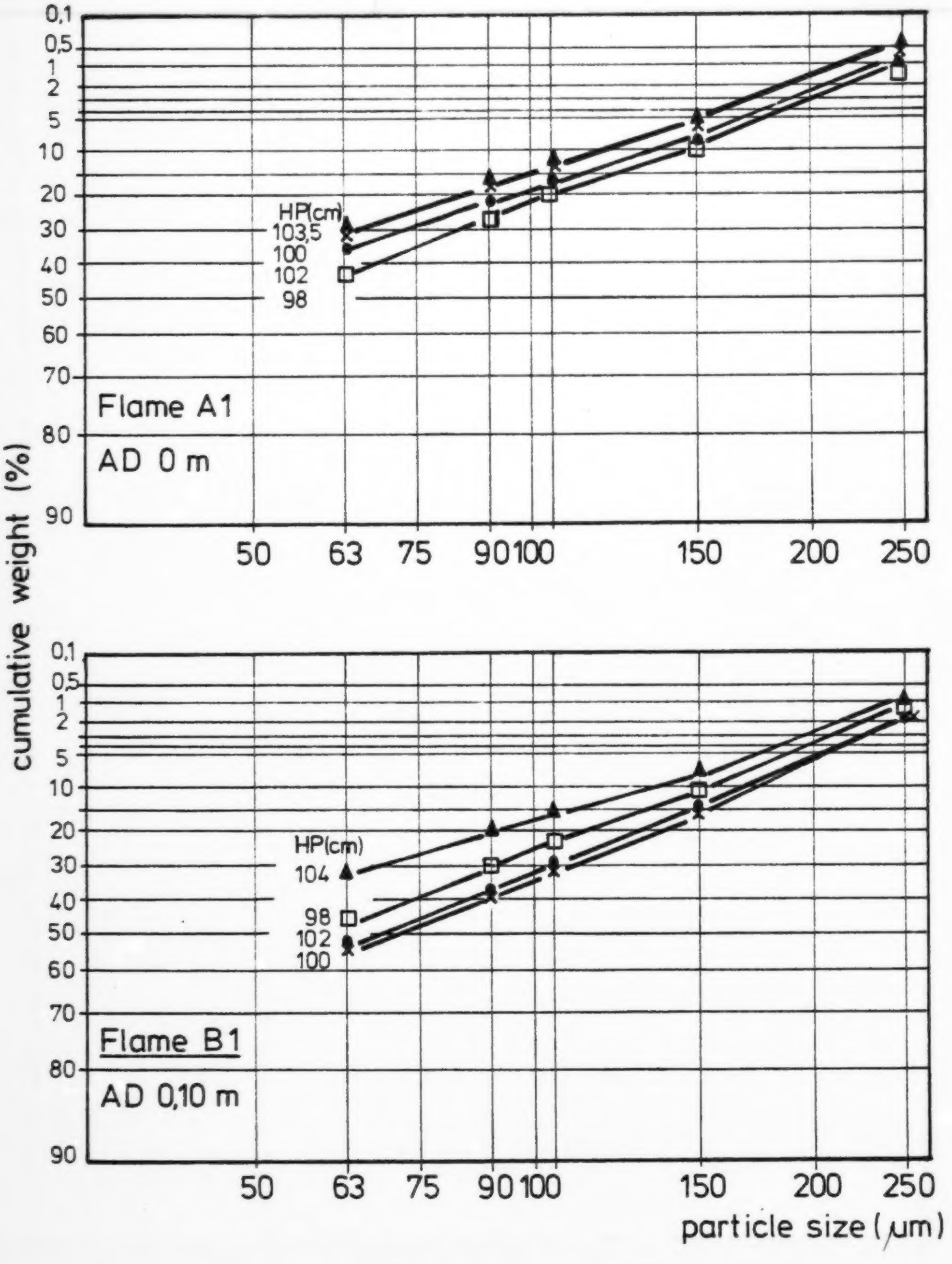

Figure 15. Particle Size Distributions Across the Coal Jet. (HP is horizontal position, AD is axial distance).

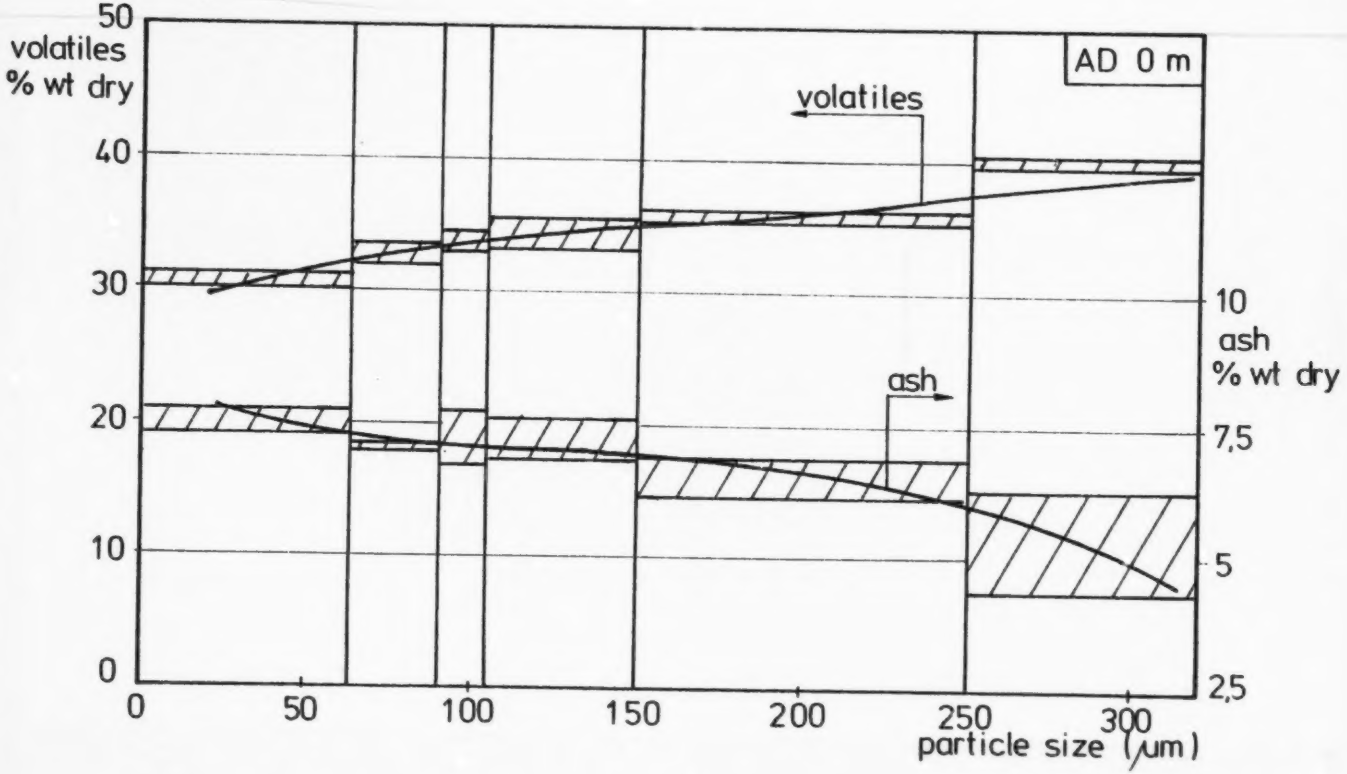

Figure 16-1. Ash and Volatile Distribution Across the Coal Jet as a Function of Particle Size. (Flame A1)

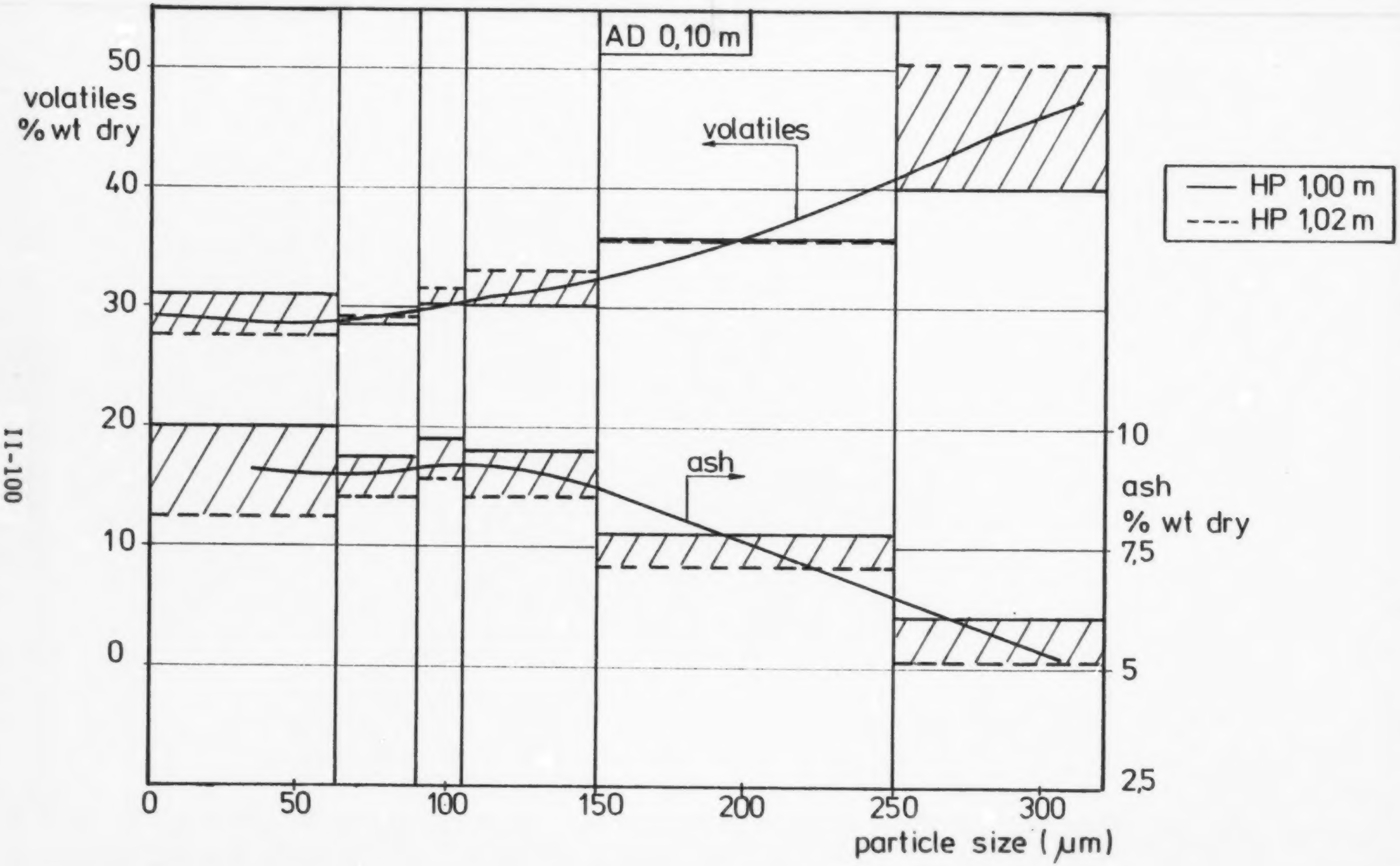

Figure 16-2. Ash and Volatile Distribution Across the Coal Jet as a Function of Particle Size. (Flame B1)

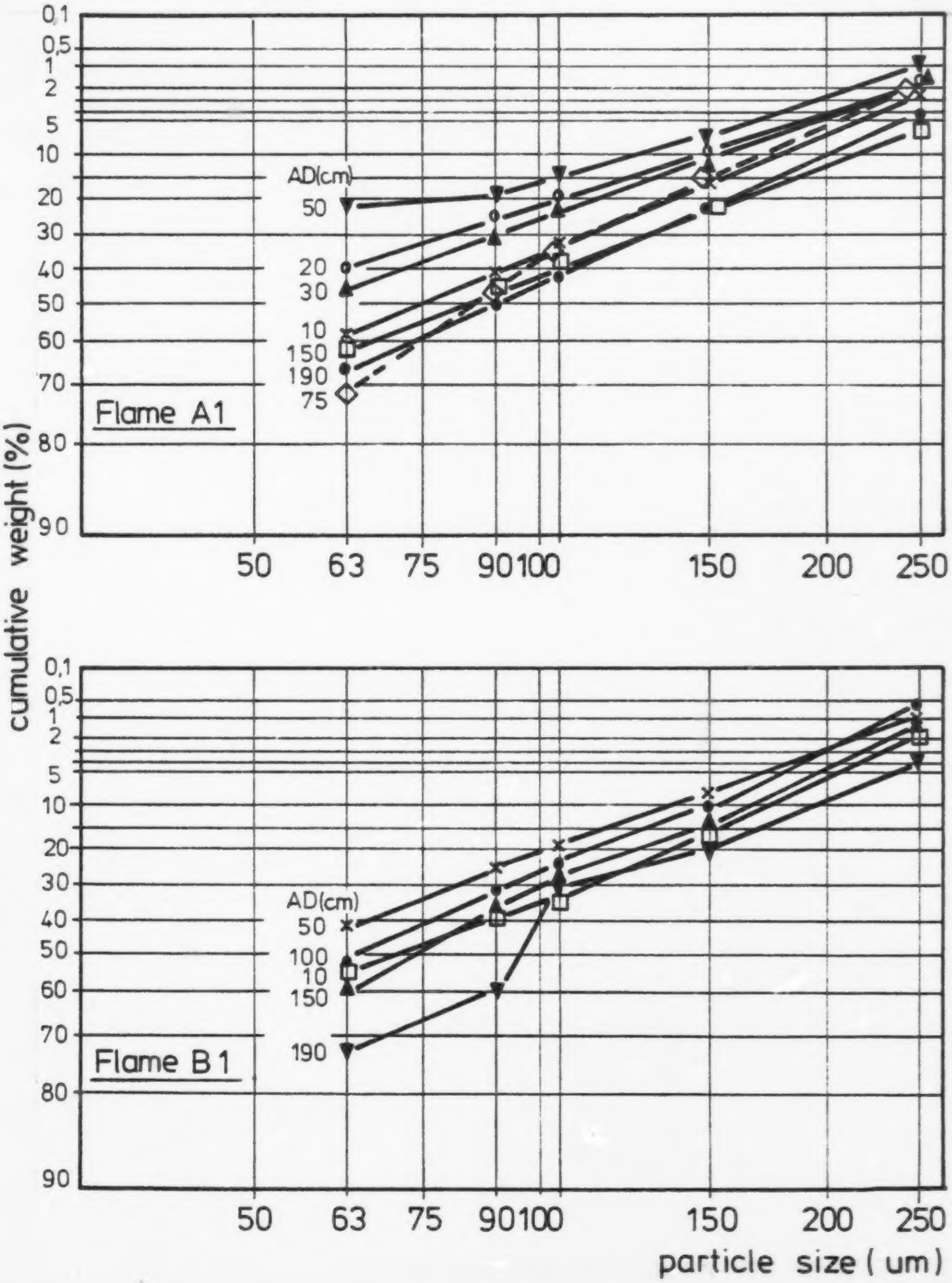

Figure 17. Particle Size Distributions Along the Axis.

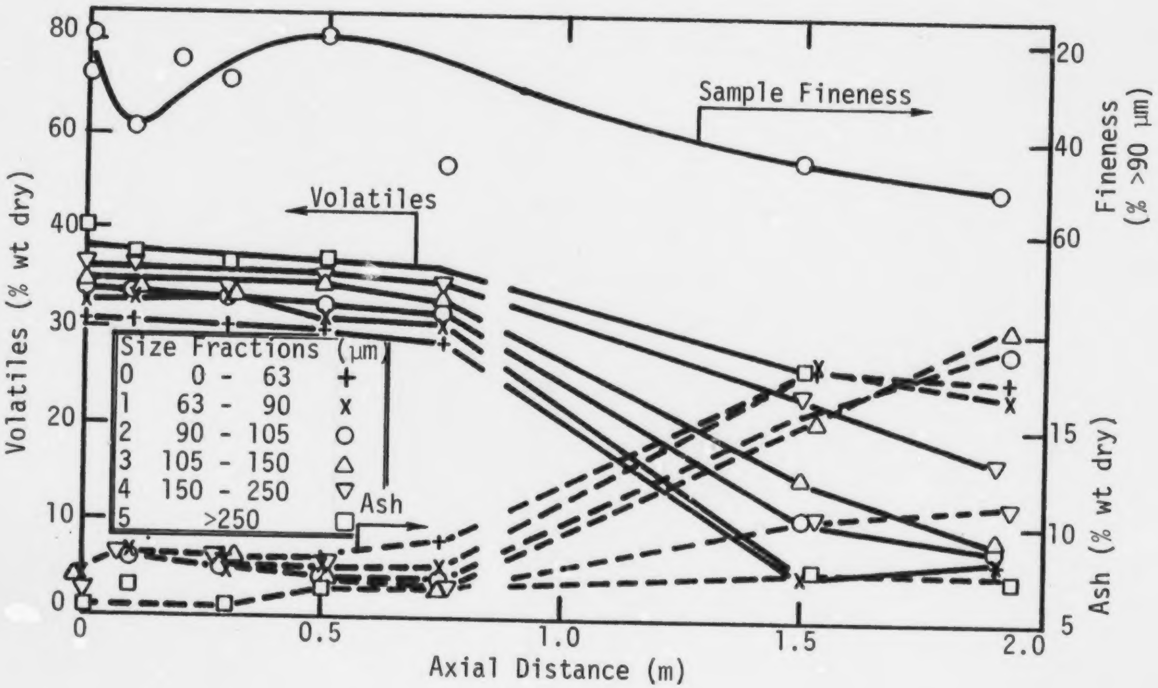

Figure 18.1. Ash and Volatile Axial Profiles in Individual Size Fractions, Flame A1.

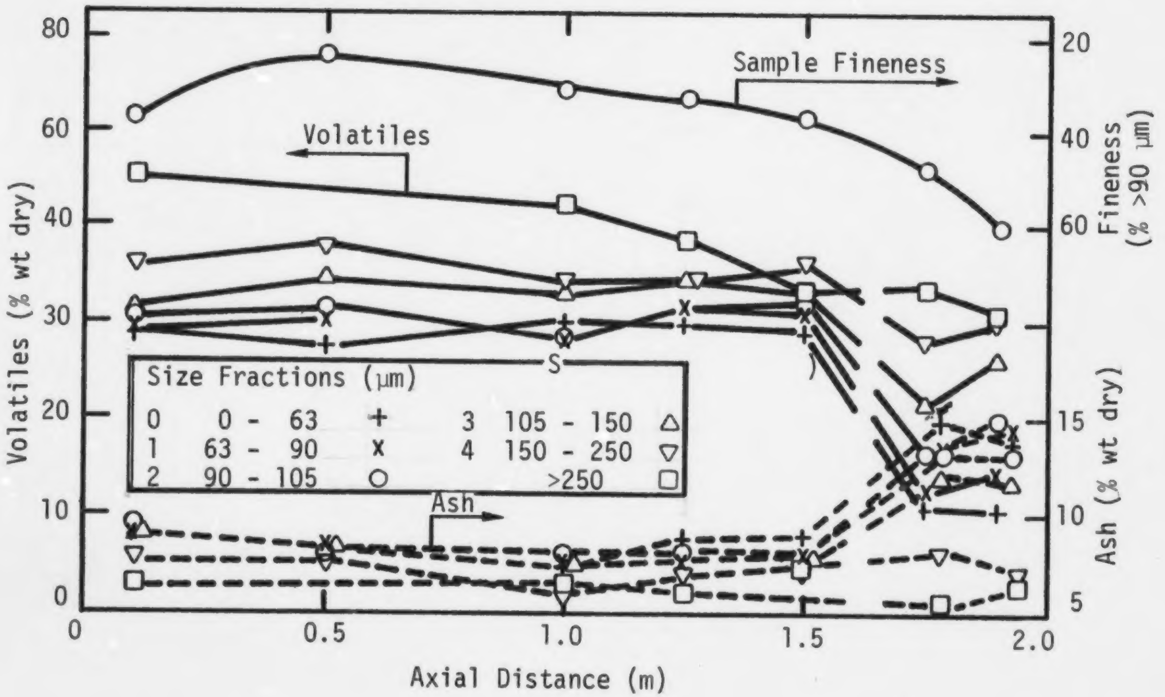

Figure 18.2. Ash and Volatile Axial Profiles in Individual Size Fractions, Flame B1.

Also, to ignore the effect of particle size for mathematical modeling could not be realistic at this stage.

5.0 CONCLUSIONS

Six long coal flames have been produced in the IFRF furnace nr. 1 with the same burner and under controlled boundary conditions. Two flames have been characterized in detail with measurements throughout their horizontal symmetrical plane and the others only partially along their axis. Severe difficulties of measurements have been encountered, particularly for gas and solid sampling, in regions of high temperature and solid concentrations. These were mainly due to the existence of very steep gradients which complicated the typical problems encountered with p.f. turbulent diffusion flames. Such difficulties have been solved with the use of different or modified probe equipment although the inherent "averaging" effect could obviously not be prevented.

Good consistency was generally found between the various measurements which all indicate that mixing is the determining mechanism for the overall combustion processes.

All data have been tabulated to allow more fundamental computations and detailed interpretation, and this should fulfill the objectives of this work. A qualitative discussion of the results has however been felt necessary, especially to describe the accuracy and representativeness of the data. In particular, the evidence that NH_3 concentrations were always very low should be attributed to the high temperature gradients and very short residence times in the reaction zones; also the very rapid and significant formation of HCN (1100-4000 ppm) seems to indicate that HCN in this case can be the only intermediate nitrogen species present at an early stage in the flame, but that it evolves in a major part to molecular nitrogen. Moreover, a certain amount of the fuel nitrogen is found to evolve "directly" to molecular nitrogen as well, beyond the region of HCN formation; the use of nitrogen burnout data indicates that this may be 40-60% of the total fuel nitrogen. Further evaluation is required to quantify more precisely all these mechanisms, and it is felt that simple mathematical models could serve this purpose. The results of this work are thus promising, particularly for the amount of detailed information that could be gained in a realistic semi-industrial situation and during a short period.

The same type of information should however be required to develop further our understanding of the fuel bound nitrogen evolution processes and in particular:

- for the effect of variable fuel kinetics, such as may be obtained with different coals and/or with variable oxidant partial pressure (e.g. vitiated air).
- for the effect of flame and furnace scale in order to allow the transfer of information with more confidence from one scale to another.

6.0 REFERENCES

1. Conference on Coal Combustion Technology and Emission Control, California Institute of Technology, Pasadena, February 5-7, 1979.

2. Influence du type de bruleur, de la finesse du charbon, de la proportion d'air primaire et de la temperature sur la combustion du charbon pulverise. IFRF Doc. No. F 32/a/32, 1965. J. Chedaille and K. Hemsath, Essais C-10.

3. Etude du mechanisme d'inflammation et de la recirculation des produits de combustion. IFRF Doc. No. F 32/a/35, 1967. J. Chedaille and K. Hemsath, Essais C-11.

4. Influence de la nature du charbon sur son inflammation et sa combustion. IFRF Doc. No. F 32/a/36, 1967. J. Chedaille and K. Hemsath, Essais C-12.

5. Behavior of non swirling pulverized coal flames. IFRF Doc. No. F 32/a/41, 1971. K. Hein.

6. "Chemiluminescent Measurement of Nitric Oxide in Combustion Products", Vol. III, Part I of this report series.

7. Analytical chemistry. pp. 356-364. D. C. Favy.

8. Technical services to members. IFRF Doc. No. C 72/a/9, September 1979.

9. Industrial flames - vol. 1 Measurements in Flames. J. Chedaille and Y. Braud. Edward Arnold publishers, London 1972.

7.0 TABLES OF FLAME POINT DATA

Remark

- Whenever a particular measurement has not be made (e.g., H_2, CH_4), the place is left as blank, while zero is indicated when nothing was found
- The calculation of N and M2 has also been carried out within the recirculation zones (A1, B1) even when sampling of solids was not made since solid concentrations in these regions were always negligible.
- The values of ash content between brackets are those given by external laboratory analysis.
- The correction of solid concentration for sampling velocity has been made along the axis only and from burner exit to the acial position marked "S".

Definitions of the various derived quantities are as follows:

- $$M_2 = \frac{\left.\frac{\text{kg } O_2}{\text{kg Fuel}}\right|_{\text{flame point}}}{\left.\frac{\text{kg } O_2}{\text{kg Fuel}}\right|_{\text{stoichiometric}}} \quad = \text{stoichiometric mixing factor}$$
- $$N = \frac{\text{kg } O_2 \text{ reacted}}{\text{kg } O_2 \text{ reacted} + \text{kg } O_2 \text{ needed}} \quad = \text{degree of oxidation}$$
- $$\text{"burnout" of component } \alpha = \frac{\left.\frac{\text{kg } \alpha}{\text{kg dry coal}}\right|_{\text{Flame point}}}{\left.\frac{\text{kg } \alpha}{\text{kg dry coal}}\right|_{\text{Input}}} \quad = 1 - \frac{\alpha}{\alpha_o} \cdot \frac{a_o}{a}$$

(a = ash content, subscript o stands for input)

We can thus form six burnout factors:

- C_x - Total combustibles (1-ash)
- Z_x - Volatiles
- C_{Fix} - Fixed combustibles (1-ash-volatiles)
- Z_c - Carbon
- Z_h - Hydrogen
- Z_n - Nitrogen

Table 5. Flame Al

		GAS COMPONENTS											SOLIDS ANALYSIS					DERIVED QUANTITIES							
AD	HP	O_2	CO_2	CO	H_2	CH_4	NO	NH_3	HCN	Temp.	Vel.	Solids	Ash	Volat.	C	H	N	N	N_2	C_x	Z_x	C_{fix}	Z_c	Z_h	Z_n
cm		% volume dry					ppm			°C	m/s	g/m^3	% wt. dry												
0	98	21	0	0			0					1075	6.52	30.11	73.62	4.48	1.05	.005	.131						
	100	21	0	0			0			150	21.9	1075	6.12	28.73	74.35	4.51	1.05	.006	.130						
	102	21	0	0			0					1075	7.59	29.82	73.52	4.48	1.07	.005	.131	0	.066	-.04	.013	.045	.041
	103.5	21	0	0			0					1075	6.96	29.69	73.45	4.50	1.07	.004	.130						
10	20	1.8	16.6	0			210			1200	-3.5	3.7	89.93	3.07	8.73	.06	.21	.997	1.092	.990	.991	.990	.990	.993	.984
	40	1.8	16.5	0			210			1200	-0.6							1.0	1.096						
	60	1.8	16.5	0			230			1190	-2.4							1.0	1.096						
	70									1195															
	75									1190															
	80	2.3	15.8	0			250			1175	1.73							1.0	1.127						
	85	5.0	14.0	0						1150	2.08							1.0	1.313						
	87.5	10.0	11.0	0			0			815	10.0							1.0	1.796						
	90	16.0	7.5	0			0			610	29.4	0						1.0	2.867						
	92.5	20.5	0	0			0			575	30.0	0						0							
	95	21.0	0	0			0			580	28.9	0						0							
	100	21.0	0	0			0			350	23.0	1020	7.95	31.51	73.88	4.58	1.03	.002	.134	.047	.058	.041	.053	.068	.120
20	100	19.8	.25	0			0	4	4	400	25.0	1000	8.40	30.49	73.99	4.63	1.05	.003	.129	.103	.137	.084	.103	.103	.151
30	40	1.8	16.5	0			245			1200	-4.5	4.4	92.48	.63	8.67	.04	.20	.996	1.091	.993	.998	.990	.990	.999	.985
	60	1.8	16.5	0			245			1200								1.0	1.096						
	70																								
	80	2.3	16.1	0			240			1175	2.71	3.8	91.37	1.54	9.11	.16	.23	.997	1.121	.992	.995	.990	.989	.997	.982
	85	10.5	10.2	0			130			1035	13.2							1.0	1.901						
	87.5									840															
	90	19.5	1.3	0			23			740	31.2	0,4	66.43	10.47	12.63	.15	.31	.994		.958	.962	.956	.980	.996	.968
	92.5									650			85.54												
	95	20.0	.25	0						800	25.5	800													
	100	20.0	.25	0			9-20	5	3	550	26.0	950	7.88	32.96	74.10	4.64	1.03	.003	.137	.038	.006	.055	.042	.047	.113
													7.17	31.41	73.93	4.70	.98	.002	.136	-.06	-.04	-.08	.05	-.06	.072
40	100							7	10																

Table 5. Flame A1

		GAS COMPONENTS											SOLIDS ANALYSIS					DERIVED QUANTITIES							
AD	HP	O_2	CO_2	CO	H_2	CH_4	NO	NH_3	HCN	Temp.	Vel.	Solids	Ash	Volat.	C	H	N	N	N_2	C_x	Z_x	C_{fix}	Z_c	Z_h	Z_n
cm		% volume dry					ppm			°C	m/s	g/m³	% wt. dry												
50	40	1.8	16.5	0			240			1200								1.0	1.096						
	60									1195															
	70									1170															
	75									1170															
	80	5.5	14.15	0			140			1090								1.0	1.340						
	85	13.0	8.2	.03						925								.999	2.381						
	90	17.8	3.0	.19	0	0	55			760		0.6	32.58 49.07	24.72	44.21	.88	.65	.962	5.77	.829	.819	.835	.861	.956	.864
	100	19.0	1.5	.14	0	0	18-50	7	20	800	26.9	(850)	6.69	30.82	73.79	4.70	1.14	.012	.153	-.15	-.09	-.18	-.12	-.14	-.16
	100	19.5	.25	.09	0	0	50						8.32	32.94	73.98	4.69	1.06	.002	.148	.093	.059	.111	.094	.088	.135
	110	18.5	1.8				110			760		1.3	14.49	13.36	74.76	2.02	1.02	.917	9.09	.514	.781	.373	.474	.774	.522
60	100							4	53																
70	100							1	247																
75	40	1.8	16.5				250			1230								1.0	1.096						
	60									1210															
	70	1.8	16.4	.03	.56	0	225	0	10	1175								.985	1.080						
	75									1120															
	80	10.2	10.4	0	.35	0	150	0	6	1030								.986	1.844						
	82.5									945															
	85	14.3	7.0	0	.31	0	120	0	0	930								.982	2.768						
	87.5									990															
	90	18.5	2.6	.15			70	0	9	1200								.977	6.867						
	92.5									1360															
	95	13.8	6.25	.50	.59	0	235	3	620	1335															
	97.5									1100															
	100	11.5	7.5	5.0			140	1	350	1040	25.6	550	7.82	30.41	74.13	4.60	1.07	.120	.233	.03	.076	.006	.034	.048	.071
	*100												11.42	18.73	73.76	2.84	1.17	.171	.287	.362	.610	.230	.342	.597	.304
	110	14.5	6.6	0			215	0	161	1350															
	115	14.3	6.65	0			110											1.0	2.882						
80	100							0	297																
90	100							74	1930																
100	100							50	670																
100	100							2	992																

* 8 probe in a vertical position

Table 5. Flame A1

		GAS COMPONENTS											SOLIDS ANALYSIS					DERIVED QUANTITIES							
AP	HP	O_2	CO_2	CO	H_2	CH_4	NO	NH_3	HCN	Temp.	Vel.	Solids	Ash	Volat.	C	H	N	N	N_{ξ}	C_x	Z_x	C_{fix}	Z_c	Z_h	Z_n
cm		% volume dry					ppm			°C	m/s	g/m^3	% wt. dry												
100	40	1.8	16.8	.03			260			1230	-3.49	4.4	89.03	2.77	10.73	.10	.20	.995	1.088	.989	.992	.988	.987	.998	.984
	60	2.2	16.8	.04			200				-2.0							1.0	1.113						
	70	3.9	15.0	.13	.20	0	180			1200	0							.991	1.216						
	75	9.0	11.4	.02	0	0	200			1060	7.33	3.7	69.47	3.41	26.23	.16	.34	.986	1.665	.963	.988	.950	.961	.996	.996
	80	11.5	9.65	.05	.16	0	150	0	15	1050	15.8	4.9	46.22	7.82	48.36	.45	.61	.954	1.946	.904	.959	.874	.893	.984	.910
	85	13.0	8.20	.20			200	0	1	1300	24.5							.990	2.345						
	87.5	11.5	8.60	3.3			320			1360								.884	1.730						
	90	8.5	9.40	4.5	.82	0	375	1	29	1370	25.3	7.8	19.50	5.01	75.96	.86	.92	.7877	1.281	.660	.938	.512	.603	.928	.679
													16.08	8.32	74.46	.42	.98	.7897	1.284	.570	.877	.408	.528	.957	.586
	95	1.5	10.50	9.0	4.72	1.0	490			1340	24.0														
S	100	1.0	9.5	10.0			350±50	2	1603	1235	23.7	400	12.24	24.26	71.48	3.29	1.04	.2414	.2524	.410	.529	.347	.405	.565	.423
													7.89												
105	100							22	2580																
110	60	5.2	14.25				210											1.0	1.319						
	70							1	1																
	80	12.5	8.75	.05			240	6	64									.998	2.241						
	85							1	60																
	90	9.4	10.25	3.6			450	1	180									.891	1.484						
	95							2	947																
	100	3.0	9.5	9.6			420	2	2110																
	105							2	1800																
	110							3	360																
115	100							21	3000																
120	40	1.8	16.7	0			250											1.0	1.094						
	60	2.0	16.4	0			200											1.0	1.107						
	70	6.2	13.5	0			200											1.0	1.401						
	75	8.8	11.5	0	.11	0	230											.996	1.665						
	80	9.8	10.4	.22	.21	.19	245	1	1									.954	1.746						
	85	10.1	9.85	.50	.38	0	275	1	95									.965	1.818						
	90	5.5	10.75	5.4	.90	0	390	1.4	300																
	95																								
	100	2.2	10.4	9.0	1.63	.24	440	8.4	1290	1320	22.0														
130	100							8.3	1240																
140	100							4.8	1070																

Table 5. Flame A1

		GAS COMPONENTS											SOLIDS ANALYSIS					DERIVED QUANTITIES							
AD	RP	O_2	CO_2	CO	H_2	CH_4	NO	NH_3	HCN	Temp.	Vel.	Solids	Ash	Volat.	C	H	N	M	M_c	C_x	Z_x	Cfix	Z_c	Z_h	Z_n
cm		% volume dry					ppm			°C	m/s	g/m³	% wt. dry												
150	40	1.9	16.3	0			250			1250	-3.5							1.0	1.102						
	60	4.8	14.5				240			1270	3.5							1.0	1.290						
	65	4.9	14.4		.23	0	220			1275	5.0							.993	1.291						
	70	7.5	13.1	.02	.18	0	250			1280	9.3	6.7	34.70	3.66	60.57	.10	.73	.948	1.421	.845	.974	.776	.822	.995	.857
	75									1285	13.2														
	80	9.2	11.9	.24	.22	0	280			1290	16.8	14.3	18.05	1.88	78.27	.71	.92	.860	1.427	.626	.975	.441	.558	.936	.654
	85									1420	20.2														
	90	6.0	11.4	6.0	.39	0	370			1490	20.2														
	95									1460	19.3														
	100	2.9	11.15	7.8	2.24	.36	460			1400	19.2	267	12.03	11.44	78.19	1.87	1.05	.315	.358	.398	.774	.199	.338	.748	.407
	100											138	17.28	8.31	78.43	.97	.92	.432	.495	.606	.885	.458	.537	.909	.638
	105									1460	19.6														
	110									1370	23.7														
	115									1280	18.5														
	120									1240	12.0														
160	100							4.9	560																
180	100							1.5	360																
190	40	2.5	15.6	0			255			1230	-6.0							1.0	1.140						
*	40	3.0	15.4	0			250			1170								1.0	1.171						
	50	4.1	15.25	0			260			1150	-3.5							1.0	1.235						
	60	6.5	13.3	0	.12	0	225			1230	7.9							.996	1.424						
	60	6.8	13.15	.03			290			1160								.999	1.451						
	70	8.5	12.0	.08			300			1180	12.6							.997	1.613						
	80	9.0	11.75	.16	.41	0	250			1300	14.0	26	26.07	5.84				.980	1.640	.766	.94[illegible]	.671	.822	.995	.857
	80	7.3	12.5	.50			360			1330								.984	1.475						
	85	5.5	12.5	3.6			400			1380		68.5	18.54	7.25	76.55	.70	.93	.616	.803	.638	.907	.496	.579	.938	.659
	90	6.0	12.0	4.2	.75	0	310			1440	24.4														
	90	4.5	12.5	4.2			420			1420		219	16.97	9.65	74.46	.42	.98	.410	.497	.597	.864	.455	.553	.959	.608
	95	4.0	12.0	4.8	.80	0	360			1460															
	95	4.0	12.75	4.8			440			1430		131	18.30	11.78	75.67	.77	1.09	.500	.598	.632	.847	.519	.579	.931	.595
	100	3.5	12.0	4.8	.82	0	390			1470	20.9	203	17.63	5.75	79.93	.76	.97	.394	.461	.615	.922	.453	.538	.930	.626
	100	4.0	12.5	4.8			420			1420	20.9	88	16.69	4.26	79.93	.76	.97	.561	.677	.589	.939	.404	.512	.926	.605
	100	4.0	12.5	4.8						1420	20.9	192	15.38	7.28	79.85	.67	.90	.419	.500	.547	.887	.367	.471	.929	.602

* velocity traverse measured at A.D 200

Table 5. Flame A1

		GAS COMPONENTS											SOLIDS ANALYSIS					DERIVED QUANTITIES							
AP	HP	O_2	CO_2	CO	H_2	CH_4	NO	NH_3	HCN	Temp.	Vel.	Solids	Ash	Volat.	C	H	N	N	N_2	C_z	Z_z	C_{fix}	Z_c	Z_h	Z_n
cm		% volume dry					ppm			°C	m/s	g/m^3	% wt. dry												
190	110	6.5	12.0	3.9	.80	0	310			1400	24.7	223	16.73	3.16	80.56	.35	.94	.382	.501	.590	.955	.397	.509	.966	.618
	120	8.5	11.7	.15			240			1180		82	23.86	4.50	72.48	.18	.85	.588	.917	.737	.955	.622	.690	.987	.758
200	100							0.5	280																
280	40																								
	60																								
	80											51	25.17	3.50	75.85	.10	.80			.755	.966	.643	.693	.993	.784
	90											84	23.58	10.51	75.10	.17	.90			.733	.894	.648	.675	.988	.741
	95											94	23.30	8.00	73.46	.39	.90			.729	.918	.628	.679	.972	.737
	100	3.7	13.5	1.0								73	23.12	7.21	75.79	.42	.88	.628	.761	.726	.925	.620	.666	.970	.741
300	100	4.5	13.5	.25						1400	14.2	20	20.74	3.78	76.89	.34	.82	.847	1.085	.685	.956	.542	.622	.953	.731
		4.2	14.5	.39			360				14.3	51	25.44	11.57	72.06	.57	.93	.722	.893	.758	.891	.688	.711	.964	.751
350	20	1.8	16.5	0			250			1230	-3.5							1.0	1.096						
	40	1.8	16.5	0			250			1230	-2.5	7	55.11	8.53	44.19	.16	.64	.973	1.066	.933	.963	.916	.918	.995	.921
	40											5.4	77.50	7.36	20.94	.03	.28	.989	1.084	.976	.977	.975	.972	.999	.975
	60	1.8	16.5				270			1270	7.9							1.0	1.096						
	80	2.0	15.9	.14			320			1300	12.3	14	28.70	3.94	68.31	.09	.74	.913	1.012	.795	.967	.704	.757	.994	.825
	80											11	42.80	2.87	56.37	.04	.64	.260	.280	.890	.984	.840	.865	.998	.898
	100	3.4	14.6	.20			300	0	12	1320	13.5	20	26.93	4.71	70.56	.25	.83	.867	1.039	.776	.958	.680	.733	.984	.790
												16.3	35.53	4.58	62.51	.06	.73	.899	1.078	.850	.969	.787	.820	.997	.860
	120										10.1														
500	50									1240	4.9														
	70									1270	5.0														
	80									1280	7.1														
	100	2.2	15.6	0			265	0	1.6	1290	9.4	9	43.11	4.70	55.40	.09	.62	.953	1.070	.891	.974	.847	.869	.996	.902
	120									1280	8.7														
800	100												60.59	4.27	28.46	.05	.34	.972	1.063	.946	.983	.927	.995	.998	.961
800	100	1.8	16.7				280						67.06	2.08	28.46	.05	.34			.959	.992	.942	.956	.998	.965
800	100	1.93	16.46				273			1230		11	65.51	1.12	33.12	.17	.36	.966	1.065	.956	.995	.935	.948	.995	.962
800	100	1.8	16.8										77.14	4.31						.975	.986	.969	.956	.996	.968

Table 6. Flame A2

		GAS COMPONENTS											SOLIDS ANALYSIS					DERIVED QUANTITIES							
AD	HP.	O_2	CO_2	CO	H_2	CH_4	NO	NH_3	HCN	Temp.	Vel.	Solids	Ash	Volat.	C	H	N	N	H_2	C_x	Z_x	C_{fix}	Z_c	Z_h	Z_n
cm		% volume dry					ppm			°C	m/s	g/m^3	% wt. dry												
10	100	20.8	0	.06	.52	.41	10			440		470	8.08	32.08	72.71	4.49	1.05	0	.285	.064	.057	.068	.083	.101	.118
20	100	20.5	.25	.15	.17	0	10-50	1.7		510		470	8.30 (8.05)	32.51	72.68	4.51	1.02	.006	.288	.091 .060	.069 .040	.102 .070	.108 .080	.121 .094	.166 .140
30	100	20.3	0	.06			10	1.4		700		460	8.06	32.23	72.75	4.65	1.11	0	.286	.061	.050	.067	.081	.067	.065
40	100	18.8	.60	3.1			70	2.7																	
50	100	17.0	1.0	4.3			90	1.3	244	1080		420	8.53 (8.98)	30.90	72.93	4.55	1.05	.057	.296	.117 .166	.139 .182	.106 .157	.129 .173	.137 .180	.164 .206
60	100							7.6	1993	1255															
75	100	11.4	3.75	6.0			330			1370		360	8.72 (0.39)	28.69	73.28	3.90	1.07	.143	.312	.139 .290	.218 .344	.096 .262	.144 .281	.276 .393	.167 .301
80	100		7.0				420	25/2.4	2039	1390															
100	100	4.5-6	10.4	7.0	.56	0	470			1435		320	10.39 (12.25)	25.87	73.10	3.22	1.08	.267 .279	.342 .355	.290 .416	.408 .502	.228 .370	.283 .397	.498 .578	.294 .406
100	100	5.5	10.25	9.0			440	22/7	1345																
110	100	2.5	11.3				560	27/6	2480																
120	100	1.8	11.0	7.6			480	14/20	3320																
130	100	1.2	11.3	8.7			440	8.1	4060																
140	100	1.5	11.5	8.1			400	34/8	1820																
S 150	100	2.2	12.5	6.9	4.01	.47	360	6.1	2360	1430		200	15.61 (18.12)	13.01	75.40	1.07	1.06	.374 .379	.413 .410	.555 .628	.802 .829	.424 .521	.508 .576	.889 .904	.539 .603
150	100	1.8	12.7	7.5	4.01	.47	420	5.8	2880																
190	100	1.7	13.7	2.5	2.0	0	350			1425		130	17.27 (18.22)	4.72	75.32	0.86	0.93	.485	.529	.605 .630	.935 .938	.431 .467	.555 .579	.919 .923	.634 .653
200	100	1.5	14.15	1.0	1.47	0	350	4.2	877	1425															
300	100							2.4	120																

Table 6. Flame A2

		GAS COMPONENTS											SOLIDS ANALYSIS					DERIVED QUANTITIES							
AD	MP.	O_2	CO_2	CO	N_2	CH_4	NO	NH_3	HCN	Temp.	Vel.	Solids	Ash	Volat.	C	H	N	N	N_2	C_x	Z_x	C_{fix}	Z_c	Z_h	Z_n
cm		% volume dry					ppm			°C	m/s	g/m^3	% wt. dry												
350	100	1.5	16.55	.60	.39	0	270			1345		20	20.10*	5.55*	73.40	0.43	0.70	.862	.928	.673	.934	.534	.628	.965	.763
													36.0	4.0						.853	.973	.790	.792	.980	.868
500	100	1.8	17.0	.30	.26	0	230			1290		9.4	49.03	2.4	52.56	0.23	0.64	.944	1.031	.914	.883	.930	.890	.992	.911
800	100	1.8	17.0	.02	.42	0	280			1250		6.1	66.67	3.87	32.58	0.03	0.50	.972	1.062	.958	.986	.944	.950	.999	.949
800	100	1.6	16.7				350			1290		9.2	71.49	7.01	30.57	0.11	0.43	.974	1.056	.967	.976	.962	.956	.997	.959

* Large coal flow increase

Table 7. Flame A4

		GAS COMPONENTS											SOLIDS ANALYSIS					DERIVED QUANTITIES							
AD	HP	O_2	CO_2	CO	H_2	CH_4	NO	NH_3	HCN	Temp.	Vel.	Solids	Ash	Volat.	C	H	N	N	M_i	C_x	Z_x	C_{fix}	Z_c	Z_h	Z_n
cm		% volume dry					ppm			°C	m/s	g/m^3	% wt. dry												
10	100									360															
20	100	20.0	0	1.0	1.1	0	5	0	50	520		450	7.58	32.02	72.52	4.33	1.06	.010	.294	0	0	0	.025	.076	.051
30	100						16			600															
40	100	10.3	4.25	4.5	3.2	.27	180	1	196	800		352	8.96	27.45	72.78	4.12	1.11	.111	.270	.164	.272	.106	.173	.256	.159
50	100									1170															
60	100	3.7	8.8	6.6	8.3	.47	400	10	390	1350		276	10.55	22.11	74.12	3.33	1.12	.197	.252	.302	.502	.196	.284	.489	.279
75	100						520																		
80	100	1.5	10.6	8.8	7.0	.44	440	2	1460	1450		178	13.94	15.67	76.17	1.29	1.04	.341	.366	.492	.733	.364	.443	.850	.493
80	100	1.2	11.3	9.0			560						14.97	10.03	76.06	1.19	1.03	.429	.45	.532	.840	.369	.482	.871	.533
85	100	1.0	11.0	9.0			520																		
100	100	1.5	12.1	6.3	3.1	.40	480	3	1540	1495		137	16.98	12.65	77.94	0.52	0.91	.440	.472	.597	.823	.478	.532	.950	.636
100	100	1.0	11.9	7.8			440					120	18.35	6.22	77.29	0.95	0.85	.504	.527	.634	.919	.482	.571	.916	.685
125	100						420			1500															
150	100	2.2	14.15	4.2	.57	0	350	0	128	1480		24.3	22.62	4.80	73.14	0.15	0.81	.779	.866	.718	.949	.596	.670	.989	.757
190	100	2.8	14.4	3.9			320																		
200	100						280	0	45	1450		24.4	21.75	5.78	73.20	0.09	0.80	.795	.907	.704	.936	.580	.657	.993	.750
													(22.21)							.711	.938	.592	.664	.993	.755
300	100	2.4	15.2	.32			320																		
350	100	2.0	15.5	.30			300	0		1340		16.6	39.10	4.91	59.56	0.05	0.67	.906	1.006	.871	.970	.819	.844	.997	.883
500	100	1.9	16.0	.10				0	6	1270		9.8	50.81	4.64	49.04	0.05	0.59	.953	1.051	.920	.978	.889	.901	.998	.921
800	100	1.8	16.7	.04			250			1250		11.3	58.26	6.94	42.82	0.09	0.48	.956	1.046	.941	.971	.924	.925	.997	.944

Table 8. Flame B1

		GAS COMPONENTS											SOLIDS ANALYSIS					DERIVED QUANTITIES							
AD	HP	O_2	CO_2	CO	H_2	CH_4	NO	NH_3	HCN	Temp.	Vel.	Solids	Ash	Volat.	C	H	N	B	H_2	C_x	Z_x	C_{fix}	Z_c	Z_h	Z_n
cm		% volume dry					ppm			°C	m/s	g/m^3	% wt. dry												
10	40	7.8	12.5	0			300			1025	0							1.0	1.55						
	70	7.8	12.5	0			300			1020	0±3							1.0	1.55						
	80	13.5	8.05	0			160			830	4.7							1.0	2.47						
	90	21.0	0	0			0			610	12.2							0							
	95	21.0	0	0			0					0						0							
	96	21.0	0	0			0			250		2.8	8.48	30.43	72.73	4.34	1.08	.001	4.87						
	98	21.0	0	0			0			250		(632)	6.96	32.34	74.27	4.62	1.06	.002	.213						
	100	21.0	0	0	0	0	0			250	39.6	(632)	8.41	32.82	73.41	4.52	1.08	.004	.217	.104	.073	.120	.111	.130	.128
	102	21.0	0	0			0			250		(632)	7.46	32.72	73.34	4.43	1.07	.006	.221						
	104	21.0	0	0			0			250		133	7.63	31.60	72.62	4.25	1.08	.011	.221						
	105	21.0	0	0			0					0						0							
50	40	7.5	12.4	0			300			1025	-3.0							1.0	1.53						
	70	9.5	11.0	0			240			970	0							1.0	1.76						
	80	16.0	5.5	0			100			810	7.1							1.0	3.55						
	90	20.8	0	0			9			630	11.6														
	95	20.8	0	0			0			350	17.1	106	11.86	37.00	69.72	4.18	1.10	.008	1.34	.394	.265	.463	.406	.434	.375
	98	20.8	0	0			0			260	25.6	413	7.49	32.09	73.14	4.45	1.12	.005	.331	-.02	-.02	-.02	.005	.039	-.02
	100	20.8	0	0	0	0	0			260	38.0	783	8.10	30.00	73.39	4.53	1.13	.003	.174	.066	.120	.038	.077	.095	.053
	105	20.8	0	0			0			350	16.9	693	7.30	28.96	74.04	4.53	1.12	.004	.196	-.04	.057	-.10	-.03	-.0	-.04
	110	20.8	0	0			7			650	14.6	30	13.63	37.78	72.50	4.32	1.18	.008	4.52	.478	.341	.551	.458	.487	.412
75	100	20.7	0	0	0	0	0			300	36.5														
100	20	7.5	12.4	.015			260			1030								1.0	1.53						
	40	7.8	12.3	.013			260			1030	-3.2							1.0	1.55						
	60	10.8	10.4	.007			220			1010	-3.0							1.0	1.91						
	70	13.2	8.1	.003			160			900	0							1.0	2.43						
	80	16.8	4.7	.002			90			810	7.4							1.0	4.13						
	90	18.8	2.1	.002			35	4.1	.4	700	11.2							1.0	8.83						
	95	20.0	0.4	.001			25	4.1	.8	450	22.1	93	7.57	29.69	72.46	4.25	1.00	.042	1.10	-.0	.068	-.04	.025	.092	.103
	97.5							6.4	.5																
	100	20.5	0	0	0	0	0	13.2	.8	430	31.7	695	7.83	31.69	72.51	4.37	1.05	.007	.199	.031	.038	.028	.057	.097	.09
	105	20.5	0	0			0	2.4	75	450	24.0	299	7.51	30.29	73.55	4.47	1.07	.006	.446	-.01	.042	-.04	.002	.037	.033
	110									700	12.6	20	27.73	31.29											
																				.786	.732	.814	-.03	-0.	-.04

Table 8. Flame B1 (Cont'd.)

		GAS COMPONENTS											SOLIDS ANALYSIS					DERIVED QUANTITIES							
AD	HP	O_2	CO_2	CO	H_2	CH_4	NO	NH_3	HCN	Temp.	Vel.	Solids	Ash	Volat.	C	H	N	N	N_T	C_x	Z_x	C_{fix}	Z_c	Z_h	Z_n
cm		% volume dry					ppm			°C	m/s	g/m³	% wt. dry												
125	40	7.4	12.5	.004	0	0	245			1020	-2.5							1.0	1.52						
	60	10.3	10.45	.003	0	0	205			990	-2.2							1.0	1.86						
	70	12.5	8.5	.001	0	0	140			940	1.0							1.0	2.29						
	80	16.0	5.9	.010	.04	0	100			860	8.1	9.1	33.31	12.56	57.60	1.47	0.90	.869	2.90	.835	.910	.795	.823	.928	.816
	90	18.0	3.8	.055	0	0	60	2.2	5.7	810	12.0	64	16.13	16.82	71.28	1.48	1.05	.384	1.67	.572	.752	.476	.550	.851	.558
	92.5							2.6	4.9																
	95	20.0	1.25	.065	.05	0	50	2.8	3.9	1050	26.6	207	14.41	17.15	72.97	2.40	1.12	.115	.716	.511	.717	.402	.484	.730	.472
	97.5							8.0	2.6																
	100	20.6	0	.05	.03	0	10	3.0	3.5	1050	32-35	(700)	7.72	31.0	72.87	4.35	1.02	.085	.199	.016	.046	.001	.039	.088	.103
	105	20.4	0	.10			35	5.0	84	800	20.2	587	7.48	30.80	72.91	4.34	1.05	.009	.235	-.02	.022	-.04	.007	.061	.047
	110	15.5	4.6	(3)			(100)	2.0	80	820	12.3	115	13.01	18.17	71.84	3.07	1.14	.310	.903	.450	.668	.336	.437	.618	.405
150	40	7.5	12.45	.008	0	0	240			1040	-3.0							1.0	1.53						
	60	10.0	10.45	.005	0	0	180			1010	-3.9							1.0	1.84						
	70	12.8	8.3	.008	0	0	160			970	2.0							1.0	2.35						
	80	15.0	6.65	.04	.09	0	120			920	7.8	4.6	35.43	23.17	51.07	2.10	1.02	.935	2.78	.853	.846	.856	.855	.905	.807
	90	16.3	5.1	.15	.09	0	140	1.8	99	885	12.0	59	11.48	23.92	71.30	3.40	1.13	.418	1.51	.365	.505	.291	.367	.521	.332
	92.5							1.3	86																
	95	9.2	7.9	4.5	.59	1.35	300	1.8	240	950	18.4	159	10.11	22.98	73.68	3.58	1.14	.285	.508	.268	.460	.167	.258	.427	.234
	97.5							2.5	122																
	100	17.0	3.5	3.0	4.05	2.46	110	5.7	138	1550	30.6	625	7.19	30.78	73.89	4.44	1.06	.044	.198	-.06	-.02	-.09	-.05	.001	-.0
	102.5							3.0	156																
	105	8.5	6.0	3.9	4.1	0.50	300	3.2	352	1590	20.9	135	10.14	23.87	75.36	2.94	1.03	.251	.501	.271	.440	.181	.243	.531	.310
	110	13.0	5.5	3.0	.83	1.0	210	3.6	338	1410	16.4	(50)	12.51	18.84	74.46	2.28	1.00	.413	1.102	.424	.642	.309	.394	.705	.457
175	40	8.2	11.65	.02	0	0	225											1.0	1.61						
	60	10.0	10.45	.05	0	0	180											.998	1.83						
	70	12.8	8.5	.05	0	0	150											.998	2.31						
	80	14.0	7.0	.05	0	0	190	6.3	37			1.6	31.78	11.32	59.33	1.46	0.85	.975	2.67	.823	.915	.775	.809	.925	.818
	90	12.5	8.1	.50	.11	0	330	3.5	163			65	17.23	14.19	72.99	1.57	0.91	.516	1.14	.604	.804	.499	.568	.852	.641
	92.5							2.0	384																
	95	7.0	9.75	6.0	1.30	.24	350	2.0	254			186	14.07	(10.32)	77.20	1.90	1.04	.354	.497	.497	.825	.323	.441	.781	.448
	97.5							2.4	587																
	100	2.0	7.75	9.0	4.83	.20	625	2.4	1042	1600		462	12.00	16.29	77.72	2.22	1.13	.198	.219	.396	.677	.248	.340	.700	.361

Table 8. Flame B1 (Cont'd.)

		GAS COMPONENTS											SOLIDS ANALYSIS					DERIVED QUANTITIES							
AD	HP.	O_2	CO_2	CO	H_2	CH_4	NO	NH_3	HCN	Temp.	Vel.	Solids	Ash	Volat.	C	H	N	N	N_2	C_x	Z_x	C_{Eff}	Z_c	Z_h	Z_n
cm		% volume dry					ppm			°C	m/s	g/m³	% wt. dry												
175	102.5							3.2	1305																
	105	3.2	9.25	4.8	3.41	1.44	330	4.5	2955			273	11.09	13.43	75.18	2.53	1.07	.130	.211	.340	.712	.143	.309	.631	.345
	110							3.8	651																
190	40	8.1	11.9	.006	0	0	220			1040	-3.0							1.0	1.60						
	60	11.1	9.75	.009	0	0	185			1005	0							1.0	1.99						
	70	13.0	8.4	.03	0	0	170			1000	8.0		68.23	8.30				.999	2.35	.961	.971	.957			
	80	13.0	8.05	.05	0	0	180			985	7.6	13	31.53	17.89	59.64	1.39	0.89	.862	2.06	.821	.865	.798	.807	.928	.808
	85	13.5	7.7	.14	.04	0	250	4.7	67	1020	10.6	24	20.12	15.02	70.20	1.38	1.03	.739	1.82	.673	.822	.594	.644	.889	.652
	90	11.5	8.75	.48	.10	0	420	3.8	90	1385	10.9	105	16.20	12.46	70.94	1.31	0.98	.457	.897	.574	.817	.445	.554	.869	.589
	95	8.8	10.4	4.5	.77	0	500	1.5	250	1515	30.1	184	14.48	9.47	74.70	1.36	1.02	.385	.577	.514	.844	.339	.474	.848	.522
	97.5							4.9	415																
	100	3.0	8.65	10.0	4.66	1.53	600	5.3	1140	1540	29.7	256	11.31	12.00	75.51	2.48	1.13	,252	.294	.355	.748	.147	.320	.645	.322
	102.5							5.0	722																
	105	2.1	10.75	10.0	4.47	.28	620	5.4	880	1540	16.5	(260)	11.04	11.00	73.99	2.74	1.18	.296	.325	.424	.763	.111	.370	.799	.462
	110	6.0	10.0	5.5	1.26	0	600	4.1	890	1570	15.4	197	12.5	12.29	77.27	1.55	0.99	.359	.480						
195	100							3.2	792																
300	40	8.1	12.5	.004	0	0	310			1115	-7.5	4.5	67.96	(12.18)	10.91	0.11	0.23	.994	1.56	.988	.967	1.0	.987	.997	.982
	60	8.4	12.15	.012	0	0	300			1140	-1.0	5.5	75.70	6.05	22.83	0.18	0.34	.983	1.57	.973	.901	.969	.969	.996	.969
	80	7.1	12.5	.15	0	0	390	5.3	37	1280	7.1	11.5	51.34	3.10	46.63	0.27	0.46	.933	1.39	.922	.985	.888	.907	.991	.939
	90	5.0	13.75	4.8	.29	0	530	6.0	73	1410	10.9	54.4	21.16	0.97	73.87	0.68	0.74	.670	.837	.693	.989	.536	.644	.948	.762
	100	1.7	13.9	6.0	1.73	0	580	5.4	254	1420	14.6	152	17.19	2.37	78.53	0.86	0.80	.465	.611	.603	.967	.411	.534	.919	.684
	105							4.8	345																
	110	2.1	13.3	6.0	2.05	0	500	4.9	150	1425	14.7	127	17.24	2.16	77.14	0.73	0.96	.490	.538	.609	.970	.411	.544	.931	.622
	120	4.5	14.0	3.0	.49	0	570	5.0	92	1430	11.8	56.2	22.03	4.60	73.79	0.30	0.77	.675	.835	.708	.950	.580	.658	.977	.762
350	110	2.5	14.4	3.9			540																		
450	40	4.5	14.6	.012	0	0	380			1155		5.3	89.36	3.48	8.35	0.03	0.19	.995	1.26	.990	.990	.989	.990	.999	.985
	60	4.1	14.6	.04	0	0	410	6.0	1.4	1160	3.4	5.8	74.94	1.78	25.31	0.16	0.27	.983	1.22	.972	.994	.960	.965	.996	.975
	80	3.5	15.0	.10	0	0	450	5.4	2.2	1230	8.8	21.5	51.56	1.44	50.26	0.30	0.46	.897	1.08	.922	.993	.885	.900	.990	.939
	100	2.5	15.5	.42	0	0	460	5.2	4.4	1285	8.0	31.3	31.87	2.49	65.57	0.50	0.68	.825	.937	.824	.989	.740	.799	.974	.855
	120	2.5	15.5	.42	0	0	470	6.4	0.7	1305	8.1	37.9	30.01	2.61	67.88	0.44	0.77	.794	.901	.808	.979	.717	.769	.976	.825
	140	4.3	14.6	.04	0	0	430			1300		12.3	43.52	3.11	53.77	0.32	0.61	.933	1.17	.893	.983	.845	.874	.988	.904
530	40	4.0	15.0	.005	0	0	400																		
	60	3.5	15.0	.018	0	0	420																		
	100	2.8	15.5	.18	0	0	440		.7	1270	9.1	16.1	42.04 45.06	2.17	54.17	0.30	0.36	.917	1.06	.886	.987	.833	.868	.988	.941

Table 8. Flame B1 (Cont'd.)

		GAS COMPONENTS											SOLIDS ANALYSIS					DERIVED QUANTITIES							
AD	HP	O_2	CO_2	CO	H_2	CH_4	NO	NH_3	HCN	Temp.	Vel.	Solids	Ash	Volat.	C	H	N	N	N_2	C_x	Z_x	C_{fix}	Z_c	Z_h	Z_n
cm		% volume dry					ppm			°C	m/s	g/m^3	% wt. dry												
	120	3.0	15.5	.08	0	0	430																		
	160	4.0	14.7	.026	0	0	420																		
800	100	1.8	16.8	.02	0		380			1220		8.9	65.41	3.78	31.05	0.12	0.36	.974	1.07	.956	.986	.940	.951	.997	.962
													57.15	1.94	43.15	0.11	0.45			.938	.991	.909	.923	.996	.946
												11.4	65.76	2.70						.957	.990	.939			

Table 9. Flame B2

		GAS COMPONENTS											SOLIDS ANALYSIS					DERIVED QUANTITIES							
AD	HP	O_2	CO_2	CO	H_2	CH_4	NO	NH_3	HCN	Temp.	Vel.	Solids	Ash	Volat.	C	H	N	N	M_2	C_x	Z_x	C_{fix}	Z_c	Z_h	Z_m
cm		% volume dry					ppm			°C	m/s	g/m³	% wt. dry												
20	100	20.8	0	0			2		0	260		586	7.68	33.78	72.85	4.50	1.08	.003	.233	.011	-.04	.040	.034	.052	.045
20	100												8.18	34.17											
50	100	20.5	0.3	0			5	4.6	0	380		570	7.01	32.70	72.54	4.33	1.13	.012	.246	.076 -.09	-.007 -.11	.113 -.08	.093 -.05	.110 .001	.104 -.09
50	100												8.02	35.16						.056	-.04	.108	.079	.126	.043
80	100	20.4	0.4	0			3	11.8	0	520		560	7.59	30.01	73.33	4.29	1.03	.016	.250	-0.	.060	-.03	.016	.086	.079
100	100	20.8	0	0			6	11.8	0	620		540	7.13	31.20	71.53	4.20	1.06	.011	.265	-.07	-.04	-.09	-.02	.047	-.01
120	100	20.2	0.5	.04			15	26	0	720		480	7.60	30.00	72.28	4.32	1.03	.016	.289	0	.062	-.03	.031	.080	.080
140	100	17.5	3.0	.50			26	3.0	4	920		400	7.48	30.04	71.30	4.16	1.08	.069	.341	-.02	.046	-.05	.029	.100	.020
150	100	5.5	6.2	4.2	1.0	0		1	12	1090															
160	100	3.0	8.75	9.0	6.8	.7	340	3.1	75	1200		331	10.03	23.91	71.04	4.00	1.06	.183	.220	.262	.433	.171	.278	.355	.282
170	100	1.8	8.9	12.0	11.3	2.4	400			1430			8.68							.134	.345	.022	.166	.254	.171
180	100	2.2	10.5	15.0	4.3	.58	530	3.6	909	1450		264	10.06	25.20	73.09	3.25	1.09	.301	.327	.264	.405	.190	.260	.477	.264
190	100	2.2	11.0	14.6	3.8	1.5	580		988	1460		248	10.76	24.60	72.68	3.21	1.06	.301	.327	.317	.457	.244	.312	.517	.331
200	100	1.4	11.5	12.5			600	6.9	1115	1460															
220	100							11	368																
280	100	1.3	13.75	6.6	2.1	1.0	560	13	250	1420		155	15.04	6.51	76.86	1.20	0.91	.429	.453	.535	.897	.343	.479	.870	.589
300	100	1.2	14.15	6.0	1.8	0	500			1400															
310	100	1.3	14.4	5.2	1.7		450	3.5	317	1395		89.5	18.35	3.72	78.09	0.88	0.85	.565	.598	.634	.951	.465	.566	.922	.685
330	100	1.5	14.7	4.4			430			1380		66.6	20.97	2.92	76.96	0.76	0.84	.647	.693	.690	.966	.543	.626	.941	.728
350	100	1.7	15.0	3.2				6.1	136	1375		,29.1	25.87	7.57	71.53	0.60	0.77	.788	.855	.764	.930	.676	.718	.962	.798
450	100	2.1	15.5	.54			420	3.5	10	1340															
500	100	2.1	16.4	.28			420			1325		18.4	47.34	4.30	51.60	0.26	0.50	.912	1.012	.908	.978	.871	.889	.991	.928
800	100	1.9	16.7	.01			430			1300		6.3	68.00	1.66				.988	1.086	.961	.994	.943	.969	.996	.973
		1.9	16.7	.01								5.1	78.57	4.16	20.35	0.14	0.27	.990	1.088	.977	.987	.972	.973	.997	.976

Table 10. Flame B3

		GAS COMPONENTS											SOLIDS ANALYSIS					DERIVED QUANTITIES							
AD	Mr	O_2	CO_2	CO	H_2	CH_4	NO	NH_3	HCN	Temp.	Vel.	Solids	Ash	Volat.	C	H	N	N	N_2'	C_x	Z_x	C_{fix}	Z_c	Z_h	Z_n
cm		% volume dry					ppm			°C	m/s	g/m^3	% wt. dry												
0	100	21	0	0			0			350		343	7.53	32.95	74.09	4.58	1.14	.003	.393	-.01	-.04	.005	-.0	.016	-.03
10	100	21	0	0			0			600		340	7.56	31.63	74.23	4.63	1.13	.002	.394	-0.	.006	-.01	0	.009	-.01
15	100									675															
20	100	20.9	0	.002			15			885		340	7.41	31.40	74.57	4.61	1.13	.003	.392	-.03	-.01	-.04	-.02	-.01	-.03
													7.59	30.82											
30	100	20.8	.1	.004			10			1020		340	7.56	31.98	74.50	4.62	1.08	.005	.392	-.0	-.0	-.01	-.0	.011	.03
													6.53	30.97											
50	100	19.5	1.5	.05	.11	0	30	5	19	1300		330	7.61	31.65	73.91	4.40	1.12	.040	.405	.001	.012	-.0	.011	.065	.001
80	100	7.8	9.0	5.2	1.0	.13	270	17	1670	1470		310	8.67	28.43	75.43	4.07	1.12	.216	.333	.133	.221	.087	.114	.240	.123
100	100	4.5	10.5	6.0	1.8	.19	560	4	2510	1520		274	12.87	12.05	76.12	2.44	1.08	.290	.361	.443	.777	.265	.397	.693	.430
													(11.98)							.395	.761	.202	.353	.670	.388
120	100	2.8	11.4	6.6	2.5	1.2	580	3	2720	1515		237	12.00	9.15	78.32	1.49	1.04	.320	.364	.396	.818	.173	.335	.799	.411
													(12.54)							.426	.826	.214	.364	.807	.437
150	100	2.0	12.1	6.6	3.1	1.8	550	3	2320	1465		155	14.52	5.09	79.99	0.98	0.87	.375	.411	.515	.916	.303	.439	.890	.593
190	100	2.2	12.9	6.0	2.4	0	450	3	1160	1450		120	16.20	6.65	80.59	0.73	0.84	.483	.535	.574	.902	.400	.493	.427	.648
265	100	2.3	14.75	4.2	0.93	0	400	3	120	1425															
280	100	2.8	14.75	3.5	0.6	0	380			1420		12.6	23.97	2.18	72.04	0.53	0.81	.841	.962	.739	.978	.612	.694	.964	.770
350	100	2.5	15.65	0.4			340			1405		25.7	34.72	3.15	60.23	0.39	0.69	.861	.977	.845	.978	.774	.823	.981	.865
350	100											16.0	37.01	5.36				.905	1.028	.660	.965	.804	.834	.982	.873
500	100	2.4	16.25	.06			330			1335		13.4	46.95	2.30	47.58	0.30	0.51	.941	1.061	.907	.988	.863	.896	.989	.926
500	100											12.3	53.29	2.38				.945	1.066	.927	.989	.895	.909	.990	.935
800	100	1.0	17.0	.017			320			1260		9.3	66.52	4.31	30.91	0.09	0.37	.974	1.064	.950	.984	.944	.952	.997	.962

8.0 PHOTOGRAPHS OF FLAMES

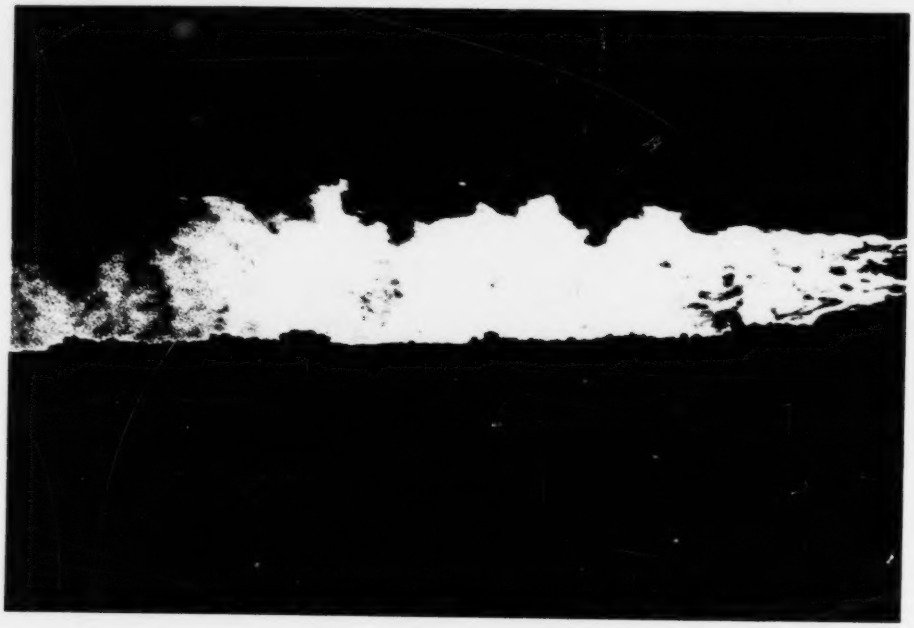

FLAME A4

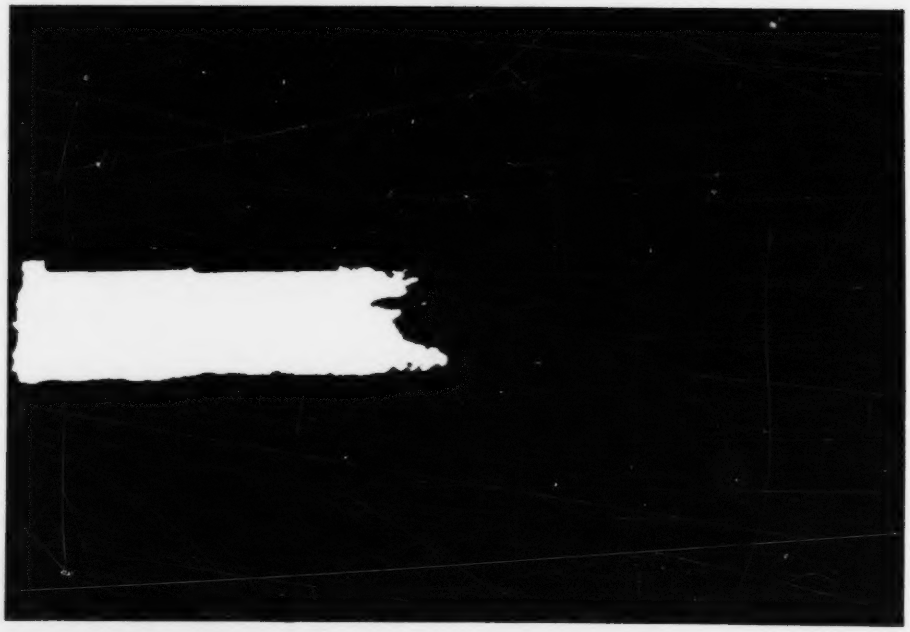

FLAME B1

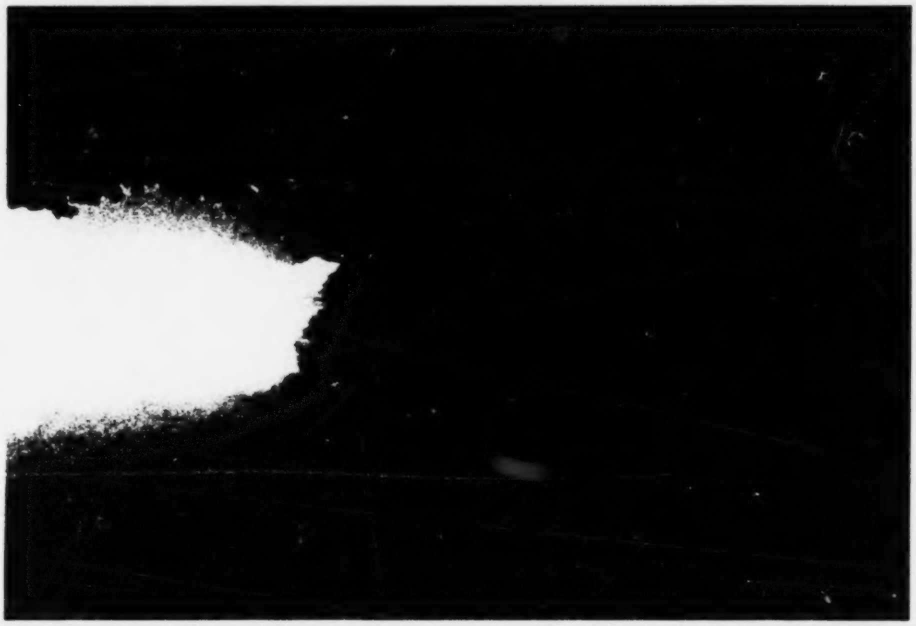

FLAME B2

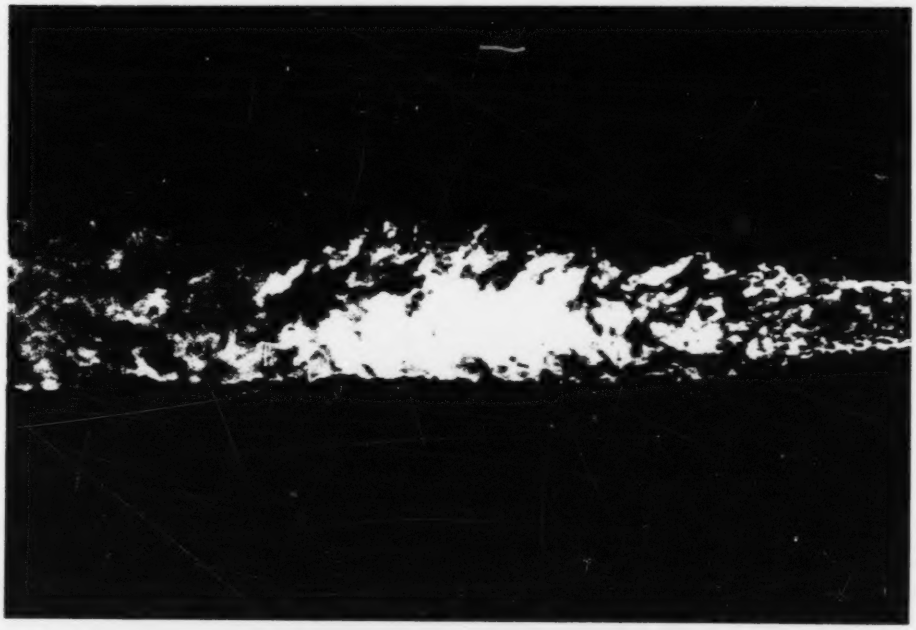

FLAME B3

III. HEAVY OIL SPRAY COMBUSTION IN SHEAR LAYERS

Prepared by:

A. Vranos
B. A. Knight

United Technologies Research Center
East Hartford, Connecticut

Prepared for:

Energy & Environmental Research Corporation
EER Subcontract No. EER-8318-7

TABLE OF CONTENTS

Section Page

LIST OF FIGURES. . . . . III-iii

LIST OF TABLES . . . . III-iv

ABSTRACT III-1

1.0 INTRODUCTION III-3

2.0 APPARATUS - DESIGN AND DESCRIPTION III-4

2.1 Combustor III-4

2.1.1 Droplet Trajectories III-4
2.1.2 Fuel Injection System III-9
2.1.3 Wind Tunnel. III-14
2.1.4 Hot Gas Generator. III-14
2.1.5 Combustion Chamber III-15

2.2 Fuel System III-15
2.3 Sampling Probe. III-17
2.4 Sampling System III-19

3.0 TEST RESULTS III-23

3.1 Fuel Injector Development III-23
3.2 Cold Flow Velocity Profiles III-25
3.3 Recirculation Studies III-27
3.4 Flame Stability Tests III-29
3.5 Flame Probing III-30

3.5.1 Apparatus Improvements III-31

3.6 Flame Photography III-34

4.0 CONCLUSIONS. III-36

5.0 REFERENCES III-37

LIST OF FIGURES

Figure		Page
1	Heavy Oil Spray Combustor	III-5
2	Droplet Trajectories.	III-7,8
3	Multiple Capillary Fuel Manifolds	III-10
4	Fuel Injectors on Support Rack.	III-12
5	Oil Droplet Injector Enclosure.	III-13
6	Heavy Oil Combustor Fuel System	III-16
7	Phase Sensitive Probe	III-18
8	Heavy Oil Combustor Gas Sampling System	III-20
9	Velocity Profiles	III-28
10	Oxygen Profiles	III-32
11	Shear Layer and Droplet Combustion Photographs.	III-35

LIST OF TABLES

Table Page

I Calibration Gas Data III-22

II No. 2 Oil Injection Test Results: Single Capillary. . III-24

III No. 6 Oil Injection Test Results: Multiple Capillary. III-26

ABSTRACT

This report summarizes the work done under Contract EER-8318-7, a twelve month study of heavy oil spray combustion in shear layers. The program consisted of two phases: (1) design and fabrication of an apparatus, and (2) preliminary combustion experiments. A unique shear layer mixing and combustion apparatus was developed which simulates high shear, diffusive combustion with heavy oil droplet injection as found in the near-field combustion zone of boilers and furnaces. The apparatus provides: (1) two dimensional mixing and combustion of uniform streams of air and rich combustion products fed from opposite sides of a splitter plate, (2) uniform injection of a monodisperse heavy oil spray into the shear layer by means of a linear array of fuel injectors located beneath the combustor wall, (3) control of droplet path, residence time, and extent of vaporization, (4) control of hot and cold stream inlet properties and (5) three dimensional probing of the flow field.

The design phase of the program consisted of two tasks: aerodynamic and thermodynamic design, and mechanical design. A wind tunnel, hot gas generator, combustion chamber, droplet injection system, and phase-sensitive sampling probe were designed in the first task. The design of the apparatus was influenced most strongly by the diverse requirements of the fuel injection system. The injector was designed so that the angle of droplet penetration into the shear layer could be varied over a wide range. Droplet trajectories were computed for vaporizing No. 6 oil droplets injected from the floor of the combustor into a hot, rich environment provided by a hot gas generator. Hot gas generator dimensions and injector locations were selected to accommodate the required droplet trajectories, provide complete vaporization if desired, and provide sufficient hot soak time for substantial conversion of volatile fuel nitrogen compounds to molecular nitrogen. The design of a low turbulence wind tunnel, combustion chamber, and phase sensitive probe completed this task.

The experimental phase of the program consisted of (1) verification of uniform properties of the hot and cold streams at the splitter plate trailing edge, (2) demonstration of high injection velocities and uniform droplet size and penetration with No. 2, 5 and 6 oils in vibrating multicapillary injectors, (3) determination of stable flow regimes as a function of primary and secondary

stream velocities, (4) flame stability and flashback studies, (5) high speed cinematography of the shear layer with injection of No. 2 and No. 6 fuel oil, and (6) preliminary flame probing.

1.0 INTRODUCTION

The control of NO_x and particulates from the combustion of heavy, nitrogen-containing oils is, in practice, a very difficult problem. The most promising strategy for NO_x control proposes rich combustion with high conversion of fuel nitrogen to molecular nitrogen followed by second stage combustion of unburned fuel. This strategy engenders a high risk of producing particulates, however. Although some general statements can be made as to necessary conditions for limiting NO_x and soot in homogeneous systems with simple fuels, these guidelines are not very useful in heterogeneous and/or inhomogeneous systems as found in practice. In order to develop a predictive capability, and in particular, to tie this capability to a rich burn strategy, careful experiments are first required which will provide information on the effect of key variables such as temperature, equivalence ratio, mixing rate, and droplet dynamics on the rate of combustion and the production of NO_x and particulates.

The purpose of this study was to develop an apparatus and conduct experiments with No. 6 oil, or similar fuels, which simulates high-shear, diffusive combustion with oil droplet injection as found in the near field combustion zone of boilers and furnaces. The apparatus attempts to isolate as much as possible, the effects of key variables. The shear layer in the vicinity of the fuel injector is of particular interest, and the apparatus simulates the shear layer near the injector by providing a mixing layer between a cold, fast-moving stream and a hot, slow-moving stream into which droplets may be injected. Variable angle droplet injection is provided so that two important modes of droplet distribution can be studied: (1) droplet distribution dominated by ballistics, or (2) droplet distribution dominated by turbulence. The effect of prevaporization and extended hot soak time on the formation of NO_x and particulates may also be studied by varying injection parameters.

2.0 APPARATUS - DESIGN AND DESCRIPTION

The apparatus is designed to allow control over droplet ballistics, mixing rate, and conditioning of vaporized fuel prior to combustion. Droplet trajectories were the most important factor influencing the geometry and overall scale of the apparatus. The maximum droplet velocity attainable with No. 6 oil in a vibrating capillary injector producing a monodisperse spray was an important consideration, since this determined maximum droplet penetration into a hot, moving stream. The dimensions of this stream were to be as large as possible for the purpose of minimizing temperature gradients in the stream, maximizing the working length of the combustor and for providing sufficient residence time for vaporization. Minimum hot gas flows were set by the requirements of minimum heat loss and flashback. Experiments early in this design phase established maximum attainable droplet velocities.

2.1 Combustor

A schematic of the combustor is shown in Figure 1. The combustor consists of four main sections: (1) wind tunnel, (2) hot gas generator, (3) fuel injection system, and (4) combustion chamber. Since the requirements imposed by the fuel injection system influenced the design most strongly, this section is discussed first.

2.1.1 Droplet Trajectories

One of the most important considerations in the apparatus design was the ability to conduct limit case experiments centered about the mode of transport of droplets or vaporized fuel into the shear layer. Three important cases were considered: (a) ballistic transport of droplets into the shear layer, (b) diffusional transport of droplets in the shear layer and (c) introduction of vaporized fuel into the shear layer. A concomitant factor was allowance for sufficient vapor phase residence time in fuel-rich combustion products so that substantial conversion of fuel nitrogen to molecular nitrogen could occur. The droplets are to be injected into the hot, moving stream in a manner simulating the penetration of a combustion zone in the near field of a practical combustor. Thus, in a two dimensional simulation, injection is made from injectors in the hot stream or from injectors located beneath the hot wall. The latter approach was considered the most practical. The computation of droplet trajectories strongly influenced the selection of channel height, splitter plate length and

FIG. 1 HEAVY OIL SPRAY COMBUSTOR

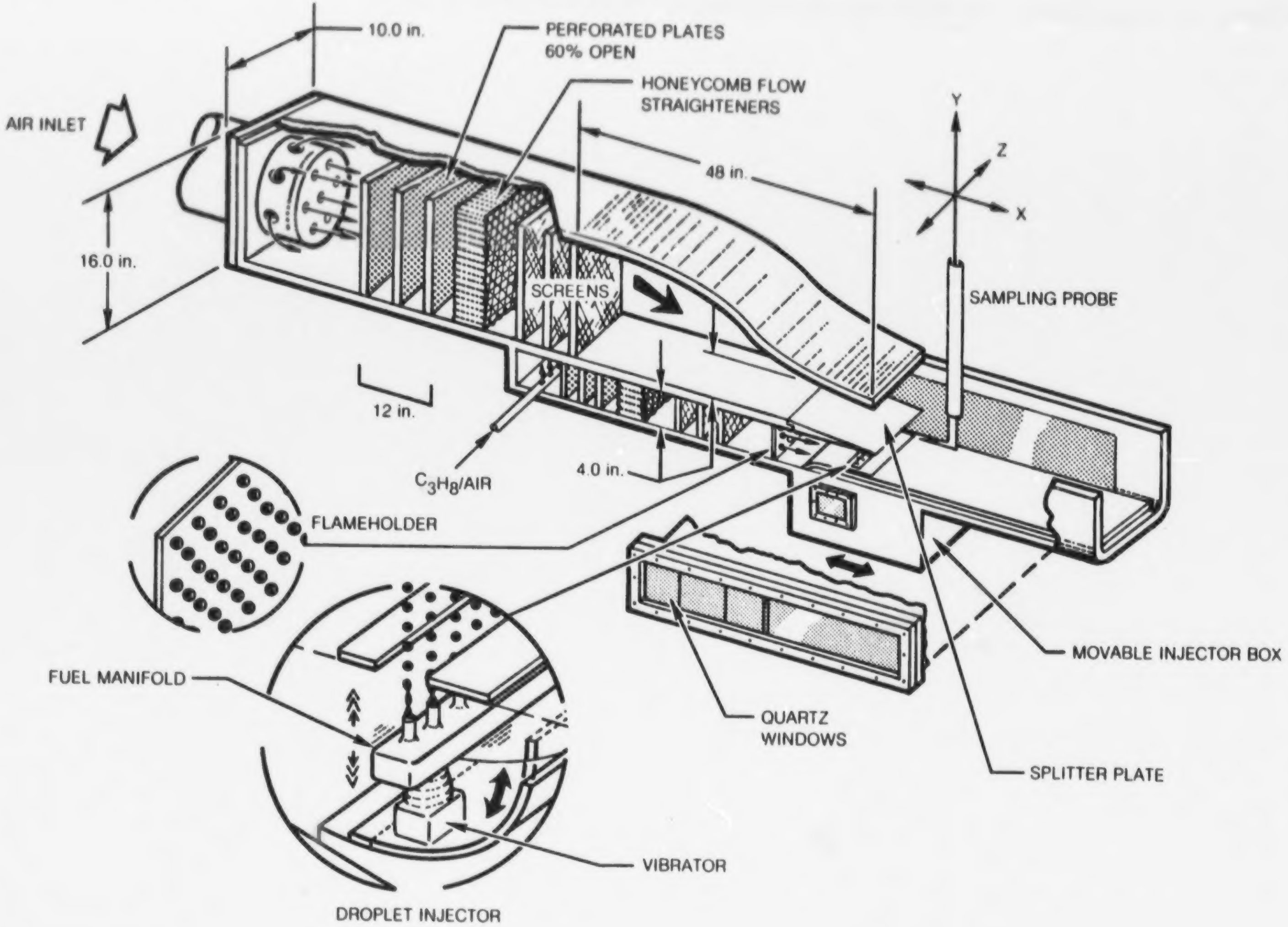
10.0 in.
PERFORATED PLATES 60% OPEN
HONEYCOMB FLOW STRAIGHTENERS
AIR INLET
48 in.
Y
Z
X
16.0 in.
SCREENS
SAMPLING PROBE
12 in.
C_3H_8/AIR
4.0 in.
FLAMEHOLDER
FUEL MANIFOLD
QUARTZ WINDOWS
MOVABLE INJECTOR BOX
SPLITTER PLATE
VIBRATOR
DROPLET INJECTOR

droplet injection location. Calculation of droplet trajectories indicated a variable injection location was required.

A computer code was developed for computing trajectories of vaporizing droplets. The code includes the effects of convective heat transfer and droplet heat-up rates. Droplet dynamics were examined for the three cases under consideration, (a) ballistic penetration of the shear layer, (b) diffusional penetration of the shear layer, and (c) prevaporization. The time history of droplet diameter and position was calculated for various initial droplet diameters as a function of gas velocity, droplet injection velocity, injection angle, and initial droplet temperature. The effect of combustor geometry upon the droplet trajectories was also investigated. The accompanying figures illustrate some of the more interesting results of these calculations. A "D-squared" burning law is assumed and the vaporization constant used for the calculations was 0.01 cm^2/sec (Kobayasi, 1955).

In order to demonstrate case (c) above, it was determined that the only way to prevaporize in a relatively short length was to inject the droplet upstream into the hot gas flow. Upstream injection enhances the vaporization because the relative velocity between droplet and fluid is increased. Computed droplet trajectories for relatively low injection velocity and for two droplet sizes are shown in Figure 2a. It is seen that a 300 micron droplet penetrates farther upstream than a 200 micron droplet, but at the first shear layer entry point (corresponding to the larger droplet), both droplets have vaporized to the same extent. The smaller droplet vaporizes to a greater extent by the time the second entry point is reached, however, excessive length is required. Therefore, case (c) is better served by large droplet diameter, and the hot gas channel height must be large enough to accommodate this droplet trajectory.

For the droplet to enter the layer partially vaporized at a shallow angle, as in case (b), the minimum entry angle occurs when the gas velocity is maximum. This also means that a droplet injection location different from case (c) must be used. Injecting at a location further upstream at a given gas and droplet velocity results in droplet entry at a shallower angle, but the droplet is more highly vaporized. Injecting too far downstream results in too steep an angle of penetration. The angle of entry and percent vaporized are strongly dependent upon droplet injection point. The gas velocity also effects the

FIG. 2 DROPLET TRAJECTORIES

SPLITTER HEIGHT: 13.2 CM

SCALE 1:2

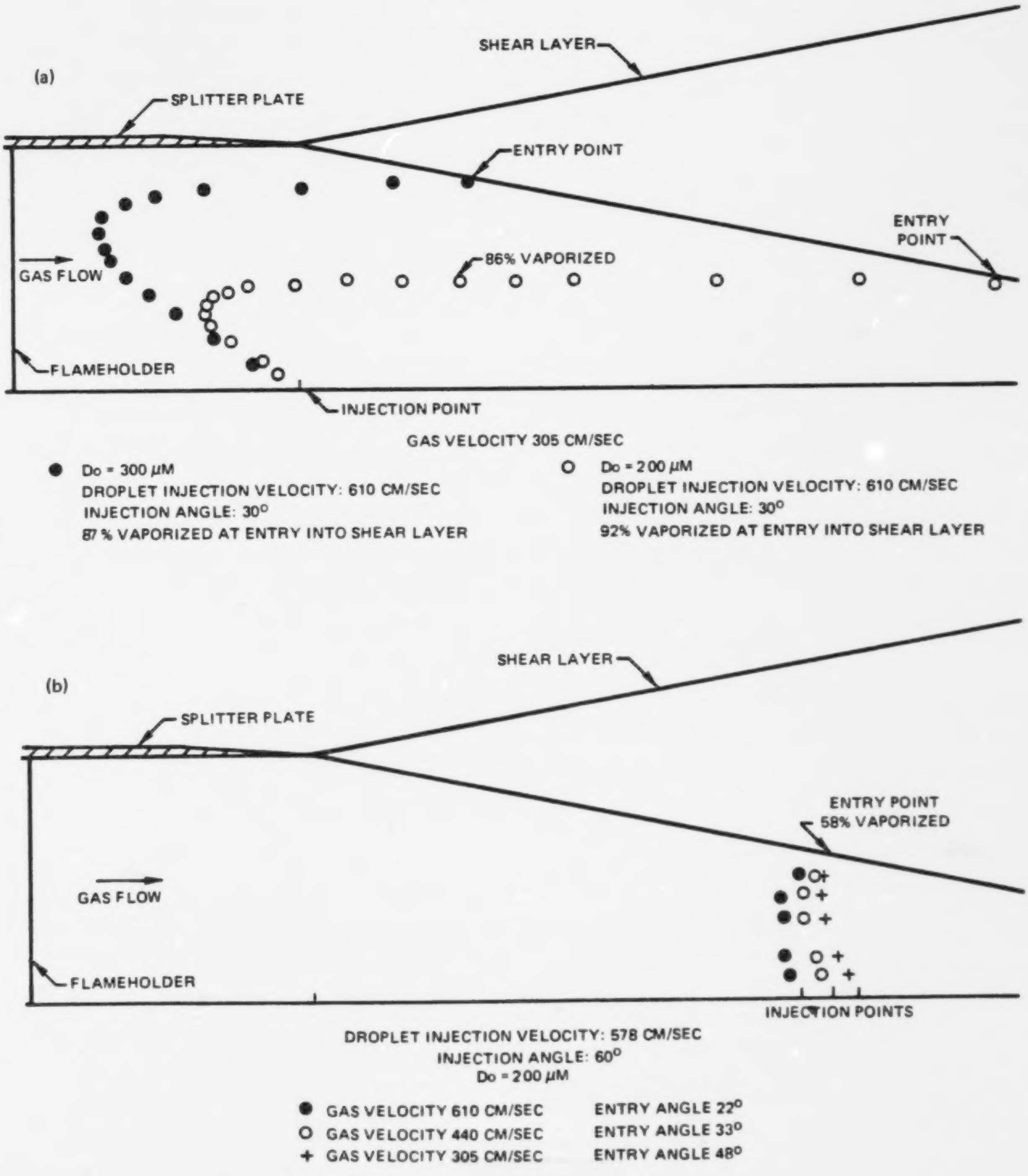
(a)
SHEAR LAYER
SPLITTER PLATE
ENTRY POINT
ENTRY POINT
86% VAPORIZED
GAS FLOW
FLAMEHOLDER
INJECTION POINT
GAS VELOCITY 305 CM/SEC
● Do = 300 μM
DROPLET INJECTION VELOCITY: 610 CM/SEC
INJECTION ANGLE: 30°
87% VAPORIZED AT ENTRY INTO SHEAR LAYER
○ Do = 200 μM
DROPLET INJECTION VELOCITY: 610 CM/SEC
INJECTION ANGLE: 30°
92% VAPORIZED AT ENTRY INTO SHEAR LAYER
(b)
SHEAR LAYER
SPLITTER PLATE
ENTRY POINT
58% VAPORIZED
GAS FLOW
FLAMEHOLDER
INJECTION POINTS
DROPLET INJECTION VELOCITY: 578 CM/SEC
INJECTION ANGLE: 60°
Do = 200 μM
● GAS VELOCITY 610 CM/SEC ENTRY ANGLE 22°
○ GAS VELOCITY 440 CM/SEC ENTRY ANGLE 33°
+ GAS VELOCITY 305 CM/SEC ENTRY ANGLE 48°

FIG. 2 DROPLET TRAJECTORIES (CONT.)

SPLITTER HEIGHT: 13.2 CM
SCALE 1:2

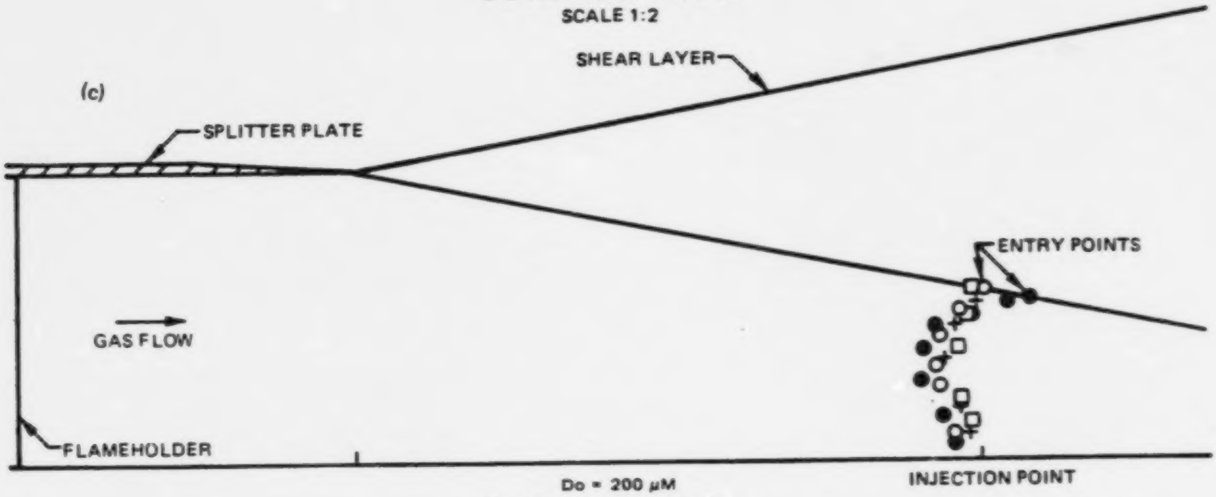
(c)
SHEAR LAYER
SPLITTER PLATE
ENTRY POINTS
GAS FLOW
FLAMEHOLDER
INJECTION POINT

Do = 200 μM
GAS VELOCITY 610 CM/SEC

●	DROPLET INJECTION VELOCITY 666 CM/SEC AT 49°	ENTRY ANGLE 8°, 67% VAPORIZED
○	DROPLET INJECTION VELOCITY 625 CM/SEC AT 53°	ENTRY ANGLE 25°, 58% VAPORIZED
+	DROPLET INJECTION VELOCITY 593 CM/SEC AT 58°	ENTRY ANGLE 42°, 51% VAPORIZED
□	DROPLET INJECTION VELOCITY 578 CM/SEC AT 60°	ENTRY ANGLE 43°, 51% VAPORIZED

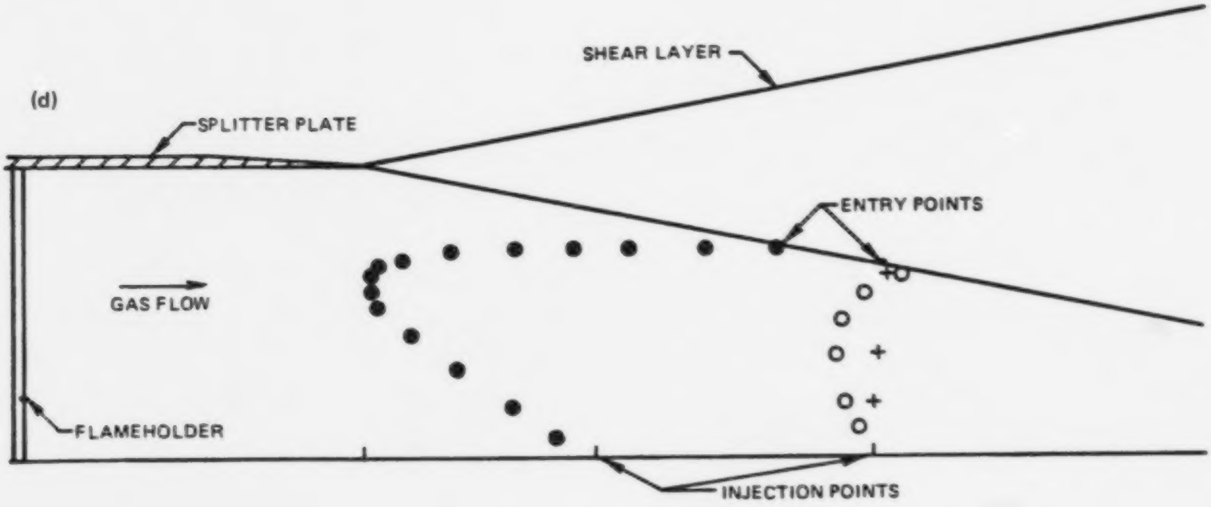
(d)
SHEAR LAYER
SPLITTER PLATE
ENTRY POINTS
GAS FLOW
FLAMEHOLDER
INJECTION POINTS

Do = 200 μM

● GAS VELOCITY 305 CM/SEC
DROPLET INJECTION VELOCITY 1000 CM/SEC
INJECTION ANGLE 30°
90% VAPORIZED AT ENTRY INTO SHEAR LAYER

+ GAS VELOCITY 305 CM/SEC
DROPLET INJECTION VELOCITY 1000 CM/SEC
INJECTION ANGLE 90°
33% VAPORIZED AT SHEAR LAYER, ENTRY AT 81%

○ GAS VELOCITY 610 CM/SEC
DROPLET INJECTION VELOCITY 635 CM/SEC AT 60°
58% VAPORIZED AT SHEAR LAYER, ENTRY AT 25°

angle of droplet entry into the shear layer as shown in Figure 2b. It is seen that for a relatively fixed injection location, entry point, and extent of vaporization, the angle of entry is controlled by gas velocity.

The effects of droplet injection velocity and angle are shown in Figure 2c. This figure illustrates an interesting point. Because the location of the shear layer is fixed by the height of the splitter plate, there is only one choice of droplet injection parameters which will result in a partially vaporized droplet entering the shear layer at a shallow angle. Altering the angle or velocity will increase one parameter (angle at entry) but decrease the other (percent vaporized at entry). Possible combinations are shown in Figure 2c.

The optimum configuration for all three cases is shown in Figure 2d. Two injection locations and two gas velocities allow all three cases to be studied. Continuous variation of injector location is provided between the two extremes shown in Figure 2d. The flameholder height (distance from bottom wall to splitter plate) for the conditions of Figure 2d is 13.2 cm. Since the maximum upstream droplet penetration location coincides with the splitter plate trailing edge location, the flameholder may be as close to this location as desired consistent with the condition that flameholder wake effects are minimized. A length of about 2.5 cm is required for this purpose. However, it may be desirable to study the effects of high vapor fuel feed rate by injecting droplets larger than 200 micron. For this case, the distance between the flameholder and splitter plate trailing edge will be approximately 15 cm (see Figure 2a) in order to provide sufficient length for vaporization of larger droplets. Also, estimates of characteristic times for conversion of vapor phase fuel nitrogen to molecular nitrogen indicate that with the long splitter plate, ample time is provided before the fuel vapor enters the shear layer (~ 80 msec).

2.1.2 Fuel Injection System

The primary fuel injection system is a two-dimensional linear array of capillaries with variable angle injection. Prior experience with electromagnatic vibrators in the production of mono-disperse single droplet streams was applied to the development of a multiple capillary injector. Figure 3 shows the configuration of the fucl manifolds. The twelve capillaries, spaced 0.635 cm apart, are 0.010 cm I.D., 0.023 cm O.D. stainless steel tubes. Each tube is carefully cut to length and polished to ensure uniformity. The

FIG. 3 MULTIPLE CAPILLARY FUEL MANIFOLDS

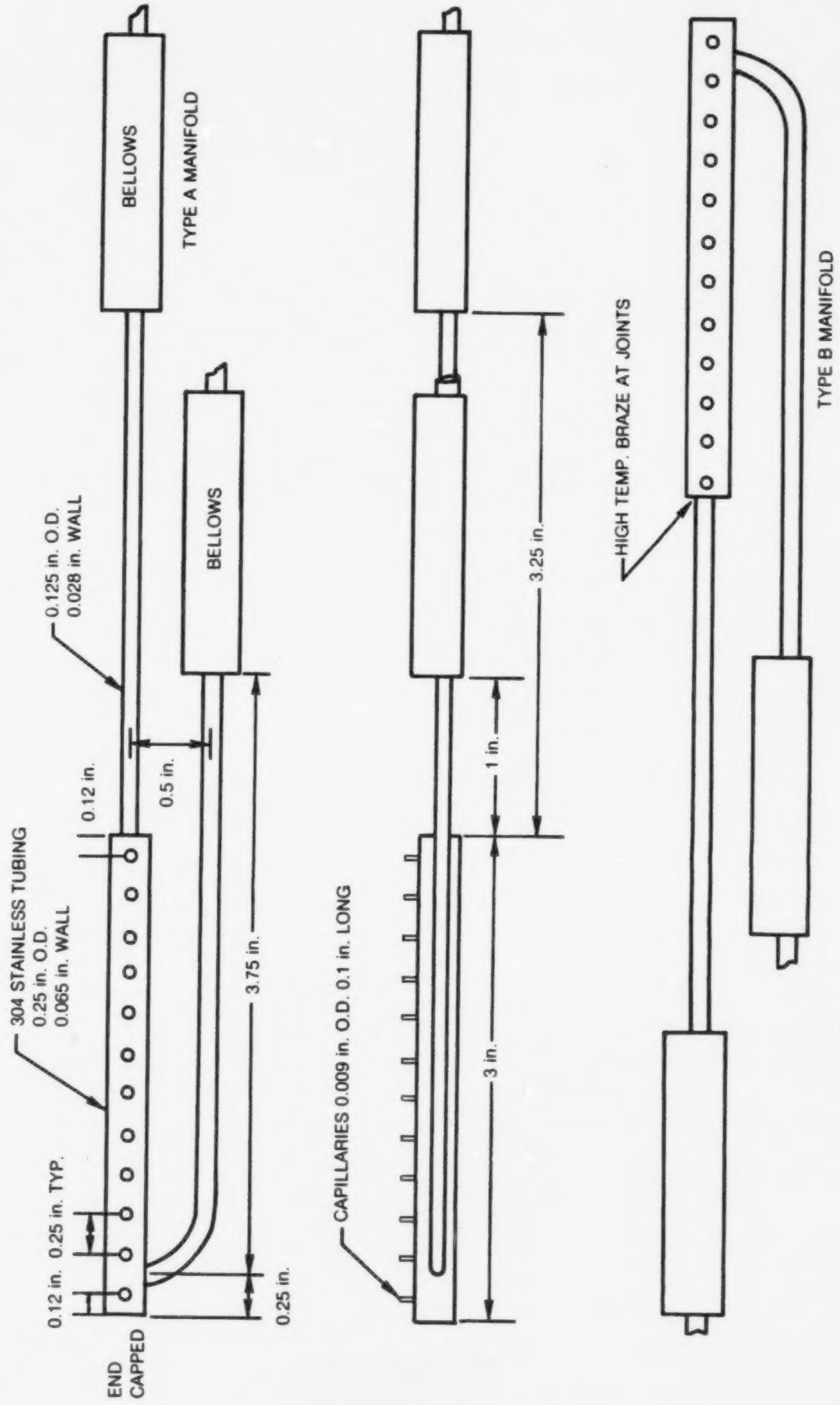
BELLOWS
TYPE A MANIFOLD
BELLOWS
0.125 in. O.D.
0.028 in. WALL
0.12 in.
0.5 in.
304 STAINLESS TUBING
0.25 in. O.D.
0.065 in. WALL
3.75 in.
0.12 in.
0.25 in.
0.25 in. TYP.
0.25 in.
END CAPPED
CAPILLARIES 0.009 in. O.D. 0.1 in. LONG
3.25 in.
1 in.
3 in.
HIGH TEMP. BRAZE AT JOINTS
TYPE B MANIFOLD

tubes are individually brazed into the main manifold using an electron-beam welder. The inlet to the capillary extends to the centerline of the main manifold tube. This reduced the possibility of forcing foreign particles into the capillaries during brazing. The manifolds are driven from below by small U-shaped shafts connected to the vibrators. Teflon sleeve bearings are used to retain the shafts in the mounting plate. Each manifold has a fuel inlet and exhaust by-pass line which is isolated from the support clamp with stainless steel bellows, thereby reducing the damping effect of the fuel lines on the vibrations of the manifolds. Electric resistance heaters are used to preheat the manifolds to desired operations temperature.

The 24 capillary manifold system is mounted on a support rack, seen in Figure 4. The vibrators and manifolds can be translated back and forth up to 2.5 cm by a manual traverse system which allows for fine positioning of the injectors. The entire support rack is mounted inside an injector box in such a manner that the rack can be rotated so that the capillaries form an angle of 30 to 90 degrees relative to the floor of the combustor. The rack is literally hung like a swing, and the angle of the capillaries relative to horizontal can be continuously adjusted between the above limits by the turning of a fine threaded rod (Figure 5).

The injector box is mounted beneath the floor of the combustor. A 2.5 cm x 15.24 cm slot in the combustor floor is located above the capillaries such that the droplet streams can be injected through the slot into the combustor. Because two injector locations are required, the entire injector box can be moved 15.24 cm (6 inches). Inserts in the combustor floor are used to accommodate the translation of the injector box in the X-direction. (See Figure 1 for clarification of X, Y, Z coordinate directions.) The slot in the combustor floor is also effectively moved through the use of inserts.

Individual capillaries are aimed by forcing trichloroethylene through the manifold and observing the stream trajectory through the slot. The entire line of droplet streams can be adjusted to pass through the slot by adjusting the slide upon which the support rack is mounted. The angle of injection is varied with the threaded rod which pushes a cam-follower. This in turn swings the support rack through an arc. The inlet fuel lines to the support rack are flexible so that the angle of injection can be varied without altering the fuel system or placing strain on the fuel lines. The injector box is a self-

Reproduced from
best available copy.

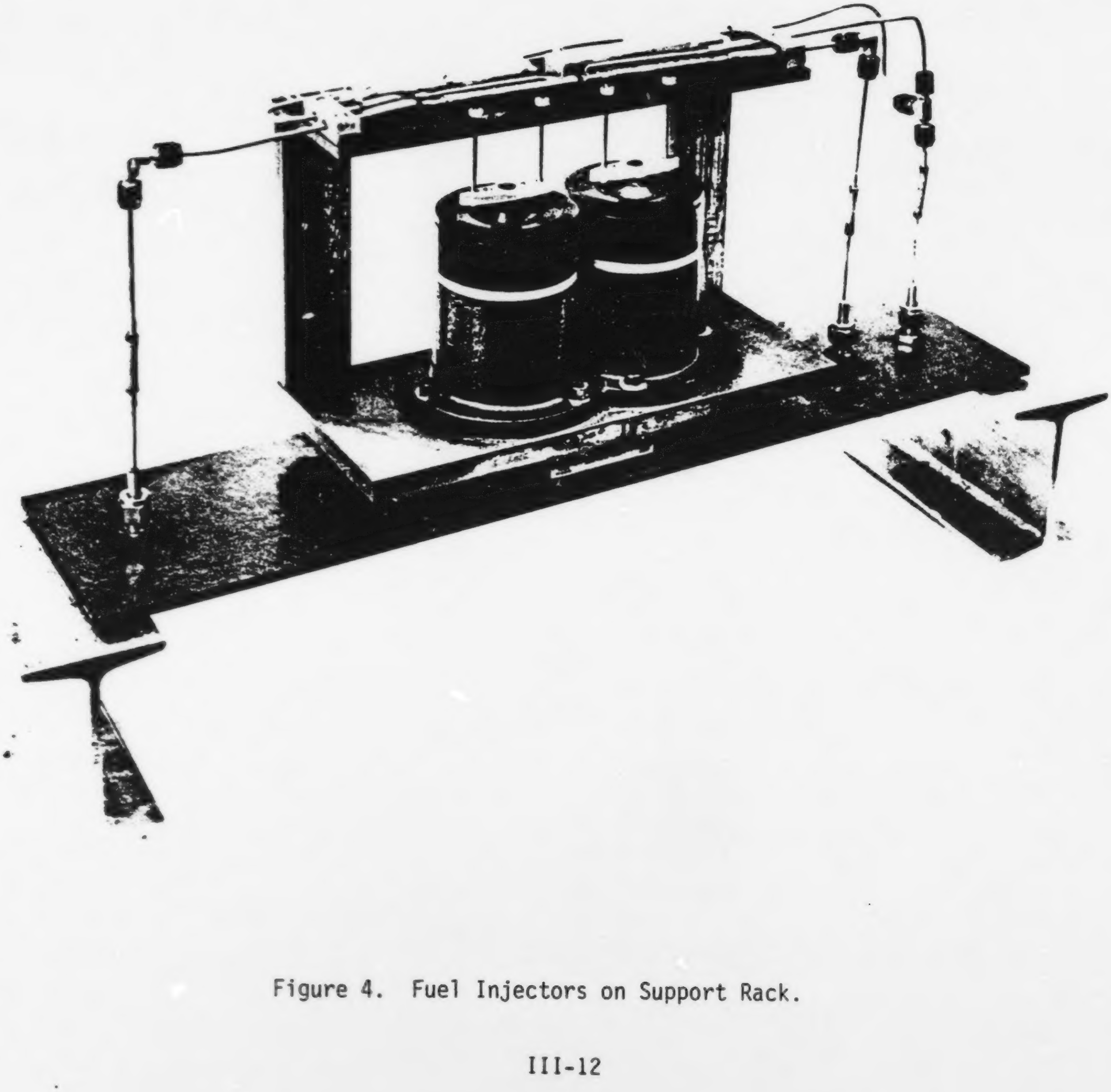

Figure 4. Fuel Injectors on Support Rack.

FIG. 5 OIL DROPLET INJECTOR ENCLOSURE

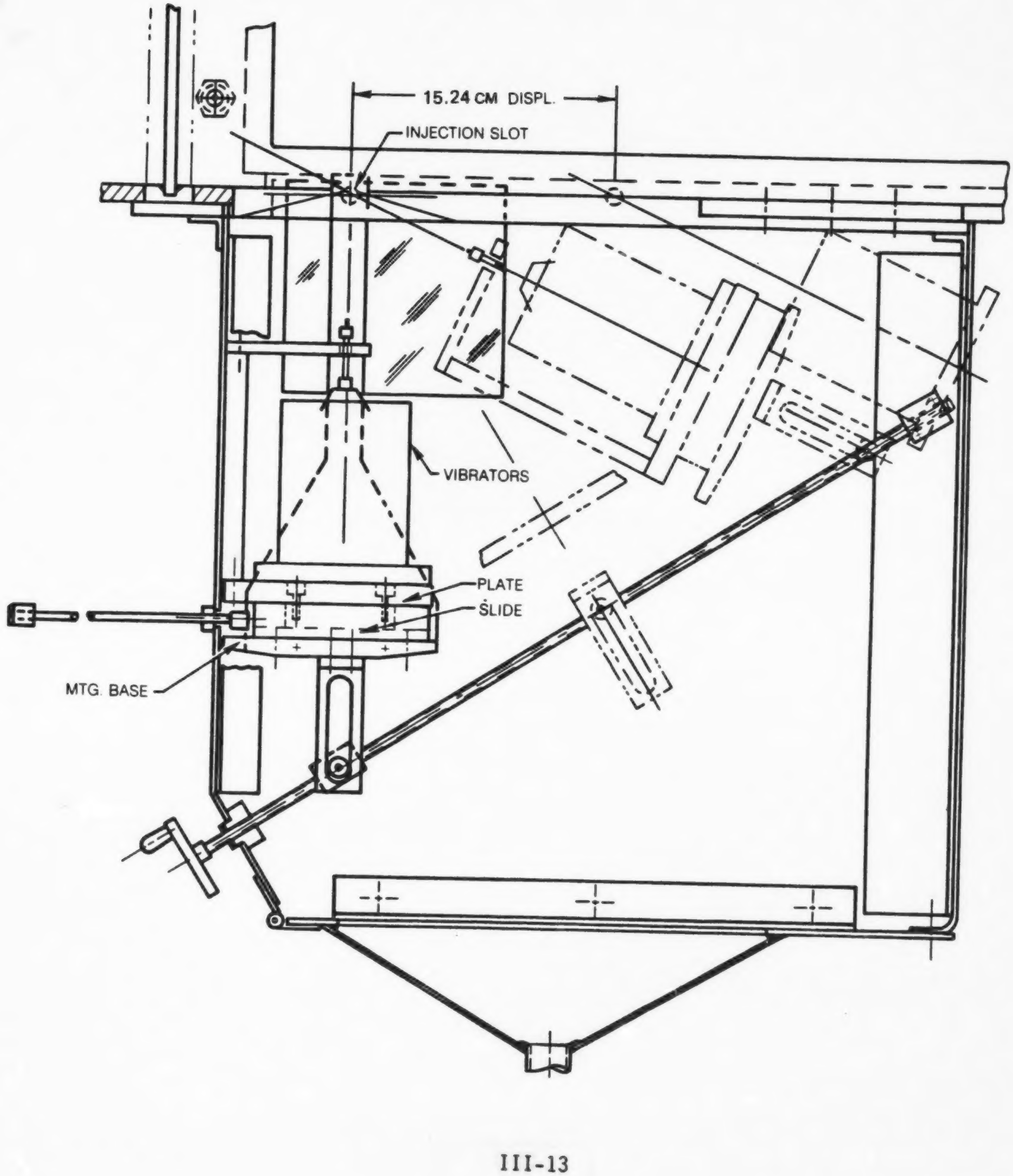
15.24 CM DISPL.
INJECTION SLOT
VIBRATORS
PLATE
SLIDE
MTG. BASE

contained unit which houses the heaters for temperature regulation, the fuel manifold system, and a collection reservoir for any oil spills which may occur during start-up or capillary misalignment.

The vibrators are driven by a stereo audio amplifier fed from a signal generator. An oscilloscope monitors the frequency and amplitude of the driving signal, and a stroboscope is triggered by the signal generator. A window in the injector box allows viewing of the droplet streams, and the strobe is used to "freeze" the droplet motion to allow tuning of the oscillator to the optimum frequency.

2.1.3 Wind Tunnel

The wind tunnel consists of a 4:1 area ratio rectangular nozzle 25.4 cm (10 inches) wide and 40.64 cm (16 inches) high at the throat. The nozzle contour consists of two cubic arcs designed to provide uniform exit flow without separation according to the method of Morel (1977). The absence of separation was verified analytically by computing the boundary layer history under the imposed potential flow field. The estimated turbulence level at the throat is 0.1% and the estimated boundary layer displacement thickness is 0.125 cm. All calculations are based on a design point throat velocity of 80.48 m/sec (100 ft/sec). The nozzle is preceded by a calming section consisting of perforated plates, honeycomb cells and screens. Screens (60 mesh) and perforated plates were 50% open to prevent jet coalescence. A 60 mesh screen was placed six cell diameters downstream of the honeycomb to suppress turbulence generation by the honeycomb (Loehrke and Nagib, 1972).

2.1.4 Hot Gas Generator

The hot gas generator consists of the upstream mixing and calming plenum, the flameholder, and the volume bounding the hot gas upstream of the splitter plate trailing edge. Fuel (propane) is injected towards the rear of the plenum through an upstream-facing manifold and is mixed uniformly with air upon passing through the perforated plate and screens. Because of the very low flow through the plenum and the possibility of flow separation, no nozzle is provided at the plenum exhaust.

The initial flameholder consisted of equi-spaced parallel rods of 0.157 cm diameter with 50% open area and was designed to provide a stable flame at ϕ = 1.5 and an approach velocity of 0.914 m/sec (3 ft/sec) (Ball, et al, 1978).

The spacing between rods was less than the quenching diameter at $\phi = 1$ (Lewis and von Elbe, 1961). Flameholder solidity was 50% to prevent jet coalescence. Assuming laminar wakes, a maximum dimension of 0.157 cm (0.62 inches) and a stream velocity of 6.096 m/sec (20 ft/sec), the distance before the wakes begin to merge is approximately 1.27 cm. The minimum splitter plate length, 5.08 cm (2 inches), was selected to provide uniform flow at the splitter plate trailing edge and is also the distance of closest approach of droplets to the flameholder without wake effects. A longer splitter plate is provided to increase the soak period of vaporized feed. Maximum splitter plate length is 15 cm.

2.1.5 Combustion Chamber

The three sided steel combustion chamber is 25.4 cm (10 inches) wide, 20.32 cm (8 inches) high, and 76.2 cm (30 inches) long. The top of the combustor is open in order to provide a more realistic simulation of the pressure field in a boiler or furnace flame. The open top also facilitates flame sampling. Each combustor side wall is fitted with 9.14 cm (3.6 inches) x 15.24 cm (6 inches) fused quartz windows, thus allowing optical access along one half the combustor length. The remainder of the side wall is a carbon steel water-cooled, filler piece. The positions of the windows and filler piece are interchangeable so that the entire combustion chamber can be probed optically. The bottom wall of the combustor is a water-cooled insert which is bolted to the combustor frame. This insert has a one inch radius inlet and thus provided a small area contraction just downstream of the flameholder plate. The results section presents rationale for addition of this insert to the experimental system.

2.2 Fuel System

The fuel system is shown schematically in Figure 6. Filtered and heated No. 6 oil is provided to the capillaries at a controlled pressure. Fuel flow rate and routing are remotely controlled. A central, remote, control panel is used to regulate pressure, read flow rates, and operate solenoid valves. The No. 6 oil is pre-filtered through a 60 micron filter and stored in a 55 gallon storage drum. This storage drum is used to preheat the fuel to 38°C (100°F) so that it can be easily pump-transferred to a five gallon fuel tank which serves as the fuel reservoir during actual testing. A high pressure gear pump is used

FIG. 6 HEAVY OIL COMBUSTOR FUEL SYSTEM

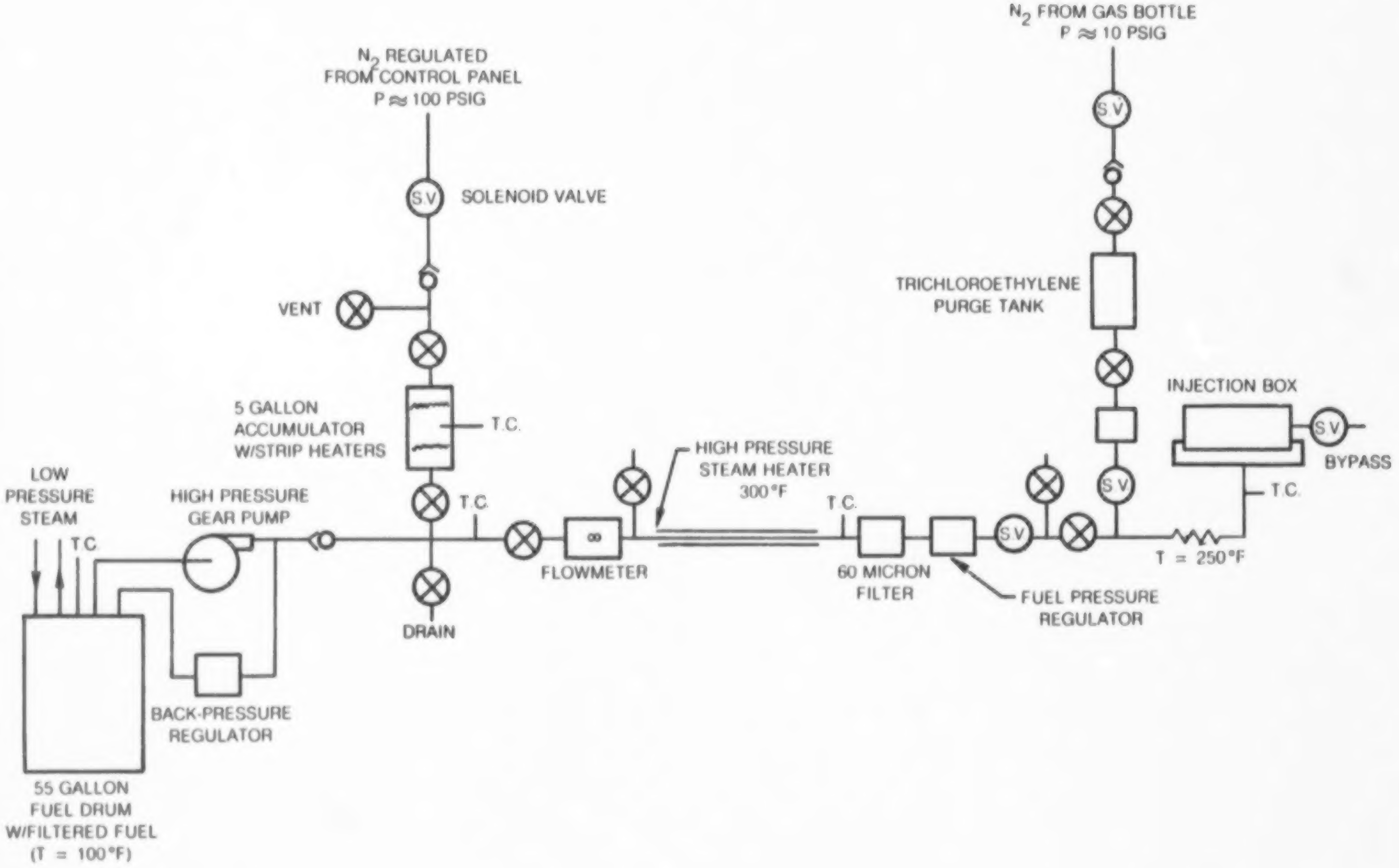

N_2 REGULATED FROM CONTROL PANEL $P \approx 100$ PSIG
S.V
SOLENOID VALVE
VENT
5 GALLON ACCUMULATOR W/STRIP HEATERS
T.C.
T.C.
DRAIN
LOW PRESSURE STEAM
T.C.
HIGH PRESSURE GEAR PUMP
BACK-PRESSURE REGULATOR
55 GALLON FUEL DRUM W/FILTERED FUEL (T = 100°F)
∞
FLOWMETER
HIGH PRESSURE STEAM HEATER 300°F
T.C.
60 MICRON FILTER
FUEL PRESSURE REGULATOR
S.V
N_2 FROM GAS BOTTLE $P \approx 10$ PSIG
S.V
TRICHLOROETHYLENE PURGE TANK
S.V
INJECTION BOX
S.V
BYPASS
T.C.
T = 250°F

for transferring the fuel. A steady supply pressure is applied to the accumulator. The upstream fuel supply pressure is independently regulated. The fuel is driven out of the accumulator, where it is kept at 38°C (100°F), through a positive-displacement flow meter and into a steam heater where it is heated from 38°C to 1210°C. After heating, the fuel is filtered again through a 60-micron filter before entering the fuel pressure regulator.

The fuel enters the injection box through an electrically heated, flexible section which allows for slight movement of the injector box. The fuel leaves the system through the exhaust bypass or is injected directly through the capillaries. After completion of a test, the fuel is purged from the capillaries in order to prevent deposit buildup. A trichloroethylene flushing system is used for this purpose. The solvent is admitted to the fuel lines downstream of the fuel filter, then passed through the fuel lines, manifold and bypass line. Once the lines are clean, the bypass is closed and the solvent is forced through the capillaries. Use of the solvent makes aiming of the capillaries and checking of trajectories particularly easy. Prior to each test the capillaries are checked for flow without spraying oil into the combustor. During startup and prior to injection through the capillaries, the fuel flows through the system and out the exhaust bypass line until all the solvent is flushed from the system.

Temperature control is particularly important in handling the No. 6 oil. Temperature is monitored in seven locations in the fuel system to control fuel delivery temperatures and to reduce the risk of overheating.

2.3 Sampling Probe

A probe was designed and constructed which can be used to obtain gas samples in regions where solid particles or liquid droplets coexist with gaseous combustion products. The well known principle of inertial separation is used to separate gases and particulates. The main stream, comprised of gas and entrained particles enters the probe and is accelerated to high velocity in a nozzle. The sample gas stream is drawn off at right-angle to the direction of flow of the main stream at the throat of the nozzle, and most of the particles and main stream are vented while the sample stream is directed to the gas analyzers. A schematic representation of the probe is shown in Figure 7.

FIG. 7 PHASE SENSITIVE PROBE

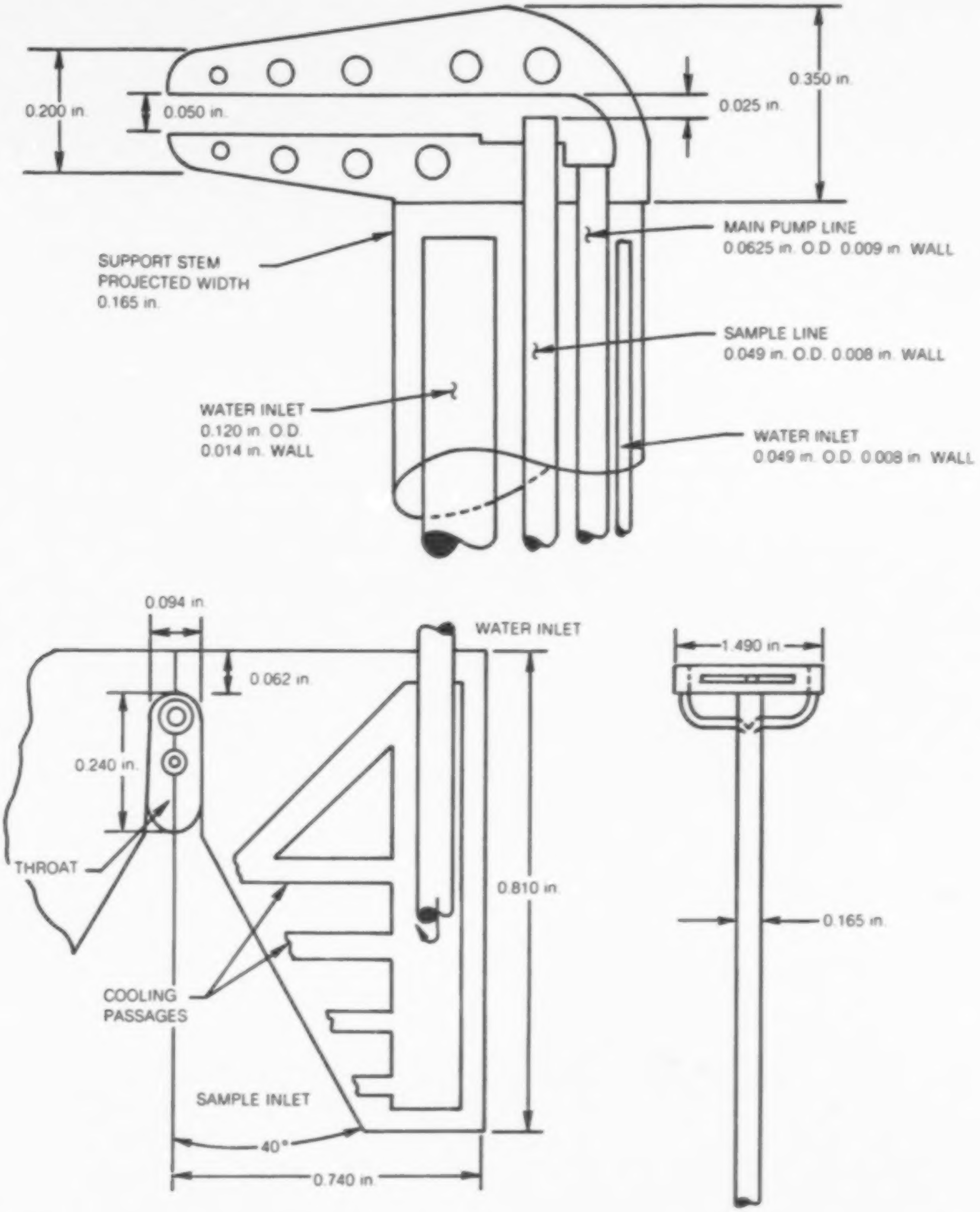
0.200 in.
0.050 in.
0.025 in.
0.350 in.
MAIN PUMP LINE
0.0625 in. O.D. 0.009 in. WALL
SUPPORT STEM
PROJECTED WIDTH
0.165 in.
SAMPLE LINE
0.049 in. O.D. 0.008 in. WALL
WATER INLET
0.120 in. O.D.
0.014 in. WALL
WATER INLET
0.049 in. O.D. 0.008 in. WALL
0.094 in.
0.062 in.
WATER INLET
1.490 in.
0.240 in.
THROAT
0.810 in.
0.165 in.
COOLING
PASSAGES
SAMPLE INLET
40°
0.740 in.

The operating characteristics of various probe designs were determined analytically. The computer code developed to compute droplet trajectories was used to calculate the paths of droplets as a function of main gas stream velocities, sample line velocities, and inlet-throat area ratios. A potential flow velocity solution was imposed on the droplets, and a rough calculation grid devised. The "cutoff" diameter for a particular probe configuration was defined as follows. All particles in a streamline 1/4 of the throat height above the sample line inlet would not be drawn into the sample line tube if their diameter was greater than the "cutoff" diameter. Some particles below the cutoff diameter would be swallowed depending on their size and position. All particles entering the probe below this streamline would be drawn into the sample line tube if their diameter was less than or equal to the cutoff diameter. Calculations were then performed for a given probe configuration to determine the effect of sampling velocity and main gas velocity on cutoff point. It was determined that to have a cutoff diameter of 10 microns it would be necessary to accelerate the main gas stream to 268 m/sec while maintaining a sample line inlet velocity of 64 m/sec. The sample line inlet velocity is determined by the flow requirements of the instrumentation (32 cc/sec) and the sample tube diameter. Because the probe is to be used in gas streams where the velocity would be about 30 m/sec, a large reduction in area was needed in order to maintain a probe inlet velocity nearly equal to that of the free stream while attaining a throat velocity of 268 m/sec. This contraction was effected in one dimension only in order to keep the probe profile small. At the same time, this inlet shape provides a spanwise average gas sample, i.e., the probe inlet width is greater than the separation between fuel injection source. The probe is cooled with high pressure water heated to 144°C. A step at the sample line inlet allows any buildup of liquid at the leading edge of the tube to be drained off into the main pump line. The sampling rate, and hence the velocities in the two streams, are regulated downstream by the use of valves.

2.4 Sampling System

Detailed profiles of composition (total hydrocarbons, NO_x, CO, CO_2, N_2, H_2) are obtained with the gas sampling system shown schematically in Figure 8. An integral part of the system, not shown here, is the probe positioning device which enables the probe to be moved in increments of as small as 0.000 318 cm, with positive position readout capability in two axes. This precise

FIG. 8 HEAVY OIL COMBUSTOR GAS SAMPLING SYSTEM

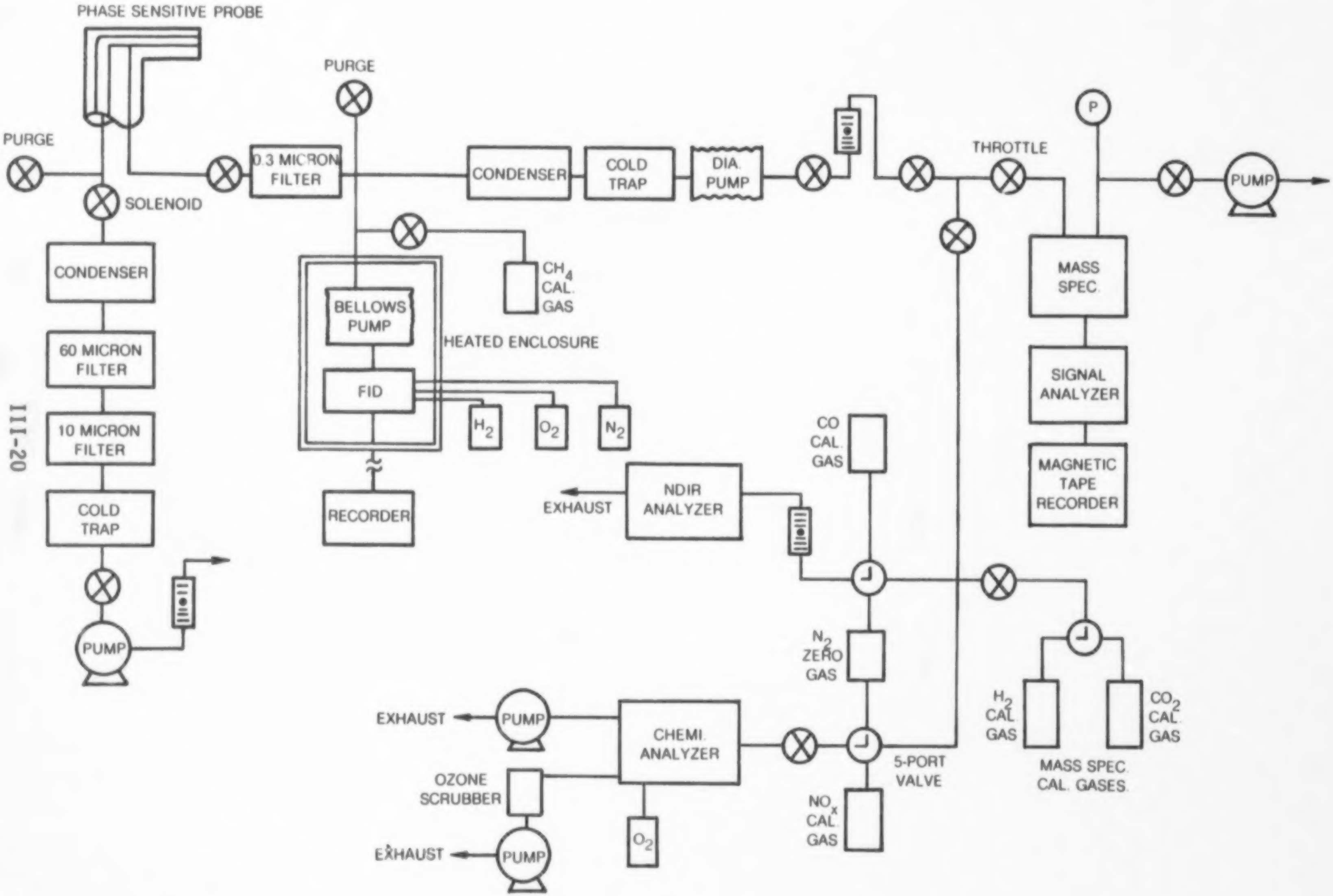
PHASE SENSITIVE PROBE
PURGE
SOLENOID
CONDENSER
60 MICRON FILTER
10 MICRON FILTER
COLD TRAP
PUMP
0.3 MICRON FILTER
PURGE
BELLOWS PUMP
FID
HEATED ENCLOSURE
RECORDER
CH$_4$ CAL. GAS
H$_2$
O$_2$
N$_2$
CONDENSER
COLD TRAP
DIA. PUMP
THROTTLE
P
PUMP
MASS SPEC.
SIGNAL ANALYZER
MAGNETIC TAPE RECORDER
NDIR ANALYZER
EXHAUST
CO CAL. GAS
N$_2$ ZERO GAS
NO$_x$ CAL. GAS
5-PORT VALVE
H$_2$ CAL. GAS
CO$_2$ CAL. GAS
MASS SPEC. CAL. GASES.
CHEMI. ANALYZER
O$_2$
PUMP
EXHAUST
OZONE SCRUBBER
PUMP
EXHAUST

probe positioning is accomplished using a variable speed stepping-motor and controller in the Y axis which provides the high accuracy mentioned above, and a constant speed drive with potentiometric readout on the Z axis. The probe can be manually traversed in the X direction where repetitive high accuracy positioning is not required.

The main gas stream from the probe passes through a condenser, two filters of 60 and 10 micron rating, and a cold trap before passing through a throttling valve into the main pump. The pumping rate, and hence the sampling velocity at the probe inlet, are controlled by the throttling valve, with total flow being measured with a rotameter at the pump exhaust.

The sample line to the hydrocarbon analyzer is teflon coated aluminum tubing, and is maintained at 150 C. The hydrocarbon analyzer was designed and built at UTRC, and consists primarily of a heated bellows pump, flame ionization detector, and temperature regulated oven. The instrument is located alongside the combustor in order to maintain sample lines as short as possible. Oxygen is used in the FID flame to ensure complete combustion of the sample gases. The electrometer and recorder are located within the control room. The gas sample is also directed through a condenser, a cold trap, and two total filters, before entering the analyzers. A diaphragm pump is used which has a teflon coated head. Sample lines and instruments downstream of the pump exhaust are at slightly positive pressure, thereby eliminating the possibility of air leakage into the sample. Sampling rate is metered. Three analyzers are used in this leg of the sampling system. A UTRC designed time-of-flight (TOF) mass spectrometer is used to determine O_2, CO_2 and N_2 concentrations. The mass spectrometer output is fed to a Northern NS-575 digital signal analyzer. A Northern NS-408F magnetic tape control interface, and a Wang MOD-7 7-track magnetic tape recorder are used to record the data. A computer program is used to convert the data to mole fractions. Mixtures of 2.76% CO or 10.3% CO_2 in nitrogen were used periodically to calibrate the mass spectrometer. Carbon monoxide (CO) concentration was determined with a Beckman model 864 Infrared Analyzer. A mixture of 2.76% CO in N_2 was used to calibrate the unit, and it was zeroed and calibrated repetitively during the course of a run. NO/NO_x concentrations were determined using a Thermo Electron model 10AR Chemiluminescent Analyzer. A calibration gas of 395 ppm NO in N_2 was used to calibrate the unit and perform periodic checks during sampling. Calibration gas data are presented in Table I. The entire sampling system was leak-checked prior to each test by using the mass spectrometer to detect the presence of O_2 after inserting the probe into a stream of N_2. The highly sensitive method of on-line leak checking ensured that accurate gas samples were obtained.

Table I. Calibration Gas Data

GAS	SUPPLIER	ACCURACY
1. 2.76% CO 97.24% N_2	Scott Environmental Technology	± 2% for CO
2. 10.3% CO_2 89.7% N_2	Scott Environmental Technology	± 2% for CO_2
3. 395 PPM NO Bal. N_2	Scott Environmental Technology	± 2% NO
4. Zero Gas 100% N_2	American Industrial & Medical Products, Inc.	UHP 99.999% min.

3.0 TEST RESULTS

Testing to date has consisted of fuel injection studies, cold flow mapping and turbulence measurements, recirculation studies, and preliminary flame probing both with and without oil injection.

3.1 Fuel Injector Development

Experiments have been conducted with No. 2, 5 and 6 oil in single and multiple capillary injectors in order to measure maximum attainable droplet velocities, insure a multicapillary capability, and to investigate possible capillary clogging with heated heavy oils.

The calculations indicate that velocities up to about 9.14 m/sec (30 fps) are required with 200 μm drops to achieve desired trajectories and fueling rates. Using an existing UTRC apparatus (Sangiovanni and Kesten, 1977) a droplet velocity of 10.7 m/sec (35 fps) was demonstrated with No. 2 oil for drops about 240 μm in diameter. This system consisted of an electromagnetic vibrator driving a stainless steel tube with a small capillary soldered in one end. The capillary was 0.15 cm (0.006 inches) in I.D. and about 0.254 cm long. Fuel pressure was about 3.4 to 4.7 atmospheres and the vibrator was driven at a frequency in the range f = 10-20 kHz. Polaroid photographs were taken of the droplet stream using a pulsed light source. Uniform drops were observed to be formed and droplet size, d, and spacing, λ_d, were measured from the photographs. Droplet velocity was then calculated using the relation

$$v = f\lambda_d$$

A typical set of data are given in Table II. Stable uniform droplets were observed over a frequency range of about f = 12-18 kHz. These parameters are consistent with prior observations in the field and show that the desired maximum velocity condition can be achieved conveniently with a drive frequency in the upper part of the audio band. Sufficient leeway exists among the parameters p, f, d_j and $f\lambda_d$ in order to vary v and d_o over the desired range.

Following the tests with the single capillary injector, a three capillary model of the final fuel injector, having the same manifold size and mounting arrangement, was used to verify that monodisperse droplets could be produced in this system. Tests were conducted with No. 2 and No. 5 oil in the multiple capillary injector to demonstrate monodisperse droplet formation from

Table II. No. 2 Oil Injection Test Results: Single Capillary

CONDITIONS

Capillary I.D. - d_c	0.0006" (0.15 mm)
Fuel Supply Pressure - p	3.0 ATM (gauge)
Vibrator Frequency - f	15 kHz

MEASUREMENTS

Droplet Spacing - λ_d	0.71 mm
Droplet Diameter - d_o	0.24 mm
Liquid Jet Diameter - d_j (vibrator off)	0.13 mm

RESULTS

Droplet Velocity - $v = f\lambda_d$	1068 cm/sec
Spacing to Jet Size Ratio - λ_j/d_j	5.5
Droplet Size to Jet Size Ratio - d_o/d_j	1.9

$$\text{calculated value} = d_o/d_j = \sqrt[3]{\frac{1.5\lambda_d}{d_j}} = 2.0$$

capillaries at the middle and extreme ends of the injector. The fuel manifold was 7.67 cm (3 inches) long and contained three capillaries of 0.015 cm (.006 inches) I.D. and .254 cm (0.1 inches) length. Initially, tests were performed with No. 2 oil at room temperature. Because of the fixed relationship between capillary I.D. and droplet size (Sangiovanni and Kesten, 1977), droplet size was estimated to be 300 microns. Three parallel streams of 300 micron diameter droplets with velocity of 775 cm/sec were produced with a fuel pressure of 20 psig and a vibrator frequency of 15.5 kHz. The monodisperse streams were well behaved at a distance 9 cm from the injector tips at this low velocity. Following the No. 2 oil demonstration, the injector was operated using No. 5 oil heated to approximately 127°C. Multiple streams of 340 micron diameter droplets were produced at a velocity of 525 cm/sec, a frequency of 5.6 kHz and a fuel pressure of 2.05 atm Velocities of 1050 cm/sec were obtained with 280 micron diameter droplets at a fuel pressure of 4.1 atm and a frequency of 10.5 kHz. The droplet streams at the high velocity were well aligned 25 cm from the injector tip.

Further tests were performed on the bench-scale capillary injector with a sample of Indonesian/Malaysian No. 6 oil. Satisfactory droplet injection was demonstrated with the oil heated to 138°C (see Table III). The following dimensionless relationship between injection velocity (v), vibrator frequency (f), and jet diameter (d_j) was found

$$\frac{v}{fd_j} = 4.76$$

This value of v/fd_j is in accord with previous experience with other liquids.

A further significant development was a demonstration of several shut-down cycles without clogging. Monodisperse droplets were produced in all capillaries with only occasional plugging of a capillary. In all cases, this plugging was eliminated by flushing trichlorethylene through the manifold. The manifold flushing system proved invaluable in facilitating restarting after a cold shutdown; hot restarts did not require any flushing.

3.2 Cold Flow Velocity Profiles

Cold flow velocity profiles were determined at several axial locations from total and static pressure measurements. Lateral and vertical profiles

Table III. No. 6 Oil Injection Test Results: Multiple Capillary

CONDITIONS

Capillary I.D. - dc	0.006" (0.15 mm)
Fuel Supply Pressure - p	3.0 ATM (gauge)
Vibrator Frequency - f	5.58 kHz

MEASUREMENTS

Droplet Spacing - d	0.81 mm
Droplet Diameter - d_o	0.32 mm

RESULTS

Droplet Velocity - $v = f\lambda_d$	450 cm/sec
Droplet Size to Jet Size Ratio - d_o/d_j	2.13

$$\text{calculated value} = d_o/d_j = \sqrt[3]{\frac{1.5\lambda_d}{d_j}} = 1.89$$

at the nozzle exit are shown in Figure 9. Figure 9a shows lateral profile two inches (5.08 cm) below the top of the air nozzle at the nozzle exit, and 40.6 cm (16 inches) downstream of the nozzle exit. Figure 9b shows vertical profiles at the nozzle mid-plane. It is seen that nozzle exit profiles are very flat. Boundary layer thicknesses are close to computed values. Figure 9b also illustrates the strong inward deflection of the primary air jet for a secondary velocity of zero. At a primary jet velocity of 30.48 m/sec, static pressure at the nozzle exit was 0.5 torr below atmospheric due to the strong pumping action of the primary jet. Later on, during combuston testing, it was found that this led to air leaks, primarily through the injection slot. Turbulence levels were measured with a hot film anemometer at various radial and axial locations. The minimum turbulence level at the nozzle exit occurred at the center of the nozzle and increased toward the nozzle walls. Turbulence intensity varied from 1.3 to 2.7%. These levels are considerably higher than predicted. Spectral analysis of the velocity fluctuations indicated no predominant frequencies which might be attributed to flow oscillations or large scale instabilities. The broad spectrum of fluctuations is, therefore, attributed to green or grid noise. Further tests are planned in order to find the cause of high turbulence levels.

3.3 Recirculation Studies

It was found during the cold flow mapping studies that, under certain conditions, recirculation occurred within the combustion chamber. Consequently several combinations of primary and secondary stream velocities were studied to define stable flow regimes. The mixing of hot and cold streams was simulated by mixing two cold streams at the same ratio of dynamic pressures as would exist under combustion conditions. For a hot stream velocity of 6.1 m/sec, the corresponding cold stream velocity is 2.3 m/sec, assuming a density ratio of about 7. Small tufts of yarn were taped to the combustor, splitter plate, and nozzle walls in order to visualize separation and secondary flows. Recirculation occurred at various locations along the combustion chamber depending upon velocity level and velocity ratio. Recirculation could be prevented by sloping either the upper or lower combustor walls (plexiglass inserts were used for this purpose) or retarding the rate of mixing by thickening the primary stream boundary layer. Boundary layer fences were used for this purpose. No recirculation was observed with a straight, open duct at a primary

FIG. 9 VELOCITY PROFILES

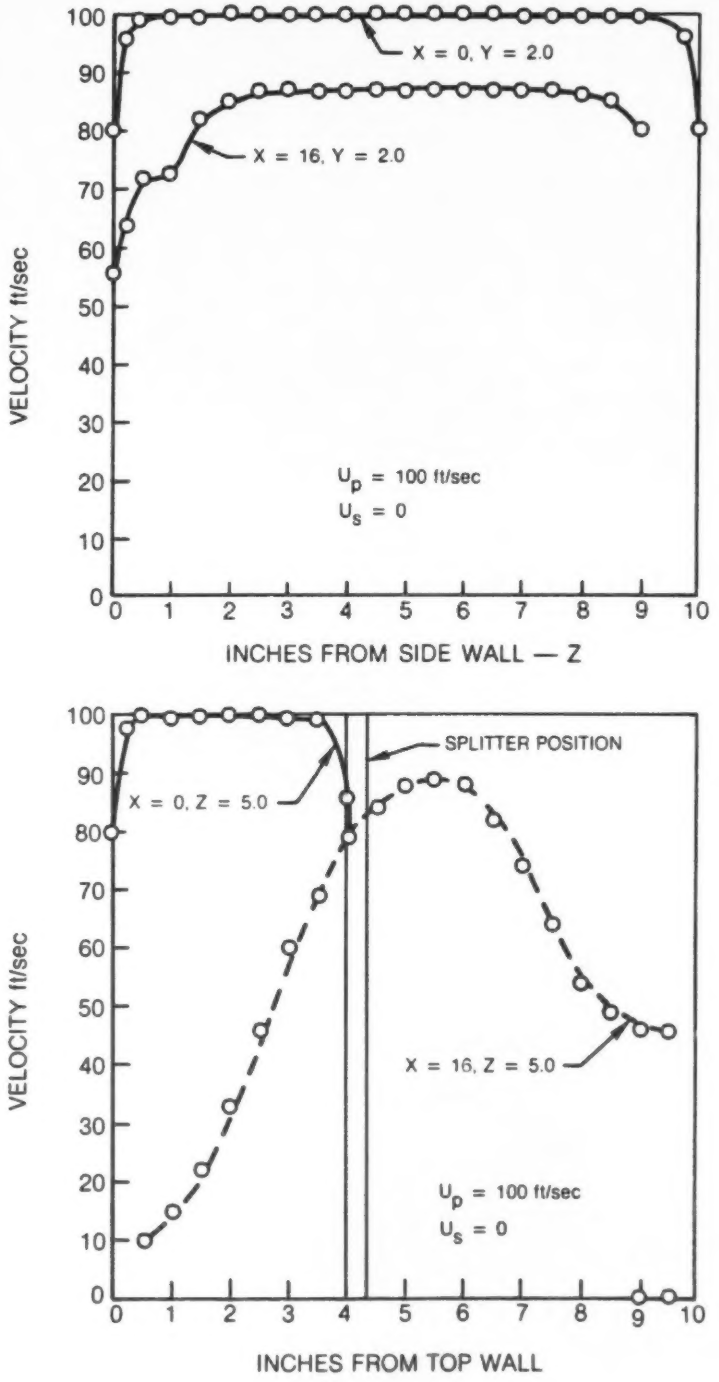

velocity of 30.5 m/sec and a secondary velocity of 4.6 m/sec. This high secondary flow is not desirable, however. At a secondary flow velocity of 2.3 m/sec, a primary velocity of 15.2 m/sec is permissible. The results were influenced by the type of flameholder, the smoothness of the walls and the nature of the boundary layer on the splitter plate. Best results were obtained with no flameholder in place. The high blockage, perforated plate flameholder caused secondary flows in some instances. A maximum primary velocity of 15.2 m/sec was attained with a flameholder in place when a smooth contoured insert was used as the combustor bottom wall. This high velocity was not previously attainable with a flameholder in place. It appears that even higher primary velocities are attainable with combustion. The flow did not appear to recirculate at a primary velocity of 22.9 m/sec when the hot gas generator was turned on. As a result of these tests, a water-cooled contoured insert was fabricated for combustion testing. This insert has a one inch (2.54 cm) radius inlet which provides a slight area contraction just downstream of the flameholder plate. Some of the test results are shown in the following table.

V_1/V_2	FLAMEHOLDER	WALL SLOPE	COMMENT
15.2/2.3	None	0	No separation with smooth wall insert
15.2/2.3	None	Slight	No separation without insert
15.2/2.3	10% Open Perforated Plate	Steep	No separation but strong cross flows on lower wall
15.2/2.3	10% Open Perforated Plate	0	No separation with contoured insert

3.4 Flame Stability Tests

The first flameholder tested had 50% open area and consisted of parallel, equi-spaced, 0.157 cm rods aligned with the floor of the combustor. The flameholder was designed to be stable to $\phi = 1.5$ with an approach velocity of 0.91 m/sec. The separation between rods was less than the quenching distance at

ϕ = 1. Unfortunately, flashback occurred even at the highest approach velocity of interest, 0.91 m/sec. The flame did not penetrate or damage the 200 mesh screen upstream of the flameholder however. It was thought flashback might have occurred from slight deviations in the rod spacing. Therefore a slotted flameholder 50% open, consisting of uniform alternating 0.157 cm slots and ribs was fabricated from 0.318 cm steel sheet stock. The slotted flameholder also allowed flashback. At this point it was decided that some turbulence and flow non-uniformity might be tolerated and several perforated plate flameholders were studied. Rich blowout limits generally increased with flameholders of higher solidity; rich blowout equivalence ratio varied from 1.12 to 2.1. Occasional flashback occurred with lower solidity flameholders. Several of the high blockage flameholders produced non-uniform flames of uneven luminosity. The first perforated plate flameholder tested was 30% open, with 0.127 cm holes. This flameholder allowed flashback at 0.61 m/sec but functioned satisfactorily at higher velocity. A second perforated plate flameholder, 10% open, with 0.157 cm holes was stable at ϕ = 1.32 and did not allow flashback at 0.61 m/sec. However, the flame appeared to be non-uniform. The most satisfactory performance was obtained with a commercially available filter screen manufactured by Michigan Dynamics. This flameholder consisted of 10% open perforated plate with 0.157 cm diameter holes. Two layers of fine screen were bonded to the back of the perforated plate. No flashback was encountered at an approach velocity of 0.46 m/sec, even at stoichiometric conditions. The appearance of the flame was uniform at all conditions. Most importantly, very rich operation was possible; blowout occurred at ϕ = 1.85 at an approach velocity of 0.76 m/sec. Thus it would appear that bonding screen to the perforated plate has a major positive influence on flashback characteristics. Subsequent gas sampling verified the uniform composition of the flame downstream of this flameholder.

3.5 Flame Probing

Initial flame probing experiments were conducted without oil injection in order to measure flame spreading rates (rich, hot gas stream), verify carbon balances and verify uniformity of the composition profiles at the hot gas generator exhaust. Since the pressure in the combustor was known to be slightly below ambient pressure, these experiments also provided information on air leaks.

Composition profiles were measured at four axial locations (X = 0, 13.0, 28.25, and 53.66 cm). In addition, some data were obtained just downstream of the injection slot trailing edge (X = 10.2 cm) in order to estimate the air inspiration rate through the slot. Oxygen profiles are shown in Figure 10. The data show that the flame width is not very sensitive to axial position; apparently, turbulent spreading of the streams is offset by the inward deflection of the streamlines. The oxygen profiles exhibit a minimum. This is attributed to air leaking through the injection slot. The data at X = 0 show that there is a small leak even before the injection slot. Taking this into account, it appears that the primary air stream has nearly penetrated to the combustor floor at the furthest downstream position. Thus, it is likely that the edge of the mixing layer will impinge upon the combustor floor near X = 76.2 cm, as intended.

Excellent carbon balances were obtained at $\phi = 0.8$ and 1.0. Metered and measured values were within 2 percent based on hot gas generator exhaust measurements. Measured CO readings were too low at $\phi = 1.3$ due to an NDIR analyzer malfunction , to give a satisfactory balance. Therefore, these data are not shown. The other composition data indicate that the hot gas generator exhaust composition is uniform. The oxygen profiles (see Figure 10) are believed to be correct.

Several attempts were made to sample the flame with No. 6 oil injection. However, testing was hampered by capillary clogging. It is believed that clogging is a result of temperature-induced deposit buildup in the fuel system. Although the capillaries could be flushed clean by use of solvent, clogging recurred in subsequent tests. Subsequent inspection of the fuel system indicated heavy deposit formation in the bellows. The bellows have been replaced by high temperature flexible tubing. Also, further tests will be conducted with diluted No. 6 oil (20% No. 2 oil) so that lower fuel operating temperatures are possible.

3.5.1 Apparatus Improvements

The composition profiles indicated that air was leaking into the combustor through the injection slot. This was attributed to the pumping action of the primary jet. In an effort to reduce the leakage rate, all the joints and feedthroughs of the injection box were sealed. Subsequent flame probing without

FIG. 10 OXYGEN PROFILES

COMBUSTOR MID-PLANE

$U_p = 75$ ft/sec

$U_s = 22$ ft/sec

$\phi_s = 1.3$

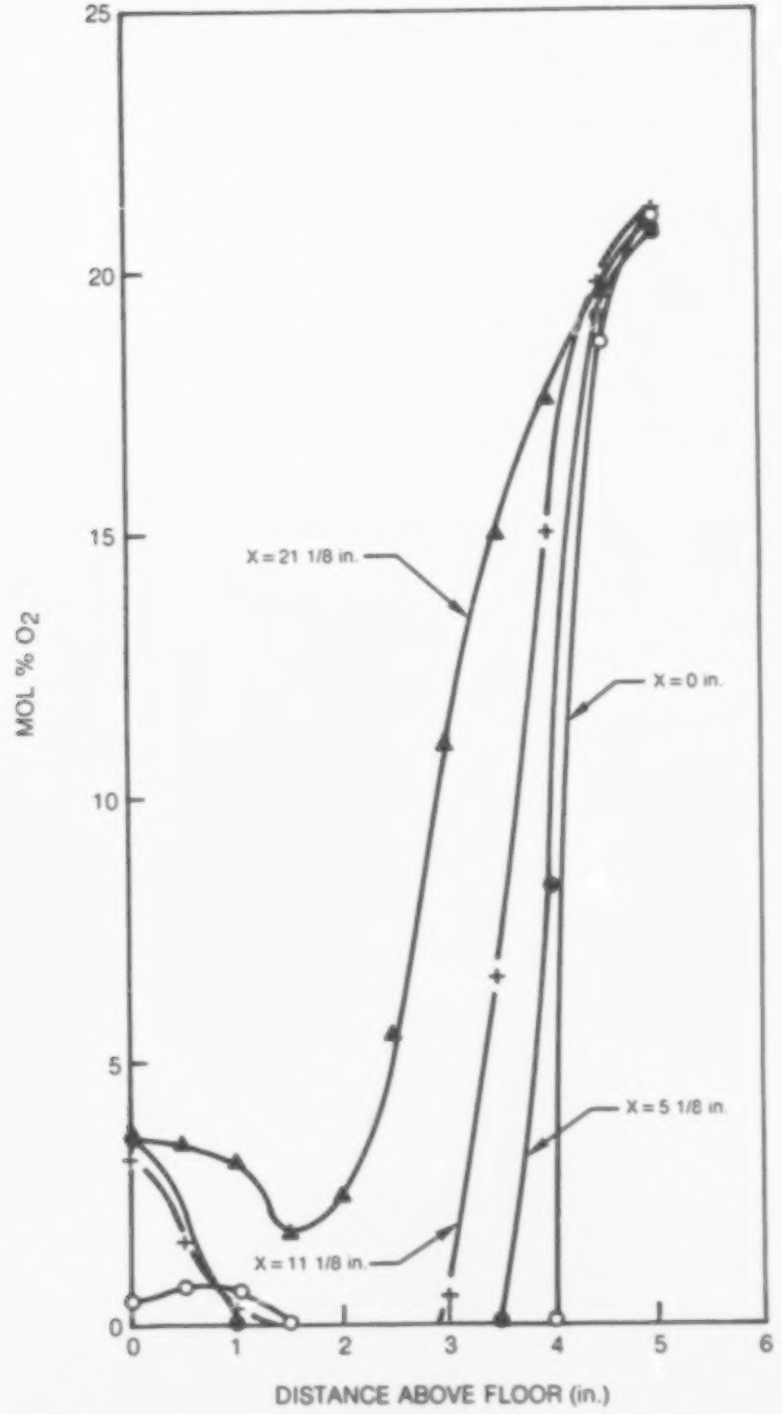

oil injection indicated that the leakage rate had been reduced substantially. However, it was found, that at this low leakage rate, and apparently as a result of an instability, hot gases entered the slot and impinged upon the capillary injectors. It was therefore decided that a combination of controlled suction and inert gas injection would be required to control the net flow of oxygen through the slot and prevent impingement of hot gases on the injectors.

An inert gas injection manifold was built and installed in the injector box. Inert gas was directed into the bottom of the box and into the upper corners of the box along the entire box width. In order to carefully control the total flow of gas through the slot, a vacuum pump was attached to the bottom of the box and the vacuum flow rate was regulated. It was hoped that the inlet flow rate of inert gas could be matched with the exhaust flow rate through the blower so that a minute trickle of inert gas would flow into the combustor through the slot. Since the box would be at a slightly higher pressure than the combustor, the flow of hot gases through the injection slot would be halted. In addition, the introduction of an inert gas into the box would reduce the explosion hazard associated with fuel vapors accumulating within the box. Argon was used as the inert gas because it could be easily detected by the mass spectrometer. The relative concentrations of oxygen, nitrogen, and argon were monitored in the hot gas stream with the probe just downstream of the injector. The argon flow rate was set, and the exhaust blower flow rate adjusted until there was effectively no flow through the slot, i.e., the argon entering the box was being pumped back out by the blower along with any air which had entered through leaks in the box. Surprisingly, this equilibrium could not be maintained for long. It appeared that after a short heating period, the pressure balance was upset and hot gas again flowed down through the slot. The exhaust flow was then adjusted until a slight positive flow into the combustor was detected. At this point, it appeared that it would be possible to match the diluent flow into the box so that there was no pressure differential across the slot, at least for a short period of time.

Prior to resuming oil injection tests, the floor of the combustor was removed and a new seal put in place at the leading edge of the floor insert. The quartz windows were also resealed, and the injection box seals were rechecked. When the slot flow was checked again under hot flow conditions, the flow had completely reversed direction, despite the fact that the diluent flow and pumping rate had not been changed from previous settings. The pressure differential was such that the exhaust blower could not be used at all. Apparently, resealing the combustor wall affected the flow through the slot. As the seals deteriorated, the flow field at the slot changed also. For this reason, it was decided to operate with a small positive flow of diluent upward through the slot, and the combustor will be operated in this manner henceforth.

3.6 Flame Photography

Short time exposure photographs and high speed cinematography have been used to examine the shear layer and droplet combustion. Both No. 2 and No. 6 oil sprays were photographed. High speed cinematography indicates the presence of large periodic disturbances in the shear layer, but the turbulence is three-dimensional. With oil injection, clearly observable droplet vapor trails were observed which move at the relative velocity of the droplets and gas stream. Droplet trajectories with No. 2 oil appear to be uniform, thus giving the flame a unique two-dimensional structure.

Flame photographs with and without oil injection are shown in Figure 11. The shear layer without oil injection is shown in Figure 11a. Luminosity arises from the combustion of the rich pilot gases (carbon monoxide). With No. 2 oil droplet injection (Figure 11b), the luminosity pattern shows two distinct zones: a luminous zone resulting from radiation of particulate pyrolysis products in the rich pilot gases, and an intensely luminous zone resulting from particulate formation in the shear layer. With No. 6 oil injection (Figure 11c), the luminosity is less intense because of slow vaporization and reduced gas phase pyrolysis. Individual soot streamers are evident in droplet wakes.

A. Shear Layer Combustion Without Oil Injection, $\phi_p = 1.3$.

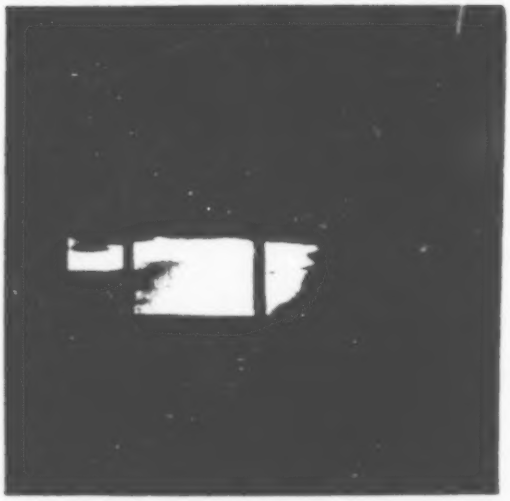

B. No. 2 Oil Combustion, $\phi_p = 0.8$.

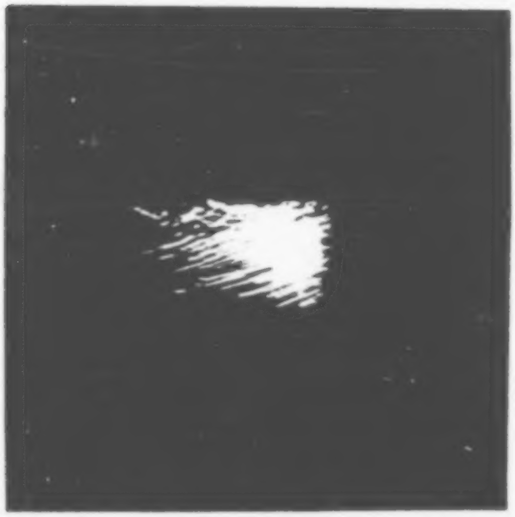

C. No. 6 Oil Combustion, $\phi_p = 0.8$.

Figure 11. Shear Layer and Droplet Combustion Photographs.

4.0 CONCLUSIONS

A unique combustion apparatus has been developed for the study of heavy oil spray combustion in shear layers. Linear arrays of mono-sized droplets may be injected with uniform trajectories into a two-dimensional shear layer. High droplet velocities necessary for ballistic penetration of the shear layer and for droplet prevaporization have been demonstrated with several fuel oils. The problem of capillary clogging with No. 6 oil is expected to be solved by diluting the oil and reducing fuel temperature.

5.0 REFERENCES

Ball, I. C., Rummel, D. H., Semerjian, H. G., and Vranos, A., "Bluff Body Stabilization of Premixed and Prevaporized Flames," Eastern States Section Combustion Institute Meeting, November 29-30 and December 1, 1978, Miami Beach, Florida.

Kobayasi, K., "An Experimental Study in the Combustion of a Fuel Droplet," Fifth Symposium (International) on Combustion, Reinhold, New York, 1955, pp. 141-148.

Lewis, B., and von Elbe, G., "Combustion, Flames and Explosion of Gases," Second Edition, Academic Press, New York, New York, 1961, p. 256.

Loehrke, R. 1., and Nagib, H. M., "Experiments on Management of Free-Stream Turbulence," Agard Report No. 598, September, 1972.

Morel, T., "Design of Two-Dimensional Wind Tunnel Contractions," J. Fluids Eng., June, 1977, pp. 371-378.

Sangiovanni, J. J., and Kesten, A. S., "Effect of Droplet Interaction on Ignition in Monodispersed Droplet Streams," Sixteenth Symposium (International) on Combustion, Reinhold, New York, 1977, pp. 577-592.